Final-state interactions in heavy-meson decays

Dissertation

zur

Erlangung des Doktorgrades (Dr. rer. nat.)

der

Mathematisch-Naturwissenschaftlichen Fakultät

der

Rheinischen Friedrich-Wilhelms-Universität Bonn

vorgelegt von

Johanna Niecknig

aus

Fulda

Bonn, Mai 2018

Angefertigt mit Genehmigung der Mathematisch-Naturwissenschaftlichen Fakultät
der Rheinischen Friedrich-Wilhelms-Universität Bonn

1. Gutachter: Professor Dr. Bastian Kubis

2. Gutachter: Professor Dr. Christoph Hanhart

Tag der Promotion: 10.07.2018

Erscheinungsjahr: 2018

Abstract

In the last decade the investigation of the heavy-meson sector has gained in importance, in particular for precision tests of the Standard Model and exploration of the physics beyond, such as CP violation. Experimentally, with the launch of the Large Hadron Collider (among several other experiments) great promise for high-precision analyses has been shown. At the same time a precise understanding and rigorous treatment of the theoretical aspects of the interactions is mandatory. In particular the strong final-state interactions, described by Quantum Chromodynamics, pose a challenge: at low energies, where the hadrons are the interacting degrees of freedom, the strong coupling becomes large and the standard perturbative solution methods fail. One non-perturbative approach is to apply dispersion relations, providing a model-independent framework that fulfills unitarity and analyticity constraints by construction. In this thesis we employ such dispersive techniques that allow one to either deduce the universal final-state interactions of light meson pairs from the accurately known $\pi\pi$, πK, and $\bar{K}K$ phase shifts, or likewise deduce crucial information on meson–meson scattering from the respective final-state interactions. The thesis is subdivided into two projects.

The first project is concerned with the decays $\bar{B}^0_{d,s} \to J/\psi(\pi\pi, \pi\eta, \bar{K}K)$, where the J/ψ is treated as an spectator and the pairwise final-state interactions of the light mesons are well described by the scalar and the vector form factors. In the scalar sector a coupled-channel treatment between the $\pi\pi$ and $\bar{K}K$ systems in the isoscalar sector and the $\pi\eta$ and $\bar{K}K$ systems in the isovector one is required. The $\bar{B}^0_{d,s} \to J/\psi\pi\pi$ channels are studied as to demonstrate the benefits of our formalism. We find very good agreement with the data up to 1.05 GeV in the $\pi\pi$ invariant mass, with a number of parameters reduced significantly compared to a phenomenological analysis. In addition, the phases of the amplitudes are correct by construction, a crucial feature for many CP violation measurements in heavy-meson decays. By means of certain symmetry and coupled-channel relations we give predictions for the other channels, providing information on $\pi\eta$ scattering.

In the second project an analysis of the semileptonic $D \to \pi K l \nu$ decay is presented. A deliberate and accurate treatment of the hadronic final-state interaction can deliver information on pion–kaon scattering. The analysis is based on a modified Omnès formalism where left-hand-cut structures are approximated by pole terms derived in Heavy-Meson Chiral Perturbation Theory. For a precision determination of the amplitudes as it is required for an extraction of πK phases further constraints, both experimental and theoretical, are highly desired.

Parts of this thesis have been published in the following articles:

- J. T. Daub, C. Hanhart and B. Kubis, *A model-independent analysis of final-state interactions in* $\bar{B}^0_{d/s} \to J/\psi\pi\pi$, JHEP **1602** (2016) 009 [arXiv:1508.06841 [hep-ph]].
- M. Albaladejo, J. T. Daub, C. Hanhart, B. Kubis and B. Moussallam, *How to employ* $\bar{B}^0_d \to J/\psi\left(\pi\eta, \bar{K}K\right)$ *decays to extract information on* $\pi\eta$ *scattering*, JHEP **1704** (2017) 010 [arXiv:1611.03502 [hep-ph]].

Furthermore, similar techniques are employed in the following publications:

- Y. H. Chen, J. T. Daub, F.-K. Guo, B. Kubis, U.-G. Meißner and B. S. Zou, *Effect of* Z_b *states on* $\Upsilon(3S) \to \Upsilon(1S)\pi\pi$ *decays*, Phys. Rev. D **93** (2016) 034030 [arXiv:1512.03583 [hep-ph]].
- Y. H. Chen, M. Cleven, J. T. Daub, F. K. Guo, C. Hanhart, B. Kubis, U.-G. Meißner and B. S. Zou, *Effects of* Z_b *states and bottom meson loops on* $\Upsilon(4S) \to \Upsilon(1S, 2S)\pi^+\pi^-$ *transitions*, Phys. Rev. D **95** (2017) 034022 [arXiv:1611.00913 [hep-ph]].

Contents

Chapter 1

Introduction

Having the itch to better understand nature, dealing with questions like what is our world made of, what are the fundamental constituents of matter and the interactions that glue these constituents together, and of what else besides the ordinary matter the universe is made up, this is what motivates to study particle physics. The Standard Model of Particle Physics, developed in the 1960s and 1970s [1–4], serves as the theoretical foundation to describe the matter particles (fermions), called quarks and leptons, and their interactions. There are four fundamental forces, the strong force, the weak force, the electromagnetic force, and the gravitational force. The first three of those are governed by the Standard Model, mediated by the exchange of vector gauge bosons, namely the gluons, the $W^{\pm}$ and Z bosons, and the photon for the strong, weak, and electromagnetic interactions, respectively. A further (scalar) boson, the Higgs boson is introduced, explaining the fermion masses, as well as those of the $W^{\pm}$ and Z bosons. The mathematical framework of the Standard Model is a quantum field theory, in which the particles are described by dynamical fields. It is driven by a Lagrangian that is invariant under the global Poincaré symmetry group as well as the local internal $SU(3) \times SU(2) \times U(1)$ gauge symmetry group. Although it is an extremely well tested and therefore the established theory of elementary particles, not least by the discovery of the Higgs boson in 2012 [5,6], there are still phenomena the Standard Model cannot describe properly and open questions to be answered, from both an experimental and a theoretical point of view. Some of these deficiencies are the unification of all four forces, i.e. including gravity in consistency with general relativity, or the nature of dark matter and energy, dominating over the ordinary matter content in the universe (due to the "Standard Model of cosmology"). Also the matter-antimatter asymmetry, the hierarchy problem, and the strong CP problem (the violation of the combination of charge conjugation C and parity P, being equivalent to a violation of time-reversal invariance T due to the CPT theorem, stating that the theory remains invariant under the combination of these three symmetries) are some famous examples requiring further contemplations of physics beyond the Standard Model.

A successful tool for quantum field theory calculations is perturbation theory, i.e. the theory is expanded in a parameter. Provided that it is small in order to ensure convergence, quantities are calculated to a certain order in that parameter. This splendidly works for processes in Quantum Electrodynamics (QED), the gauge theory that describes the electromagnetic interaction. For strong-interaction processes, however, which are described by Quantum Chromodynamics (QCD), the coupling constant and accordingly the expansion parameter strongly depend on the considered energy region. While at high energies perturbative QCD proves suitable, at low energies the strong coupling grows such that a perturbative treatment breaks down. At low energies, the QCD degrees of freedom are hadrons that are (essentially) classified into mesons

(quark-antiquark states) and baryons (three-quark states). It is hence the theoretical hadron physicist who is confronted with the problem of employing (or even developing) alternative non-perturbative methods to treat the strong-interaction processes at these low energies. Well established frameworks are Lattice QCD, Effective Field Theories such as Chiral Perturbation Theory, as well as dispersion relations.

Decays of heavy mesons (in particular those containing a b or $\bar{b}$ quark) are of special interest for Standard Model tests and beyond, there are for instance several experiments intended to measure CP violation, which is required to explain the matter-antimatter imbalance in the universe. In this context also the precise extraction of the Cabibbo-Kobayashi-Maskawa (CKM) [7,8] matrix elements describing the quark flavor mixing is of particular importance. The idea to explore neutral B decays in order to search for CP violation has grown up in 1980 [9–11], and in 2001 CP violation in B decays has been experimentally confirmed in the $B^0 \to J/\psi K_S^0$ decay (long considered a "golden mode") in the BaBar and the Belle experiments [12,13]. Ever since, the CP asymmetry $\sin 2\beta$ measured e.g. in the $B \to J/\psi K_S^0$ or likewise in the $B \to \phi K_S^0$ or $B \to f_0(980) K_S^0$ decay modes has been determined with increasing accuracy, for instance the LHCb collaboration at the Large Hadron Collider (LHC) pursues precise measurements of the B^0 and the B_s^0 meson systems to determine $\sin 2\beta_{(s)}$, e.g. by employing the decay modes $\bar{B}_{(s)}^0 \to J/\psi\{\pi^+\pi^-, K^+K^-\}$, or $\bar{B}_{(s)}^0 \to \{J/\psi, \psi(2S)\}K_s^0$ [14–18], as well as the CP parameter γ using e.g. the $B \to DK$ decays [19–21].

A further concern is the field of hadron spectroscopy—due to the heavy mass of the decaying meson a large energy range, i.e. phase space, is covered, entailing quite a number of final and intermediate states that can emerge. Amongst others so-called exotic states are observed that are not explained by the convenient quark model description as a quark-antiquark state. There are several charmonium- and bottomiumlike candidates observed close to or above the strong decay thresholds, referred to as the XYZ states, for instance in the charmonium spectrum the $X(3872)$, discovered in the Belle detector [22] in the decay processes $B^\pm \to K^\pm \pi^+\pi^- J/\psi$ (and confirmed by CDF [23], D0 [24], and BaBar [25]), or the $Y(4260)$, discovered in initial state radiation $e^+e^- \to \gamma_{ISR}\pi^+\pi^- J/\psi$ [26–28]. In the bottomium spectrum the Belle collaboration observed e.g. two charged resonances $Z_b(10610)$ and $Z_b(10650)$ in the $Y(5S) \to Y(ns)\pi^+\pi^-$, $(n = 1, 2, 3)$ and $Y(5S) \to h_b(mP)\pi^+\pi^-$, $(m = 1, 2)$ [29, 30]. Due to the increasing number of such exotic candidates it is a highly charged issue for both experimentalists and theoretical physicists how to model and interpret these states—as new forms of hadronic matter such as e.g. quark-gluon hybrids, meson molecules, tetraquarks or pentaquarks, or can these observed phenomena be explained by (anomalous) threshold effects. For details see Ref. [31, 32] and references therein.

This thesis deals with such heavy-meson decays, decaying weakly into hadrons that underlie strong final-state interactions. In order to learn about the above specified phenomena that prospectively provide an insight in New Physics beyond the SM, it is mandatory to tightly control the non-perturbative strong final-state interaction part in these decays. We apply the method of dispersion theory. Its advantage is that it provides a model-independent framework that fulfills the fundamental concepts of unitarity and analyticity by construction. The decays under investigation are discussed in Chapters 2 and 3.

In Chapter 2 the decays of the neutral $\bar{B}^0$ and $\bar{B}_s^0$ mesons into J/ψ and a light pseudoscalar meson pair, $\pi^+\pi^-$, $\pi^0\eta$, K^+K^- or $\bar{K}^0K^0$ are analyzed, with attention to the strong rescattering effects in the isoscalar and isovector light meson system. It can be described by the respective scalar and vector form factors, treated in a two-channel Muskhelishvili–Omnès formalism. In particular in the pion and kaon sectors the use of dispersion relations, employed with a phase input that is accurately determined from Roy and Roy–Steiner analyses [33–37] and experimental input, allows for a very precise understanding of the rescattering. The various final states are linked to each other by coupled-channel and flavor relations. Once the $\pi\pi$ channel is ex-

ploited to adjust unknown normalization parameters and to demonstrate that the experimental data are successfully described by the formalism, the other decay channels can be predicted. In particular this may reveal crucial information on the more scarcely known $\pi\eta$ scattering.

In Chapter 3 we explore the semileptonic decay of a charmed meson, $D^+ \to \pi^+ K^- l\nu$, where the strong final-state interaction in the πK system is rigorously treated using dispersion theory as well—the lepton-neutrino ($l\nu$) pair is not affected by the strong interaction such that the leptonic part of the matrix element factorizes from the hadronic part. The hadronic partial-wave amplitudes are calculated in Omnès representations, in which the crossed-channel effects are approximated by simple pole terms treated in Heavy-Meson Chiral Perturbation Theory. This approach however covers only a small phase space, caused by the restriction of a fixed dilepton energy to a rather large value. A generalization of the formalism by extrapolating to arbitrary dilepton energies is proposed, constrained by certain low-energy theorems.

The relevant physics background is prepended to the above-mentioned analyses, hence in this chapter certain aspects of the Standard Model, Effective Field Theories, and scattering theory are reviewed.

1.1 A survey of the Standard Model

In the Standard Model (SM) of Particle Physics three of the four fundamental forces, the electromagnetic, the weak, and the strong force, are unified. Gravitation, that is very weak compared to those, is not part of the SM. It describes the elementary particles and their interactions, where we distinguish between spin-1/2 fermions and spin-0 and spin-1 bosons. The fermions are separated into quarks and leptons, that each occur in three generations [8]: there are three $SU(2)$ doublets of quarks, built of an up and a down, a charm and a strange, and a top and a bottom quark, respectively, as well as three lepton doublets, for the electron, the muon, and the τ lepton, accompanied by the respective electron, muon, or τ neutrinos. The interactions between these particles are mediated by exchange particles, spin-1 bosons: the gluons carry the strong interactions, the photon the electromagnetic, and the $W^\pm$ and Z^0 bosons the weak interaction. In addition the SM contains a scalar particle, the Higgs boson, that was postulated in order to explain the breaking of the electroweak symmetry and to give masses to the $W^\pm$ and Z^0 bosons. The observation of the Higgs boson in the ATLAS and CMS experiments at the LHC at CERN in 2012 [5,6] (and confirmation in 2013 [40,41]) was a strengthening event for confirming the SM that caused lots of excitement in the particle physics community. The theoretical framework the SM is based on is a gauge quantum field theory. Particles are associated with fields and created or annihilated by field operators. Associated with these fields are the generators t_a of the corresponding gauge group, which obey specific commutator relations,

$$[t_a, t_b] = i f^{abc} t_c, \tag{1.1}$$

where the f^{abc} are the structure constants of the gauge group. In general $f^{abc} \neq 0$, i.e. it is a non-abelian theory. The internal gauge symmetry group contained is the local $SU(3)_C \times SU(2)_L \times U(1)_Y$, accompanied by the global Poincaré symmetry, which is characteristic of every relativistic quantum field theory. The label C denotes the color charge, Y the hypercharge (related to the electromagnetic charge Q and the third component of the isospin t_3 by $Y = 2(Q - t_3)$), and L indicates the chiral nature of the weak interaction—only left-handed fermions are grouped in $SU(2)$ doublets. Such non-abelian gauge theories that combine these symmetry properties are called Yang-Mills theories.

1.1.1 The strong sector

The strong interaction affects the quarks and the gluons, the gauge bosons of the $SU(3)_C$ gauge symmetry group. The interaction is defined by the QCD Lagrange density,[1]

$$\mathcal{L}_{\mathrm{QCD}} = -\frac{1}{4} G_a^{\mu\nu} G^a_{\mu\nu} + \bar{q}(i\not{D} - M)q, \tag{1.2}$$

with the mass matrix $M = \mathrm{diag}(m_u, m_d, m_s, ...)$, the quark fields represented by $q = (u, d, s, ...)^T$, and the covariant derivative

$$D_\mu = \partial_\mu - igA^a_\mu \frac{\lambda_a}{2}. \tag{1.3}$$

The latter contains the gluon fields A^μ_a, the coupling constant g (related to $\alpha_s = g^2/(4\pi)$), and the $SU(3)$ generators, the Gell-Mann matrices λ_a, where a is the color index (the quarks occur in $N_c = 3$ colors).

$$G^{\mu\nu}_a = \partial^\mu A^\nu_a - \partial^\nu A^\mu_a + g f_{abc} A^\mu_b A^\nu_c, \quad a = 1, \ldots, N_c^2 - 1 = 8, \tag{1.4}$$

denotes the (non-abelian) field strength tensor, where the structure constants are defined via the $SU(3)$ Lie algebra Eq. (1.1) with $t_a = \lambda_a/2$. The last term in Eq. (1.4), whose appearance results from the non-abelian nature of the strong interaction, causes the existence of the gluonic self-interaction. Such a phenomenon is not present in abelian theories like QED: there is no corresponding self-interaction between photons. This induces some peculiar differences to the extremely well known QED sector that makes the strong interaction such a challenging theory: due to an anti-screening of the color charge the strong coupling becomes weak at high energies (known as asymptotic freedom in the weak-QCD sector, cf. Refs. [42, 43]) and large at low energies (leading to the so-called confinement in the strong-QCD sector). As a consequence of confinement there are no free quarks and gluons at low energies, but they are bound to color-neutral hadrons. Furthermore, because the strong coupling increases, perturbation theory is not applicable at low energies, necessitating alternative approaches, discussed in Section 1.2. A mathematical understanding of these phenomena requires a closer look at the β_{QCD}-function of the renormalization group equation of QCD that describes how the strong coupling depends on the energy scale. Perturbatively expanding it to one-loop order yields the following differential equation with the solution $\alpha_s(Q^2)$,

$$\begin{aligned} \beta_{\mathrm{QCD}}(\alpha_s) \equiv Q^2 \frac{\mathrm{d}\alpha_s(Q^2)}{\mathrm{d}Q^2} &= -\left(11 - \frac{2N_f}{3}\right) \frac{\alpha_s(Q^2)}{2\pi} + \mathcal{O}(\alpha_s^3) \\ \Rightarrow \alpha_s(Q^2) &\approx \frac{\alpha_s(\mu^2)}{1 + \frac{33-2N_f}{12\pi} \ln\left(\frac{Q^2}{\mu^2}\right)}, \end{aligned} \tag{1.5}$$

with Q being the momentum transfer and μ a reference scale the β_{QCD} function depends on implicitly only (a popular choice is $\mu = m_{Z^0}$). N_f is the number of the considered quark flavors. As long as $N_f \leq 16$ β_{QCD} is negative, which straightforwardly implies the alluded decrease of the coupling parameter α_s at high-momentum transfer and vice versa. This is shown in Figure 1.1, together with the extraction of the world average value of $\alpha_s(M_Z^2)$, provided by the particle data group [44].

1.1.2 The weak sector

The weak interaction is mediated via a charged $W^\pm$ or a neutral Z^0, which couple to both quarks and leptons. The term "weak" applies to a strength several orders of magnitude weaker

[1] For simplicity, we here ignore terms like the Θ-term or possible gauge fixing and ghost terms.

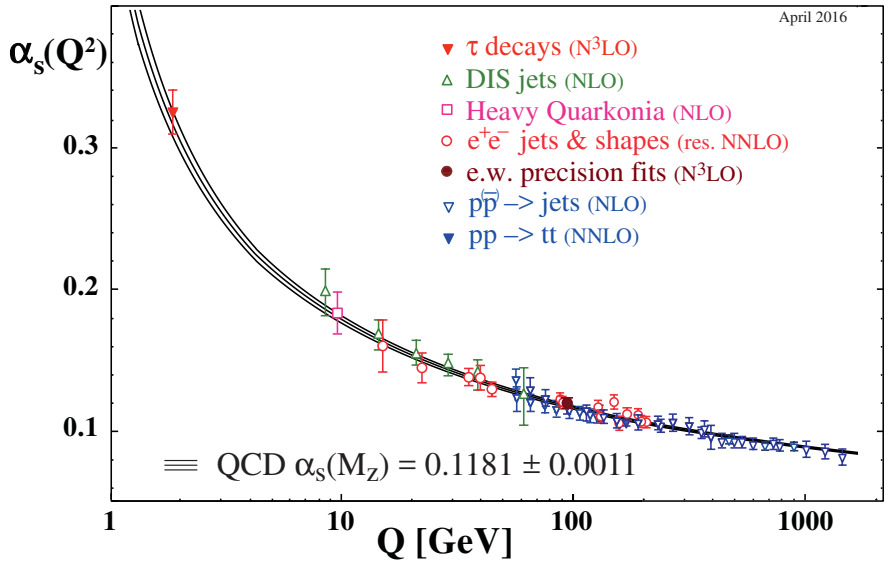

Figure 1.1: Energy scale dependence of the strong coupling $\alpha_s(Q^2)$ as determined from several measurements and extracted in perturbative QCD to the specified order (NLO: next-to-leading order; NNLO: next-to-NLO; res. NNLO: NNLO matched with resummed NLO logs; N^{3}LO: next-to-NNLO). The world average value for $\alpha_s(M_Z^2)$ as provided by the particle data group is cited. The graph is taken from Ref. [44].

than the strong force. This is combined with a short-range character of the weak force due to the large masses of the gauge bosons (due to the uncertainty principle). In the SM the weak and the electromagnetic interaction are unified to the electroweak interaction, which is described by the Glashow-Weinberg-Salam (GWS) theory and accomplished under the $SU(2)_L \times U(1)_Y$ part of the SM gauge symmetry group. Four initially massless gauge bosons (W_1, W_2, W_3, B) are linearly combined to the physical gauge bosons: the charged bosons $W^\pm$ are given by the combinations

$$W^\pm = \frac{W_1 \pm iW_2}{\sqrt{2}}, \tag{1.6}$$

and the W_3 boson mixes with the B, producing the physical neutral Z^0 boson and photon γ,

$$\begin{pmatrix} \gamma \\ Z^0 \end{pmatrix} = \begin{pmatrix} \cos\theta_W & \sin\theta_W \\ -\sin\theta_W & \cos\theta_W \end{pmatrix} \begin{pmatrix} B \\ W_3 \end{pmatrix}, \tag{1.7}$$

where the weak mixing angle θ_W is determined in terms of the weak isospin g and hypercharge g' by $\cos\theta_W = g/\sqrt{g^2 + g'^2}$. While the photon, mediating the electromagnetic interaction, remains massless, the three gauge bosons corresponding to the weak interaction become massive. This results from the spontaneous breaking of the $SU(2)_L \times U(1)_Y$ symmetry down to $U(1)_{\text{em}}$

(at energies below the electroweak breaking scale $\Lambda = 246$ GeV) through the Higgs mechanism.[2] The number of mass-acquiring bosons is in accordance with the number of broken generators: three $SU(2)_L$ generators $t_i = \sigma_i/2$ (with the Pauli matrices σ_i), which are the components of the weak isospin and obey Eq. (1.1) with $f^{abc} \to \epsilon^{abc}$. According to the Higgs mechanism the (large) masses of the $W^\pm$ or Z^0 are generated by the interaction with the Higgs field, a complex $SU(2)$ doublet with two scalar components,

$$\phi = \begin{pmatrix} \phi^+ \\ \phi^0 \end{pmatrix}. \tag{1.8}$$

The scalar Higgs potential reads

$$V(\phi) = -\mu^2 \phi^\dagger \phi + \lambda (\phi^\dagger \phi)^2, \tag{1.9}$$

where $\lambda > 0$ assures vacuum stability. For $\mu^2 > 0$ a nonzero vacuum expectation value emerges that may be written as

$$\langle \phi \rangle = \begin{pmatrix} 0 \\ \frac{v}{\sqrt{2}} \end{pmatrix}, \quad v = \sqrt{\frac{\mu^2}{\lambda}}. \tag{1.10}$$

In the unitary gauge, where the Higgs doublet is chosen as

$$\phi = \begin{pmatrix} 0 \\ \frac{v+h}{\sqrt{2}} \end{pmatrix} \tag{1.11}$$

and in which the appearance of any Goldstone boson fields in the Lagrange density is removed, but only the Higgs boson h is introduced after the spontaneous symmetry breaking (SSB), the Lagrangian offers the desired expressions of the gauge boson mass terms. The mass generated in this way effectively transforms as an $SU(2)_L$ doublet rather than as a scalar (naively adding a mass term for these gauge bosons would spoil the gauge invariance of the theory).

A special feature of the weak interaction is that it allows for a flavor change between quarks or leptons, such that for instance a d quark can be converted into a u quark or an electron into an electron neutrino. The strength of the flavor mixing is driven by the unitary CKM matrix in the case of quarks, determined by the Yukawa couplings of the Higgs boson to the fermions. The magnitudes of the diagonal matrix elements significantly dominate the off-diagonal elements, i.e. a transition within the same generation of quarks ("Cabibbo-favored") is much more probable than between quarks of different generations ("Cabibbo-suppressed"). The Pontecorvo–Maki–Nakagawa–Sakata (PMNS) matrix is the corresponding lepton flavor mixing matrix.

The $V - A$ (vector minus axial-vector or left-handed) nature of the weak interaction (it acts on left-handed $SU(2)_L$ doublets only) corresponds to maximal violation of parity P (which turns the left-handed into a right-handed fermion) or likewise of charge conjugation C; only the product of these two, CP symmetry, is a rather good symmetry. However, even a violation of the combined CP transformation is possible, first discovered in 1964 in neutral K decays by Cronin and Fitch [45]. The investigation of CP violating phenomena, and accordingly the precise determination of the CKM matrix elements, is still of major interest in the current state of research, both theoretically and experimentally. Its importance becomes apparent in the explanation of the huge preference of matter over primordial antimatter in the universe, as the existence of C and CP violation in the early universe is one of the so-called "Sakharov conditions" that were proposed to explain that imbalance. A remarkable success of the theory

[2] The specific value of the breaking scale is taken to be the vacuum expectation value of the Higgs field, $v = (G_F\sqrt{2})^{-1}$ with the Fermi constant G_F.

was the prediction [8] of a third particle generation in order to explain the non-conservation of CP symmetry, and the succeeding experimental confirmation by the discoveries of the charm quark in 1974 [46,47], the τ lepton in 1976 [48], and finally the bottom and top quarks in 1977 and 1995 [49–51]. Three generations allow for an irreducible phase δ in the CKM matrix, in which the CP violation in the quark sector manifests itself. A (not unique though commonly used) parametrization of the CKM matrix with four significant parameters, e.g. three rotation angles θ_{12}, θ_{13}, and θ_{23}, and the phase δ, reads

$$\begin{aligned} V_{\mathrm{CKM}} &= \begin{pmatrix} V_{ud} & V_{us} & V_{ub} \\ V_{cd} & V_{cs} & V_{cb} \\ V_{td} & V_{ts} & V_{tb} \end{pmatrix} \\ &= \begin{pmatrix} c_{12}c_{13} & s_{12}c_{13} & s_{13}e^{-i\delta} \\ -s_{12}c_{23} - c_{12}s_{23}s_{13}e^{i\delta} & c_{12}c_{23} - s_{12}s_{23}s_{13}e^{i\delta} & s_{23}c_{13} \\ s_{12}s_{23} - c_{12}c_{23}s_{13}e^{i\delta} & -c_{12}s_{23} - s_{12}c_{23}s_{13}e^{i\delta} & c_{23}c_{13} \end{pmatrix}, \end{aligned} \tag{1.12}$$

with $s_{ij} = \sin\theta_{ij}$ and $c_{ij} = \cos\theta_{ij}$. Unitarity of the CKM matrix yields the constraints

$$\sum_k V_{ik}V_{jk}^* = \delta_{ij}, \quad \text{and} \quad \sum_k V_{ki}V_{kj}^* = \delta_{ij}, \tag{1.13}$$

of which the six orthogonality relations ($i \neq j$) form unitarity triangles in the complex plane, whose surface areas are half of the magnitude of the Jarlskog invariant

$$J = \pm\mathrm{Im}\left(V_{ik}V_{jl}V_{il}^*V_{jk}^*\right) = c_{12}c_{13}^2c_{23}s_{12}s_{13}s_{23}\sin\delta, \quad (i \neq j,\, l \neq k), \quad |J| = (3.05 \pm 0.18)\cdot 10^{-5}, \tag{1.14}$$

which is a measure of CP violation. Most attention is paid to the triangle determined by CKM matrix elements with large phases,

$$V_{ud}V_{ub}^* + V_{cd}V_{cb}^* + V_{td}V_{tb}^* = 0, \tag{1.15}$$

giving a promising experimental access to CP violation and SM tests via measurements of the angles of the unitarity triangle defined by

$$\alpha = \arg\left(-\frac{V_{td}V_{tb}^*}{V_{ud}V_{ub}^*}\right), \quad \beta = \arg\left(-\frac{V_{cd}V_{cb}^*}{V_{td}V_{tb}^*}\right), \quad \gamma = \arg\left(-\frac{V_{ud}V_{ub}^*}{V_{cd}V_{cb}^*}\right) \tag{1.16}$$

and the sides

$$R_t = \left|\frac{V_{td}V_{tb}^*}{V_{cd}V_{cb}^*}\right|, \quad R_u = \left|\frac{V_{ud}V_{ub}^*}{V_{cd}V_{cb}^*}\right|, \quad R_c = \left|\frac{V_{cd}V_{cb}^*}{V_{cd}V_{cb}^*}\right| = 1. \tag{1.17}$$

The convenient representation of experimental constraints is given in the $(\bar{\rho}, \bar{\eta})$ plane, with

$$\bar{\rho} + i\bar{\eta} = R_u e^{i\gamma}, \tag{1.18}$$

where the coordinates $(\bar{\rho}, \bar{\eta})$ determine the only non-trivial apex of the normalized triangle, the others fixed to $(0,0)$ and $(1,0)$. The latest status of experimental constraints provided by the CKMfitter group in their global fit is shown in Figure 1.2. A detailed review on the experimental and theoretical input and the methodology is given in Ref. [52].

Three types of CP violation (CPV) have been investigated, direct CPV, indirect CPV, and CPV due to the interference between the direct decay and mixing amplitudes.
Direct (time-independent) CP violation can arise e.g. in kaon [53–56], and B-meson decays [12, 13], if the decay amplitude $A_f = \langle M|H|f\rangle$ of a meson M into a final state f is different from the amplitude $\bar{A}_{\bar{f}}$ describing the CP conjugate decay $\bar{M} \to \bar{f}$. H is the Hamiltonian that describes

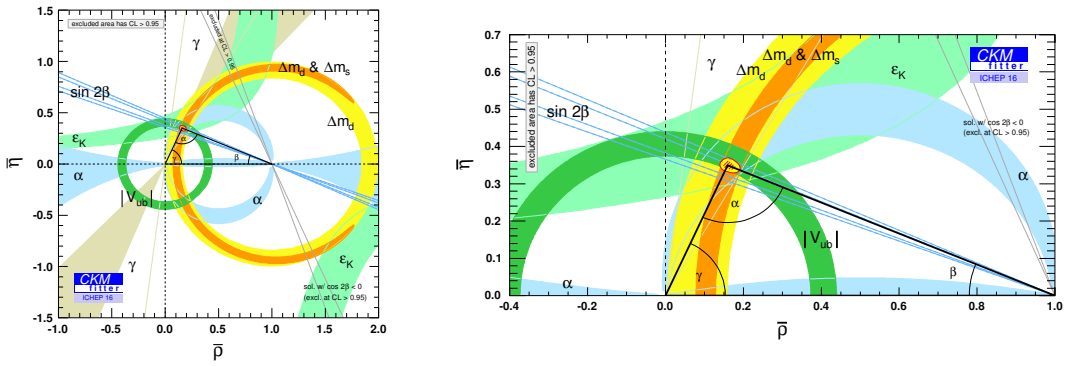

Figure 1.2: Constraints for the CKM unitarity triangle are shown in the $(\bar{\rho}, \bar{\eta})$ plane, for which experimental and theoretical results for all CKM parameters enter the global fit of the CKMfitter group. The red contoured area that combines all constraints corresponds to 68% confidence limit. In the left panel the region of interest is magnified. The figures are taken from Ref. [52].

the decay. Contrary to the other types of CPV it can occur in both neutral and charged meson decays as it does not rely on mixing. Its observation requires the contribution of weak CP-odd phases ϕ_j and at the same time strong CP-even phases δ_j, demanding for a tight control of the strong-interaction effects as well. A nonzero asymmetry, defined by

$$\mathcal{A}_{CP} = \frac{\Gamma(B \to f) - \Gamma(\bar{B} \to \bar{f})}{\Gamma(B \to f) + \Gamma(\bar{B} \to \bar{f})}, \quad \text{with} \quad \Gamma(B \to f) = |A_f|^2 \quad \text{and} \quad \Gamma(\bar{B} \to \bar{f}) = |\bar{A}_{\bar{f}}|^2, \tag{1.19}$$

can emerge if the transition $B \to f$ involves at least two amplitudes

$$A_j = |A_j| e^{i(\phi_j + \delta_j)}, \quad A_f = \sum_{j=1}^{n} A_j, \quad n \geq 2. \tag{1.20}$$

Consider a process with $n = 2$. The transition amplitude and its CP conjugate read

$$\begin{aligned} A_f &= |A_1| e^{i(\delta_1 + \phi_1)} + |A_2| e^{i(\delta_2 + \phi_2)}, \\ \bar{A}_{\bar{f}} &= |A_1| e^{i(\delta_1 - \phi_1)} + |A_2| e^{i(\delta_2 - \phi_2)}, \end{aligned} \tag{1.21}$$

such that the CP asymmetry is evaluated to

$$\mathcal{A}_{CP} = \frac{2|A_1||A_2| \sin(\Delta\delta) \sin(\Delta\phi)}{|A_1|^2 + |A_2|^2 + 2|A_1||A_2| \cos(\Delta\delta) \cos(\Delta\phi)}. \tag{1.22}$$

Consequently, direct CPV is only observable for nonzero phase differences $\Delta\delta = \delta_1 - \delta_2 \neq 0$ and $\Delta\phi = \phi_1 - \phi_2 \neq 0$.

Indirect (time-dependent) CP violation relies on oscillations in neutral meson systems, e.g. $\bar{K}^0$–K^0 and $\bar{B}^0$–B^0 mixing, observable if a neutral meson state converts to its CP conjugate with a probability different from the one for the reverse process. The transition to a CP conjugate state can proceed via a second order weak current box diagram, as depicted at the example of a $\bar{B}^0$–B^0 oscillation in Figure 1.3. The time-dependent CP asymmetry is given by

$$\mathcal{A}_{CP}(t) = \frac{\Gamma(B^0 \to f)(t) - \Gamma(\bar{B}^0 \to f)(t)}{\Gamma(B^0 \to f)(t) + \Gamma(\bar{B}^0 \to f)(t)}, \quad \text{with} \quad \Gamma(B^0 \to f)(t) = |\left\langle f|H|B^0(t)\right\rangle|^2. \tag{1.23}$$

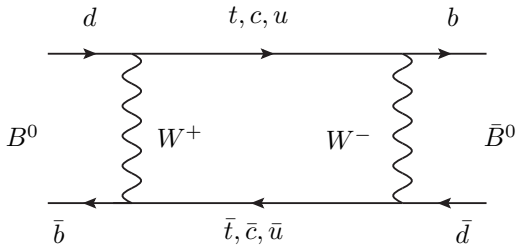

Figure 1.3: The figure shows the $\Delta B = 2$ box diagram, transferring a B^0 meson into its CP conjugate $\bar{B}^0$. This gives rise to $\bar{B}^0$–B^0 oscillations.

The time-dependent amplitudes for the respective transition to a final CP eigenstate f that enter this asymmetry read

$$\begin{aligned}\left\langle f|H|B^0(t)\right\rangle &= e^{-imt}e^{-\frac{\Gamma t}{2}}\left[A_f\cos\left(\frac{\Delta m_B t}{2}\right)+i\frac{q}{p}\bar{A}_f\sin\left(\frac{\Delta m t}{2}\right)\right],\\ \left\langle f|H|\bar{B}^0(t)\right\rangle &= e^{-imt}e^{-\frac{\Gamma t}{2}}\left[i\frac{p}{q}A_f\sin\left(\frac{\Delta m t}{2}\right)+\bar{A}_f\cos\left(\frac{\Delta m_B t}{2}\right)\right],\end{aligned} \tag{1.24}$$

where the coefficients p and q occur in the transformation of the B^0 and $\bar{B}^0$ states into eigenstates of the weak Hamiltonian H, a light (L) and a heavy (H) one,

$$\left|B^0_{L,H}\right\rangle = p\left|B^0\right\rangle \pm q\left|\bar{B}^0\right\rangle; \tag{1.25}$$

m is the average mass, and Δm is the difference of the masses of the weak eigenstates (we take the difference of the widths of B^0_L and B^0_H to be negligibly small). The box diagram, which is dominated by the contribution from intermediate top quarks, yields

$$\frac{q}{p} = \frac{V^*_{tb}V_{td}}{V_{tb}V^*_{td}}. \tag{1.26}$$

Using Eq. (1.24) the decay rates are evaluated to

$$\begin{aligned}\Gamma(B^0\to f)(t) &\propto 1+\frac{2\mathrm{Im}\,\lambda_f}{1+|\lambda_f|^2}\sin(\Delta m\,t)-\frac{1-|\lambda_f|^2}{1+|\lambda_f|^2}\cos(\Delta m\,t),\\ \Gamma(\bar{B}^0\to f)(t) &\propto 1-\frac{2\mathrm{Im}\,\lambda_f}{1+|\lambda_f|^2}\sin(\Delta m\,t)+\frac{1-|\lambda_f|^2}{1+|\lambda_f|^2}\cos(\Delta m\,t), \quad \lambda_f=\frac{q}{p}\frac{\bar{A}_f}{A_f},\end{aligned} \tag{1.27}$$

such that

$$\mathcal{A}_{CP} = \underbrace{\frac{2\mathrm{Im}\,\lambda_f}{1+|\lambda_f|^2}}_{\text{mixing}}\sin(\Delta m\,t)-\underbrace{\frac{1-|\lambda_f|^2}{1+|\lambda_f|^2}}_{\text{direct}}\cos(\Delta m\,t), \tag{1.28}$$

where the prefactors represent either CPV in the direct decay or due to the mixing.

Finally, CP violation can occur if a particle M and its CP conjugate $\bar{M}$ decay into the same final state f, such that M can decay directly or via mixing, $M \to \bar{M} \to f$. It is thus based on the interference between the decay amplitude with and without mixing.

Originally, CP violation was investigated in kaon decays; today, major efforts in the matter are made, adducting the field of B-physics where large CP asymmetries are expected and an

appreciable sensitivity to New Physics beyond the SM is present. Such research was and still is a main purpose of B-physics experiments, rendering plenty experimental evidence, e.g. at the first generation asymmetric B factories like the Belle experiment at the KEKB collider (upgraded to Belle II at the SuperKEKB accelerator) and the BaBar experiment at the PEP-II collider at SLAC, likewise at the Fermilab Tevatron by the CDF and D0 collaborations, and now continued by LHCb at the LHC, where e.g. the golden mode $B^0 \to J/\psi K^0$ is investigated, as well as the CP violation in the strange sector, $B_s^0 \to J/\psi\phi$.

1.2 Effective field theories

The non-applicability of perturbation theory for strong-interaction processes in the low-energy regime, where quarks and gluons are confined within color-neutral bound states, the hadrons, requires alternative approaches to hadron physics. Established methods are Effective Field Theories (EFTs), Lattice QCD, and Dispersion Theory. This section introduces the concept of EFTs, illustrated at the examples of Chiral Perturbation Theory (ChPT) and Heavy-Meson Chiral Perturbation Theory (HMChPT), both being of central importance in this thesis.

The main idea in constructing an EFT is to focus on the energy/mass region of interest, i.e. a theory that is supposed to describe strong-interaction processes at low energies is driven by a Lagrangian where the hadrons are the relevant degrees of freedom rather than the quarks and gluons that are the degrees of freedom of the underlying theory. This prerequires a clear scale separation in order to identify and reliably suppress the irrelevant degrees of freedom: if we for instance intend to describe the dynamics of the lightest hadrons (with a mass m_L) in the particle spectrum, a theory in which the particles above a given energy scale (e.g. hadrons that contain a c or b quark) are integrated out proves beneficial, given that the heavy masses are $m_H \gg m_L$. The effective theory can then be expanded in a controlled way according to the power-counting argument: given that the expansion parameter α, defined by the ratio between the low and the high energy scale, is a sufficiently small parameter, operators $\mathcal{O}_\nu \sim f(\ell_i)\alpha^\nu$ that are of low order in α dominate over higher-dimension operators, allowing for a systematic ordering of the operators. The prefactor $f(\ell_i)$ is a function of an a priori unknown so-called low-energy constant (LEC) ℓ_i that contains information about high-energy effects, to be fixed phenomenologically from experiment or derived from the fundamental theory, e.g. by using lattice simulations; furthermore, $f(\ell_i) \sim \mathcal{O}(1)$ (naturalness argument). At a given order both tree-level and loop diagrams must be considered preserving (perturbative) unitarity.

The effective theory is constrained by the underlying symmetries of the fundamental theory (the Lagrangians discussed in this section are required to be invariant under the QCD symmetry transformations).

Note that the knowledge of the fundamental theory is not mandatory for the construction of the effective theory that just relies on symmetry principles. This was heuristically conjectured by Weinberg [57] and reformulated in the folk theorem (referred to as such by himself) [58]:

> "if one writes down the most general possible Lagrangian, including all terms consistent with assumed symmetry principles, and then calculates S-matrix elements with this Lagrangian to any order of perturbation theory, the result will simply be the most general S-matrix consistent with analyticity, perturbative unitarity, cluster decomposition, and the assumed symmetry principles."

Unitarity and analyticity constraints ensure that the theory conserves probability and causality, respectively, while cluster decomposition is linked to locality.

The established EFT of QCD at low energies (in the meson sector), where the 8 Goldstone bosons $\pi^\pm, \pi^0, K^\pm, K^0, \bar{K}^0, \eta$, the lightest hadrons in the particle spectrum, become the relevant

effective degrees of freedom, is ChPT [59,60]. It exploits chiral symmetry, being an exact QCD symmetry in the limit of vanishing quark masses $m_q \to 0$. This symmetry is spontaneously broken, which entails the generation of the Goldstone bosons. The theory is systematically expanded in powers of the Goldstone boson momenta/energies p or masses M over the chiral symmetry breaking scale, p/Λ_χ or M/Λ_χ, $\Lambda_\chi \approx 1$ GeV.[3] Accordingly, the range of applicability is restricted to momenta or masses well below the chiral breaking scale.

On the contrary, for processes where mesons containing one heavy (c or b) quark are involved Heavy-Quark Effective Theory (HQET) is an appropriate approach. There the $m_q \to \infty$ limit is studied in which the heavy quark depends on its four-velocity v_μ only but not on its spin or mass, i.e. if N_f heavy quarks are considered the theory is invariant under an $SU(2N_f)$ spin flavor symmetry.[4] An effective theory that exploits both chiral and spin flavor symmetry is HMChPT, discussed in Section 1.2.2, after a brief review of ChPT given in Section 1.2.1.

1.2.1 Chiral Perturbation Theory

Projecting the quark fields on left- and right-handed fields,

$$q_{L/R} = P_{L/R} q, \quad P_{R/L} = \frac{1}{2}\left(1 \pm \gamma_5\right), \quad P_L + P_R = 1, \quad P_L \cdot P_R = 0 \tag{1.29}$$

exhibits a decoupling of the left- and right-handed fields in the kinetic part of the QCD Lagrangian Eq. (1.2) (contrary to the mass term $\mathcal{L}_{\text{mass}}$), such that $\mathcal{L}_{\text{kin}}$ is invariant under independent global rotations in flavor space,

$$\mathcal{L}_{\text{kin}} = -\frac{1}{4} G_a^{\mu\nu} G^a_{\mu\nu} + i\left(\bar{q}_L \not{D} q_L + \bar{q}_R \not{D} q_R\right), \quad \mathcal{L}_{\text{mass}} = (-\bar{q}_R M q_L - \bar{q}_L M q_R), \tag{1.30}$$

with $\mathcal{L}_{\text{QCD}} = \mathcal{L}_{\text{kin}} + \mathcal{L}_{\text{mass}}$. This results in exact chiral symmetry of the QCD Lagrangian in the chiral limit, $m_q \to 0$,

$$U(N_f)_L \times U(N_f)_R = \underbrace{U_L(1) \times U_R(1)}_{= U_V(1) \times \cancel{U_A(1)}} \times SU(N_f)_L \times SU(N_f)_R, \tag{1.31}$$

where N_f massless quarks are considered (a convenient choice is $N_f = 2$ or $N_f = 3$, while the heavy quarks are integrated out). Right- and left-handed symmetry transformations are combined to vector, $V = R + L$, and axial-vector, $A = R - L$, ones. While the Noether current of the $U(1)_V$ symmetry, associated with the baryon number, is conserved, the $U(1)_A$ symmetry is anomalously broken due to quantum effects and hence not a symmetry of QCD.

A continuous exact global symmetry of a Lagrangian can be realized in two different ways (Goldstone alternative): either the symmetry remains unbroken in both the equations of motion and the ground state (Wigner-Weyl realization of the symmetry) or the symmetry is spontaneously broken (Nambu-Goldstone mode), such that the vacuum is not invariant under the symmetry transformation. The annihilation of the vacuum that characterizes the Wigner-Weyl mode implies the existence of degenerate particle multiplets. In the case of the $SU(N_f)_L \times SU(N_f)_R$ symmetry the occurrence of parity doublets is expected. However, these

[3] The size of Λ_χ can be estimated in studying $\pi\pi$ scattering: a dimensional analysis approach, where up to $\mathcal{O}(p^4)$ contributions (loop vs. tree-level) are compared, yields $\Lambda_\chi \approx 4\pi F_\pi \approx 1.2$ GeV ($F_\pi \approx 92$ MeV being the pion decay constant), which is of the same order of magnitude as the estimation based on a phenomenological model of resonance exchange (the lightest being the ρ meson) indicating $\Lambda_\chi \approx M_{\text{res}} \gtrsim M_\rho = 770$ MeV.

[4] Note that these symmetries are exact only in the considered limit, i.e. if for instance the charm quark ($m_c \approx 1.5$ GeV) is involved rather large corrections of order $\mathcal{O}(\Lambda_{\text{QCD}}/m_c)$ ($\Lambda_{\text{QCD}} \approx 200$ MeV being the QCD reference scale) may spoil the predictiveness of the effective theory.

are not observed in the hadronic spectrum, being one of several existing arguments why the Wigner-Weyl realization is excluded. Instead, the chiral symmetry is spontaneously broken to the vectorial subgroup,

$$SU(N_f)_L \times SU(N_f)_R \to SU(N_f)_V. \tag{1.32}$$

The $SU(N_f)_V$ subgroup is preserved from a further SSB according to the Vafa-Witten theorem [61],[5] and can only be broken explicitly due to nonzero quark masses. Due to the Goldstone theorem for every broken generator a new minimum-energy vacuum state appears, such that the $N_f^2 - 1$ broken axial generators due to the spontaneous breaking of the chiral symmetry, Eq. (1.32), yield the same number of massless particles, the Goldstone bosons. Depending on the number of flavors that are taken into account, i.e. whether the strange quark is considered to be massless (chiral $SU(3)$ symmetry) or only the $m_u, m_d \to 0$ limit is considered (chiral $SU(2)$ symmetry), the theory involves eight Goldstone bosons (three pions, four kaons, and the eta meson) or the pion triplet, respectively. These mesons are the lightest though not massless pseudoscalar mesons in the particle spectrum. This is explained by the non-zero quark masses: chiral symmetry is an approximate symmetry, broken explicitly by the light quark masses, $m_q \neq 0$. Since $m_q \ll \Lambda_\chi$, a rather small effect is expected. In a similar way, the vector symmetries $SU(2)_V$ and $SU(3)_V$ are approximate ones, broken by quark mass differences. In particular the $SU(2)_V$ symmetry, whose breaking yields isospin-violating effects (ascribed to $m_u \neq m_d$) that are manifest e.g. in the kaon mass differences or in $\eta \to 3\pi$, still proves to be a very good symmetry; $SU(3)_V$ symmetry shows larger corrections on a 30% level, driven by the strange quark mass that is still an order of magnitude larger than $m_{u,d}$.

Having clarified the relevant degrees of freedom, the Goldstone bosons, the underlying QCD symmetries and the discussed pattern of spontaneous chiral-symmetry breaking are built into an effective Lagrangian. One ingredient is the unitary matrix

$$U = \exp\left(\frac{i\lambda_a \phi_a}{F}\right), \tag{1.33}$$

which transforms as $U \to U' = RUL^\dagger$, $R, L \in SU(N_f)_{R,L}$, under the chiral rotation. The Goldstone bosons are encoded in an $N_f \times N_f$ real matrix; we focus on the three-flavor case in the following (the reduction to the $SU(2)_V$ symmetry is performed straightforwardly) with

$$\frac{1}{\sqrt{2}}\lambda_a \phi_a = \begin{pmatrix} \frac{\pi^0}{\sqrt{2}} + \frac{\eta}{\sqrt{6}} & \pi^+ & K^+ \\ \pi^- & -\frac{\pi^0}{\sqrt{2}} + \frac{\eta}{\sqrt{6}} & K^0 \\ K^- & \bar{K}^0 & -\frac{2}{\sqrt{6}}\eta \end{pmatrix}, \tag{1.34}$$

and neglecting π^0–η mixing. In the chiral limit the constant F equals the pion decay constant $F \approx F_\pi = (92.1 \pm 1.2)$ MeV [62], which is e.g. measured in the pion decay $\pi^+ \to l^+ \nu_l$.

In order to ensure the theory to be invariant under Lorentz transformations, odd powers in the Goldstone boson momenta or the derivatives, respectively, are forbidden, such that the effective Lagrangian has the schematic representation

$$\mathcal{L}_{\text{eff}} = \mathcal{L}^{(2)} + \mathcal{L}^{(4)} + \dots . \tag{1.35}$$

$\mathcal{L}^{(0)}$ is a constant contribution without physically meaningful impact and is therefore ignored. Hence the leading order (LO) Lagrangian comprises terms that are of quadratic order in the derivatives and meson masses, the latter being consistent with linear order in the quark masses

[5] The Vafa-Witten theorem states that vector gauge theories (as QCD without Θ-term) have an unbroken vector symmetry, such that only the axial symmetry can be broken spontaneously.

due to the Gell-Mann-Oakes-Renner relation (discussed later in this section). A general expression of the LO Lagrangian supplemented by the coupling to external fields reads

$$\mathcal{L}^{(2)} = \frac{F^2}{4} \left\langle D_\mu U D^\mu U^\dagger + \chi U^\dagger + U\chi^\dagger \right\rangle , \tag{1.36}$$

$\langle \dots \rangle$ denotes the trace in flavor space. The coupling to vector (v_μ) and axial-vector (a_μ) external sources enters via the covariant derivative,

$$D_\mu U = \partial_\mu U - i r_\mu U + i U l_\mu, \quad r_\mu = v_\mu + a_\mu, \quad l_\mu = v_\mu - a_\mu, \tag{1.37}$$

and scalar (s) and pseudoscalar (p) sources are introduced by

$$\chi = 2B(s + ip). \tag{1.38}$$

The (symmetry breaking) mass term is recovered by $s = \mathrm{diag}(m_u, m_d, m_s)$, thus it enters the effective Lagrangian together with a constant B, called the order parameter of SSB, which is not fixed by chiral symmetry. A comparison of the derivatives of the QCD and the effective ground state ($U = U_0 = \mathbb{1}$) energies with respect to the quark masses yields a relation between B and the chiral quark condensate,

$$B = \left| \frac{\langle 0|\bar{q}q|0\rangle}{3F^2} \right|_{m_u, m_d, m_s \to 0} \quad \text{with} \quad \frac{1}{3}\langle 0|\bar{q}q|0\rangle = \langle 0|\bar{u}u|0\rangle = \langle 0|\bar{d}d|0\rangle = \langle 0|\bar{s}s|0\rangle \neq 0. \tag{1.39}$$

Considering next the mass term expanded to second order in the pseudoscalar meson fields one can read off a proportionality of the squared pion, kaon, and eta masses to the (linear) quark masses (Gell-Mann-Oakes-Renner relation),

$$\begin{aligned} &M_{\pi^\pm}^2 = B\hat{m}, \quad M_{K^\pm}^2 = B(m_u + m_s), \quad M_{K^0}^2 = B(m_d + m_s), \\ &M_{\pi^0}^2 = B\hat{m} + \mathcal{O}((m_u - m_d)^2), \quad M_\eta^2 = \frac{B}{3}(\hat{m} + 4m_s) + \mathcal{O}((m_u - m_d)^2), \\ &\hat{m} = m_u + m_d, \end{aligned} \tag{1.40}$$

where electromagnetic effects are neglected that induce isospin breaking.

The violation of isospin symmetry is manifest in the $\pi^0\eta$ mixing, lowering the neutral pion mass compared to the charged one, and increasing the eta mass of order $(m_u - m_d)^2 \ll \hat{m}^2$. Both the parameter B and the quark masses depend on the QCD renormalization scale. However, the scale dependence cancels in the product such that the mass relations are invariant under the QCD renormalization group.

Next-to-leading (NLO) (and higher) order calculations include a considerably larger variety of contributing operators: the NLO Lagrangian $\mathcal{L}^{(4)}$ contains operator structures with four derivatives, two derivatives and χ, or χ^2. An explicit form reads [60]

$$\begin{aligned} \mathcal{L}^{(4)} \;=\; & L_1 \langle D_\mu U D^\mu U^\dagger \rangle^2 + L_2 \langle D_\mu U D_\nu U^\dagger \rangle \langle D^\mu U D^\nu U^\dagger \rangle \\ & + L_3 \langle D_\mu U D^\mu U^\dagger D_\nu U D^\nu U^\dagger \rangle + L_4 \langle D_\mu U D^\mu U^\dagger \rangle \langle \chi^\dagger U + \chi U^\dagger \rangle \\ & + L_5 \langle D_\mu U D^\mu U^\dagger (\chi^\dagger U + \chi U^\dagger) \rangle + L_6 \langle \chi^\dagger U + \chi U^\dagger \rangle^2 \\ & + L_7 \langle \chi^\dagger U - \chi U^\dagger \rangle^2 + L_8 \langle \chi^\dagger U \chi^\dagger U + \chi U^\dagger \chi U^\dagger \rangle \\ & - i L_9 \langle F_{\mu\nu}^R D^\mu U D^\nu U^\dagger + F_{\mu\nu}^L D^\mu U^\dagger D^\nu U \rangle + L_{10} \langle U^\dagger F_{\mu\nu}^R U F^{L\mu\nu} \rangle, \end{aligned} \tag{1.41}$$

with LECs L_i (note that in the $SU(2)$ version the LECs are denoted by ℓ_i). The field strength tensors $F_{\mu\nu}^{L,R}$ that contribute in Eq. (1.41) are defined via

$$F_{\mu\nu}^R = \partial_\mu r_\nu - \partial_\nu r_\mu - i\,[r_\mu, r_\nu], \quad F_{\mu\nu}^L = F_{\mu\nu}^R(r_\mu \to l_\mu). \tag{1.42}$$

Considering diagrams at NLO there can be an insertion from $\mathcal{L}^{(4)}$, or one-loop graphs based on $\mathcal{L}^{(2)}$ contribute. The latter generate divergences, which are canceled by appropriately renormalized LECs,[6]

$$L_i = L_i^r + \frac{\Gamma_i}{32\pi^2}\mu^{d-4}\left[\frac{2}{d-4} - (\ln(4\pi) + \Gamma'(1) + 1)\right], \tag{1.43}$$

This explicit form holds for dimensional regularization, with real coefficients Γ_i and dimension d. This alludes to the importance of the subject of renormalizability in the NLO domain—for an elaborated understanding see Refs. [63–67].

1.2.2 Heavy-Meson Chiral Perturbation Theory

An EFT that combines the approximate chiral symmetry of the QCD Lagrangian ($m_q \to 0$ for the light quarks $q = u, d, s$) and the heavy quark symmetry in the limit of infinite masses ($m_Q \to \infty$ for heavy quarks $Q = c, b$) is Heavy-Meson Chiral Perturbation Theory (HMChPT). The latter limit manifests itself in three aspects:

- an $SU(n_f)$ flavor symmetry: the heavy quark flavor becomes irrelevant in the $m_Q \to \infty$ limit,
- an $SU(2)$ spin symmetry: the gluon decouples from the quark spin, implying e.g. a degenerate multiplet of ground-state pseudoscalar (P_a) and vector ($P^*_{a\mu}$) states,
- the velocity superselection rule: the velocity v is only affected by the weak and the electromagnetic interaction but not by the strong interaction such that one cannot distinguish between the heavy meson and the heavy quark velocity.

The spin and flavor symmetry are combined to the larger $SU(2n_f)$ spin-flavor symmetry for each velocity. It is broken by finite quark masses, corrections of order $\mathcal{O}(\Lambda_{\mathrm{QCD}}/m_Q)$ are systematically incorporated order by order.

Both chiral and heavy quark symmetry are implemented in a Lagrangian that describes the dynamics between a light pseudoscalar and a heavy meson (containing a single heavy quark and having $Q\bar{q}^a$ flavor quantum numbers, $a = 1, 2, 3$).[7] The light antiquark can be a $\bar{u}$, $\bar{d}$ or $\bar{s}$ quark such that the field operators P_a and $P^*_{a\mu}$ that annihilate the heavy mesons with velocity v form $SU(3)_V$ antitriplets that consist of D and D^* mesons for $Q = c$, or B and B^* mesons for $Q = b$, respectively,

$$\begin{aligned}
(P_1, P_2, P_3) &= (D^0, D^+, D_s^+) \qquad \text{and} \qquad (P_1^*, P_2^*, P_3^*) = (D^{*0}, D^{*+}, D_s^{*+}),\\
(P_1, P_2, P_3) &= (B^-, \bar{B}^0, \bar{B}_s^0) \qquad \text{and} \qquad (P_1^*, P_2^*, P_3^*) = (B^{*-}, \bar{B}^{*0}, \bar{B}_s^{*0}).
\end{aligned} \tag{1.44}$$

These fields are of mass dimension 3/2 as factors of $\sqrt{m_{D,B}}$ and $\sqrt{m_{D^*,B^*}}$ are absorbed in P_a and P_a^*, respectively. The physical polarization of vector particles constrains the fields by $\epsilon \cdot v = 0$, hence $P^* \cdot v = 0$. The operators P_a and $P^*_{a\mu}$ are combined in a single object and can be represented by the composite field

$$H_a = \frac{1+\not{v}}{2}\left(P^*_{a\mu}\gamma^\mu - P_a\gamma_5\right), \quad \bar{H}_a = \gamma_0 H_a^\dagger \gamma_0, \tag{1.45}$$

[6] The scale dependence of the L_i^r is compensated by the finite part of the loop graph, such that the physical quantities are scale invariant.

[7] HMChPT is also applicable for processes in which light mesons interact with heavy quarkonia, charmonia or bottomia. Though in this case the heavy flavor symmetry $SU(n_f)$ is broken, there are many parallels in constructing the effective Lagrangian that is introduced in Section 2.7.3.

that transforms under a Lorentz transformation Λ as

$$H_a \to D(\Lambda) H_a D(\Lambda)^{-1}, \quad v \to \Lambda v, \quad x \to \Lambda x, \tag{1.46}$$

where $D(\Lambda)$ is the 4×4 representation of the Lorentz group, and as

$$H_a \to S H_a, \quad H_a \to H_b V_{ab}^\dagger \tag{1.47}$$

under a heavy-quark spin transformation S that belongs to $SU(2)$ with $[\not{v}, S] = 0$, and with a unitary matrix V in flavor space.

At leading-order the Lagrangian reads [68, 69]

$$\mathcal{L} = -i\mathrm{Tr}\bar{H}_a v_\mu \partial^\mu H_a + \frac{1}{2}\mathrm{Tr}\bar{H}_a H_b v^\mu (u^\dagger \partial_\mu u + u \partial_\mu u^\dagger)_{ba} + \frac{ig}{2}\mathrm{Tr}\bar{H}_a H_b \gamma^\mu \gamma_5 (u^\dagger \partial_\mu u - u \partial_\mu u^\dagger)_{ba}. \tag{1.48}$$

The Goldstone bosons are collected in $u = U^{1/2}$; the unitary matrix U is defined in Eq. (1.33). The normalized coupling g occurring in Eq. (1.48), which is flavor-independent in the limit of exact chiral, spin and heavy-flavor symmetry, is related to the strong couplings $g_{B^* B\pi}$ and $g_{D^* D\pi}$. Since the decay $B^* \to B\pi$ is kinematically forbidden it can be determined from the partial decay width for $D^{*+} \to D^0 \pi^+$, $g = g_{D^* D\pi} F_\pi / \sqrt{2 m_D m_{D^*}} = 0.570 \pm 0.004 \pm 0.005$, where the more precisely measured width of the BaBar collaboration [70, 71] (compared to the older CLEO measurements [72, 73]) is taken.

To determine the propagators we take into account the higher-order Lagrangian terms

$$\mathcal{L}_\lambda = \lambda_1 \mathrm{Tr}\bar{H}_a H_b (u m_q u + u^\dagger m_q u^\dagger)_{ba} + \lambda_1' \mathrm{Tr}\bar{H}_a H_a (m_q U + m_q U^\dagger)_{bb} + \lambda_2 \mathrm{Tr}\bar{H}_a \sigma_{\mu\nu} H_a \sigma^{\mu\nu}, \tag{1.49}$$

that are responsible for the leading chiral-symmetry and heavy-quark-spin breaking effects, i.e. for the mass splitting between the strange and the non-strange D/B mesons and between the pseudoscalar and the vector triplets. After a redefinition of the heavy meson fields $P_a^{(*)} \to \exp(i\,{}^3\!/_4 \Delta v \cdot x) P_a^{(*)}$ the effective P_a and P_a^* propagators can be written as

$$\frac{i\delta^{ab}}{2(k \cdot v - \mu \delta_{as})} \quad \text{and} \quad \frac{-i\delta^{ab}(g_{\mu\nu} - v_\mu v_\nu)}{2(k \cdot v - \Delta - \mu \delta_{as})}, \tag{1.50}$$

respectively, where k denotes the small residual momentum of the propagating meson and $\Delta = m_{P^*} - m_P = -\frac{8\lambda_2}{m_Q}$, $\mu = m_{P_s} - m_P = 2\lambda_1(m_s - \hat{m})$ [68], $\hat{m} = (m_u + m_d)/2$; δ_{as} indicates a contribution in the case of a strange propagating heavy meson (while $a \neq s$ yields $\delta_{as} = 0$).

The purpose of the remaining section is to provide an example for an application. Processes for which HMChPT is a readily feasible approach are for instance semileptonic decays of heavy mesons. In the following we restrict ourselves to semileptonic decays of the D meson in order to simplify the notation (the B decay can be treated in analogy). In particular we calculate $D \to \pi K l \nu$ (abbreviated by D_{l4}) tree-level processes, which are shown in Figure 1.4; the diagrams (B) and (C) contain t-channel D^*-pole terms. The coupling to the left-handed leptonic current, involving a light meson q and a heavy meson Q,

$$L_{\nu a} = \bar{q}^a \gamma_\nu (1 - \gamma_5) Q, \tag{1.51}$$

has to be determined. In HMChPT this current can be rewritten as [68]

$$L_{\nu a}^{(0)} = \frac{i f_D \sqrt{m_D}}{2} \mathrm{Tr}\left[\gamma_\nu (1 - \gamma_5) H_b u_{ba}^\dagger\right] + \ldots, \tag{1.52}$$

where the ellipsis denotes terms of higher order in the heavy-mass or chiral power counting. The D-meson decay constant $f_D = (209.2 \pm 3.3)\,\mathrm{MeV}$ is taken from Ref. [74], where lattice

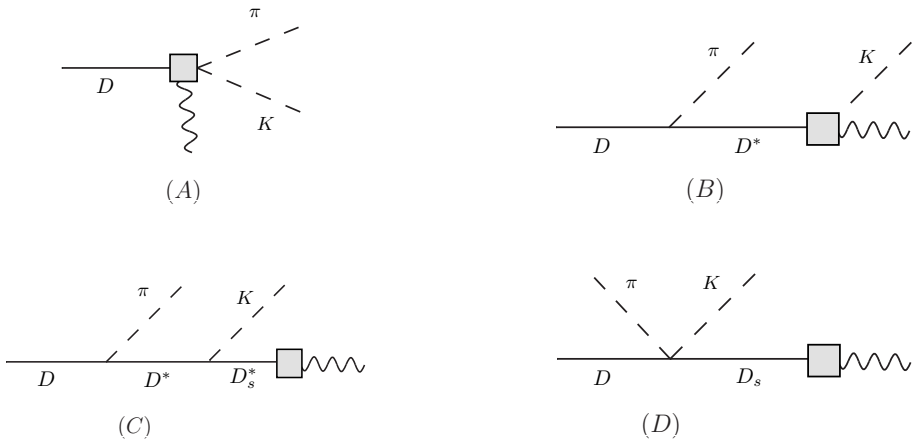

Figure 1.4: Tree-level diagrams for $D \to \pi K$ + leptonic current. D-mesons are represented by solid lines, pseudoscalars by dashed lines and the insertion of the leptonic current is denoted by the shaded square.

calculations with $2+1$ dynamical quark flavors are averaged. So far we have only considered terms at leading chiral order. Following Ref. [75] we take into account also terms coming from the heavy-meson Lagrangian at chiral order $\mathcal{O}(E_\pi^1)$, as well as the next-to-leading (NLO) effects arising artefactually already from the leading-order expression. We translate the Lagrangian given in Ref. [75] into an expression similar to Eq. (1.52), using the conventions of Ref. [69],

$$L_{\nu a}^{(1)} = -\frac{\beta_1}{2\sqrt{m_D}}\mathrm{Tr}\left[\gamma_\nu(1-\gamma_5)\gamma_\mu H_c u_{cb}(\partial^\mu U^\dagger)_{ba}\right] - \frac{\beta_2 m_D^2}{2\sqrt{m_D}}\mathrm{Tr}\left[\gamma_\nu(1-\gamma_5)v_\mu H_c u_{cb}(\partial^\mu U^\dagger)_{ba}\right]. \tag{1.53}$$

The unknown couplings β_1 and β_2 need to be constrained either phenomenologically or by considerations involving the underlying symmetry. In this thesis we propose a method to determine the couplings by means of a low-energy theorem for $p_K \to 0$: it relates the D_{l4} decay matrix elements to the $D^+ \to \pi^0 l^+ \nu_l$ ones, exploiting the simpler structure of the latter, cf. Appendix B.1.

To the considered next-to-leading order also $SU(3)$ breaking effects occur in the interaction vertices, where in the case of D_{l4} the only contribution of the symmetry-violating Lagrangian Eq. (1.49) comes from the terms $\propto \lambda_1$ and λ_1'. In addition there is an NLO contribution to the four-vertex (diagram D) coming from [76]

$$\mathcal{L}_\sigma = \sigma_1 \mathrm{Tr}\bar{H}_a H_b (u^\mu u_\mu)_{ba} + \sigma_2 \mathrm{Tr}\bar{H}_a H_b v_\mu v_\nu (\{u^\mu, u_\mu\})_{ba}. \tag{1.54}$$

However, this Lagrangian only becomes important for a massive final-state lepton—if the limit of vanishing electron mass is considered these corrections can be omitted. Other possible terms at the NLO level [77] can be incorporated into redefinitions of the coupling constants, for example we explicitly take into account the $f_D - f_{D_s^{(*)}}$ splitting, using the averaged lattice results $f_{D_s} = (249.8 \pm 2.3)$ MeV [74] and from sum-rule calculations $f_{D^*} = (252.2 \pm 22.3 \pm 4)$ MeV and $f_{D_s^*} = (305.5 \pm 26.8 \pm 5)$ MeV [78]. Also the $SU(3)$ splitting between the decay constants F_π and F_K is considered explicitly, with $F_K = (110.0 \pm 0.3)$ MeV [62].

The NLO-corrected tree-level amplitudes, supplemented by subleading effects in the chiral

expansion as well as in the $1/m_D$ expansion, read

$$\begin{aligned}
A^{\chi\mathrm{NLO}} =& ip_\pi^\mu \frac{f_D - 2\beta_1}{2F_\pi F_K} + iL^\mu \frac{f_D - 4m_D\beta_2 v\cdot p_\pi}{4F_\pi F_K},\\
B^{\chi\mathrm{NLO}} =& ip_\pi^\mu \frac{g}{2F_\pi F_K}\frac{f_{D^*}m_{D^*} + 2\beta_1 v\cdot p_K + 2\beta_2 m_D m_{D^*} v\cdot p_K}{v\cdot p_\pi + \Delta} - ip_K^\mu \frac{g f_{D^*}}{2F_\pi F_K}\frac{v\cdot p_\pi}{v\cdot p_\pi + \Delta}\\
&+ iL^\mu \frac{g}{2F_\pi F_K m_{D^*}}\frac{f_{D^*}(p_\pi^2 - m_D v\cdot p_\pi) - 2\beta_1 p_K\cdot p_\pi - 2\beta_2 m_D^2 v\cdot p_\pi v\cdot p_K}{v\cdot p_\pi + \Delta}\\
&- \epsilon^{\mu\nu\rho\sigma} L_\nu p_{\pi\rho} p_{K\sigma}\frac{\beta_1 g}{F_\pi F_K}\frac{1}{v\cdot p_\pi + \Delta},\\
C^{\chi\mathrm{NLO}} =& - iL^\mu \frac{g^2 f_{D_s}}{2m_{D^*}F_\pi F_K}\frac{m_{D^*}p_\pi\cdot p_K - m_{D^*}(v\cdot p_\pi)(v\cdot p_K) + (v\cdot p_K)p_\pi^2 + (v\cdot p_\pi)(p_\pi\cdot p_K)}{[v\cdot p_\pi + \Delta][v\cdot(p_\pi + p_K) + \mu]}\\
&- \epsilon^{\mu\nu\rho\sigma} L_\nu p_{\pi\rho} p_{K\sigma}\frac{g^2 f_{D_s^*}}{2F_\pi F_K}\frac{1}{[v\cdot p_\pi + \Delta][v\cdot(p_\pi + p_K) + \Delta + \mu]},\\
D^{\chi\mathrm{NLO}} =& - iL^\mu \frac{f_{D_s}}{4F_\pi F_K}\frac{v\cdot(p_K - p_\pi) + 8\sigma_1 p_\pi\cdot p_K + 16\sigma_2 v\cdot p_K\, v\cdot p_\pi + 8\hat{m}\lambda_1 + \mu}{v\cdot(p_K + p_\pi) + \mu}.
\end{aligned} \tag{1.55}$$

Note that Δ and μ corrections are of the order of the pion mass and thus their importance in the power counting is comparable to the chiral next-to-leading order [68]. Due to Eq. (1.49) μ is related to the quark-mass difference $m_s - \hat{m}$, which conventionally is counted as chiral order $\mathcal{O}(p^2)$. We have thus only taken into account such quark-mass driven $SU(3)$-breaking contributions to the Lagrangian which affect the D-mass (and not for instance in the case of the coupling to the current, which is therefore corrected by hand by replacing f_D by the appropriate couplings $f_{D_{(s)}}^{(*)}$). Finally, chiral NLO momentum corrections are included into the numerators of the vector propagators, e.g.

$$-i\left(g^{\mu\nu} - v^\mu v^\nu\right) \to -i\left(g^{\mu\nu} - \frac{m_D^2}{m_{D^*}^2}\left(v^\mu - \frac{q_K^\mu + q_\pi^\mu}{m_D}\right)\left(v^\nu - \frac{q_K^\nu + q_\pi^\nu}{m_D}\right)\right). \tag{1.56}$$

1.3 Scattering theory

The methodology we mainly pursue in this thesis is dispersion theory. For physical quantities such as scattering amplitudes or form factors dispersion relations allow to recover the full amplitude from the discontinuity across branch cuts and single poles. These singularities as the complete analytic structure stem from the unitarity and analyticity requirements the amplitude exhibits, which are developed in S-matrix theory, see Ref. [79]. In this section we first introduce the principles of unitarity, crossing symmetry, and analyticity and then show how to exploit them together with Cauchy's integral formula to derive a dispersive representation of an amplitude. We then focus on a specific dispersive setting, in which the amplitudes are represented in terms of Omnès functions that are analytic solutions of the dispersion integrals for elastic scattering processes [80, 81]. The onset of inelastic contributions requires to derive coupled-channel Muskhelishvili–Omnès representations that may be solved numerically.

1.3.1 The S-matrix

The scattering of particles in quantum field theories is commonly expressed via the S-matrix, which is separated into an interaction part, driven by the T-matrix, and a free non-interacting part given by the identity operator, i.e. $S = \mathbb{1} + iT$. The transition probability of an initial

(incoming) asymptotic state vector $|i\rangle$ scattering into a final (outgoing) asymptotic state vector $|f\rangle$ is given by

$$|\langle f|S|i\rangle|^2 \,, \tag{1.57}$$

where S is the S-matrix operator on the respective Hilbert space that specifies the underlying interaction. The states $|i\rangle$, $|f\rangle$ are demanded to be asymptotically free states, which requires short-range interactions, ensuring the above squared S-matrix element to be meaningful, unique, and experimentally observable. Moreover, there are certain physically mandatory prerequisites that constrain the S-matrix further: causality has profound impact on the analytic structure of the S-matrix, the superposition principle resulting in a linear S-matrix, and probability conservation linked to unitarity and crossing symmetry. In the remaining section we discuss the consequences of these essential constraints, with a focus on the principles of unitarity and analyticity (we restrict ourselves to the scattering of scalar, isoscalar particles). As a pedagogical example we will consider a two-particle scattering process, with two incoming particles A and B, and two outgoing particles C and D,

$$A(p_A)B(p_B) \to C(p_C)D(p_D), \tag{1.58}$$

where p_i are the respective four-momenta. The scattering amplitude $\mathcal{F}(s,t,u)$ is defined by

$$(2\pi)^4\delta^4(p_A+p_B-p_C-p_D)\mathcal{F}(s,t,u) = \langle p_A, p_B|T|p_C, p_D\rangle, \tag{1.59}$$

being a Lorentz scalar function of the Mandelstam variables s,t,u, given by

$$\begin{aligned} s =& (p_A+p_B)^2 = (p_C+p_D)^2, \\ t =& (p_A-p_C)^2 = (p_D-p_B)^2, \\ u =& (p_A-p_D)^2 = (p_C-p_B)^2, \\ \text{and} \quad & s+t+u = M_A^2+M_B^2+M_C^2+M_D^2 =: 3s_0. \end{aligned} \tag{1.60}$$

$\mathcal{F}(s,t,u)$ is an analytic function in the complex plane, except for the non-analytic structures demanded by unitarity and crossing symmetry.

Unitarity of the S-matrix, $SS^\dagger = \mathbb{1}$, implies $T - T^\dagger = iTT^\dagger$, and in terms of matrix elements $T_{jk} = \langle j|T|k\rangle$ the unitarity relation reads

$$T_{fi} - T_{if}^* = i(2\pi)^4 \sum_m \delta^{(4)}(p_m - p_f) T_{fm} T_{im}^* \overset{T_{if}=T_{fi}}{=} 2i\,\mathrm{Im}\; T_{fi}, \tag{1.61}$$

where the δ-function ensures energy and momentum conservation, and the sum runs over all possible intermediate states m. The second equality holds for symmetric matrix elements $T_{if} = T_{fi}$, i.e. for processes that are invariant under time reversal symmetry T (or likely under CP symmetry due to the CPT theorem) like strong-interaction processes. However, even without specifying to symmetric processes, T_{fi} and T_{if}^* are related to each other due to hermitian analyticity: considering e.g. an s-channel two-particle scattering process Eq. (1.58), both matrix elements are described by the same analytic function $\mathcal{F}(s,t,u)$ in the complex s-plane, but the physical amplitude corresponding to T_{fi} is the limit on the real axis from the upper-half s-plane,

$$\mathcal{F}(s,t,u) = \lim_{\epsilon\to 0^+} \mathcal{F}(s+i\epsilon,t,u) \tag{1.62}$$

while for T_{if}^* the real s axis is approached from below, $s - i\epsilon$. The left-hand side of the unitarity relation Eq. (1.61) thus can be rewritten by the discontinuity of that analytic function,

$$\begin{aligned} \mathrm{disc}\,\mathcal{F}(s,t,u) &= \lim_{\epsilon\to 0} \left(\mathcal{F}(s+i\epsilon,t,u) - \mathcal{F}(s-i\epsilon,t,u)\right) \\ &= i(2\pi)^4 \sum_m \delta^{(4)}(p_m - p_f) T_{fm} T_{im}^*. \end{aligned} \tag{1.63}$$

This equation dictates the singularity structure the (otherwise analytic) amplitude $\mathcal{F}(s,t,u)$ exhibits. If we exclude bound states and consider an elastic scattering process ($AB = CD$), i.e. we consider energies below the onset of inelastic channels, there occurs only one single intermediate state, and the sum in Eq. (1.63) reduces to a sole contribution for energies above the elastic energy threshold $s_{\text{thr}} = (M_C + M_D)^2$,

$$\operatorname{disc}\mathcal{F}(s,t,u) = \frac{i}{16\pi^2 S}\frac{\lambda^{1/2}(s,M_C^2,M_D^2)}{2s}\,\Theta(s-s_{\text{thr}})\int \mathrm{d}\Omega\; T_{ff}^* T_{fi}\,, \tag{1.64}$$

where $\int \mathrm{d}\Omega$ denotes angular integration, S is the symmetry factor, $S = 1$ in the case of distinguishable and $S = 2$ for identical particles, and

$$\lambda(x,y,z) = x^2 + y^2 + z^2 - 2xy - 2yz - 2zx \tag{1.65}$$

defines the Källén triangle function. At the two-particle threshold s_{thr} a branch cut opens, by convention running along the real s axis to infinity, connecting two copies of the complex s-plane (two Riemann sheets). For higher energies, inelastic scattering effects (like multiparticle or higher-mass intermediate states) give rise to additional terms in the unitarity relation, which induce further cuts, each inelastic threshold corresponding to a new branch point, and further Riemann sheets, accordingly. In addition to these so-called right-hand cuts there may exist other non-analytic structures: poles (pointlike singularities) below the elastic threshold associated with intermediate bound states, as well as left-hand cuts due to crossing symmetry. We discuss the latter in the following.

Due to the property of crossing symmetry different kinematical regions can be related to each other: the scattering amplitude that is known in a certain channel, e.g. in the s-channel, can be analytically continued over the unphysical region to describe the dynamics in another region of the Mandelstam plane,[8] as shown in Figure 1.5, i.e. the (crossed) t- or u-channel scattering or the decay in the case of unstable particles. Hence, all these processes are described by the same analytic function, exploiting that it depends on kinematical invariants, such that it is invariant under a sign flip in the energy p_i^0. It even describes further processes, related to each other by CPT and PT symmetry.

For the two-particle s-channel scattering example Eq. (1.58) the following processes are obtained by crossing, i.e. by intertwining incoming and outgoing particles,

$$\begin{aligned}
A(p_A) + \bar{C}(-p_C) &\;\to\; \bar{B}(-p_B) + D(p_D), && t\text{−channel},\\
A(p_A) + \bar{D}(-p_D) &\;\to\; \bar{B}(-p_B) + C(p_C), && u\text{−channel},\\
A(p_A) &\;\to\; \bar{B}(-p_B) + C(p_C) + D(p_D) && \text{decay}.
\end{aligned}$$

The decay reaction requires particle A to be unstable. The bar indicates the crossed negative-energy states to be interpreted as antiparticles.

In order to learn about the effect of crossing symmetry on the analyticity structure we evaluate the Mandelstam variables in a specific reference frame and demonstrate their dependencies on each other. We choose the s-channel center-of-mass frame, with three-momenta and energies

$$\mathbf{p}_A = -\mathbf{p}_B \equiv \mathbf{p}, \quad \mathbf{p}_C = -\mathbf{p}_D \equiv \mathbf{p}', \quad E_i = (M_i^2 + |\mathbf{p}_i|^2)^{1/2}, \tag{1.66}$$

in which the scattering angle is defined by $\theta_s = \angle(\mathbf{p}_A, \mathbf{p}_C)$ and the center-of-mass momenta read

$$|\mathbf{p}| = \frac{\lambda^{1/2}(s,M_A^2,M_B^2)}{2\sqrt{s}}, \quad |\mathbf{p}'| = \frac{\lambda^{1/2}(s,M_C^2,M_D^2)}{2\sqrt{s}}. \tag{1.67}$$

[8] The Mandelstam plane, spanned by combinations of the Mandelstam variables, e.g. $t-u$ versus s, is used to illustrate kinematically allowed regions for the diverse scattering and decay processes.

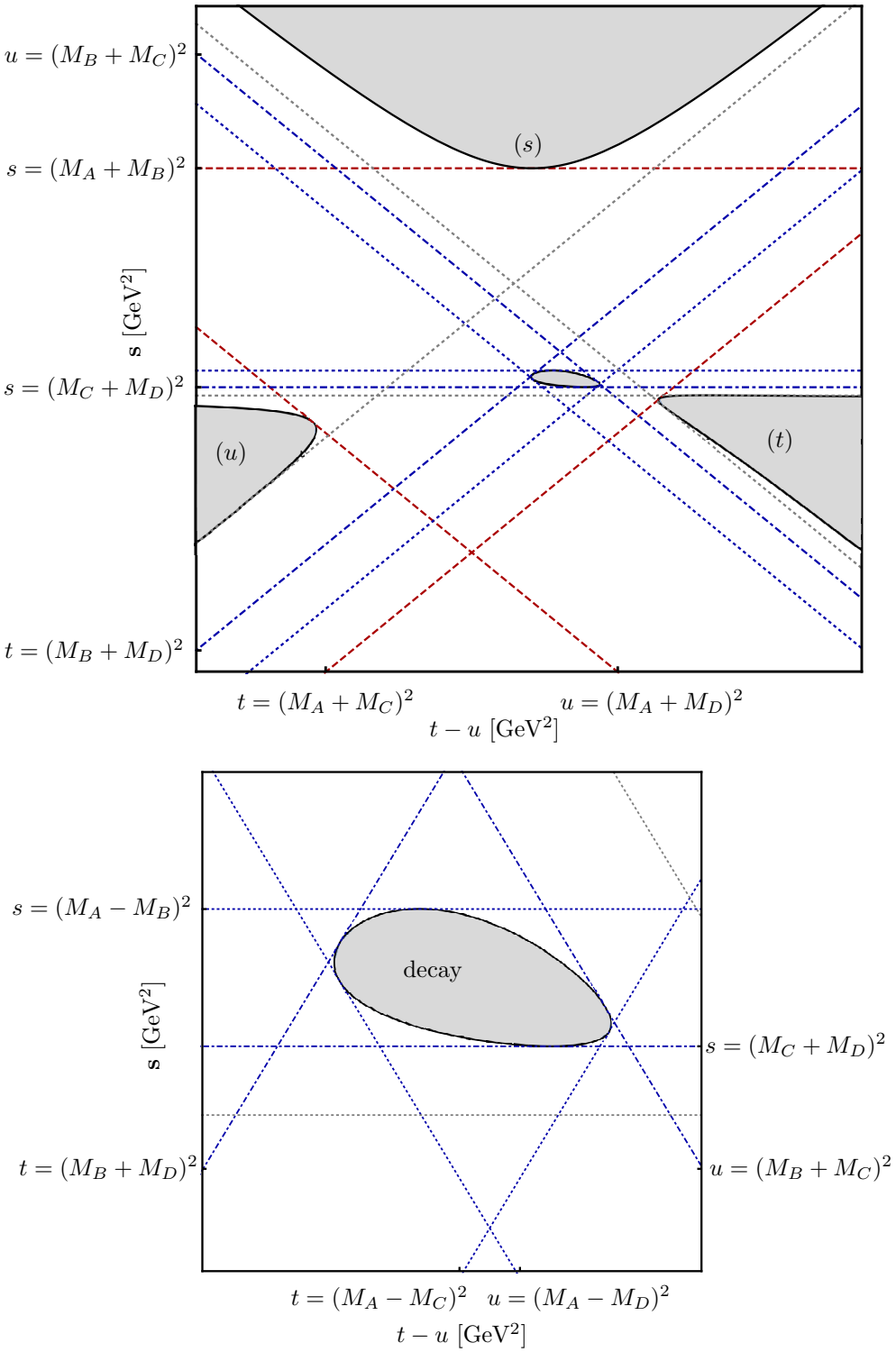

Figure 1.5: The Mandelstam plane with Mandelstam variables $t - u$ versus s is depicted. The shaded areas show the physical regions for s-, t-, and u-channel scattering processes with unequal masses, $M_A > M_B + M_C + M_D$, as well as the decay region, which is enlarged in the bottom panel.

For states with equal masses ($M_A = M_B \equiv m$ or $M_C = M_D \equiv m$) commonly also the function σ is used, $\sigma(s) = \lambda^{1/2}(s, m^2, m^2)/s$. In the chosen frame the Mandelstam variables are given by

$$\begin{aligned} s &= (E_A + E_B)^2 = (E_C + E_D)^2, \\ t &= M_A^2 + M_C^2 - 2E_A E_C + 2|\mathbf{p}||\mathbf{p}'|\cos\theta_s, \\ u &= M_A^2 + M_D^2 - 2E_A E_D - 2|\mathbf{p}||\mathbf{p}'|\cos\theta_s, \end{aligned} \tag{1.68}$$

allowing to rewrite t and u as functions of s and θ_s, and to express the scattering angle in terms of s, t, and u,

$$\begin{aligned} t(s,\cos\theta_s) &= \frac{3s_0 - s}{2} + \left(\frac{\lambda^{1/2}(s, M_A^2, M_B^2)\lambda^{1/2}(s, M_C^2, M_D^2)}{2s}\,\cos\theta_s - \frac{\Delta_{12}\Delta_{34}}{2} \right), \\ u(s,\cos\theta_s) &= \frac{3s_0 - s}{2} - \left(\frac{\lambda^{1/2}(s, M_A^2, M_B^2)\lambda^{1/2}(s, M_C^2, M_D^2)}{2s}\,\cos\theta_s - \frac{\Delta_{12}\Delta_{34}}{2} \right), \\ &\Rightarrow \cos\theta_s = \frac{s(t-u) + \Delta_{12}\Delta_{34}}{\lambda^{1/2}(s, M_A^2, M_B^2)\lambda^{1/2}(s, M_C^2, M_D^2)}, \quad \Delta_{ij} = M_i^2 - M_j^2. \end{aligned} \tag{1.69}$$

Similar expressions are obtained for $s(t,\cos\theta_t)$, $s(u,\cos\theta_u)$, $t(u,\cos\theta_u)$, and $u(t,\cos\theta_t)$.

Eq. (1.68) implies that the minimal energy for s-channel scattering is the threshold energy $s_{\rm thr} = \max((M_A + M_B)^2, (M_C + M_D)^2)$, and $s \geqslant s_{\rm thr}$ covers the physical region, corresponding to a branch cut as discussed above. Similarly, at the threshold energies for the other channels, $t_{\rm thr} = \max((M_A + M_C)^2, (M_B + M_D)^2)$, and $u_{\rm thr} = \max((M_A + M_D)^2, (M_B + M_C)^2)$, the physical regions for t- and u-channel scattering start, generating right-hand cuts for $t \geqslant t_{\rm thr}$ on the real axis in the complex t-plane, and for $u \geqslant u_{\rm thr}$ in the complex u-plane. According to Eq. (1.69) these cuts are transferred onto the complex s-plane (and similarly vice versa), where they occur as left-hand cuts.

Once calculations of scattering amplitudes or form factors become explicit, it is expedient to deal with partial-wave unitarity relations, obtained by expanding the full amplitudes $T_{ij}(s,\cos\theta_s)$ in terms of Legendre polynomials, with attention to a particular isospin I,

$$\begin{aligned} T_{fi}^I(s,\cos\theta_s) &= 16\pi S \sum_{\ell=0}^{\infty} (2\ell+1) P_\ell(\cos\theta_s) \mathcal{F}_\ell^I(s), \\ T_{ff}^I(s,\cos\theta_s) &= 16\pi S \sum_{\ell=0}^{\infty} (2\ell+1) P_\ell(\cos\theta_s) T_\ell^I(s). \end{aligned} \tag{1.70}$$

On the one hand, angular integration that arises e.g. in Eq. (1.64) can be avoided. On the other hand an important theorem, the Watson theorem [82], is known to hold for elastic partial-wave scattering. It states that below the lowest inelastic threshold the phase shift $\delta_\ell^I(s)$ of a partial-wave amplitude $\mathcal{F}_\ell^I(s) = |\mathcal{F}_\ell^I(s)| \exp\left(i\delta_\ell^I(s)\right)$ is given by the phase shift $\delta_\ell^{I,\rm el}(s)$ (modulo π) of the elastic final-state scattering amplitude $T_\ell^I(s) = |T_\ell^I(s)| \exp\left(i\delta_\ell^{I,\rm el}(s)\right)$. Eq. (1.64) simplifies for a process with $|i\rangle = |f\rangle$, as e.g. for $\pi\pi \to \pi\pi$ or $\pi K \to \pi K$ scattering, which yields the partial-wave unitarity relation

$$\mathrm{Im} T_\ell^I(s) = \frac{\lambda^{1/2}(s, M_C^2, M_D^2)}{s}\,|T_\ell^I(s)|^2 = \frac{2|\mathbf{p}|}{\sqrt{s}}\,|T_\ell^I(s)|^2. \tag{1.71}$$

The matrix elements $T_\ell^I(s)$ are related to partial-wave decomposed S-matrix elements $S_\ell^I(s)$ by

$$S_\ell^I(s) = 1 + \frac{4i|\mathbf{p}|}{\sqrt{s}}\,T_\ell^I(s), \quad |S_\ell^I(s)| \leq 1, \tag{1.72}$$

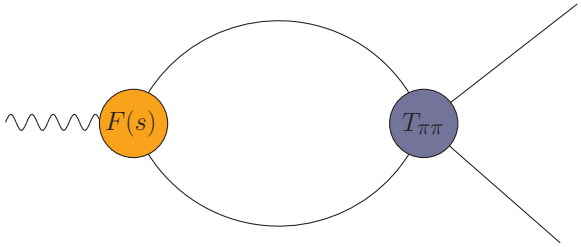

Figure 1.6: Diagrammatic representation of the vector form factor, depicted by the orange circle (left), driving the coupling of two pions (solid lines) to the electromagnetic current (curly line). The blue circle at the right side denotes the elastic $\pi\pi$ scattering amplitude.

where in the elastic, single-channel treatment $|S_\ell^I(s)| = 1$ (elastic unitarity), which yields the parametrizations

$$S_\ell^I(s) = e^{2i\delta_\ell^{I,\mathrm{el}}(s)} \quad \Rightarrow \quad T_\ell^I(s) = \sqrt{s}\,\frac{e^{2i\delta_\ell^{I,\mathrm{el}}(s)} - 1}{4i|\mathbf{p}|} = \frac{\sqrt{s}}{2|\mathbf{p}|}\, e^{i\delta_\ell^{I,\mathrm{el}}(s)} \sin\,\delta_\ell^{I,\mathrm{el}}(s). \tag{1.73}$$

A quantity for which the assumption of elastic unitarity works very well (at low energies $s \lesssim 1\,\mathrm{GeV}^2$) is the pion vector form factor $(\mathcal{F}_\pi)_{\ell=1}^{I=1} \equiv \mathcal{F}_\pi^V(s)$, defined by the coupling of a pion–pion system to an electromagnetic current j_{em},

$$\langle 0|j_{\mathrm{em}}^\mu(0)|\pi^+(p_1)\pi^-(p_2)\rangle = (p_2 - p_1)^\mu \mathcal{F}_\pi^V(s), \quad j_{\mathrm{em}}^\mu = \frac{2}{3}\bar{u}\gamma^\mu u - \frac{1}{3}\bar{d}\gamma^\mu d. \tag{1.74}$$

It can be directly measured via the processes $e^-e^+ \to \pi^+\pi^-$ [83–88] or, via an isospin rotation, using $\tau^- \to \pi^-\pi^0\nu_\tau$ [89]. The diagram that contributes to the discontinuity of the vector form factor is shown in Figure 1.6. A further discussion can be found in Section 2.4.1.

At energies above the onset of inelasticities and the breakdown of elastic unitarity, Eq. (1.73) must be extended to a coupled-channel version, involving the so-called inelasticity parameters $0 \leq \eta_i^\ell(s) \leq 1$. As an example the two-channel scattering amplitude $T_0^0(s)$ will be given in Section 1.3.4. We employ next the example of an elastic two-particle scattering process with $|i\rangle \neq |f\rangle$ to demonstrate Watson's final-state theorem. Unitarity together with the parametrization Eq. (1.73) implies

$$\begin{aligned} \mathrm{Im}\,\mathcal{F}_\ell^I(s) &= \frac{2|\mathbf{p}|}{\sqrt{s}} T_\ell^{I\,*}(s)\,\mathcal{F}_\ell^I(s) \\ \Leftrightarrow \mathrm{Im}\,\mathcal{F}_\ell^I(s) &= \mathcal{F}_\ell^I(s) e^{-i\delta_\ell^{I,\mathrm{el}}(s)} \sin\,\delta_\ell^{I,\mathrm{el}}(s)\Theta(s - s_{\mathrm{thr}}), \end{aligned} \tag{1.75}$$

such that

$$\sin\,\delta_\ell^I(s) = e^{i\left(\delta_\ell^I(s) - \delta_\ell^{I,\mathrm{el}}(s)\right)} \sin\,\delta_\ell^{I,\mathrm{el}}(s)\Theta(s - s_{\mathrm{thr}}). \tag{1.76}$$

This equation demands the right-hand side to be real (the left-hand side obviously is), which yields the constraint

$$\delta_\ell^{I,\mathrm{el}}(s) = \delta_\ell^I(s) \mathrm{mod}(\pi) \tag{1.77}$$

in the elastic scattering regime.

1.3.2 Dispersion theory

One of the pillars of non-perturbative approaches to strong-interaction processes is dispersion theory. With the powerful tools of complex analysis, dispersion theory exploits the fundamental

physical principles of micro causality, probability conservation, and crossing symmetry. In the previous section we have discussed the analytic structure of physical amplitudes, illustrating that amplitudes are analytic functions in the complex plane except for non-analytic structures such as branch cuts and poles, that are dictated by the above fundamental physical principles. These fundamental physical principles constrain the amplitude under consideration such that ideally the amplitudes can be reconstructed with little further input via Cauchy's integral theorem.

Let Ω be a simply connected open subset of the complex plane $\mathbb{C}$ and let $f : U \to \mathbb{C}$ be a holomorphic function, which is continuous on $\partial\Omega$. Then Cauchy's integral theorem states that for $y \in \Omega$,

$$\oint_{\partial\Omega} \mathrm{d}y \; f(y) = 0, \tag{1.78}$$

and Cauchy's integral formula reads

$$f(z) = \frac{1}{2\pi i} \oint_{\partial\Omega} \mathrm{d}y \; \frac{f(y)}{y - z}. \tag{1.79}$$

In order to illustrate how dispersion relations are constructed we will first discuss the example of a physical amplitude $\mathcal{F}(s)$ that depends only on a single kinematic variable s and exhibits only a branch cut on the positive real axis. Such a physical scenario is provided by form factors like the pion vector form factor. We will then turn on the more general case of elastic two-particle scattering processes, which we already focused on in Section 1.3.1.

The analytic structure of our form factor example in the complex s-plane is depicted in Figure 1.7, where the branch cut on the real axis starts at the squared threshold energy s_{thr}. Thus $\mathcal{F}(s)$ can be reconstructed at a point s in the complex plane via Cauchy's integral theorem provided that the amplitude is holomorphic in the encircled area Ω,

$$\mathcal{F}(s) = \frac{1}{2\pi i} \int_{\gamma} \frac{\mathcal{F}(s')}{s' - s} \, \mathrm{d}s' \; , \tag{1.80}$$

where γ denotes the closed integration contour $\partial\Omega$.

This integration contour can be deformed exploiting Cauchy's integral theorem again, with the condition that no non-analytic regions are crossed, which yields the contour depicted in the right panel of Figure 1.7. Provided that $\mathcal{F}(s)$ vanishes sufficiently fast at complex infinity we can enlarge the contour to complex infinity such that Eq. (1.80) reduces to a contour integral above minus below the branch cut, i.e. to an integral over the discontinuity,

$$\mathcal{F}(s) = \frac{1}{2\pi i} \int_{\gamma_+ + \gamma_-} \frac{\mathcal{F}(s')}{s' - s} \, \mathrm{d}s' = \frac{1}{2\pi i} \int_{s_{\mathrm{thr}}}^{\infty} \frac{\mathrm{disc}\, \mathcal{F}(s')}{s' - s - i\epsilon} \, \mathrm{d}s'. \tag{1.81}$$

For time-invariant processes Schwarz's reflection principle $\mathcal{F}(s^*) = \mathcal{F}(s)^*$ holds, see Eq. (1.61), which allows us to replace the discontinuity by the imaginary part,

$$\mathrm{disc}\, \mathcal{F}(s) = 2i \, \mathrm{Im} \; \mathcal{F}(s). \tag{1.82}$$

Eq. (1.81) is the desired s-channel dispersion relation representing single-variable functions like the form factors.

If a sufficient decrease of $\mathcal{F}(s)$ for large s, required to ensure the convergence of the dispersion integral, is not guaranteed, the *unsubtracted* representation Eq. (1.81) must be modified. For example for a function that behaves like $\mathcal{F}(s) \propto s^{n-1}$ for $|s| \to \infty$ with $n \in \mathbb{N}$ the dispersion integral must be subtracted n-times, according to the following considerations. We define the auxiliary function $\mathcal{G}(s) = \mathcal{F}(s)/p^n(s)$ with $p^n(s)$ being a polynomial of order n and tune n such

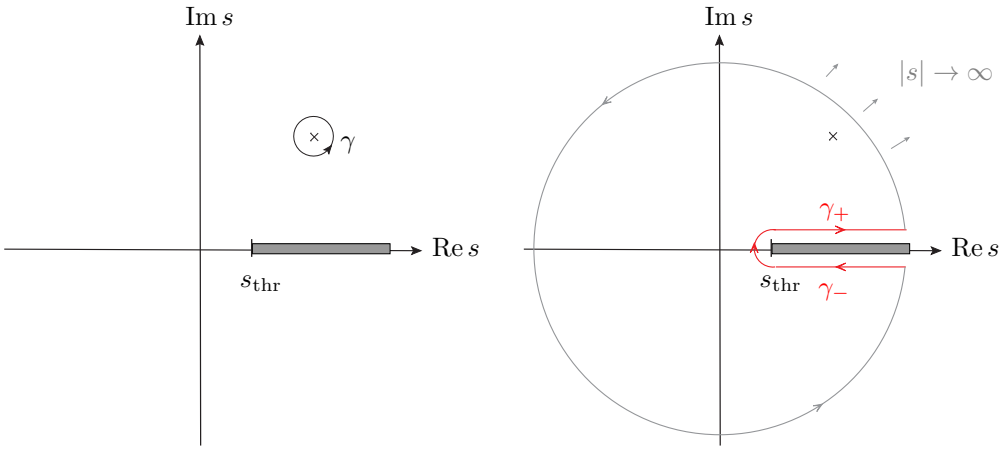

Figure 1.7: Integration path. In the left panel the closed circular integration contour γ around a point s in the complex s-plane according to Eq. (1.80) is depicted. How this contour is enlarged to an arc with radius $|s| \to \infty$, encircling (thus not crossing) the branch cut (gray shaded) that starts at the threshold s_{thr}, is illustrated in the right panel. For sufficiently fast decreasing integrands the integral over the arc vanishes and the integral above minus below the cut remains, $\gamma_+ + \gamma_-$.

that $\mathcal{G}(s)$ falls off fast enough at complex infinity to obtain a convergent dispersion integral. Dividing by such a polynomial entails a suppression of the unknown high-energy behavior, however, n additional poles are introduced to the function $\mathcal{G}(s)$. These result in unknown constants (called subtraction constants) in the dispersion relation for $\mathcal{F}(s)$, which have to be determined by other means (e.g. experimental data or supplemental theory input). We can choose the polynomial $p^n(s)$ to be given by $p^n(s) = (s - s_0)^n$, where s_0 is called the subtraction point. With the above established procedure and taking into account the additional poles, we obtain the following dispersion relation for $\mathcal{G}(s)$

$$\mathcal{G}(s) = \frac{1}{2\pi i} \int_{\gamma_{s_0}} \frac{\mathcal{G}(s')}{s' - s} \, \mathrm{d}s' + \frac{1}{\pi} \int_{s_{\text{thr}}}^{\infty} \frac{\operatorname{Im} \mathcal{G}(s')}{s' - s - i\epsilon} \, \mathrm{d}s', \tag{1.83}$$

where γ_{s_0} denotes the closed contour encircling the subtraction point s_0. The first integral evaluates to a rational function of order -1 in s according to the residue theorem and we thus obtain an n-times subtracted representation of the function $\mathcal{F}(s)$,

$$\mathcal{F}(s) = P_{n-1}(s) + \frac{(s - s_0)^n}{\pi} \int_{s_{\text{thr}}}^{\infty} \frac{\operatorname{Im} \mathcal{F}(s')}{(s' - s_0)^n (s' - s - i\epsilon)} \, \mathrm{d}s', \tag{1.84}$$

where $P_{n-1}(s)$ is called the subtraction polynomial of order $n - 1$, involving n unknown subtraction constants that require further constraints from experiment or further theory input.

The single-variable dispersion relation Eq. (1.84), however, is not valid in the more general[9] case for scattering amplitudes $\mathcal{F}(s, t, u)$ that depend on several variables. Considering the two-body scattering process Eq. (1.58), the presence of an additional left-hand-cut structure caused by crossed-channel effects necessitates to consider the integration over these cuts as well. In order to construct a dispersion relation for processes depending on multiple kinematical

[9] Remember that throughout this section we specify to the case of scattering of spinless particles.

variables that exhibit right- and left-hand-cut structures, we apply the so-called reconstruction theorem [90–95]. The main idea of this procedure is to fix kinematical variables to an arbitrary constant without loss of generality, allowing us to write down fixed-variable dispersion relations, which are employed to reconstruct the amplitude in question via symmetrisation. For simplicity, we consider elastic two-body scattering of identical particles and fix one of the Mandelstam variables, e.g. $t = t_0 < 0$. The constraint $s + t + u = 3s_0$ allows then to write the fixed-t amplitude as a function composed of terms depending on one single variable only. With the analytic structure in the s-plane given by the right-hand cut ($s \geq s_{\text{thr}}$) and the left-hand cut due to the u-channel contribution ($u \geq u_{\text{thr}}$) one obtains the following fixed-t dispersion relation (or similarly a fixed-u dispersion relation by keeping u at a fixed value),

$$\mathcal{F}(s,t_0,u) = P_{n-1}(s,t_0,u) + \frac{s^n}{\pi}\int_{s_{\text{thr}}}^{\infty} \frac{\text{Im}\ \mathcal{F}(s',t_0,u(s'))}{s'^n(s'-s-i\epsilon)}\ \text{d}s' + \frac{u^n}{\pi}\int_{u_{\text{thr}}}^{\infty} \frac{\text{Im}\ \mathcal{F}(s(u'),t_0,u')}{u'^n(u'-u-i\epsilon)}\ \text{d}u'. \tag{1.85}$$

If we further decompose this amplitude into partial waves

$$\mathcal{F}(s,t_0,u(s)) = \sum_\ell f_\ell(s) P_\ell(\cos\theta_s), \qquad \mathcal{F}(s(u),t_0,u) = \sum_\ell f_\ell(u) P_\ell(\cos\theta_u), \tag{1.86}$$

where $P_\ell(\cos\theta_x)$ denotes the Legendre-Polynomials with the x-channel scattering angle $\cos\theta_x$ and f_ℓ the partial waves of angular momenta ℓ, we obtain

$$\begin{aligned}\mathcal{F}(s,t_0,u) = P_{n-1}(s,t_0,u) &+ \frac{s^n}{\pi}\int_{s_{\text{thr}}}^{\infty} \frac{\sum_\ell P_\ell(\cos\theta_{s'})\,\text{Im}\ f_\ell(s')}{s'^n(s'-s-i\epsilon)}\ \text{d}s' \\ &+ \frac{u^n}{\pi}\int_{u_{\text{thr}}}^{\infty} \frac{\sum_l P_\ell(\cos\theta_{u'})\,\text{Im}\ f_\ell(u')}{u'^n(u'-u-i\epsilon)}\ \text{d}u'.\end{aligned} \tag{1.87}$$

Note that considering elastic two-particle scattering implies that all crossed-channels yield the same scattering process and partial-wave decomposition, such that the amplitude is highly symmetrical in the kinematical variables. Due to Eq. (1.69) we can express the s-channel scattering in terms of Mandelstam variables, $\cos\theta_s = (t-u)/(s-s_{\text{thr}})$ (and likewise for $\cos\theta_t$ and $\cos\theta_u$), which yields

$$\begin{aligned}\mathcal{F}(s,t_0,u) =& P_{n-1}(s,t_0,u) + \frac{s^n}{\pi}\int_{s_{\text{thr}}}^{\infty} \frac{\text{Im}\ f_0(s')}{s'^n(s'-s-i\epsilon)} \\ &+ (t_0-u)\frac{s^n}{\pi}\int_{s_{\text{thr}}}^{\infty} \frac{\text{Im}\ f_1(s')}{s'^n(s'-s_{\text{thr}})(s'-s-i\epsilon)} + \dots \\ &+ \frac{u^n}{\pi}\int_{u_{\text{thr}}}^{\infty} \frac{\text{Im}\ f_0(u')}{u'^n(u'-u-i\epsilon)} \\ &+ (t_0-s)\frac{u^n}{\pi}\int_{u_{\text{thr}}}^{\infty} \frac{\text{Im}\ f_1(u')}{u'^n(u'-u_{\text{thr}})(u'-u-i\epsilon)} + \dots,\end{aligned} \tag{1.88}$$

where the dots denote higher partial-wave contributions. Similarly, we obtain fixed-s and fixed-u dispersion relations. Symmetrization of the three representations yields

$$\mathcal{F}(s,t,u) = \mathcal{F}_0(s) + \mathcal{F}_0(t) + \mathcal{F}_0(u) + (t-u)\mathcal{F}_1(s) + (t-s)\mathcal{F}_1(u) + (s-u)\mathcal{F}_1(t) + \dots, \tag{1.89}$$

where the single-variable amplitudes $\mathcal{F}_\ell$ incorporate the corresponding dispersion integrals of angular momenta ℓ as well as parts of the polynomials $P_{n-1}(s,t,u)$, which can be absorbed in the subtraction polynomials P_ℓ^{n-1} of order $n-1$:

$$\mathcal{F}_\ell(x) = P_\ell^{n-1}(x) + \frac{x^n}{\pi}\int_{x_{\text{thr}}}^{\infty} \frac{\text{Im}\ f_\ell(x')}{x'^n(x-x_{\text{thr}})(x'-x-i\epsilon)}. \tag{1.90}$$

Furthermore, one straightforwardly observes that the fixed-variable dispersion relations can be retained from this representation by fixing the corresponding variable.

1.3.3 Omnès solution

A classical method to solve the unitarity relation in a dispersive framework refers to the Omnès problem [80]. Mathematically known as homogeneous Hilbert-type problem described in Ref. [81] its application to hadron physics and explicitly to form factors has been noted in Ref. [80, 96–99]. For an elastic two-particle scattering scenario it exhibits the feature that it provides an analytic solution of the unitarity relation Eq. (1.64). The vector form factor $\mathcal{F}_\pi^V(s)$, defined in Eq. (1.74), is an ideal showcase example due to the absence of left-hand cuts on the one hand, and a (phenomenologically) well justified elastic approximation up to energies $\sqrt{s} \approx 1$ GeV on the other hand. We demonstrate the solution of the Omnès problem in an elementary matter assuming these two prerequisites, i.e. for a form factor $\mathcal{F}_\ell^I(s)$ that obeys the elastic partial-wave unitarity relation Eq. (1.75). The concrete determination of the pion vector form factor is sketched in Section 2.4.1. A generalized treatment that takes into account inelastic channels or crossed-channel effects complicates the problem and is discussed in some aspects afterwards.

The unitarity condition Eq. (1.75) is solely driven by the elastic scattering phase shift $\delta_\ell^{I,\mathrm{el}}$ (coinciding with the phase $\delta_\ell^I(s)$ of the form factor regarding Watson's final-state theorem). Hence, all the physics that enters the Omnès problem is incorporated in that phase that will determine the dispersion integral in the representation of the Omnès function. The Omnès function is introduced via the ansatz

$$\mathcal{F}_\ell^I(s) = P_\ell^I(s)\Omega_\ell^I(s), \tag{1.91}$$

where $P_\ell^I(s)$ is an arbitrary polynomial and $\Omega_\ell^I(s)$, constrained by

$$\Omega_\ell^I(0) = 1 \text{ and } \Omega_\ell^I(s) \neq 0 \;\forall\; s, \tag{1.92}$$

solves the dispersion integral

$$\mathcal{F}_\ell^I(s) = \frac{1}{\pi}\int_{s_\mathrm{thr}}^\infty \frac{\mathrm{Im}\;\mathcal{F}_\ell^I(s')}{s'-s-i\epsilon}\,\mathrm{d}s', \tag{1.93}$$

with $\mathrm{Im}\;\mathcal{F}_\ell^I(s)$ given by the unitarity relation Eq. (1.75). It is appropriate to consider the logarithm of the Omnès function $\ln\,\Omega_\ell^I(s)$, for which the discontinuity takes a simple form,

$$\mathrm{disc}\left(\ln\Omega_\ell^I(s)\right) = \ln\,\left(\Omega_\ell^I(s+i\epsilon)\right) - \left(\Omega_\ell^I(s-i\epsilon)\right) = 2i\delta_\ell^I(s), \tag{1.94}$$

with $\Omega_\ell^I(s\pm i\epsilon) = |\Omega_\ell^I(s)|\exp(\pm i\delta_\ell^I)$. This yields the dispersive representation

$$\begin{aligned}
\ln\Omega_\ell^I(s) &= P_{n-1}(s) + \frac{(s-s_0)^n}{2\pi i}\int_{s_\mathrm{thr}}^\infty \frac{\mathrm{disc}\left(\ln\Omega_\ell^I(s')\right)}{(s'-s_0)^n(s'-s-i\epsilon)}\,\mathrm{d}s' \\
\Rightarrow\quad \Omega_\ell^I(s) &= \exp\left(P_{n-1}(s) + \frac{(s-s_0)^n}{\pi}\int_{s_\mathrm{thr}}^\infty \frac{\delta_\ell^I(s')}{(s'-s_0)^n(s'-s-i\epsilon)}\,\mathrm{d}s'\right) \\
\Rightarrow\quad \Omega_\ell^I(s) &= \exp\left(\frac{s}{\pi}\int_{s_\mathrm{thr}}^\infty \frac{\delta(s')}{s'(s'-s-i\epsilon)}\,\mathrm{d}s'\right),
\end{aligned} \tag{1.95}$$

where in the last step one subtraction enforces the demanded normalization, as well as ensures a converging dispersion integral (assuming that the phase is bounded).

We need to pay special attention to the high-energy region: demanding the asymptotic behavior of the form factor and correspondingly of the Omnès function to be at least $\propto 1/s$ (as known from perturbative QCD [100]) yields a constraint for the asymptotic value of the input phase. In the typical scope of application for the Omnès formalism like processes that involve pions or kaons, the scattering phase shifts are known very precisely at low energies, e.g. from Roy and Roy–Steiner analyses [33–39], but not for large s, where we can however employ the relation between the phase and the fall-off of the Omnès function,

$$\delta_\ell^I(s) \overset{s\to\infty}{\longrightarrow} n\pi \quad \Longleftrightarrow \quad \Omega_\ell^I(s) \overset{s\to\infty}{\longrightarrow} s^{-n},\, n \geq 1. \tag{1.96}$$

Above a certain cutoff energy we therefore guide the phases smoothly to a multiple of π to ensure the required high-energy behavior.

Beyond the elastic case the coupling between various channels that we will discuss in the next section affects the above relation: the asymptotic behavior of the Omnès solution depends on the *sum* of eigen phase shifts $\sum \delta_\ell^I(s)$ [101],

$$\sum \delta_\ell^I(s) \overset{s\to\infty}{\longrightarrow} m\pi \quad \Omega_\ell^I(s) \overset{s\to\infty}{\longrightarrow} \frac{1}{s}\,. \tag{1.97}$$

We briefly want to discuss how scattering and decay processes, which exhibit left-hand cut structures, can be treated in the Omnès representation framework. In the previous section we have constructed dispersion relations for these processes employing the so-called reconstruction theorem. However, it has been shown that simple dispersion relations for the single-variable amplitudes are not necessarily unique [102]. This drawback can be cured by extending the above Omnès solution to the Khuri–Treiman framework [103]. The starting point is once again the unitarity relation and the decomposition of the amplitude in question into single-variable amplitudes Eq. (1.89). For simplicity we resort to the case of elastic scattering of a specific isospin, such that the unitarity relation is given by Eq. (1.64). Projecting the unitarity relation on the corresponding angular moments provides unitarity relations for the single-variable amplitudes analogously to Eq. (1.75),

$$\mathrm{disc}\mathcal{F}_\ell(s) = 2i\left(\mathcal{F}_\ell(s) + \hat{\mathcal{F}}_\ell(s)\right) e^{-i\delta_\ell^{\mathrm{el}}(s)} \sin\,\delta_\ell^{\mathrm{el}}(s)\,\Theta(s - s_{\mathrm{thr}}), \tag{1.98}$$

where $\hat{\mathcal{F}}_\ell(s)$ denotes the projection of the full amplitude on the ℓth angular moment neglecting the corresponding single-variable amplitude $\mathcal{F}_\ell(s)$,

$$\hat{\mathcal{F}}_\ell(s) = \frac{2\ell+1}{2}\int_{-1}^{1} \mathrm{d}\cos\theta_s\, \mathcal{F}\left(s, t(s,\cos\theta_s), u(s,\cos\theta_s)\right) P_\ell(\cos\theta_s) - \mathcal{F}_\ell(s). \tag{1.99}$$

Thus the crossed channels and therefore the left-hand cuts contribute through the function $\hat{\mathcal{F}}_\ell$ to the single-variable amplitude of angular moment ℓ, $\mathcal{F}_\ell$. In the case of decays it gives rise to crossed-channel rescattering contributions and three-particle rescattering. The unitarity relation (1.98) is an inhomogeneous Hilbert problem, which reduces to the homogeneous Hilbert problem Eq. (1.75) in the special case of $\hat{\mathcal{F}} = 0$. The latter problem is solved by the Omnès solution. It is therefore natural to solve the unitarity relation for the single-variable amplitudes by the following product ansatz,

$$\mathcal{F}_\ell(s) = \Omega_\ell(s)\phi(s), \tag{1.100}$$

where $\Omega_\ell(s)$ is the Omnès solution and $\phi(s)$ is to be determined. The product ansatz results in the following dispersion relation, which is known as Khuri–Treiman dispersion relation,

$$\mathcal{F}_\ell(s) = \Omega_\ell(s)\left\{P_{n-1}(s) + \frac{s^n}{\pi}\int_{s_{\mathrm{thr}}}^{\infty} \mathrm{d}x \frac{\sin\,\delta_\ell^{\mathrm{el}}(x)\hat{\mathcal{F}}_\ell(x)}{|\Omega_\ell(x)|x^n(s-x)}\right\}, \tag{1.101}$$

where P_{n-1} again denotes the subtraction polynomial of order $n-1$.

1.3.4 Coupled-channel Omnès formalism

A strong coupling between various hadronic systems necessitates a combined treatment of these channels in the determination of quantities like e.g. form factors. Such a dependency of two systems occurs for instance in the scalar isoscalar sector between the S-wave pions and kaons, and in the scalar isovector channel between the S-wave $\pi^0\eta$ and the two-kaon systems. Consequently the derivation of these scalar form factors requires a coupled-channel approach, and it is thus mandatory to generalize the single-channel Omnès problem presented in the previous section to the two-channel Muskhelishvili–Omnès problem. We demonstrate this on the example of the pion and kaon scalar form factors. These form factors are defined by the matrix elements

$$\left\langle 0 \left| (\bar{q}q)_{I=0} \right| M_1^+ M_2^- \right\rangle = \mathcal{B}_0^q \Gamma_{M_1 M_2}^{q,I=0}(s), \tag{1.102}$$

with the isoscalar scalar currents $(\bar{q}q)_{I=0} = (\bar{u}u + \bar{d}d)/2$ for the light non-strange quarks ($q = n$), or $(\bar{q}q)_{I=0} = \bar{s}s$ for the strange quarks ($q = s$). Furthermore,

$$\mathcal{B}_0^n = \frac{M_\pi^2}{m_u + m_d}, \quad \mathcal{B}_0^s = \frac{2M_K^2 - M_\pi^2}{2m_s}. \tag{1.103}$$

More details concerning these definitions can be found in Section 2.4.2. Parts of this section are taken from Ref. [104], where further details are provided.

The two-channel unitarity relation reads

$$\operatorname{disc} \mathbf{\Gamma}(s) = 2iT_0^{0*}(s)\Sigma(s)\mathbf{\Gamma}(s), \tag{1.104}$$

where the components of the two-dimensional vector $\mathbf{\Gamma}(s)$ are the pion and kaon scalar isoscalar form factors, and $T_0^0(s)$ and $\Sigma(s)$ are two-dimensional matrices,

$$T_0^0(s) = \begin{pmatrix} \dfrac{\eta_0^0(s)e^{2i\delta_0^0(s)} - 1}{2i\sigma_\pi(s)} & |g_0^0(s)|e^{i\psi_0^0(s)} \\ |g_0^0(s)|e^{i\psi_0^0(s)} & \dfrac{\eta_0^0(s)e^{2i(\psi_0^0(s) - \delta_0^0(s))} - 1}{2i\sigma_K(s)} \end{pmatrix}, \tag{1.105}$$

and $\Sigma(s) = \operatorname{diag}\left(\sigma_\pi(s)\Theta(s - 4M_\pi^2), \sigma_K(s)\Theta(s - 4M_K^2)\right)$, with $\sigma_i(s) = \left(1 - 4M_i^2/s\right)^{1/2}$ and $\Theta(.)$ denoting the Heaviside function. *Three* functions serve as input for the T-matrix, the $\pi\pi$ S-wave isoscalar phase shift $\delta_0^0(s)$ and the $\pi\pi \to K\bar{K}$ S-wave amplitude $g_0^0(s) = |g_0^0(s)|\exp(i\psi_0^0(s))$ with modulus and phase. The modulus $|g_0^0(s)|$ is related to the inelasticity parameter $\eta_0^0(s)$ by

$$\eta_0^0(s) = \sqrt{1 - 4\sigma_\pi(s)\sigma_K(s)|g_0^0(s)|^2\Theta(s - 4M_K^2)}. \tag{1.106}$$

In the limit of a single channel $\eta_0^0 \to 1$ the $\left(T_0^0\right)_{11}$ matrix element reduces to the elastic scattering case Eq. (1.73). Writing down the two-dimensional dispersion integral over the discontinuity (1.104) leads to a system of coupled Muskhelishvili–Omnès equations,

$$\mathbf{\Gamma}(s) = \frac{1}{\pi}\int_{4M_\pi^2}^{\infty} \frac{T_0^{0*}(s')\Sigma(s')\mathbf{\Gamma}(s')}{s' - s - i\epsilon}\mathrm{d}s'. \tag{1.107}$$

A solution can be constructed introducing a two-dimensional Omnès matrix, which is connected to the form factors by means of a multiplication with a vector containing the normalizations $\Gamma_{\pi\pi}^{q,I=0}(0)$ and $\Gamma_{KK}^{q,I=0}(0)$ [105],

$$\begin{pmatrix} \Gamma_{\pi\pi}^{q,I=0}(s) \\ \frac{2}{\sqrt{3}}\Gamma_{KK}^{q,I=0}(s) \end{pmatrix} = \begin{pmatrix} \Omega_{11}(s) & \Omega_{12}(s) \\ \Omega_{21}(s) & \Omega_{22}(s) \end{pmatrix} \begin{pmatrix} \Gamma_{\pi\pi}^{q,I=0}(0) \\ \frac{2}{\sqrt{3}}\Gamma_{KK}^{q,I=0}(0) \end{pmatrix}, \tag{1.108}$$

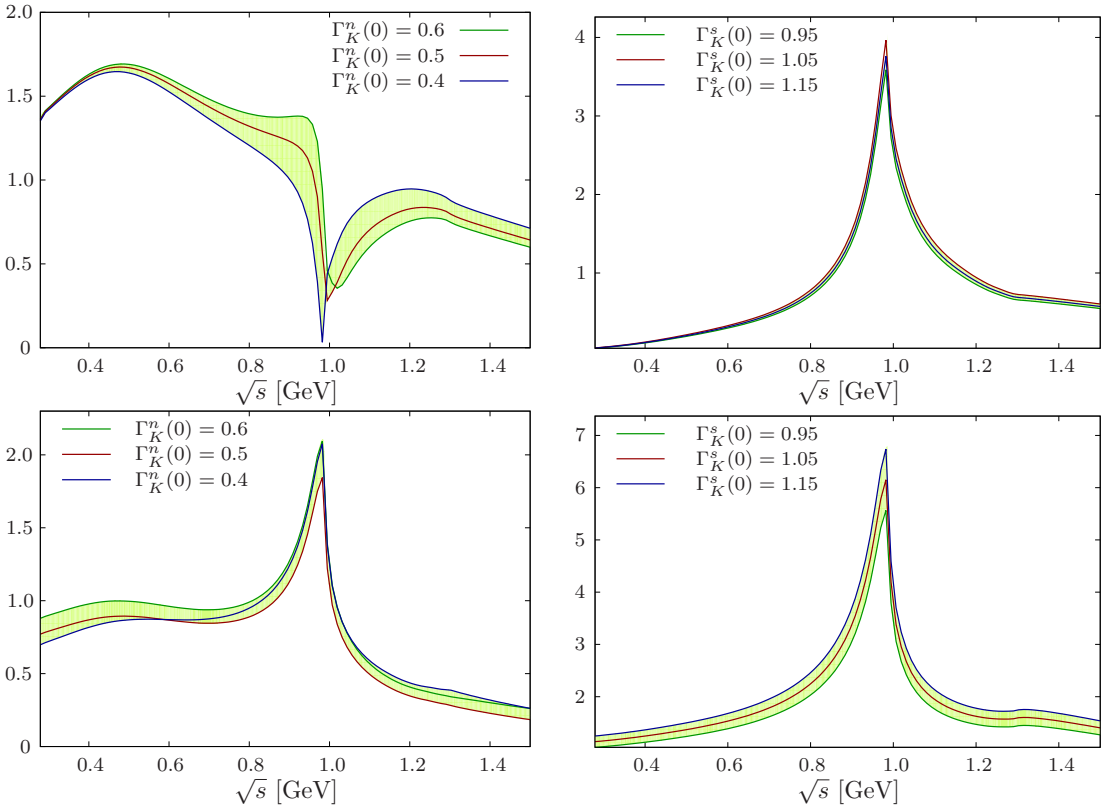

Figure 1.8: Modulus of the scalar pion (top) and kaon (bottom) non-strange (left panels) and strange (right panels) form factors $\Gamma^{q,I=0}_{\pi\pi,KK}(s)$, $q = n, s$, depicted for three different normalizations inside the allowed range, illustrated by the uncertainty band.

where $\Gamma^{q,I=0}_{\pi\pi,KK}(s)$ represents both strange ($q = s$) and non-strange ($q = n$) form factors, which differ merely in their respective normalizations. Thus the problem reduces to finding a matrix $\Omega(s)$ that fulfills

$$\text{Im}\ \Omega(s) = T_0^{0*}(s)\Sigma(s)\Omega(s), \quad \Omega(s) = \frac{1}{\pi}\int_{4M_\pi^2}^{\infty} \frac{T_0^{0*}(s')\Sigma(s')\Omega(s')}{s' - s - i\epsilon}\mathrm{d}s', \quad \Omega(0) = \mathbb{1}. \tag{1.109}$$

While the single-channel Omnès problem can be solved analytically this is not the case in the coupled-channel approach, where one has to resort to numerical methods [101, 104–107]. An adequate asymptotic behavior of the two-channel Omnès solution is ensured by guiding the sum of the eigen phase shifts to 2π, cf. Eq. (1.97). Figure 1.8 shows the results obtained for the moduli of the pion and kaon form factors (see also Ref. [112]). The sensitivity due to the uncertainty in the kaon form factor normalization is illustrated by the uncertainty bands. The strange form factor exhibits a peak around 1 GeV, which is produced by the $f_0(980)$ resonance. On the contrary in the pion non-strange form factor the σ meson appears as a broad bump (notice the non-Breit–Wigner shape) around 500 MeV.

According to the Feynman–Hellmann theorem [108, 109], the form factors for zero momentum are related to the corresponding Goldstone boson masses, which at next-to-leading order in the chiral expansion in terms of quark masses depend on certain low-energy constants. These are determined in lattice simulations with $N_f = 2 + 1$ dynamical flavors at a running scale

$\mu = 770$ MeV [110], limiting the form factor normalizations to the ranges[10]

$$\begin{aligned} &\Gamma_{\pi\pi}^{n,I=0}(0) = 0.984 \pm 0.006, && \Gamma_{\pi\pi}^{s,I=0}(0) = (-0.001 \ldots 0.006) \approx 0, \\ &\Gamma_{KK}^{n,I=0}(0) = (0.4 \ldots 0.6), && \Gamma_{KK}^{s,I=0}(0) = (0.95 \ldots 1.15). \end{aligned} \tag{1.110}$$

[10] Similar ranges, with slightly increased values in the case of the kaon form factor normalizations, are found in simulations with $N_f = 2 + 1 + 1$ dynamical flavors [111], cf. Eq. (2.50).

Chapter 2

Final-state interactions in $\bar{B}^0_{d/s} \to J/\psi\{\pi\pi, \pi\eta, \bar{K}K\}$[1]

2.1 Introduction

B-meson decays can be exploited for Standard Model tests and beyond, in particular to determine the Cabibbo–Kobayashi–Maskawa (CKM) couplings and to study CP violation. For a theoretical description of many of these decays, it is mandatory to understand the strong final-state interactions in terms of amplitude analysis techniques [115], with tight control over the magnitudes and phase motions of the various partial waves involved. For example, the decays $B \to f_0(980)K_S$ and $B \to \phi(1020)K_S$ are explored for an experimental determination of the CP asymmetry $\sin 2\beta$ [116–119], β being one of the angles of the unitarity triangle. An analysis of decays into scalar final states such that the former of those decay channels requires precise knowledge of the strange and non-strange scalar form factors that we discuss in this chapter.

We focus on the decays $\bar{B}^0_{d,s} \to J/\psi M_1 M_2$, with $M_1 M_2$ being a pair of light pseudoscalar hadrons, $\pi^+\pi^-$, $\pi^0\eta$, K^+K^- or $\bar{K}^0K^0$. The tree-level process of the weak decay into J/ψ and a $q\bar{q}$ pair is depicted in Figure 2.1 (exemplarily for the $\bar{B}^0_s$ decay). The interactions of the lightest hadrons, the pions, with themselves as well as with kaons, the next-lightest strongly-interacting particles within the pseudoscalar ground-state octet, are known to excellent precision. The combination of dispersion relations in the form of Roy or Roy–Steiner equations, constrained by chiral perturbation theory at lowest energies and using experimental data as input, has increased our knowledge of the leading partial waves of pion–pion [33–36] and pion–kaon [37–39] scattering enormously. This has a large impact on a wide range of scattering or decay processes in which pions and kaons are produced: dispersion relations allow to relate the final-state interactions to the scattering phase shifts in a model-independent way [113, 120–131]. The hadronizations into pions and kaons and the rescattering in the $\pi\pi$ and $K\bar{K}$ systems for S- and P-waves can be described by the pion and kaon scalar and vector form factors, a consequence of the universality of the final-state interactions.

Contrary to the vector form factor, where a single-channel (elastic) treatment as it is explained in Section 1.3.3 works well below 1 GeV, the elastic approximation breaks down in the scalar sector: both reactions—$\pi\pi$ and πK scattering—are closely intertwined in the isospin-0

[1] published in Refs. [113, 114]

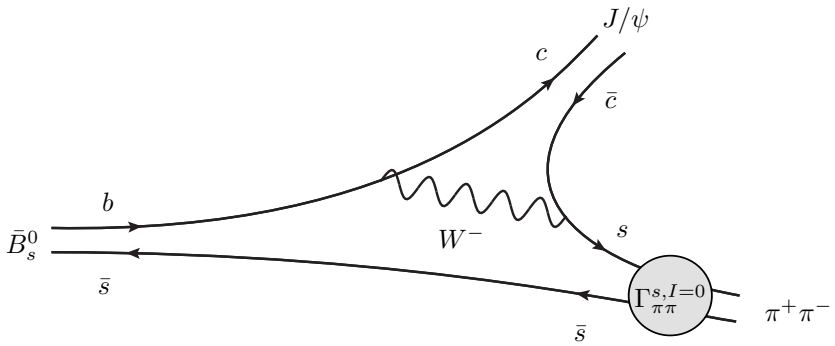

Figure 2.1: The $\bar{B}^0_s \to J/\psi\pi^+\pi^-$ diagram to leading order via W^- exchange. The hadronization into pions (S-wave dominated) proceeds through the pion strange scalar form factor $\Gamma^{s,I=0}_{\pi}(s)$. In the case of the $\bar{B}^0_d \to J/\psi\pi^+\pi^-$ decay, with $s \leftrightarrow d$, the pions are generated out of a non-strange scalar source, i.e. $\Gamma^{s,I=0}_{\pi}(s)$ is replaced by the pion non-strange scalar form factor $\Gamma^{n,I=0}_{\pi}(s)$ for S-wave and by the vector form factor for P-wave pions. For the (S-wave dominated) $\bar{B}^0_d \to J/\psi\pi^0\eta$ final state the isoscalar scalar form factor is replaced by the isovector scalar form factor $\Gamma^{n,I=1}_{\pi\eta}$. Considering $K\bar{K}$ final states, the kaons emerge from both isoscalar and isovector form factors, $\Gamma^{n,I=0}_{K\bar{K}}$ and $\Gamma^{n,I=1}_{K\bar{K}}$, in the $\bar{B}^0_d$ decay, while it is purely isoscalar, $\Gamma^{s,I=0}_{K\bar{K}}$, in the $\bar{B}^0_s$ decay.

S-wave system. There the reaction $\pi\pi \to \bar{K}K$, the crossed process of πK scattering, dominates the inelasticity in pion–pion scattering near the $\bar{K}K$ threshold, the region of the $f_0(980)$ resonance; for these (scalar) quantum numbers, therefore a coupled-channel treatment is mandatory [101, 105]. A two-channel approach breaks down at energies where inelasticities caused by 4π states become important, we are thus not able to cover the complete phase space, but restrict ourselves to the low-energy range $\sqrt{s} \leq 1.05\,\text{GeV}$. Information on the scattering of pions off the η, which would complete our understanding of pion reactions off the pseudoscalar ground-state octet, is much scarcer. Two important resonances are known in the $I(J^P) = 1(0^+)$ sector, namely the $a_0(980)$ and $a_0(1450)$ [44]. Several models for the $\pi\eta$ S-wave scattering amplitude have been proposed in the literature [132–136], some of them constrained by the results from chiral perturbation theory at threshold [137]. Very recently, first information about this amplitude has also come from lattice QCD simulations [138, 139]. There is one remarkable similarity of $\pi\eta$ S-wave scattering to the $\pi\pi$ $I = 0$ S-wave: for $\pi\eta$, the first important inelastic channel is given by $\bar{K}K$, whose threshold also there coincides with the presence of a scalar resonance, the isospin-1 $a_0(980)$ resonance. Therefore in this case, a coupled-channel treatment of $\pi\eta$ and $\bar{K}K$ (in $I = 1$) is required as well in order to describe the energy region around 1 GeV. A corresponding unitary T-matrix has recently been constructed in Ref. [140], to which chiral constraints [60] have been imposed as well as experimental information available on the $a_0(980)$ and $a_0(1450)$ resonances. However, the result still has considerable uncertainties due to the limited accuracy of the experimental input.

To demonstrate that the description in terms of form factors, constructed in Muskhelishvili–Omnès representations, works very well, we consider the decays $\bar{B}^0_d \to J/\psi\pi^+\pi^-$ and $\bar{B}^0_s \to J/\psi\pi^+\pi^-$, measured by the LHCb collaboration [141, 142]. These analyses complement former related studies of $\bar{B}^0_d$ and $\bar{B}^0_s$ decays by the BaBar [143], Belle [144], CDF [145], and D0 [146] Collaborations as well as older LHCb results [147, 148]. In the LHCb analyses no obvious structures in the $J/\psi\pi^+$ invariant mass distribution are found, suggesting that left-hand-cut contributions in the $\pi^+\pi^-$ system due to the crossed-channel $J/\psi\pi^+$ interaction are small and

can be neglected.

In Ref. [141] the $\bar{B}_d^0$ decay is described by six resonances in the $\pi^+\pi^-$ channel, $f_0(500)$, $\rho(770)$, $\omega(782)$, $\rho(1450)$, $\rho(1700)$, and $f_2(1270)$, which are modeled by Breit–Wigner functions. This parametrization of especially the $f_0(500)$ meson is somewhat precarious, as the broad bump structure of this scalar resonance is not well described by a Breit–Wigner shape. As demonstrated for the first time in the context of B decays in Ref. [149], it should be replaced by the corresponding scalar form factor. In the present work this idea is extended and rigorously applied using form factors derived from dispersion theory. The advantage of the dispersive framework is that all constraints imposed by analyticity (i.e., causality) and unitarity (probability conservation) are fulfilled by construction. Further, it is a model-independent approach, so we do not have to specify any contributing resonances or conceivable non-resonant backgrounds. In particular, there is no need to parametrize any resonance, since the input required to describe the final-state interactions is taken from known phase shifts, and therefore the $f_0(500)$ appears naturally in the non-strange scalar form factor. The $\bar{B}_s^0$ decay, described in the experimental analysis by five resonances, $f_0(980)$, $f_0(1500)$, $f_0(1790)$, $f_2(1270)$, and $f_2'(1525)$ (Solution I) or with an additional non-resonant contribution (Solution II), dominantly occurs in an S-wave state [142], while the P-wave is shown to be negligible. Given the almost pure $\bar{s}s$ source the pions are generated from, this decay shows great promise to provide insight into the strange scalar form factor.

The idea of such a "scalar-source model", where an S-wave pion pair is generated out of a quark–antiquark pair and the final-state interactions are described by the scalar form factor, is also used in Ref. [150] for the description of the $\bar{B}_s^0$ and $\bar{B}_d^0$ decays into the scalar resonances $f_0(980)$ and $f_0(500)$, respectively. It was employed earlier e.g. in analyses of the decay of the J/ψ into a vector meson (ω or ϕ) and a pair of pseudoscalars ($\pi\pi$ or $K\bar{K}$) [151, 152]. In these references the strong-interaction part is described by a chiral unitary theory including coupled channels, which yields a dynamical generation of the scalar mesons. In contrast to the present study, the very precise information available on pion–pion [35, 36, 153, 154] and pion–kaon [37–39] phase shifts is not strictly implemented there. Related studies using the chiral unitary approach are performed in Ref. [155], where the J/ψ–vector-meson final state is analyzed, and in Ref. [156], which includes resonances beyond 1 GeV. In contrast to models of dynamical resonance generation, the scalar resonances are considered as $q\bar{q}$ or tetraquark states in Ref. [157]. Other theoretical approaches employ light-cone QCD sum rules to describe the form factors [158]. Progress on the short-distance level is made in Ref. [159], where factorization formulae are improved in a perturbative QCD framework.

While our main interest in studying the $\bar{B}_{d,s}^0 \to J/\psi\pi^+\pi^-$ is to show whether the dispersive formalism works and to adjust the amplitude normalizations using available data, we can give predictions also for the other final state, namely for the $\bar{B}_s^0 \to J/\psi K^+K^-$ S-wave as well as the S-wave dominated decays $\bar{B}_d^0 \to J/\psi\{K^+K^-, \bar{K}^0K^0\}$ and $\bar{B}_d^0 \to J/\psi\pi^0\eta$. Because the strange source $\bar{s}s$ has an isoscalar component only, the $\bar{B}_s^0 \to J/\psi K^+K^-$ S-wave, where the kaon pair emerges from a strange source $\bar{s}s$, can be predicted straightforwardly based on the $\pi\pi$–$\bar{K}K$ coupled-channel relations solely. Considering the non-strange mode $\bar{B}_d^0 \to J/\psi\bar{K}K$ the source term is given dominantly in terms of $\bar{d}d$ quark bilinears; it produces isoscalar and isovector meson pairs with known relative sign and strengths. With the strength of the dimeson source fixed from experimental data on $\bar{B}_d^0 \to J/\psi\pi^+\pi^-$, and given the analogous isovector scalar form factors for $\pi\eta$ and $\bar{K}K$ [140], we can thus give an absolute prediction for the $\bar{B}_d^0 \to J/\psi\pi^0\eta$ channel. The combination of isoscalar and isovector scalar form factors for the kaons then allows one to fully analyse the physical K^+K^- and $K^0\bar{K}^0$ final states.

The outline of this chapter is as follows. In Section 2.2, we review the construction of the transversity amplitudes and partial waves, after sketching elementary kinematics, exemplified on the $\bar{B}_d^0 \to J/\psi\pi^0\eta$ channel. We provide explicit expressions that relate the theoretical quantities

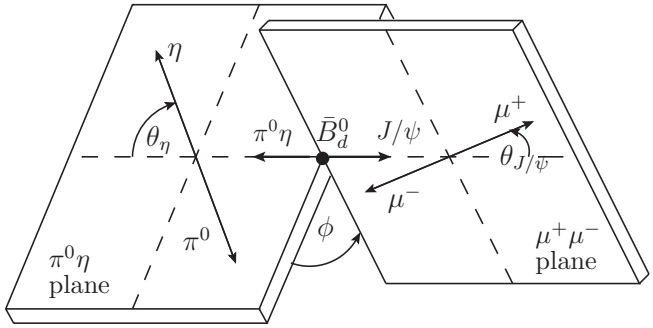

Figure 2.2: Definition of the kinematical variables for $\bar{B}^0_d \to J/\psi\pi^0\eta$.

to the angular moments determined in experiment. We introduce the required dimeson scalar and vector form factors in Section 2.4, and construct the amplitudes for the respective decay modes in terms of these form factors. The fits to the LHCb data, using the $\bar{B}^0_{d,s} \to J/\psi\pi^+\pi^-$ angular moment distributions, are discussed in Section 2.5, where we use several configurations with and without D-wave corrections to study the impact of certain corrections to our fits. Results for $\bar{B}^0_d \to J/\psi\pi^0\eta$ predictions are presented in Section 2.6. Section 2.7 provides further arguments for our treatment of the S-wave in terms of scalar form factors and the suppression of higher partial waves in the $\bar{B}^0_d \to J/\psi\pi^0\eta$ decay. Potential contributions due to t- and u-channel exchange of the $\psi(2S)$ and B^* mesons are studied, the latter also for the $\bar{B}^0_{d,s} \to J/\psi\pi^+\pi^-$ decay. The predictions for the $\bar{K}K$ final states are treated in Section 2.8. We conclude in Section 2.9.

2.2 Kinematics, decay rate, and angular moments

In this section we introduce the elementary decay kinematics and derive the decay rates in terms of partial-wave amplitudes up to D-waves, employing the transversity formalism of Ref. [160]. This is exemplified on the $\bar{B}^0_d \to J/\psi\pi^0\eta$ decay mode, where final-state hadrons of unequal masses are involved, exhibiting the most general structure of the decays under investigation. We therefore do not spell out the formulae for the $\pi\pi$ and $\bar{K}K$ final states explicitly—they can be obtained from the following in a straightforward manner.

The kinematics of the decay $\bar{B}^0_d(p_B) \to J/\psi(p_\psi)\pi^0(p_1)\eta(p_2)$ ($J/\psi \to \mu^+\mu^-$) can be described by four variables: the invariant dimeson mass squared, $s = (p_1 + p_2)^2$, and three helicity angles, see Figure 2.2, namely

- the angle $\theta_{J/\psi}$ between the μ^+ in the J/ψ rest frame ($\Sigma_{J/\psi}$) and the J/ψ in the $\bar{B}^0_d$ rest frame (Σ_B);
- the angle θ_η between the η in the $\pi^0\eta$ center-of-mass frame $\Sigma_{\pi\eta}$ and the $\pi^0\eta$ line-of-flight in Σ_B;
- the angle ϕ between the $\pi^0\eta$ and the dimuon planes, where the latter originate from the decay of the J/ψ.

The three-momenta of the pion or the η in the $\pi^0\eta$ center-of-mass system ($\mathbf{p}_{\pi\eta}$) and that of the J/ψ in the $\bar{B}^0_d$ rest frame ($\mathbf{p}_\psi$) are given by

$$|\mathbf{p}_{\pi\eta}| = \frac{\lambda^{1/2}(s, M_\pi^2, M_\eta^2)}{2\sqrt{s}} \equiv \frac{Y\sqrt{s}}{2}, \quad |\mathbf{p}_\psi| = \frac{\lambda^{1/2}(s, m_\psi^2, m_B^2)}{2m_B} \equiv \frac{X}{m_B}, \tag{2.1}$$

with the Källén function $\lambda(a,b,c) = a^2 + b^2 + c^2 - 2(ab + ac + bc)$. The function Y reduces to $\sigma_P = (1 - 4M_P^2/s)^{1/2}$ in the case of equal-mass final-states. We define two further Mandelstam variables as

$$t = (p_B - p_1)^2 \quad \text{and} \quad u = (p_B - p_2)^2, \tag{2.2}$$

where the difference of these two determines the scattering angle θ_η,

$$t - u = -2YX\cos\theta_\eta + \frac{\Delta_m}{s}, \quad \Delta_m = (m_B^2 - m_\psi^2)(M_\eta^2 - M_\pi^2). \tag{2.3}$$

We decompose the matrix element for the decay in the following way:

$$\begin{aligned}
\mathcal{M}_{fi} &= \frac{G_F}{\sqrt{2}} V_{cb} V_{cd}^* \mathcal{M}^{\text{eff}}, \\
\mathcal{M}^{\text{eff}} &= f_\psi m_\psi \epsilon^{*\mu} \big(P_\mu \mathcal{A}_1 + Q_\mu \mathcal{A}_2 + (p_\psi)_\mu \mathcal{A}_3 + i\epsilon_{\mu\nu\rho\sigma} p_\psi^\nu P^\rho Q^\sigma \mathcal{V} \big) \\
&= f_\psi m_\psi \epsilon_\mu^*(p_\psi,\lambda) \left(\frac{p_\psi^\mu}{m_\psi} \mathcal{F}_t + \frac{m_\psi P_{(0)}^\mu}{X} \mathcal{F}_0 + \frac{Q_{(\parallel)}^\mu}{\sqrt{s}} \mathcal{F}_\parallel - \frac{i\bar{p}_{(\perp)}^\mu}{\sqrt{s}} \mathcal{F}_\perp \right) =: f_\psi m_\psi \epsilon^{*\mu} \mathcal{M}_\mu^{\pi\eta},
\end{aligned} \tag{2.4}$$

where $f_\psi \approx 405\,\text{MeV}$ is the J/ψ decay constant, $G_F = 1.166365 \times 10^{-5}\,\text{GeV}^{-2}$ is the Fermi constant, V_{cb} and V_{cd} are the CKM matrix elements for $c \to b$ and $c \to d$, and $\epsilon_\mu^*(p_\psi,\lambda)$ is the corresponding polarization vector of helicity λ. The matrix element containing the $\pi\eta$ system is given on the one hand in the standard basis of momentum vectors (p_ψ^μ, $P^\mu = p_1^\mu + p_2^\mu$, $Q^\mu = p_1^\mu - p_2^\mu$) associated with three axial form factors $\mathcal{A}_i$ and one vector form factor $\mathcal{V}$; on the other hand it is represented by the transversity form factors $\mathcal{F}_t$, $\mathcal{F}_0$, $\mathcal{F}_\parallel$, and $\mathcal{F}_\perp$, reflecting the polarization states of the J/ψ. The *unphysical* time component $\mathcal{F}_t$ does actually not contribute. In the ongoing study we will use the set of transversity form factors $\mathcal{F}_\tau$. They correspond to the orthogonal basis of momentum vectors [160]

$$\begin{aligned}
P_{(0)}^\mu &= P^\mu - \frac{P\cdot p_\psi}{p_\psi^2} p_\psi^\mu, \qquad \bar{p}_{(\perp)}^\mu = \frac{\epsilon^{\mu\alpha\beta\gamma}}{X} (p_\psi)_\alpha P_\beta Q_\gamma, \\
Q_{(\parallel)}^\mu &= Q^\mu + \frac{p_\psi^2 (P\cdot Q) - (P\cdot p_\psi)(Q\cdot p_\psi)}{X^2} P^\mu + \frac{P^2 (Q\cdot p_\psi) - (P\cdot p_\psi)(P\cdot Q)}{X^2} p_\psi^\mu,
\end{aligned} \tag{2.5}$$

thus generalizing the formulae discussed previously [160] to unequal masses. Again, the relations for the $\pi\pi$ and $\bar{K}K$ final states simplify accordingly. We employ $\epsilon_{\mu\alpha\beta\gamma}$ with the convention $\epsilon_{0123} = -\epsilon^{0123} = +1$. The associated orthonormal basis of polarization vectors of the J/ψ meson reads [160]

$$\epsilon^\mu(t) = \frac{p_\psi^\mu}{M_\psi}, \quad \epsilon^\mu(0) = -\frac{M_\psi}{X} P_{(0)}^\mu, \quad \epsilon^\mu(\pm) = -\frac{1}{\sqrt{2s}\, Y \sin\theta_\eta} \left(Q_{(\parallel)}^\mu \mp i\bar{p}_{(\perp)}^\mu \right) e^{\mp i\phi}. \tag{2.6}$$

The transversity (or helicity) form factors are then defined via the contractions of the hadronic matrix element $\mathcal{M}_\mu^{\pi\eta}$ with the respective polarization vectors,

$$\mathcal{H}_\lambda = \mathcal{M}_\mu^{\pi\eta}\, \epsilon^{\mu\dagger}(\lambda). \tag{2.7}$$

Both transversity and helicity form factors are related via

$$\mathcal{H}_t = \mathcal{F}_t, \quad \mathcal{H}_0 = \mathcal{F}_0, \quad \mathcal{H}_\pm = (\mathcal{F}_\parallel \pm \mathcal{F}_\perp) \frac{Y}{\sqrt{2}} \sin\theta_\eta e^{\pm i\phi}. \tag{2.8}$$

Although dealing with three sets of form factors may cause confusion, it still helps to establish understanding of the remaining section. In particular the partial-wave expansions are well-known for helicity amplitudes,

$$\mathcal{H}_\lambda(s) = \sum_\ell \sqrt{2\ell+1}\mathcal{H}_\lambda^{(\ell)}(s) d^\ell_{\lambda 0}(\theta_\eta) e^{\lambda i\phi}, \tag{2.9}$$

where the $d^\ell_{\lambda\lambda'}$ are the small Wigner-d functions. Using

$$d^\ell_{00}(\theta_\eta) = P_\ell(\cos\theta_\eta), \quad d^\ell_{10}(\theta_\eta) = -d^\ell_{-10}(\theta_\eta) = -\frac{\sin\theta_\eta}{\sqrt{\ell(\ell+1)}} P'_\ell(\cos\theta_\eta), \tag{2.10}$$

we see that the zero-component $\mathcal{H}_0(s)$ is expanded in terms of Legendre polynomials $P_\ell(\cos\theta_\eta)$ and thus contains all S-, P-, and D-wave contributions, while the $\mathcal{H}_\pm(s)$ partial-wave expansions, proceeding in derivatives of the Legendre polynomials $P'_\ell(\cos\theta_\eta)$, start with the P-wave amplitudes, i.e.

$$\begin{aligned}
\mathcal{H}_0(s) &= \mathcal{H}_0^{(S)}(s) + \sqrt{3}\cos\theta_\eta \mathcal{H}_0^{(P)}(s) + \frac{\sqrt{5}}{2}\left(3\cos^2\theta_\eta - 1\right)\mathcal{H}_0^{(D)}(s) + \dots\,, \\
\mathcal{H}_\pm(s) &= \mp\sqrt{\frac{3}{2}}\sin\theta_\eta \left(\mathcal{H}_\pm^{(P)}(s) + \sqrt{5}\cos\theta_\eta \mathcal{H}_\pm^{(D)}(s)\right) e^{\pm i\phi} + \dots,
\end{aligned} \tag{2.11}$$

where the ellipses denote F-waves and larger.[2] Equivalently, due to Eq. (2.8) and using $\mathcal{H}_\pm^{(\ell)}(s) = \mp\frac{Y}{\sqrt{2}}\big(\mathcal{F}_\parallel^{(\ell)}(s) \pm \mathcal{F}_\perp^{(\ell)}(s)\big)$, we arrive at the partial-wave expansion of the transversity form factors,

$$\begin{aligned}
\mathcal{F}_0(s,\theta_\eta) &= \sum_\ell \sqrt{2\ell+1}\,\mathcal{F}_0^{(\ell)}(s) P_\ell(\cos\theta_\eta) \\
&= \mathcal{F}_0^{(S)}(s) + \sqrt{3}\cos\theta_\eta \mathcal{F}_0^{(P)}(s) + \frac{\sqrt{5}}{2}\left(3\cos^2\theta_\eta - 1\right)\mathcal{F}_0^{(D)}(s) + \dots\,, \\
\mathcal{F}_{\parallel,\perp}(s,\theta_\eta) &= \sum_\ell \frac{\sqrt{2\ell+1}}{\sqrt{\ell(\ell+1)}} \mathcal{F}_{\parallel,\perp}^{(\ell)}(s) P'_\ell(\cos\theta_\eta) = \sqrt{\frac{3}{2}}\left(\mathcal{F}_{\parallel,\perp}^{(P)}(s) + \sqrt{5}\cos\theta_\eta \mathcal{F}_{\parallel,\perp}^{(D)}(s)\right) + \dots.
\end{aligned} \tag{2.12}$$

The partial waves defined in this way still contain kinematical zeros that have to be removed for a dispersive treatment, such that the transversity partial waves are represented by functions whose only non-analytic behavior is related to unitarity. We relate the transversity amplitudes to the standard set $\{\mathcal{A}_i, \mathcal{V}\}$,

$$\begin{aligned}
\mathcal{F}_\perp &= -\sqrt{s}X\mathcal{V}, \quad \mathcal{F}_\parallel = \sqrt{s}\mathcal{A}_2, \quad \mathcal{F}_0 = \frac{X}{M_\psi}\mathcal{A}_1 + \left(\frac{Y\cos\theta_\eta (P\cdot p_\psi)}{M_\psi} + \frac{X}{M_\psi}\frac{M_\pi^2 - M_\eta^2}{s}\right)\mathcal{A}_2, \\
\mathcal{F}_t &= \frac{P\cdot p_\psi}{M_\psi}\mathcal{A}_1 + \frac{1}{M_\psi}\left(XY\cos\theta_\eta + \frac{(P\cdot p_\psi)(M_\pi^2 - M_\eta^2)}{s}\right)\mathcal{A}_2 + M_\psi \mathcal{A}_3,
\end{aligned} \tag{2.13}$$

in order to make the reader aware of the kinematical factors $\sqrt{s}$, X and Y introduced into the transversity form factors. These factors give rise to artificial branch cuts in the unphysical

[2] Though we expect the D- and higher waves to be small and therefore describe only S- and P-waves in the Omnès formalism, we present the formulae including the D-wave contribution, as we will study their impact at a later stage.

region. Given that the form factors $\mathcal{A}_i$ and $\mathcal{V}$ are regular, we can read off from Eq. (2.13) how to construct partial waves $f_\tau^{(\ell)}$ that are free of such kinematical singularities,

$$\begin{aligned} \mathcal{CF}_0^{(S)}(s) &= X f_0^{(S)}(s), & \mathcal{CF}_0^{(P)}(s) &= Y f_0^{(P)}(s), \\ \mathcal{CF}_\parallel^{(P)}(s) &= \sqrt{s} f_\parallel^{(P)}(s), & \mathcal{CF}_\perp^{(P)}(s) &= \sqrt{s} X f_\perp^{(P)}(s), \end{aligned} \tag{2.14}$$

where $\mathcal{C}$ is defined in Eq. (2.21). The partial waves $f_\tau^{(\ell)}$ are treated in the Omnès formalism as presented in Sections 1.3.3 and 2.4.

The structure of the matrix element in Eq. (2.4), its decomposition in terms of transversity form factors, as well as the partial-wave expansion of the latter is independent of any factorization assumption, and entirely general. Factorization of the form

$$\begin{aligned} \mathcal{M}^{\text{eff}} = a^{\text{eff}}(\mu)\mathcal{M}_\mu^{\pi\eta}\mathcal{M}^{c\bar{c}\,\mu} + \ldots, \qquad & \mathcal{M}_\mu^{\pi\eta} = \langle \pi^0(p_1)\eta(p_2)|\bar{d}\gamma_\mu(1-\gamma_5)b|\bar{B}_d^0(p_B)\rangle, \\ & \mathcal{M}^{c\bar{c}\,\mu} = \langle J/\psi(p_\psi,\epsilon)|\bar{c}\gamma^\mu c|0\rangle, \end{aligned} \tag{2.15}$$

which leads to the same decomposition as in Eq. (2.4), is only required if we want to identify the transversity form factors explicitly with those that, after an isospin rotation, describe the semileptonic decays $\bar{B}_d^0 \to \pi^+\eta\ell^-\bar{\nu}_\ell$; no such attempt is made in the following study. The effective coupling $a^{\text{eff}}(\mu)$ is related to Wilson coefficients of the effective weak Hamiltonian that governs the $b \to c\bar{c}d$ transition [161]; in terms of the usual set of 14 operators it reads

$$\mathcal{H}_{\text{eff}} = \frac{G_F}{\sqrt{2}} \sum_{p=u,c} \lambda_p \Big(C_1 Q_1^p + C_2 Q_2^p + \sum_{i=3,\ldots,10} C_i Q_i + C_{7\gamma} Q_{7\gamma} + C_{8g} Q_{8g} \Big) + \text{h.c.}, \tag{2.16}$$

using the same notation as in Ref. [162] except for the obvious replacement of s by d in the case of the $\bar{B}_d^0$ decay, in particular the λ_p are products of the CKM matrix elements for $c \to b$ and $c \to d$,

$$\lambda_c = V_{cb}V_{cd}^*, \qquad \lambda_u = V_{ub}V_{ud}^*, \tag{2.17}$$

and the local current–current operators Q_i^p read

$$\begin{aligned} Q_1^c &= 4\,\bar{c}_L\gamma^\mu b_L\,\bar{d}_L\gamma_\mu c_L = 4\,\bar{c}_L^i\gamma^\mu c_L^j\,\bar{d}_L^j\gamma_\mu b_L^i, & Q_1^u &= 4\,\bar{u}_L\gamma^\mu b_L\,\bar{d}_L\gamma_\mu u_L, \\ Q_2^c &= 4\,\bar{c}_L^i\gamma^\mu b_L^j\,\bar{d}_L^j\gamma_\mu c_L^i = 4\,\bar{c}_L\gamma^\mu c_L\,\bar{d}_L\gamma_\mu b_L, & Q_2^u &= 4\,\bar{u}_L^i\gamma^\mu b_L^j\,\bar{d}_L^j\gamma_\mu u_L^i, \end{aligned} \tag{2.18}$$

where $q_{L,R} = \frac{1}{2}(1 \mp \gamma_5)q$ and i, j are color indices. In the second step the quark operators are regrouped by means of a Fierz rearrangement. For the processes under consideration it is clear, at first, that the electromagnetic penguin operators Q_{7-10} as well as $Q_{7\gamma}$ can be neglected compared to Q_1^c, Q_2^c. We make the further assumption that the two operators Q_1^u, Q_2^u can also be neglected, such that the set of 14 operators is reduced to seven operators. The latter neglect is justified by the Okubo–Zweig–Iizuka (OZI) rule: in order to produce a J/ψ in the final state from the operators Q_1^u, Q_2^u one must proceed via quark-disconnected diagrams involving three gluons. The OZI rule is known to be quite effective for heavy-quarkonium production or decays. The effective coupling $a^{\text{eff}}(\mu)$ in Eq. (2.15) is thus given by $a^{\text{eff}}(\mu) = C_2(\mu) + C_1(\mu)/N_c$, with the ellipses in Eq. (2.15) denoting higher-order corrections to factorization that compensate for the scale dependence of $a^{\text{eff}}(\mu)$ [163] .

In order to calculate the differential decay rate for the $\bar{B}_d^0 \to J/\psi\pi^0\eta$ decay we sum over the squared helicity amplitudes,

$$\big|\overline{\mathcal{M}}\big|^2 = \frac{G_F^2}{2}|V_{cb}|^2|V_{cq}|^2 f_\psi^2 M_\psi^2 \left(|\mathcal{H}_0|^2 + |\mathcal{H}_+|^2 + |\mathcal{H}_-|^2\right) \quad (q = \{d, s\}), \tag{2.19}$$

and integrate over the invariant three-particle phase space, which is given by

$$\mathrm{d}\Phi^{(3)} = \frac{XY}{4(4\pi)^2 m_B^2}\,\mathrm{d}s\,\mathrm{d}\cos\theta_\eta\,\mathrm{d}\phi. \tag{2.20}$$

Neglecting waves higher than D-waves and integrating over ϕ we arrive at

$$\begin{aligned}
&\frac{\mathrm{d}^2\Gamma}{\mathrm{d}\sqrt{s}\,\mathrm{d}\cos\theta_\eta} \\
&= \frac{G_F^2|V_{cb}|^2|V_{cd}|^2 f_\psi^2 m_\psi^2 XY\sqrt{s}}{4(4\pi)^3 m_B^3}\left\{|\mathcal{F}_0(s,\theta_\eta)|^2 + Y^2\sin^2\theta_\eta\left(|\mathcal{F}_\parallel(s,\theta_\eta)|^2 + |\mathcal{F}_\perp(s,\theta_\eta)|^2\right)\right\} \\
&\approx \frac{XY\sqrt{s}}{4m_B}|\mathcal{C}|^2\left\{\left|\mathcal{F}_0^{(S)}(s) + \sqrt{3}\cos\theta_\eta\mathcal{F}_0^{(P)}(s) + \frac{\sqrt{5}}{2}\left(3\cos^2\theta_\eta - 1\right)\mathcal{F}_0^{(D)}(s)\right|^2\right. \\
&\quad \left. + \frac{3}{2}Y^2\sin^2\theta_\eta\left(\left|\mathcal{F}_\parallel^{(P)} + \sqrt{5}\cos\theta_\eta\mathcal{F}_\parallel^{(D)}(s)\right|^2 + \left|\mathcal{F}_\perp^{(P)} + \sqrt{5}\cos\theta_\eta\mathcal{F}_\perp^{(D)}(s)\right|^2\right)\right\}, \\
&\mathcal{C} = \frac{G_F V_{cb}V_{cd}^* f_\psi m_\psi}{\sqrt{(4\pi)^3}\,m_B},
\end{aligned} \tag{2.21}$$

where in the second step partial waves up to and including D-waves are considered.

By weighting this decay rate by spherical harmonic functions $Y_\ell^0(\cos\theta_\eta)$, we define the angular moments

$$\langle Y_\ell^0\rangle(s) = \int_{-1}^{1}\frac{\mathrm{d}^2\Gamma}{\mathrm{d}\sqrt{s}\,\mathrm{d}\cos\theta_\eta}Y_\ell^0(\cos\theta_\eta)\mathrm{d}\cos\theta_\eta, \tag{2.22}$$

commonly used by the LHCb collaboration, as well as later in this text. With the orthogonality property

$$\int_{-1}^{1} Y_i^0(\cos\theta_\eta)Y_j^0(\cos\theta_\eta)\mathrm{d}\cos\theta_\eta = \frac{\delta_{ij}}{2\pi}, \tag{2.23}$$

we obtain

$$\begin{aligned}
\sqrt{4\pi}\langle Y_0^0\rangle &= \frac{XY\sqrt{s}}{2m_B}\,|\,\mathcal{C}|^2\left\{\left|\mathcal{F}_0^{(S)}(s)\right|^2 + \left|\mathcal{F}_0^{(P)}(s)\right|^2 + \left|\mathcal{F}_0^{(D)}(s)\right|^2\right. \\
&\quad \left. + Y^2\left(\left|\mathcal{F}_\parallel^{(P)}(s)\right|^2 + \left|\mathcal{F}_\parallel^{(D)}(s)\right|^2 + \left|\mathcal{F}_\perp^{(P)}(s)\right|^2 + \left|\mathcal{F}_\perp^{(D)}(s)\right|^2\right)\right\}, \\
\sqrt{4\pi}\langle Y_1^0\rangle &= \frac{XY\sqrt{s}}{m_B}\,|\,\mathcal{C}|^2\left\{\mathrm{Re}\left(\mathcal{F}_0^{(S)}\mathcal{F}_0^{(P)^*}\right) + \frac{2}{\sqrt{5}}\mathrm{Re}\left(\mathcal{F}_0^{(P)}\mathcal{F}_0^{(D)^*}\right)\right. \\
&\quad \left. + \sqrt{\frac{3}{5}}Y^2\left[\mathrm{Re}\left(\mathcal{F}_\perp^{(P)}\mathcal{F}_\perp^{(D)^*}\right) + \mathrm{Re}\left(\mathcal{F}_\parallel^{(P)}\mathcal{F}_\parallel^{(D)^*}\right)\right]\right\}, \\
\sqrt{4\pi}\langle Y_2^0\rangle &= \frac{XY\sqrt{s}}{m_B}\,|\,\mathcal{C}|^2\left\{\mathrm{Re}\left(\mathcal{F}_0^{(S)}\mathcal{F}_0^{(D)^*}\right) + \frac{1}{\sqrt{5}}\left|\mathcal{F}_0^{(P)}\right|^2 + \frac{\sqrt{5}}{7}\left|\mathcal{F}_0^{(D)}\right|^2\right. \\
&\quad \left. - \frac{Y^2}{2\sqrt{5}}\left(\left|\mathcal{F}_\parallel^{(P)}\right|^2 + \left|\mathcal{F}_\perp^{(P)}\right|^2\right) + \frac{\sqrt{5}\,Y^2}{14}\left(\left|\mathcal{F}_\parallel^{(D)}\right|^2 + \left|\mathcal{F}_\perp^{(D)}\right|^2\right)\right\},
\end{aligned} \tag{2.24}$$

where $\langle Y_0^0\rangle$ corresponds to the differential decay rate $\mathrm{d}\Gamma/\mathrm{d}\sqrt{s}$, $\langle Y_1^0\rangle$ describes the interference between S- and P-wave as well as P- and D-wave amplitudes, and $\langle Y_2^0\rangle$ contains P-wave, D-wave, and S–D-wave interference contributions.

When comparing the angular moments to the experimental data—available for the $\pi^+\pi^-$ and K^+K^- final states—we have to deal with flavor-averaged expressions due to the B^0–$\bar{B}^0$ mixing and take into account the CP-conjugated amplitudes (the B_d^0 decay mode) as well. For the $\bar{B}_d^0 \to J/\psi\pi^+\pi^-$ decay mode the interfering term between the amplitudes is found to be negligibly small [141], hence the decay rate can be written as the sum of the decay rates for the direct $\bar{B}_d^0$ and the mixed CP-conjugated B_d^0 mode,

$$\frac{\mathrm{d}^2\Gamma\left(\bar{B}_d^0 \to J/\psi\pi^+\pi^-\right)}{\mathrm{d}\sqrt{s}\,\mathrm{d}\cos\theta_\pi} \approx \frac{\mathrm{d}^2\Gamma\,(\text{direct})}{\mathrm{d}\sqrt{s}\,\mathrm{d}\cos\theta_\pi} + \frac{\mathrm{d}^2\Gamma\left(B_d^0 \to J/\psi\pi^+\pi^-\right)}{\mathrm{d}\sqrt{s}\,\mathrm{d}\cos\theta_\pi}. \tag{2.25}$$

This neglect is less justified when applying the formulae to the $\bar{B}_s^0 \to J/\psi\pi^+\pi^-$ decay rate. In the analysis of Ref. [142] an interference term is added to Eq. (2.25). However, in Section 2.5.2 we find that it is sufficient to take into account S-waves. In that case the interference term does not affect the fit procedure and merely generates a tiny shift of the resulting fit parameter (the normalization c_0^s). The same argument applies to the $\pi^0\eta$ final state: we prove the S-wave dominance compared to P-waves in Section 2.7: as we discuss in Section 2.7.1, the production vertex for a $\pi\eta$ P-wave is chirally suppressed; it is generically smaller relative to the S-wave by a factor of $YM_K^2/(4\pi F_\pi)^2$, which around 1 GeV amounts to one order of magnitude. In Sections 2.7.2 and 2.7.3, we calculate the P-wave contributions generated by t- and u-channel resonance exchanges, and find them to be even more suppressed than this generic estimate. Furthermore, the $\pi\eta$ P-wave has exotic quantum numbers; final-state-interaction effects should thus be small below 1 GeV. We therefore find it safe to assume it to be negligible in the energy range considered in this study, and well within the uncertainty of the S-wave contribution. We will briefly discuss the impact of D-waves in Section 2.7, mainly to demonstrate that they also only become important for dimeson energies well above 1 GeV.

The expressions we have provided in this section refer to one particular mode. The corresponding expressions for the CP-conjugated modes are related straightforwardly to the above equations by certain sign changes due to the CP eigenvalues $\eta_{CP} = \pm 1$ in the definitions of the transversity partial-wave amplitudes. We declare the amplitudes $\mathcal{F}_\tau^{(\ell)}$ to describe the B_d^0 decay, then the corresponding $\bar{B}_d^0$ decay amplitudes are given by

$$\bar{\mathcal{F}}_\tau^{(\ell)} = \eta_{CP}\mathcal{F}_\tau^{(\ell)}, \tag{2.26}$$

with $\eta_{CP} = +1$ for the $\tau = 0, \parallel$ P-waves and the $\tau = \perp$ D-wave, and $\eta_{CP} = -1$ otherwise. Consequently the angular moments $\langle Y_0^0\rangle$ and $\langle Y_2^0\rangle$ are unchanged under CP conjugation, while the conjugated moment $\langle Y_1^0\rangle$ has opposite sign, such that when considering flavor-averaged quantities and summing over the B_d^0 and $\bar{B}_d^0$ contributions, $\langle Y_1^0\rangle$ vanishes. In the following we thus consider $\langle Y_0^0\rangle$ and $\langle Y_2^0\rangle$ only.

2.3 Chiral-symmetry based relations

In this section we demonstrate how the $\bar{B}_d^0 \to J/\psi\pi^0\eta$ S-wave can be predicted by means of a flavor relation to the $\bar{B}_d^0 \to J/\psi\pi^+\pi^-$ S-wave. To begin with we briefly discuss how this relation can be derived based on chiral symmetry. For this purpose we consider the effective weak Hamiltonian, Eq. (2.16). In Section 2.2 we explained that seven of the usual 14 operators can be neglected. The remaining seven operators all transform simply as $\bar{d}_L$ under the $SU(3)_L \times SU(3)_R$ chiral group. We can then construct a chiral Lagrangian that encodes this transformation property and describes the dynamics in the region where the light pseudoscalar meson pair has a very small energy; this is detailed in the subsequent subsection. At leading order in the chiral expansion, the following relation can be derived between the $\bar{B}_d^0$-decay

amplitudes and the vacuum matrix elements of $\bar{d}d$ operators:

$$\frac{\langle J/\psi(\pi^0\eta)_{\ell=0}|\mathcal{O}_{\bar{d}}|\bar{B}^0_d\rangle}{\langle J/\psi(\pi^+\pi^-)_{\ell=0}|\mathcal{O}_{\bar{d}}|\bar{B}^0_d\rangle} = \frac{\langle \pi^0\eta|\bar{d}d|0\rangle}{\langle \pi^+\pi^-|\bar{d}d|0\rangle}. \tag{2.27}$$

This relation will be used at energy $s = 0$.

We emphasize that it is important to use chiral symmetry to derive this result rather than flavor symmetry alone. Indeed, under the flavor symmetry group $SU(3)_F$, the state $(\pi\pi)_{I=0}$ appears both in the singlet and in the octet representations, while $(\pi\eta)$ belongs to the octet. Therefore, no relation can be derived between the corresponding $\bar{B}^0_d$ decay amplitudes based on flavor symmetry alone. For simplicity, we will however still refer to these as flavor relations in the following.

2.3.1 Flavor relations from a chiral Lagrangian for $B^0_d \to J/\psi M_1 M_2$

In the following we construct a chiral Lagrangian that provides the above derived relation between the $\bar{B}^0_d$-decay amplitudes and the $\bar{d}d$ matrix elements, Eq. (2.27), that we use in Section 2.4.4 for predicting the $\bar{B}^0_d \to J/\psi\pi^0\eta$ S-wave. We consider the decays $B^0_d \to J/\psi M_1 M_2$, where M_i is a light pseudoscalar meson (π, K, η). We assume that there exists a kinematical regime where the light mesons are soft, and that we can describe the dynamics in this situation via a chiral expansion. We can write a chiral Lagrangian that reflects the chiral transformation properties of the weak transition operator following the method described e.g. in [165] for $K \to \pi\pi$ and $K \to 3\pi$ decays, where the K was assumed to be heavy. The two dominant operators have the following structure:

$$O_d \sim \bar{c}_L \gamma_\mu d_L \, \bar{b}_L \gamma^\mu c_L, \tag{2.28}$$

such that, under the chiral symmetry group $SU(3)_L \times SU(3)_R$, they transform simply as d_L. In order to construct a chiral Lagrangian we introduce a three-vector spurion field t_L, which transforms as

$$t_L \to g_L \, t_L, \qquad g_L \in SU(3)_L, \tag{2.29}$$

such that $t^\dagger_L(O_u, O_d, O_s)$ is a chiral invariant. t_L will ultimately be set to $t_L = (0, 1, 0)^t$. The heavy vector field Ψ^μ is left invariant by chiral symmetry, while the B^0_d can be considered as part of a three-vector $B = (B^+, B^0_d, B^0_s)^t$, which transforms as

$$B \to h \, B, \tag{2.30}$$

where h is the non-linear realization of the chiral group. That is, if U is the chiral field matrix and $U = u^2$,

$$U \to g_R \, U \, g^\dagger_L, \qquad u \to g_R \, u \, h^\dagger = h \, u \, g^\dagger_L, \qquad g_R \in SU(3)_R. \tag{2.31}$$

At leading chiral order the Lagrangian that describes the decays $B^0_d \to J/\psi +$ light mesons has two independent terms:

$$\mathcal{L}_1 = g_{1a} \, t^\dagger_L \, u^\dagger u_\mu B \, \Psi^\mu + i g_{1b} \, t^\dagger_L \, u^\dagger \nabla_\mu B \, \Psi^\mu + \text{h.c.}, \tag{2.32}$$

with

$$u_\mu = i(u^\dagger \partial_\mu u - u \partial_\mu u^\dagger), \qquad \nabla_\mu \, B = (\partial_\mu + \Gamma_\mu) B, \qquad \Gamma_\mu = \frac{1}{2}(u^\dagger \partial_\mu u + u \partial_\mu u^\dagger), \tag{2.33}$$

using the same notation as e.g. in Ref. [166]. We are interested in the production of meson pairs: expanding the Lagrangian (2.32) to quadratic order in the light fields and using integration by parts, we find

$$\mathcal{L}^{\phi^2}_{1,B^0_d} = -\frac{ig_1}{4F_\pi^2}\Psi^\mu\Big\{\partial_\mu B^0_d\Big[\frac{1}{2}(\pi^0)^2 + \pi^+\pi^- - \frac{1}{\sqrt{3}}\pi^0\eta + \frac{1}{6}\eta^2 + K^0\bar{K}^0\Big] + B^0_d\Big[\pi^+\partial_\mu\pi^- - \pi^-\partial_\mu\pi^+ + \bar{K}^0\partial_\mu K^0 - K^0\partial_\mu\bar{K}^0\Big]\Big\} + \text{h.c.}, \tag{2.34}$$

with $g_1 = 2g_{1a} + g_{1b}$. The second line in Eq. (2.34) contributes to amplitudes where the M_1M_2 pair is in a P-wave (note that there is no contribution to $\pi\eta$ at this order). The first line in Eq. (2.34) contributes to amplitudes where the pair is in a relative S-wave. This gives a set of definite relations among $\pi\pi$, $\pi\eta$, and $\bar{K}K$ S-wave amplitudes. These are exactly the same as for the $\bar{d}d$ scalar form factors at chiral order p^2. Indeed, the $\bar{d}d$ form factors at leading order are obtained by expanding the $\mathcal{O}(p^2)$ chiral Lagrangian piece

$$\mathcal{L}_2 = \frac{F_\pi^2}{4}\langle\chi_+\rangle, \tag{2.35}$$

with $\chi_+ = u^\dagger\chi u^\dagger + u\chi^\dagger u$, $\chi = 2\mathcal{B}_0\,\mathrm{diag}(0,1,0)$. Similar arguments to derive such relations have also been formulated in Ref. [167].

In addition we can write the contributions to the decays of the B^+ meson, $B^+ \to J/\psi M_1M_2$, as

$$\mathcal{L}^{\phi^2}_{1,B^+} = -\frac{ig_1}{4F_\pi^2}\Psi^\mu\Big\{\partial_\mu B^+\Big[\sqrt{\frac{2}{3}}\pi^-\eta + K^0K^-\Big] + B^+\Big[\sqrt{2}(\pi^0\partial_\mu\pi^- - \pi^-\partial_\mu\pi^0) + K^-\partial_\mu K^0 - K^0\partial_\mu K^-\Big]\Big\} + \text{h.c.}. \tag{2.36}$$

The above derivation is rather general: it does not rely on factorization, the large-N_c expansion, or other hypotheses. The relations obtained are, however, valid only at leading order. Indeed, at next-to-leading order, the one-loop divergences of the $\bar{d}d$ form factors are absorbed into the standard chiral coupling constants L_i [60], while the one-loop divergences of the B^0_d amplitudes are absorbed into coupling constants g_{3a}, g_{3b}, …, pertaining to the higher-order generalization of the Lagrangian (2.32). These are obviously unrelated to the couplings L_i. It is also likely that the chiral logarithms of the B^0_d amplitudes will be different from those of the $\bar{d}d$ form factors.

2.4 Partial waves and Omnès formalism

We describe the S- and P-wave amplitudes that contribute to the angular moments, Eq. (2.24), using dispersion theory. This approach allows us to treat the rescattering effects in the $\pi\pi$, $\pi\eta$ or $\bar{K}K$ systems in a model-independent way, based on the fundamental principles of unitarity and analyticity, see Section 1.3.1: the partial waves are analytic functions in the whole s-plane except for a branch-cut structure dictated by unitarity. In the following we deal with the functions $f^{\ell,I}_\tau(s)$ (referring to isospin I, transversity τ and angular momentum ℓ and introduced in Eq. (2.14)) that possess a right-hand cut starting at the respective two-meson threshold: the pion–pion threshold $s_{\text{thr}} = 4M_\pi^2$ in the isoscalar or the pion–eta threshold $s_{\text{thr}} = (M_\pi + M_\eta)^2$ in the isovector sector. They are analytic elsewhere, i.e. we do not consider any left-hand-cut or pole structure related to crossing symmetry. In the case of the $\pi\pi$ system this is justified from

the observation that there are practically no structures observed for the (exotic) crossed $J/\psi\pi^+$ channel in the region of interest [141]. This phenomenology-inspired assumption of negligible crossed-channel processes is adopted in the study of the related decays into $J/\psi\{K^+K^-, \bar{K}^0K^0\}$ and $J/\psi\pi^0\eta$. There, however, the justification is not quite so clear: e.g. the $\psi(2S)$ decays into $J/\psi\eta$, and therefore will show up as a resonance in the corresponding distribution.[3] However, due to the anomalous nature of the $\psi(2S) \to J/\psi\eta$ vertex, this $\psi(2S)$-exchange mechanism only contributes to the transversity form factor $\mathcal{F}_\perp$, whose partial-wave expansion begins with a P-wave, see Eq. (2.12), and hence cannot contribute to the $\pi^0\eta$ S-wave that we will concentrate on below. In addition, the coupling $\psi(2S) \to J/\psi\eta$ violates the OZI rule and is still rather weak: compare

$$\begin{aligned} \mathcal{B}(\bar{B}^0_d \to \psi(2S)\pi^0) &= (1.17 \pm 0.19) \times 10^{-5} \quad [164], \\ \mathcal{B}(\psi(2S) \to J/\psi\,\eta) &= (3.36 \pm 0.05) \times 10^{-2} \quad [44] \end{aligned} \tag{2.37}$$

to $\mathcal{B}(\bar{B}^0_d \to J/\psi\pi^+\pi^-) = (4.03 \pm 0.18) \times 10^{-5}$ [44]; we will see in Section 2.6 that the branching ratio $\mathcal{B}(\bar{B}^0_d \to J/\psi\pi^0\eta)$ is predicted to be of a comparable size. Further, in Section 2.7.2, we calculate the $\psi(2S)$-exchange contribution explicitly and show that below $\sqrt{s} \approx 1.34\,\text{GeV}$, where the $\psi(2S)$ cannot go on-shell, its effect is even more suppressed. We assume that other charmonium resonances whose exchange in the t- (or even u-)channel *can* contribute to the $\pi^0\eta$ S-wave (such as axialvector ones of negative C-parity) couple similarly weakly. Furthermore, in Section 2.7.3 we study the effect of t- and u-channel B^*-exchange diagrams in the $\bar{B}^0_d \to J/\psi\pi^0\eta$ decay, whose cut contributions lie well outside the physical decay region; however even then, the pole terms are suppressed in the S-wave due to chiral and heavy-quark symmetry. We therefore neglect the influence of left-hand cuts altogether. Such B^*-exchange diagrams may contribute to the $\bar{B}^0_d \to J/\psi\pi^+\pi^-$ decay as well. We claim that in that channel the neglect of left-hand-cut structures is well-founded on the phenomenological observations, where, however, crossed-channel effects in the strong *final-state* interaction are excluded. To also exclude that our formalism is spoiled by effects occurring already in the weak decay mechanism we provide an (a-posteriori) confirmation in Section 2.7.4 by considering the t-channel B^* exchange process.

Considering the lowest (i.e. $\pi\pi$ or $\pi\eta$, respectively) intermediate states only, Watson's theorem holds: the phase of the partial wave is given by the elastic pion–pion or pion–eta phase shift [82], and the discontinuity across the cut can be written as

$$\text{disc} f^{\ell,I}_\tau(s) = f^{\ell,I}_\tau(s+i\epsilon) - f^{\ell,I}_\tau(s-i\epsilon) = 2iY f^{\ell,I}_\tau(s) \left[t^I_\ell(s)\right]^* = f^{\ell,I}_\tau(s) e^{-i\delta^I_\ell} \sin\delta^I_\ell . \tag{2.38}$$

A solution of this unitarity relation can be constructed analytically, setting (compare Ref. [168])

$$f^{\ell,I}_\tau(s) = P_\tau(s)\Omega^I_\ell(s), \tag{2.39}$$

where $P_\tau(s)$ is a polynomial not fixed by unitarity, and the Omnès function $\Omega^I_\ell(s)$ is entirely determined by the phase shift $\delta^I_\ell(s)$ [80],

$$\Omega^I_\ell(s) = \exp\left\{\frac{s}{\pi}\int_{s_\text{thr}}^\infty \frac{\delta^I_\ell(s')}{s'(s'-s-i\epsilon)}\text{d}s'\right\}, \tag{2.40}$$

with

$$\Omega^I_\ell(0) = 1 \quad \text{and} \quad \Omega^I_\ell(s) \neq 0 \quad \forall\, s. \tag{2.41}$$

[3] Actually, the same problem arises already for $J/\psi\pi^0$, another observed decay channel of the $\psi(2S)$, which however breaks isospin symmetry and hence is very weak.

2.4.1 *P*-waves and vector form factor

The pion–pion[4] P-wave amplitudes can be well described in the elastic approximation up to energies of roughly 1 GeV. The simplest possible application is the pion vector form factor $\mathcal{F}_\pi^V(s)$, defined in Eq. (1.74), which obeys a representation like (2.39) with a linear polynomial $P_{\mathcal{F}_\pi^V}(s) = 1 + \alpha s$, $\alpha \approx 0.1\,\text{GeV}^{-2}$ [169] up to $\sqrt{s} \approx 1\,\text{GeV}$, with the exception of a small energy region around the ω resonance that couples to the two-pion channel via isospin-violating interactions. In this context it is important to note that the electromagnetic current j_{em}^μ, introduced in Eq. (1.74), can be decomposed as

$$j_{\text{em}}^\mu = \frac{1}{2}\big(\bar{u}\gamma^\mu u - \bar{d}\gamma^\mu d\big) + \frac{1}{6}\big(\bar{u}\gamma^\mu u + \bar{d}\gamma^\mu d\big). \tag{2.42}$$

Thus it contains with the first term an isovector and with the second term an isoscalar component. The latter couples directly to the ω, whose decay into $\pi^+\pi^-$ is suppressed by isospin, but enhanced by a small energy denominator (i.e., the small width of the ω), hence leading to a clearly observable effect in the pion form factor [87, 88, 170]. Theoretically, this effect is correctly taken into account by the replacement [99, 171, 172]

$$P_{\mathcal{F}_\pi^V}(s)\Omega_1^1(s) \longrightarrow P_{\mathcal{F}_\pi^V}(s)\Omega_1^1(s)\left(1 + \frac{\kappa_{\text{em}}\, s}{M_\omega^2 - iM_\omega\Gamma_\omega - s}\right). \tag{2.43}$$

Note that in case of the ω the use of a Breit–Wigner parametrization is appropriate since the ω pole is located far above the relevant decay thresholds and since $\Gamma_\omega = 8.5\,\text{MeV}$ is very small. A fit of the form factor parametrization introduced in Eq. (2.43) to the KLOE data [88] yields $\kappa_{\text{em}} \approx 1.8 \times 10^{-3}$ [173]. This fixes the strength of the so-called ρ–ω mixing amplitude phenomenologically. The isospin-violating coupling κ_{em} is of the usual size, however, near the ω peak its smallness is balanced by the factor $M_\omega/\Gamma_\omega \approx 90$ from the ω propagator, giving rise to an isospin-violating correction as large as 15% on the amplitude level, corresponding to 30% in observables due to interference with the leading term. Note also that the ρ–ω mixing amplitude has been pointed out to significantly enhance certain CP-violating asymmetries in hadronic B-meson decays [174].

The effect of the ω on the $\bar{B}_d^0 \to J/\psi\pi^+\pi^-$ decay can be related straightforwardly to that on the pion vector form factor. To see this observe that the source term for the pion–pion system is $\bar{d}d$ at tree level, see Figure 2.1, such that the isospin decomposition of the corresponding vector current reads

$$\bar{d}\gamma^\mu d = -\frac{1}{2}\big(\bar{u}\gamma^\mu u - \bar{d}\gamma^\mu d\big) + \frac{1}{2}\big(\bar{u}\gamma^\mu u + \bar{d}\gamma^\mu d\big). \tag{2.44}$$

Comparison to Eq. (2.42) shows that the relative strength of the isoscalar component differs from the electromagnetic current by a factor of -3, such that we will fix the ρ–ω mixing contribution in analogy to Eq. (2.43), but with the replacement $\kappa_{\text{em}} \to \kappa = -3\kappa_{\text{em}} \approx -5.4 \times 10^{-3}$. Notice that this is in contrast with the experimental analysis [141], where the ω contribution is fitted with free coupling constants.

2.4.2 *S*-waves and scalar form factors

The (elastic) single-channel treatment, introduced in the beginning of this section, cannot be used in the S-wave case: there are strong inelastic effects in the region around 1 GeV due to

[4] Out of the considered final-state meson pairs only for the two-pion system P-waves are considered in the dispersive representation, the other channels are either dominated by the S-wave that is treated below or at least the S-wave background is of particular interest. The P-wave in the $\bar{K}K$ final-state is dominated by the ϕ-resonance, which has a sufficiently small width such that it is well described by a Breit–Wigner parametrization.

the opening of the $K\bar{K}$ channel, coinciding with the $I = 0$ $f_0(980)$ resonance or the $I = 1$ $a_0(980)$ resonance, respectively. This affects the phase of the scalar isoscalar pion or isovector pion-eta form factors (see e.g. the discussion in Ref. [175]). Thus the Omnès formalism has to be generalized to a coupled-channel problem, with the Watson theorem fulfilled in the elastic region and inelastic effects included above the $K\bar{K}$ threshold. This leads to the two-channel Muskhelishvili–Omnès equations that intertwine the scalar isoscalar pion and kaon form factors on the one hand, defined as

$$\begin{aligned} \left\langle \pi^+(p_1)\pi^-(p_2)\,|(\bar{q}q)_{I=0}|\,0\right\rangle &= \mathcal{B}_0^q \Gamma^{q,I=0}_{\pi\pi}(s), \\ \left\langle K^+(p_1)K^-(p_2)\,|(\bar{q}q)_{I=0}|\,0\right\rangle &= \mathcal{B}_0^q \Gamma^{q,I=0}_{\bar{K}K}(s), \end{aligned} \tag{2.45}$$

and on the other hand the scalar isovector $\pi\eta$ and $\bar{K}K$ form factors

$$\begin{aligned} \left\langle \pi^0(p_1)\eta(p_2)\,|(\bar{q}q)_{I=1}|\,0\right\rangle &= \mathcal{B}_0^\Delta \Gamma^{I=1}_{\pi\eta}(s), \\ \left\langle K^+(p_1)K^-(p_2)\,|(\bar{q}q)_{I=1}|\,0\right\rangle &= \mathcal{B}_0^\Delta \Gamma^{I=1}_{\bar{K}K}(s). \end{aligned} \tag{2.46}$$

The quark flavors in the isovector sector are $(\bar{q}q)_{I=1} = (\bar{u}u - \bar{d}d)/2$ and the isoscalar scalar currents may be either $(\bar{q}q)_{I=0} = (\bar{u}u + \bar{d}d)/2$ for the light quarks, with the superscript $q = n$ denoting the corresponding scalar form factor, or $(\bar{q}q)_{I=0} = \bar{s}s$ for strange quarks (with superscript $q = s$). The strange scalar current is purely isoscalar, therefore there are two isoscalar but only one isovector form factor. Furthermore, $\mathcal{B}_0^\Delta$ is related to the QCD mass difference $M^2_{K^+} - M^2_{K^0}$, $\mathcal{B}_0^\Delta = (M^2_{K^+} - M^2_{K^0})/\Delta_{ud}$, $\Delta_{ud} = m_u - m_d$; for the definitions of the $\mathcal{B}_0^q$, see Eq. (1.103). Note that the form factors $\Gamma^{q,I}_{M_1M_2}(s)$ are invariant under the QCD renormalization group, while the hadronic matrix elements are not due to the scale dependence inherent in the factors $\mathcal{B}_0^{q,\Delta}$. This in turn allows for the cancellation of the scale dependence in the Wilson coefficients introduced in the effective Hamiltonian of Section 2.2. Some details concerning the isospin and physical states involved in the definitions of the form factors can be found in Appendix A.1.

Appealing to the tree-level diagram of Figure 2.1, we expect the non-strange scalar form factors to contribute dominantly in the $\bar{B}^0_d$ decay, while the strange ones should feature mainly in the corresponding decay of the $\bar{B}^0_s$. As discussed in detail in Section 2.5, these expectations are confirmed by the data analysis of $\bar{B}^0_{d,s} \to J/\psi\pi^+\pi^-$.

The two-channel Muskhelishvili–Omnès formalism was briefly reviewed for the isospin-0 pion and kaon form factors in Section 1.3.4. The isoscalar T-matrix parametrization requires *three* input functions: in addition to the $\pi\pi$ phase shift already necessary in the elastic case, modulus and phase of the $\pi\pi \to K\bar{K}$ S-wave amplitude also need to be known. Our main solution is based on the Roy equation analysis by the Bern group [153, 154] for the $\pi\pi$ phase shift, the modulus of the $\pi\pi \to K\bar{K}$ S-wave as obtained from the solution of Roy–Steiner equations for πK scattering performed in Orsay [37], and its phase from partial-wave analyses [176, 177]. Alternatively, we employ the T-matrix constructed by Dai and Pennington (DP) in Ref. [127]: here, a coupled-channel K-matrix parametrization is fitted to $\pi\pi$ data [178–182], and the Madrid–Kraków Roy-equation analysis [36] is used as input; furthermore, the $K\bar{K}$ threshold region is improved by fitting also to Dalitz plot analyses of $D^+_s \to \pi^+\pi^-\pi^+$ [183] and $D^+_s \to K^+K^-\pi^+$ [184] by the BaBar Collaboration.

For the isovector sector, we use the result of Ref. [140]. In that work, a coupled-channel T-matrix is constructed that fulfills unitarity, and the amplitudes are approximately matched with the perturbative ones derived from $\mathcal{O}(p^4)$ chiral perturbation theory. With this method six phenomenological parameters are introduced, to be determined by experimental information about the $a_0(980)$ and $a_0(1450)$ resonances. Specifically, five experimental constraints are imposed, and hence there is still a one-parameter freedom in the model that can be associated

with the sum of the phase shifts of the $\pi\eta$ (δ_{11}) and $\bar{K}K$ (δ_{22}) channels at the mass of the $a_0(1450)$, $\delta_{12} \equiv (\delta_{11} + \delta_{22})(s = m^2_{a_0(1450)})$.

The scalar coupled-channel form factors in the Omnès formalism read

$$\begin{pmatrix} \Gamma^{I=0}_{\pi\pi}(s) \\ \frac{2}{\sqrt{3}}\Gamma^{I=0}_{KK}(s) \end{pmatrix} = \begin{pmatrix} \Omega^{I=0}_{11}(s) & \Omega^{I=0}_{12}(s) \\ \Omega^{I=0}_{21}(s) & \Omega^{I=0}_{22}(s) \end{pmatrix} \cdot \begin{pmatrix} \Gamma^{I=0}_{\pi\pi}(0) \\ \frac{2}{\sqrt{3}}\Gamma^{I=0}_{KK}(0) \end{pmatrix} \tag{2.47}$$

for the isoscalar meson pairs, and

$$\begin{pmatrix} \Gamma^{I=1}_{\pi\eta}(s) \\ \sqrt{2}\Gamma^{I=1}_{KK}(s) \end{pmatrix} = \begin{pmatrix} \Omega^{I=1}_{11}(s) & \Omega^{I=1}_{12}(s) \\ \Omega^{I=1}_{21}(s) & \Omega^{I=1}_{22}(s) \end{pmatrix} \cdot \begin{pmatrix} \Gamma^{I=1}_{\pi\eta}(0) \\ \sqrt{2}\Gamma^{I=1}_{KK}(0) \end{pmatrix} \tag{2.48}$$

for the isovector $\pi\eta$–$\bar{K}K$ system. The resulting form factors depend on two normalization constants $\Gamma^I_{M_1M_2}(0)$, i.e. even in the simplest case, corresponding to the polynomial of Eq. (2.39) reducing to a constant, the channel coupling manifests itself through the fact that the scalar form factors depend on *two* such constants. In contrast to the single-channel case, here the shape of the resulting form factors depends on the relative size of these two normalization constants; on the other hand, once this relative strength is fixed, it relates the final states $\pi\pi$ and $K\bar{K}$ in the isospin-0 case or $\pi\eta$ and $K\bar{K}$ in the isospin-1 case to each other unambiguously. We will make use of this additional predictiveness in Section 2.8.1.

We constrain the form factor normalizations from their chiral one-loop (or next-to-leading-order) representations. The $\pi\pi$ and $\bar{K}K$ matrix elements at $s = 0$ are related to quark-mass derivatives of the corresponding Goldstone boson masses via the Feynman–Hellmann theorem, while the $\pi\eta$ one obeys a Ward identity relating it to a similar vector-current matrix element [140]. At leading order in the chiral expansion we find the normalizations

$$\Gamma^{n,I=0}_{\pi\pi}(0) = 1,\ \Gamma^{n,I=0}_{KK}(0) = \frac{1}{2},\ \Gamma^{s,I=0}_{\pi\pi}(0) = 0,\ \Gamma^{s,I=0}_{KK}(0) = 1,\ \Gamma^{I=1}_{\pi\eta}(0) = \frac{1}{\sqrt{3}},\ \Gamma^{I=1}_{KK}(0) = \frac{1}{2}. \tag{2.49}$$

The next-to-leading order results depend on certain low-energy constants. We emphasize that for these, the universality of the relative couplings to different mesons, comparing the scalar form factors and the S-waves appearing in the $\bar{B}^0_d$ decays, see Eq. (2.27), is not guaranteed, and one might argue in favor of simply using the leading-order relations of Eq. (2.49); see the discussion in Section 2.3. However, in order to obtain at least a realistic estimate of the uncertainties induced by next-to-leading-order corrections, we take those from the scalar form factor matrix elements. The corresponding low-energy constants are determined in lattice simulations with $N_f = 2+1+1$ dynamical flavors at a running scale $\mu = 770\,\text{MeV}$ [111], limiting the form factor normalizations to the ranges[5]

$$\begin{aligned} &\Gamma^{n,I=0}_{\pi\pi}(0) = 0.984 \pm 0.006, && \Gamma^{n,I=0}_{KK}(0) = (0.44 \ldots 0.68), \\ &\Gamma^{s,I=0}_{\pi\pi}(0) = (0.001 \ldots 0.013) \approx 0, && \Gamma^{s,I=0}_{KK}(0) = (1.0 \ldots 1.2), \\ &\Gamma^{I=1}_{\pi\eta}(0) = (0.56 \ldots 0.87), && \Gamma^{I=1}_{KK}(0) = (0.38 \ldots 0.56). \end{aligned} \tag{2.50}$$

Since the form factor shape depends on the relative size of the two pairs of normalization constants, there is some uncertainty in the shape of the isoscalar scalar form factors. The variations in the isovector form factor normalizations are strongly correlated, i.e. their ratio for small and large values of the low-energy constants varies at the 5% level only.

[5]Note that in Ref. [113] the form factor normalizations are based on lattice simulations with $N_f = 2 + 1$ dynamical flavors [110], which yields similar ranges. In particular, for the fits performed in Ref. [113] and presented in Section 2.5 the normalization of the isoscalar kaon form factor was set to the leading-order result $\Gamma^{n,I=0}_{KK}(0) = 0.5$, which is compatible with both normalization ranges (according to either the $N_f = 2 + 1 + 1$ or the $N_f = 2 + 1$ lattice simulation).

2.4.3 $\pi\pi$ partial waves in the Omnès formalism

We start with the discussion of the representation of the partial waves in the system. As this channel is measured it provides a test how well the data are described by our ansatz. In order to apply the Omnès formalism to the transversity partial waves we have to deal with the partial waves $f_\tau^{(\ell)}(s)$ that we have constructed in Eq. (2.14), being free of kinematical singularities. The S- and P-waves read

$$f_0^{(S,I=0)}(s) = P_0^{(S,n)}(s)\Gamma_{\pi\pi}^{n,I=0}(s) + P_0^{(S,s)}(s)\Gamma_{\pi\pi}^{s,I=0}(s), \qquad f_\tau^{(P,I=1)}(s) = P_\tau^{(P)}(s)\Omega_1^1(s). \quad (2.51)$$

For the S-wave, we a priori allow for contributions of both non-strange (n) and strange (s) scalar form factors. The coefficients of the polynomials $P_\tau^{(\ell)}(s)$ are to be determined from a fit to the efficiency-corrected and background-subtracted LHCb data, in particular to the angular moments $\langle Y_0^0\rangle$ and $\langle Y_2^0\rangle$.

Basically we assume the various polynomials to be well approximated by constants. However, to study the impact of a linear correction at a later stage, we also consider linear polynomials $P_0^{(S,n)} = b_0^n(1 + b_0'^n s)$ and $P_\tau^{(P)} = a_\tau(1 + a'_\tau s)$ for the non-strange S-wave and the P-wave amplitudes, respectively. The strange S-wave contribution is expected to be very small (in the LHCb analysis of $\bar{B}_d^0 \to J/\psi\pi^+\pi^-$ the $f_0(980)$ meson is not seen), but tested in the fits. On the contrary, the $\bar{B}_s^0 \to J/\psi\pi^+\pi^-$ distribution is dominated by the $f_0(980)$ resonance, described by a constant polynomial times Omnès function, $P_0^{(S,s)} = c_0^s$, while there is no structure in the $f_0(500)$ region reported by LHCb. Thus in that case the non-strange S-wave amplitude is assumed to be negligible, to be confirmed in the fits.

Although the first D-wave resonance seen is the $f_2(1270)$, it may affect also the region below $\sqrt{s} \approx 1\,\text{GeV}$ due to its finite width, $\Gamma_{f_2} = 185.1^{+2.9}_{-2.4}\,\text{MeV}$ [62]. Therefore we also test its influence on the fit. The D-waves could be treated in the same dispersive way as S- and P-waves, but this would increase the number of free parameters in our fits to the LHCb data. As the effect of D-wave corrections is rather small, we avoid introducing additional fit parameters and take over the amplitudes (with fixed couplings) used in the LHCb analysis, where the $f_2(1270)$ resonance is modeled by a Breit–Wigner shape.

Combining Eqs. (2.24), (2.14) and (2.51) in order to write $\langle Y_i^0\rangle$ in terms of Omnès functions for S- and P-waves, supplemented by the D-wave resonance contribution, yields

$$\begin{aligned}
\sqrt{4\pi}\langle Y_0^0\rangle &= \mathcal{N}_\pi^q \frac{XY\sqrt{s}}{2m_B}\Big\{ X^2\big|b_0^n(1+b_0'^n s)\Gamma_{\pi\pi}^{n,I=0}(s) + c_0^s\Gamma_{\pi\pi}^{s,I=0}(s)\big|^2 \\
&\quad + Y^2\left|\Omega_1^1(s)\right|^2\Big(\big[a_0(1+a_0's)\big]^2 + s\big[a_\parallel(1+a'_\parallel s)\big]^2 + sX^2\big[a_\perp(1+a'_\perp s)\big]^2\Big) \\
&\quad + \sum_{\tau=0,\perp,\parallel}\left|\alpha_\tau^{f_2}e^{i\phi_\tau^{f_2}}\mathcal{A}_{f_2}^{(\tau)}(s)\right|^2\Big\} = \mathcal{N}_\pi^q\sqrt{4\pi}\langle Y_0^0\rangle_{\text{LHCb}}\,, \\
\sqrt{4\pi}\langle Y_2^0\rangle &= \mathcal{N}_\pi^q \frac{XY\sqrt{s}}{2m_B}\left\{2\text{Re}\left(X\Big[b_0^n(1+b_0'^n s)\Gamma_{\pi\pi}^{n,I=0}(s) + c_0^s\Gamma_{\pi\pi}^{s,I=0}(s)\Big]\Big[\alpha_0^{f_2}e^{i\phi_0^{f_2}}\mathcal{A}_{f_2}^{(0)}(s)\Big]^*\right)\right. \\
&\quad + \frac{Y^2}{\sqrt{5}}\left|\Omega_1^1(s)\right|^2\Big(2\big[a_0(1+a_0's)\big]^2 - s\big[a_\parallel(1+a'_\parallel s)\big]^2 - sX^2\big[a_\perp(1+a'_\perp s)\big]^2\Big) \\
&\quad \left. + \frac{\sqrt{5}}{7}\left(2\left|\alpha_0^{f_2}e^{i\phi_0^{f_2}}\mathcal{A}_{f_2}^{(0)}(s)\right|^2 + \sum_{\tau=\parallel,\perp}\left|\alpha_\tau^{f_2}e^{i\phi_\tau^{f_2}}\mathcal{A}_{f_2}^{(\tau)}(s)\right|^2\right)\right\} = \mathcal{N}_\pi^q\sqrt{4\pi}\langle Y_2^0\rangle_{\text{LHCb}}\,.
\end{aligned} \quad (2.52)$$

For details concerning the definition of the Breit–Wigner amplitudes $\mathcal{A}_{f_2}^{(\tau)}(s)$, $\tau = 0, \parallel, \perp$, see Ref. [141].

Since the experimental data for the $\bar{B}_d^0 \to J/\psi\pi^+\pi^-$ spectrum [141], used for the determination of the unknown parameters in Section 2.5, are given in arbitrary units, we introduce the normalization constants $\mathcal{N}_\pi^q$, $q = \{n, s\}$, that relate the LHCb angular moments to properly normalized ones. This will allow us to adapt the fit results of the $\pi^+\pi^-$ distribution to the $\pi\eta$ and $\bar{K}K$ predictions. For this purpose we use the absolute branching fractions [44]

$$\begin{aligned}\mathcal{B}\left(\bar{B}_d^0 \to J/\psi\pi^+\pi^-\right) &= (4.03 \pm 0.18) \times 10^{-5},\\ \mathcal{B}\left(\bar{B}_s^0 \to J/\psi\pi^+\pi^-\right) &= (2.14 \pm 0.18) \times 10^{-4},\end{aligned} \tag{2.53}$$

and define the strengths $\bar{b}_0^n = \sqrt{\mathcal{N}_\pi^n} b_0^n$ and $\bar{c}_0^s = \sqrt{\mathcal{N}_\pi^s} c_0^s$ with the normalization constants

$$\mathcal{N}_\pi^{n,s} = \frac{\mathcal{B}(\bar{B}_{d/s}^0 \to J/\psi\pi^+\pi^-)\,\Gamma^{\rm tot}(\bar{B}_{d/s}^0)}{N(\bar{B}_{d/s}^0 \to J/\psi\pi^+\pi^-)}. \tag{2.54}$$

For the respective total numbers of signal events in Refs. [141, 142], defined by

$$N(\bar{B}_{d/s}^0 \to J/\psi\pi^+\pi^-) = \sqrt{4\pi}\int \left\langle Y_0^0\left(\bar{B}_{d/s}^0 \to J/\psi\pi^+\pi^-\right)\right\rangle \mathrm{d}\sqrt{s}, \tag{2.55}$$

we find $N(\bar{B}_d^0 \to J/\psi\pi^+\pi^-) = 24080.5 \pm 148$ and $N(\bar{B}_s^0 \to J/\psi\pi^+\pi^-) = 34878 \pm 182$; further, $\Gamma^{\rm tot}(\bar{B}_{d/s}^0) = 1/\tau(\bar{B}_{d/s}^0)$, with $\tau(\bar{B}_d^0) = (1.519 \pm 0.005)\cdot 10^{-12} s$ and $\tau(\bar{B}_s^0) = (1.505 \pm 0.005)\cdot 10^{-12} s$ [44], such that $\Gamma^{\rm tot}(\bar{B}_d^0) = 4.333 \cdot 10^{-13}\,\text{GeV}$ and $\Gamma^{\rm tot}(\bar{B}_s^0) = 4.373 \cdot 10^{-13}\,\text{GeV}$.

2.4.4 $\pi\eta$ partial waves

We employ the flavor relation between the $\bar{B}_d^0$ S-wave amplitudes to the $J/\psi\pi^+\pi^-$ and the $J/\psi\pi^0\eta$ final states that we have derived in Section 2.3, see Eq. (2.27). Given that the $\bar{B}_d^0 \to J/\psi\pi^+\pi^-$ S-wave is indeed proportional to the scalar form factor (in particular, in Section 2.5.1 we will show that not even a linear polynomial is required at the present accuracy of the data [141]), the $\bar{B}_d^0 \to J/\psi\pi^0\eta$ S-wave amplitude will by analogy be proportional to the scalar $\pi\eta$ isovector form factor Eq. (2.46). Both the isoscalar and the isovector meson pairs are generated from a pure $\bar{d}d$ source. The isospin decomposition of the scalar current reads

$$\bar{d}d = -\frac{1}{2}\big(\bar{u}u - \bar{d}d\big) + \frac{1}{2}\big(\bar{u}u + \bar{d}d\big), \tag{2.56}$$

from which we read off the relative strength of the isoscalar to the isovector component, $\eta_0/\eta_1 = -1$. Thus given a known isoscalar S-wave $\mathcal{CF}_0^{(S,I=0)}(s) = X\bar{b}_0^n \Gamma_{\pi\pi}^{n,I=0}(s)$ (where the subtraction/normalization constant $\bar{b}_0^n = \sqrt{\mathcal{N}_\pi} b_0^n$ is related to the fit constant b_0^n introduced in Eq. (2.52)), we can predict the isovector S-wave

$$\mathcal{CF}_0^{(S,I=1)}(s) = -X\bar{b}_0^n \Gamma_{\pi\eta}^{I=1}(s), \tag{2.57}$$

such that the resulting angular moment $\langle Y_0^0\rangle$ or differential decay rate, respectively, is given by

$$\sqrt{4\pi}\langle Y_0^0\rangle_{\bar{B}_d^0 \to J/\psi\pi^0\eta} = \frac{\mathrm{d}\Gamma_{\bar{B}_d^0 \to J/\psi\pi^0\eta}}{\mathrm{d}\sqrt{s}} = \frac{X^3 Y\sqrt{s}}{2m_B}\left|\bar{b}_0^n \Gamma_{\pi\eta}^{I=1}(s)\right|^2. \tag{2.58}$$

The constant $\bar{b}_0^n$ is the same as for the $\pi^+\pi^-$ final state precisely due to the symmetry relation (2.27). Similarly, potential linear terms in s multiplying the scalar form factors would also be symmetry-related for both meson pairs under consideration: as long as the data do not

suggest the necessity to include such a term in the description of the $\bar{B}^0_d \to J/\psi\pi^+\pi^-$ S-wave, it will be negligible also in $\bar{B}^0_d \to J/\psi\pi^0\eta$.

By means of an isospin rotation the $\pi\eta$ form factor Eq. (2.46) likewise describes the transition to a charged $\pi^+\eta$ pair via a $\bar{u}d$ source,

$$\left\langle \pi^+(p_1)\eta(p_2)\,|\bar{u}d|\,0\right\rangle = \sqrt{2}\mathcal{B}_0^{\Delta}\Gamma^{I=1}_{\pi\eta}(s). \tag{2.59}$$

This straightforwardly allows for a prediction of the charged $B^\pm \to J/\psi\pi^\pm\eta$ mode as well, whose differential decay rate $\mathrm{d}\Gamma/\mathrm{d}\sqrt{s}$ differs from the $\bar{B}^0_d$ one, Eq. (2.58) by a factor 2 (except for negligible kinematical replacements due to isospin-violating mass differences).

2.4.5 $\bar{K}K$ partial waves

The prediction of the $\bar{B}^0_d \to J/\psi\pi^0\eta$ spectrum in Section 2.6 relies on the connection to the isoscalar $\pi^+\pi^-$ mode due to chiral symmetry. For the final states involving a $\bar{K}K$ pair we employ in addition the channel coupling between the S-wave pions and kaons to predict the $\bar{B}^0_{d/s} \to J/\psi K^+K^-$ S-waves. Given that the kaons emerge from a clean isoscalar $\bar{s}s$ source, the $\bar{B}^0_s \to J/\psi K^+K^-$ S-wave is purely isoscalar. Aside from the appropriate kinematical replacements it is straightforwardly related to the $\bar{B}^0_s \to J/\psi\pi^+\pi^-$ S-wave and reads

$$\mathcal{CG}^{(s,S)}_c(s) = X\bar{c}^s_0\Gamma^{s,I=0}_{KK}(s), \tag{2.60}$$

where the kaon form factor is defined in Eq. (2.45). Though the $\bar{B}^0_s \to J/\psi K^+K^-$ decay is P-wave dominated, this prediction allows us to calculate the S-wave background to the prominent $\phi(1020)$ resonance. To approximate the P-wave we adopt the LHCb Breit–Wigner parametrization, valid in the mass window $\pm 12\,\mathrm{MeV}$ around the $\phi(1020)$ [185], and find for the angular moment

$$\sqrt{4\pi}\left\langle Y^0_0\right\rangle\Big|^{|\sqrt{s}-m_\phi|\lesssim 12\,\mathrm{MeV}}_{\bar{B}^0_s\to J/\psi K^+K^-} \approx \frac{XY\sqrt{s}}{2m_B}\left(X^2\left|\bar{c}^s_0\Gamma^{s,I=0}_{KK}\right|^2 + \sum_\tau\left|\alpha^\phi_\tau\mathcal{A}^{(\tau)}_\phi(s)\right|^2\right). \tag{2.61}$$

On the contrary the $\bar{B}^0_d \to J/\psi\{K^+K^-, \bar{K}^0K^0\}$ decays are dominated by the S-wave. In the $\bar{K}K$ P-wave there are contributions from the ρ and ω resonances, which, in principle, can be related to the $\pi\pi$ P-wave. These resonances peak below the $\bar{K}K$ threshold, however, and their contributions are expected to be rather small above. The contribution from the ϕ resonance that dominates the $\bar{K}K$ P-wave above threshold is now suppressed by the OZI rule, as we are effectively dealing with a $\bar{d}d$ source. The suppression of the P-wave (and the dominance of the S-wave) in this decay has indeed been confirmed experimentally in Ref. [186]. Hence, we here include only the S-wave component, and make no attempt to consider $\bar{K}K$ P-wave amplitudes. Deriving the S-wave amplitudes requires both the flavor relation that links the isospin-0 to the isospin-1 meson pairs, and the coupled-channel relations between the kaons and the respective light pseudoscalars. According to Eq. (2.56) now both the isoscalar and isovector S-wave components contribute, with known relative strengths $\eta_0/\eta_1 = -1$ or $+1$ for charged or neutral kaon systems, respectively, i.e. the S-wave amplitude reads

$$\begin{aligned}\mathcal{CG}^{(n,S)}_c(s) &= X\bar{b}^n_0\big(\Gamma^{n,I=0}_{KK}(s) - \Gamma^{I=1}_{KK}(s)\big),\\ \mathcal{CG}^{(n,S)}_n(s) &= X\bar{b}^n_0\big(\Gamma^{n,I=0}_{KK}(s) + \Gamma^{I=1}_{KK}(s)\big),\end{aligned} \tag{2.62}$$

with the kaon form factors defined in Eqs. (2.45) and (2.46). The resulting angular moments

$\langle Y_0^0\rangle$ or differential decay rates, respectively, read

$$\sqrt{4\pi}\langle Y_0^0\rangle_{\bar{B}^0_d\to J/\psi K^+K^-} = \frac{X^3 Y\sqrt{s}}{2m_B}\left|\bar{b}_0^n\left(\Gamma_{KK}^{n,I=0}(s) - \Gamma_{KK}^{I=1}(s)\right)\right|^2,$$
$$\sqrt{4\pi}\langle Y_0^0\rangle_{\bar{B}^0_d\to J/\psi \bar{K}^0K^0} = \frac{X^3 Y\sqrt{s}}{2m_B}\left|\bar{b}_0^n\left(\Gamma_{KK}^{n,I=0}(s) + \Gamma_{KK}^{I=1}(s)\right)\right|^2. \tag{2.63}$$

Similarly to the $\bar{B}^0_{d/s} \to J/\psi\pi^+\pi^-$ distributions the $\bar{B}^0_{d/s} \to J/\psi K^+K^-$ angular moments provided by LHCb are not properly normalized, which we have to be aware of when we compare to these data or extract the strength of the $\phi(1020)$ Breit–Wigner amplitude in Section 2.8.2. We therefore define the normalization constants

$$\mathcal{N}_K^{n,s} = \frac{\mathcal{B}(\bar{B}^0_{d/s} \to J/\psi K^+K^-)\,\Gamma^{\rm tot}(\bar{B}^0_{d/s})}{N(\bar{B}^0_{d/s} \to J/\psi K^+K^-)}, \tag{2.64}$$

such that

$$\langle Y_0^0\rangle_{\bar{B}^0_{d/s}\to J/\psi K^+K^-} = \mathcal{N}_K^{n,s}\langle Y_0^0\rangle^{\rm LHCb}_{\bar{B}^0_{d/s}\to J/\psi K^+K^-}. \tag{2.65}$$

The absolute branching fractions are given by $\mathcal{B}\left(\bar{B}^0_s \to J/\psi K^+K^-\right) = (7.9 \pm 0.7)\times 10^{-4}$ and $\mathcal{B}\left(\bar{B}^0_d \to J/\psi K^+K^-\right) = (2.6 \pm 0.4)\times 10^{-6}$ [44]. The total number of events $N(\bar{B}^0_s \to J/\psi K^+K^-)$ is however not determined as in Eq. (2.55) since no data for the efficiency-corrected angular moments in Ref. [185] are available. We therefore calculate the normalization constant $\mathcal{N}_K^s$ by taking the published expected signal yield $N_{\rm exp}(\bar{B}^0_s \to J/\psi K^+K^-) = 19195 \pm 150$; in analogy we use $N_{\rm exp}(\bar{B}^0_d \to J/\psi K^+K^-) = 228 \pm 27$.

2.5 Final-state interactions in $\bar{B}^0_{d/s} \to J/\psi\pi\pi$

2.5.1 Fits to the LHCb data I: $\bar{B}^0_d \to J/\psi\pi^+\pi^-$

We fit the angular moments $\langle Y_0^0\rangle$ and $\langle Y_2^0\rangle$, Eq. (2.52), simultaneously. Taking up the discussion of Section 2.4, our basic fit, FIT I, includes three fit parameters (to be compared to 14 free parameters in the Breit–Wigner parametrization used in the LHCb analysis, see below): the normalization factors for the S-wave (b_0^n) and for two P-waves $f_0^{(P)}$ and $f_\parallel^{(P)}$ ($a_0, a_\parallel$). (We find that including the $\tau = \perp$ P-wave amplitude practically does not change the χ^2, i.e. $a_\perp$ is a redundant parameter.) In the basic fit only S- and P-waves are considered. Beyond that, we study the relevance of certain corrections: in FIT II we use again the same three parameters as in FIT I, but in addition we include the D-wave contributions, fixed to their strengths as determined by LHCb. To further improve FIT II, supplemental linear terms ($b_0', a_0', a_\parallel'$—cf. Eq. (2.52)) are allowed in FIT III. Performing FIT III we find that two of the slope parameters, the linear non-strange S-wave term (b_0') and the $\tau = \parallel$ P-wave slope ($a_\parallel'$), yield no significant improvement of the fits; their values are compatible with zero within uncertainties. We thus fix them to zero, and in FIT III only the four parameters b_0^n, a_0, $a_\parallel$, and a_0' are varied. Furthermore, the effect of an inclusion of a strange S-wave component is tested. Its strength is found to be compatible with zero, justifying its omission.

Note that the scalar pion form factors depend on the normalizations of both the pion and kaon form factors. While the normalizations in the case of the pion form factor are known quite precisely, there are considerable uncertainties for the kaon form factor normalizations, having an impact on the shapes of both pion form factors, see Section 1.3.4. The non-strange kaon normalization $\Gamma_{KK}^{n,I=0}(0)$ is limited to the range $(0.4\ldots0.6)$ if results for $N_f = 2+1$ lattice

simulations are used. In our fits we fix the value to $\Gamma^{n,I=0}_{KK}(0) = 0.5$, which is compatible with the current algebra result (and also with the $N_f = 2+1+1$ lattice simulation results). The effect from a variation of $\Gamma^{n,I=0}_{KK}(0)$ in the allowed interval shows up only in the second decimal place of the χ^2/ndf.

The fitted coefficients and the resulting χ^2/ndf, referring to Eq. (2.52), are listed in Table 2.1 (these parameters still ought to be multiplied by the factor $\sqrt{\mathcal{N}_\pi}$, in particular when adopting these results for the prediction of other final states, see the discussion at the end of Section 2.4.3). The large uncertainties can be traced back to the correlations between the fit parameters, especially present in FIT III. For a comparison to the LHCb fit, we insert their fit results (best model) into our definition of the χ^2. In more specific terms this means that we do *not* compare to the χ^2 published in Ref. [141], for which the full energy range up to $\sqrt{s} = 2.1\,\text{GeV}$ is fitted with 34 parameters and the data of all angular moments $\langle Y^0_i \rangle$ for $i = 0, \ldots, 5$ are included, but we calculate the χ^2 in the region we use in our fits, i.e. including data up to $\sqrt{s} = 1.02\,\text{GeV}$ and the angular moments $\langle Y^0_0 \rangle$ and $\langle Y^0_2 \rangle$ only. We obtain $\chi^2_{\text{LHCb}}/\text{ndf} = 2.08$. In this limited energy range the Breit–Wigner description, including the $f_0(500)$, $\rho(770)$ and $\omega(782)$, requires 14 fit constants, while we have three (FIT I, II) or four (FIT III) free parameters and find $\chi^2/\text{ndf} = 2.0$ (FIT I), $\chi^2/\text{ndf} = 1.5$ (FIT II) and $\chi^2/\text{ndf} = 1.3$ (FIT III). The calculated angular moments for the three fit models in comparison to the data are shown in Figure 2.3.

Probably the most striking feature of our solution is the pronounced effect of the ω that leads to the higher peak in Figure 2.3. As mentioned above, this isospin-violating contribution is fixed completely from an analysis of the pion vector form factor, however, its appearance here is utterly different, since the coupling strength is multiplied by a factor of -3. This not only enhances the impact of the ω on the amplitude level to about 50%, but also implies that the change in phase of the signal is visible a lot more clearly: while in case of the vector form factor the ω amplitude leads to an enhancement on the ρ-peak and some depletion on the right wing, forming a moderate distortion of the line shape, here we obtain a depletion on the ρ-peak accompanied by an enhancement on the right wing. The origin of this effect is illustrated in Figure 2.4, taken from Ref. [188]. The thick, red solid line shows the pion vector form factor, related to the electromagnetic current, from which the strength of the ρ–ω mixing is fixed in a fit to the data. Inverting the sign of the mixing amplitude yields the dashed, magenta line. The narrow, sharp ω-type peak that is already visible in the that curve is enhanced by a factor of 3 in the black solid line, leading to a similar signal as the one depicted in Figure 2.3. While the current data do not show the ω peak clearly, a small shape variation due to the ρ–ω interference is better seen in Ref. [187], where a finer binning is used. The ρ–ω mixing strength obtained from a fit in that reference is consistent with the strength we obtain in a parameter-free manner. Nonetheless, improved experimental data are called for, since an experimental confirmation of the ω effect on $\bar{B}^0_d \to J/\psi\pi^+\pi^-$ would allow one to establish that the $\bar{B}^0_d$ decay indeed provides a rather clean $\bar{d}d$ source.

A key feature of the formalism employed here is its correct description of the S-wave. Figure 2.5 shows the comparison of the S-wave amplitude strength of the LHCb Breit–Wigner parametrization with the ones obtained in FIT I–III, and in Figure 2.6 the corresponding phases are compared. In the elastic region, the phase of the non-strange scalar form factor $\delta_{\Gamma^n} = \arg(\Gamma^{n,I=0}_{\pi\pi})$ coincides with the $\pi\pi$ phase shift δ^0_0 that we use as input for the Omnès matrix, in accordance with Watson's theorem. Right above the $K\bar{K}$ threshold, δ_{Γ^n} drops quickly, which causes the dip in the region of the $f_0(980)$, visible in the modulus of the amplitudes as well as the non-Breit–Wigner bump structure in the $f_0(500)$ region. We find that the phase due to a Breit–Wigner parametrization largely differs from the dispersive solution, indicating that parametrizations of such kind are not well suited for studies of CP violation in heavy-meson decays.

Note that in the analysis of Ref. [187] the $f_0(500)$ is modeled not by a Breit–Wigner func-

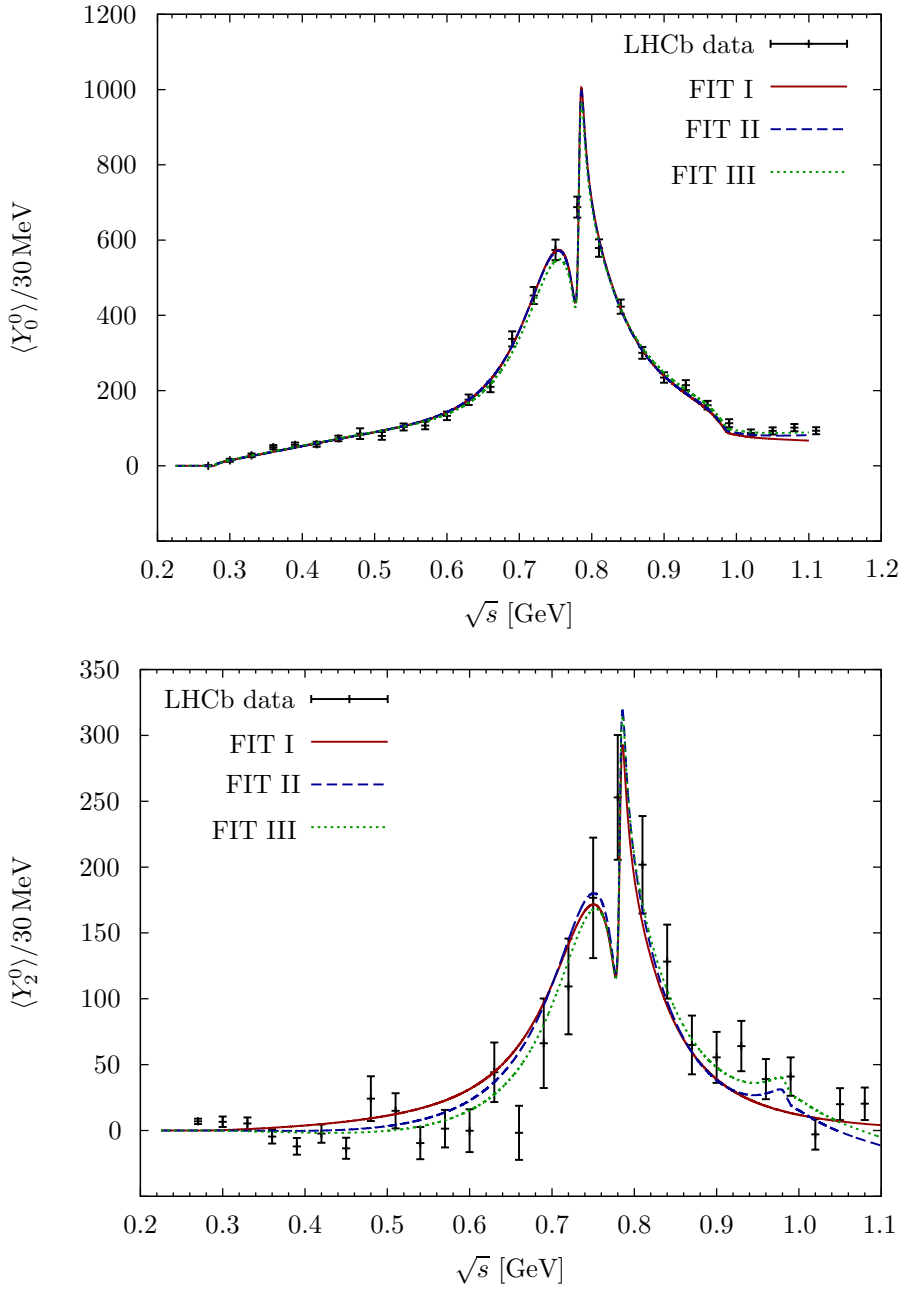

Figure 2.3: $\langle Y_0^0 \rangle$ (top) simultaneously fitted with $\langle Y_2^0 \rangle$ (bottom), using three parameters without D-wave contribution (FIT I, red, solid), and improving step by step by adding a Breit–Wigner-parametrized D-wave contribution (FIT II, blue, dashed) and by allowing for four free parameters, also supplemented by the D-wave contribution (FIT III, green, dotted).

	χ^2/ndf	$\lvert b_0^n\rvert\,[\mathrm{GeV}^{-\frac{7}{2}}]$	$\lvert a_0\rvert\,[\mathrm{GeV}^{-\frac{3}{2}}]$	$\lvert a_\parallel\rvert\,[\mathrm{GeV}^{-\frac{5}{2}}]$	$a_0'\,[\mathrm{GeV}^{-\frac{5}{2}}]$
FIT I	1.97	$10.3^{+1.5}_{-1.8}$	$46.5^{+6.0}_{-6.8}$	$51.8^{+9.0}_{-11.0}$	–
FIT II	1.54	$10.3^{+1.5}_{-1.8}$	$47.6^{+5.8}_{-6.6}$	$49.5^{+9.4}_{-11.7}$	–
FIT III	1.32	$10.6^{+1.5}_{-1.8}$	$37.7^{+20.3}_{-21.3}$	$48.2^{+9.8}_{-12.4}$	$0.4^{+2.4}_{-0.7}$

Table 2.1: Resulting fit parameters and χ^2/ndf for the various fit configurations FIT I–III for the $\bar{B}^0_d \to J/\psi\pi^+\pi^-$ decay.

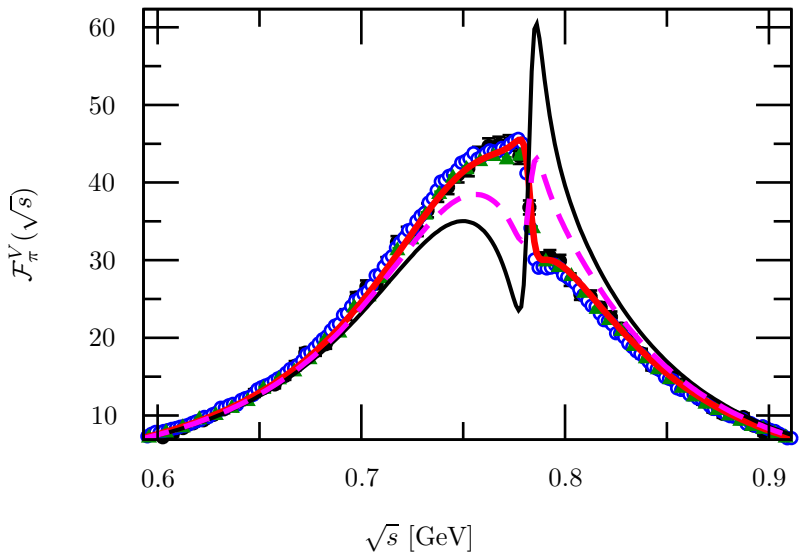

Figure 2.4: Illustration of the ρ–ω mixing strength in $\bar{B}^0 \to J/\psi\pi^+\pi^-$, emerging from the mixing in the pion vector form factor $\mathcal{F}_\pi^V(\sqrt{s})$. The figure shows a fit to data of the pion vector form factor [87,88] including mixing (red, thick solid), with the sign flip in the mixing amplitude (magenta, dashed), and with the mixing amplitude times -3 (black, thin solid). The figure is taken from Ref. [188].

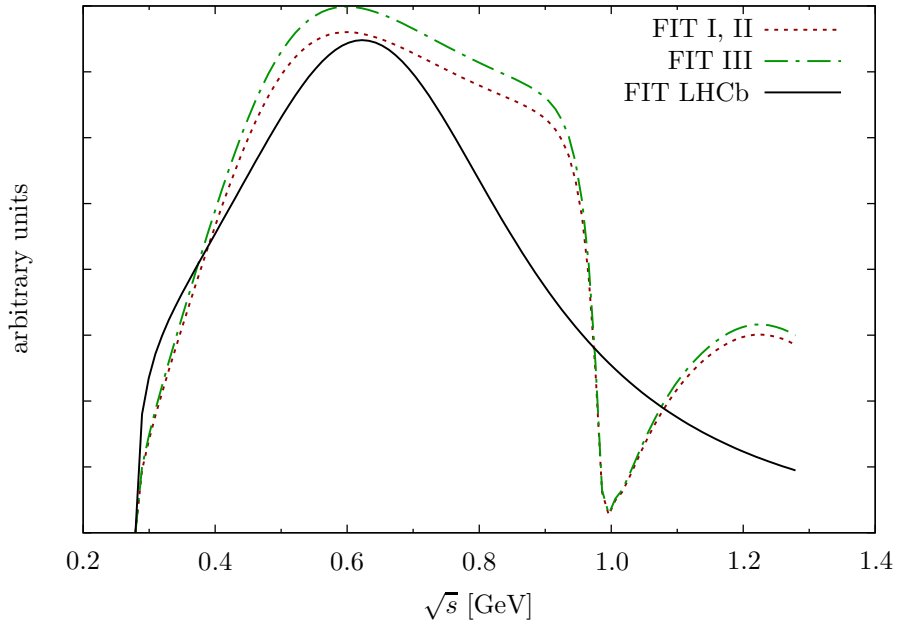

Figure 2.5: Comparison of the S-wave amplitude strength obtained in the LHCb and in our fits, respectively: the S-wave contribution to the decay rate for the three fit configurations FIT I–III is depicted together with the LHCb outcome.

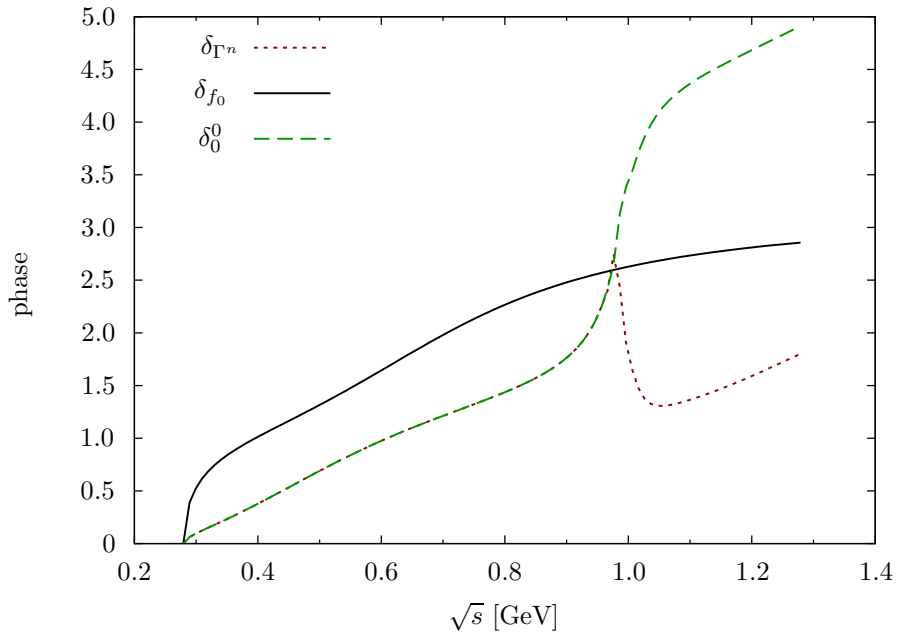

Figure 2.6: The phases of the non-strange scalar form factor δ_{Γ^n} (equal to the $\pi\pi$ S-wave phase shift δ_0^0 below the $K\bar{K}$ threshold) are compared to the S-wave phase δ_{f_0} extracted from the LHCb analysis.

tion, but by the theoretically better motivated parametrization of Ref. [189]. In this work, higher resonances are included by multiplying S-matrix elements. While this procedure preserves unitarity, it produces terms at odds with any microscopic description of the coupled $\pi\pi$–$K\bar{K}$ system. As such also this approach introduces uncontrolled theoretical uncertainties into the analysis. The only stringently model-independent way to include hadronic final-state interactions is via dispersion theory.

2.5.2 Fits to the LHCb data II: $\bar{B}^0_s \to J/\psi\pi^+\pi^-$

The $\bar{B}^0_s \to J/\psi\pi^+\pi^-$ distribution in the region up to roughly 1 GeV is clearly dominated by the $f_0(980)$. We therefore describe the data with the strange S-wave component only, using a constant subtraction polynomial (c_0^s). The only non-zero contribution to the fit thus comes from $\langle Y_0^0\rangle$. Fitting the data up to $\sqrt{s} = 1.05\ (1.02)\,\text{GeV}$ yields $\chi^2/\text{ndf} = 2.2\ (1.8)$ and for both fit scenarios $c_0^s = (16.8 \pm 0.4)\,\text{GeV}^{-\frac{7}{2}}$. In analogy to the $\bar{B}^0_d$ decay we also perform the fit including the D-wave parametrization of the LHCb analysis [142]. This yields an additional non-zero contribution to $\langle Y_2^0\rangle$ due to the S–D-wave interference, which is fitted simultaneously with $\langle Y_0^0\rangle$. Further, the influence of a linear subtraction polynomial for the strange S-wave is tested. However, none of these corrections exhibits a considerable improvement.

In the LHCb analysis the full energy range, $\sqrt{s} \leq 2.1\,\text{GeV}$, is fitted with 22 (24) parameters for Solution I (II). Confining to the region we examine in our fit and considering the $f_0(980)$ resonance only, the number of fit parameters reduces to four (six), and we calculate $\chi^2_{\text{LHCb}}/\text{ndf} = 0.76\,(0.82)$, when using our definition of the χ^2.

The strange scalar form factor, or the $f_0(980)$ peak in the dispersive formalism, depends crucially on the $\pi\pi \to K\bar{K}$ S-wave transition amplitude, which is not as accurately known as elastic $\pi\pi$ scattering (and even contains subtleties as non-negligible isospin breaking effects due to the different thresholds of charged and neutral kaons, see e.g. Ref. [190]). As there are no error bands available for the Omnès matrix (or the various input quantities), to estimate the theoretical uncertainty we use and compare the fits resulting from the two different coupled-channel T-matrices described in Section 2.4. A minimization of the χ^2 using the modified Omnès solution based on Ref. [127] yields $\chi^2/\text{ndf} = 3.4$ and $c_0^s = (18.3 \pm 0.5)\,\text{GeV}^{-\frac{7}{2}}$ or $\chi^2/\text{ndf} = 2.4$ and $c_0^s = (18.2 \pm 0.5)\,\text{GeV}^{-\frac{7}{2}}$ when fitting the data up to $\sqrt{s} = 1.05\,\text{GeV}$ or $\sqrt{s} = 1.02\,\text{GeV}$, respectively.[6] The resulting $\langle Y_0^0\rangle$ curves for both fits, using the phase input from the Bern [153, 154] and Orsay [37] groups (B+O), as well the one of Ref. [127] (DP), are presented in Figure 2.7. Furthermore we show the phase shifts and the phases of the strange form factor for both phase inputs in Figure 2.8 and compare to the LHCb phase due to Solution II (with $f_0(980)$ and a non-resonant S-wave contribution) as well as Solution I ($f_0(980)$ parametrization only). While the latter phase has a negative slope for $s \lesssim 1\,\text{GeV}^2$, which does not agree with the known phase shift, the phase extracted in Solution II is remarkably close to both the Bern and Madrid phase motions.

2.6 $\bar{B}^0_d \to J/\psi\pi\eta$: a flavor related prediction

The relative strength between the production amplitudes of different isospin is known. Since we have shown in Section 2.5.1 that the dispersive formalism fits the data for the $\bar{B}^0_d \to J/\psi\pi^+\pi^-$ mode very well and the fit parameters were determined, we can make predictions for the $\bar{B}^0_d \to J/\psi\pi^0\eta$ (and the $B^\pm \to J/\psi\pi^\pm\eta$) distribution. The maximal range of this assumed dominance

[6] A similar procedure for the $\bar{B}^0_d$ decay has a rather small effect since the S-wave is not dominant in that case, and the difference of the P-wave phase of Refs. [36, 153, 154] is quite small (the S- or P-wave phase modification yields, in the most perceptible cases, a 4% correction of the χ^2).

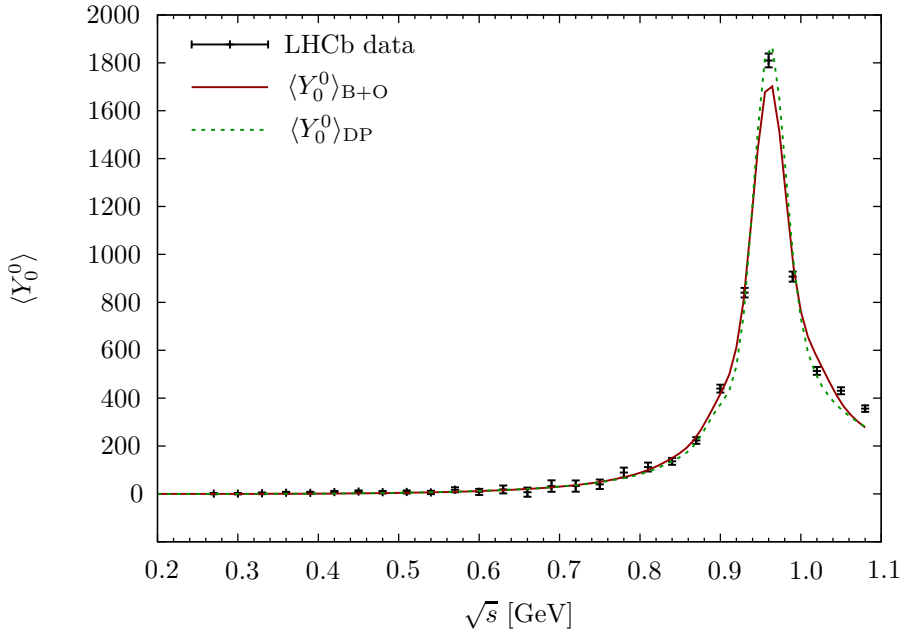

Figure 2.7: $\langle Y_0^0\rangle$ fitted using the strange S-wave with constant subtraction polynomial for two different phase inputs (red, solid: B+O input [37,153,154], green, dotted: DP input [127], based on the Madrid–Kraków analysis [36]).

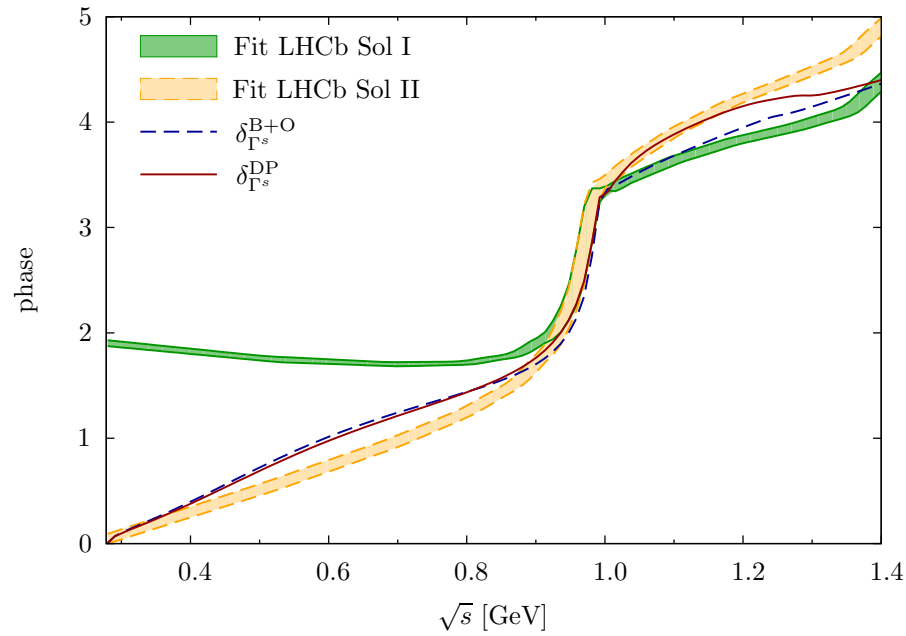

Figure 2.8: Comparison of the phase of the strange scalar pion form factor for the B+O (blue, dashed) and DP (red, solid) input, respectively, with the S-wave phase extracted from the LHCb analysis (Solution I and II, shown with error bands).

is estimated by predicting the $\pi^0\eta$ D-wave as well. Note that the $\pi\eta$ P-wave has exotic quantum numbers, such that final-state-interaction effects are supposed to be negligible. Therefore we expect the S-wave to dominate the spectrum up to the onset of the D-wave, with a significant contribution in the region of the $a_2(1320)$ resonance.

Two different values are obtained for b_0^n, namely (a) $b_0^n = 10.3\,\mathrm{GeV}^{-7/2}$ corresponding to a fit with only constant subtraction polynomials for S- and P-waves, and (b) $b_0^n = 10.6\,\mathrm{GeV}^{-7/2}$, corresponding to a fit with a linear (in s) contribution to the P-wave polynomial as well as a D-wave contribution, which has an effect on the $\pi\pi$ S-wave [141]. We therefore obtain $\bar{b}_0^n = 2.77 \cdot 10^{-10}\,\mathrm{GeV}^{-3}$ and $\bar{b}_0^n = 2.85 \cdot 10^{-10}\,\mathrm{GeV}^{-3}$, respectively, using Eq. (2.54).

In Figure 2.9 (top panel) the predicted differential decay rate $\mathrm{d}\Gamma/\mathrm{d}\sqrt{s}$ for $\bar{B}^0_d \to J/\psi\pi^0\eta$ is depicted. The distribution is shown for three different input phases $\delta_{12} = 90°, 110°, 125°$, limited to an interval compatible with constraints discussed in Ref. [140]. We see that the dependence on δ_{12}, and hence on details of the $\pi\eta$ interaction, is strong, and completely overwhelms the uncertainty due to the production strength as fixed from the corresponding $\pi^+\pi^-$ channel. In order to provide a clearer representation, we refrain from showing uncertainty bands due to the $I = 1$ $\pi\eta$ and $\bar{K}K$ form factor normalizations calculated at next-to-leading order according to Eq. (2.50). We choose the isovector form factor normalizations in the upper allowed range. This corresponds to similar low-energy constants as we used for the isoscalar form factor normalizations, though not exactly the same, as we use updated lattice results anyway. Furthermore, the isovector form factor normalizations depend on additional low-energy constants.

Our conclusion is that a measurement of this decay channel will provide important information on the final-state interactions of the $\pi\eta$ S-wave system, and in particular the $a_0(980)$ resonance, which dominates this partial wave in the energy range around 1 GeV.

To further substantiate the assumed S-wave dominance, we estimate the $\pi\eta$ D-wave background, which should become significant in the region of the $a_2(1320)$ resonance. We model the a_2 by a simple Breit–Wigner shape; its coupling strength is related to that of the $f_2(1270)$ by $SU(3)$ symmetry, which decays to $\pi^+\pi^-$ and hence is determined in the $\bar{B}^0_d \to J/\psi\pi^+\pi^-$ analysis of Ref. [141]. In the determination of the a_2 strength we employ two ratios: the ratio between the isovector and the isoscalar contributions, Eq. (2.56), that yields a relative minus sign between the $\bar{B}^0_d \to J/\psi f_2$ and the $\bar{B}^0_d \to J/\psi a_2$ couplings, as well as the relative strength between the $f_2 \to \pi^+\pi^-$ and the $a_2^0 \to \pi^0\eta$ couplings. The coupling of a tensor meson to a pseudoscalar pair is obtained from the interaction Lagrangian [129, 191]

$$\mathcal{L}_{TPP} = g_T \langle T_{\mu\nu}\{u^\mu, u^\nu\}\rangle, \tag{2.66}$$

where $\langle . \rangle$ is the trace in flavor space, $T_{\mu\nu}$ contains the a_2 and f_2 mesons and $u_\mu = i(u^\dagger\partial_\mu u - u\partial_\mu u^\dagger)$ the pseudoscalars. As we are interested in the non-strange part of the Lagrangian only, we use for simplicity the $SU(2)$ representations

$$T_{\mu\nu} = \begin{pmatrix} \frac{a_2^0}{\sqrt{2}} + \frac{f_2}{\sqrt{6}} & a_2^+ \\ a_2^- & -\frac{a_2^0}{\sqrt{2}} + \frac{f_2}{\sqrt{6}} \end{pmatrix}_{\mu\nu}, \quad u = \exp\left(\frac{i\phi}{2F_\pi}\right), \quad \phi = \begin{pmatrix} \pi^0 + \frac{\eta}{\sqrt{3}} & \sqrt{2}\pi^+ \\ \sqrt{2}\pi^- & -\pi^0 + \frac{\eta}{\sqrt{3}} \end{pmatrix}, \tag{2.67}$$

where $F_\pi = 92.2\,\mathrm{MeV}$ denotes the pion decay constant. The coupling constant $g_T = 28\,\mathrm{MeV}$ can be obtained consistently from both the $f_2 \to \pi\pi$ [191] and the $a_2 \to \pi\eta$ decay [129], confirming $SU(3)$ symmetry. From the Lagrangian we can finally read off the relative strength of the coupling to $\pi\pi$ and $\pi\eta$ and find $g^2_{a_2\pi\eta} = g^2_{f_2\pi\pi}/3$.

The right panel of Figure 2.9 shows the predicted D-wave. Compared to the S-wave contribution shown in the left panel the D-wave is negligible in the energy region we consider here, justifying the assumed S-wave dominance.

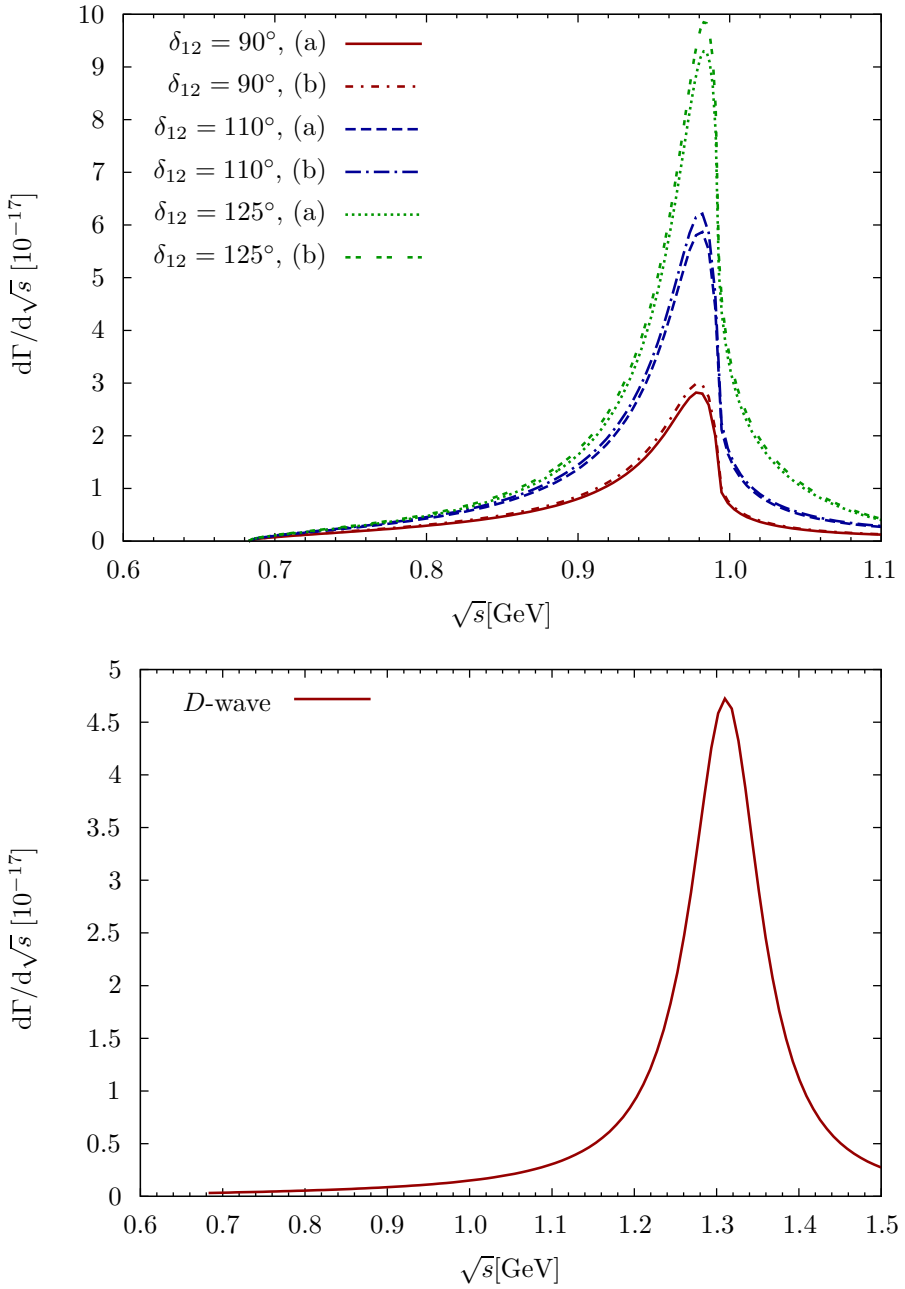

Figure 2.9: Top panel: $\mathrm{d}\Gamma/\mathrm{d}\sqrt{s}$ for $\bar{B}_d^0 \to J/\psi\pi^0\eta$. The distribution is plotted for three different input phases $\delta_{12} = 90°, 110°, 125°$ and two normalization constants $\bar{b}_0^n$ due to the fits (a) and (b). The bottom panel shows the predicted D-wave contribution to $\mathrm{d}\Gamma/\mathrm{d}\sqrt{s}$ (note the different ranges of the axes).

Finally we quote the branching fraction for $\bar{B}^0_d \to J/\psi\pi^0\eta$ from the $a_0(980)$ region. We integrate the spectrum in the region of the $a_0(980)$ and find

$$\begin{aligned}\mathcal{B}\left(\bar{B}^0_d \to J/\psi\pi^0\eta\right)\Big|_{\sqrt{s}\leq 1.1\,\mathrm{GeV}} &= \frac{1}{\Gamma^{\mathrm{tot}}(\bar{B}^0_d)}\int_{M_\pi+M_\eta}^{1.1\,\mathrm{GeV}} \frac{\mathrm{d}\Gamma(\bar{B}^0_d \to J/\psi\pi^0\eta)}{\mathrm{d}\sqrt{s}}\mathrm{d}\sqrt{s} \\ &= \begin{cases} (6.0\ldots 6.4)\times 10^{-6} & \text{for} \quad \delta_{12} = 90^\circ, \\ (1.1\ldots 1.2)\times 10^{-5} & \text{for} \quad \delta_{12} = 110^\circ, \\ (1.6\ldots 1.7)\times 10^{-5} & \text{for} \quad \delta_{12} = 125^\circ, \end{cases} \end{aligned} \tag{2.68}$$

where the lower and upper values of the given ranges correspond to the $\bar{b}^n_0$ fit results (a) and (b), respectively. We can compare our results with those of Ref. [192]. Even if this latter work predicts the $\bar{B}^0_d \to J/\psi\pi^0\eta$ differential decay width without absolute normalization, our distribution can be seen to be narrower. We further note that the numbers in Eq. (2.68) are around 3 to 8 times larger than the value $(2.2 \pm 0.2)\times 10^{-6}$ estimated in Ref. [192], which however only refers to the $a_0(980)$ contribution. To compute it, the authors remove a smooth but large background from the differential decay. Hence, it is quite natural to obtain a larger value for this branching ratio than the one quoted in Ref. [192].

The corresponding numbers for $\mathcal{B}(B^\pm \to J/\psi\pi^\pm\eta)\big|_{\sqrt{s}\leq 1.1\,\mathrm{GeV}}$ are obtained from Eq. (2.68) by multiplying the $\bar{B}^0_d$ branching fractions with a factor of 2.15, taking into account the relative isospin factor of 2 and a small correction due to the different lifetimes of $B^\pm$ and $\bar{B}^0_d$ [44].

2.7 Estimates for the $\pi\eta$ P-waves and left-hand cuts

Developing the formalism for the $\bar{B}^0_d \to J/\psi\pi^0\eta$ prediction in the previous sections involves two assumptions: the absence of considerable crossed-channel effects on the one hand and the suppression of P- and higher waves (up to the energy region around 1 GeV) on the other hand. We now aim for a quantification of our arguments for the treatment of the S-wave in terms of scalar form factors and its dominance. For this purpose we demonstrate in Section 2.7.1 the generic chiral suppression of the $\pi\eta$ P-wave production vertex, and provide explicit calculations of P- and D-wave contributions that are generated by potential t- and u-channel resonances in Sections 2.7.2 and 2.7.3. Besides justifying the neglect of P- and higher waves these calculations are supposed to theoretically assure the absence of crossed-channel effects.

Although in the $\bar{B}^0_d \to J/\psi\pi^+\pi^-$ case the absence of left-hand-cut structures is confirmed by the experimental analysis, in Section 2.7.4 we rerun the calculation of the B^* t- and u-channel exchange in that mode as well, in analogy to what we do for the $\pi^0\eta$ final state.

2.7.1 Chiral Lagrangians

In order to generate a non-vanishing $\pi\eta$ P-wave contribution, the chiral Lagrangian that was constructed in Section 2.3 needs to involve an explicit symmetry-breaking mass term $\propto \chi_\pm = u^\dagger\chi u^\dagger \pm u\chi^\dagger u$, where $\chi = 2\mathcal{B}_0\,\mathrm{diag}(m_u, m_d, m_s)$ is proportional to the quark mass matrix. The lowest-order chiral Lagrangian that can produce a $\pi\eta$ pair in a P-wave is

$$\mathcal{L}_3 = \frac{g_3}{8}t^\dagger_L u^\dagger B\,\psi^\mu\langle\chi_+\,u_\mu\rangle + \frac{g_3'}{16}t^\dagger_L u^\dagger u_\mu B\,\psi^\mu\langle\chi_-\rangle + \mathrm{h.c.}. \tag{2.69}$$

An expansion of $\mathcal{L}_3$ to quadratic order in the light fields yields

$$\mathcal{L}_3^{\phi^2} = \frac{i(M_K^2 - M_\pi^2)}{4\sqrt{3}F_\pi^2}\left[(g_3+g_3')\partial_\mu(\pi^0\eta) + (-g_3+g_3')(\partial_\mu\pi^0\eta - \partial_\mu\eta\pi^0)\right] B_d\,\psi^\mu + \ldots + \mathrm{h.c.}, \tag{2.70}$$

where the ellipsis denotes terms involving other meson pairs than $\pi\eta$. The last term contributes to a P-wave amplitude, which we can compare to the S-wave:

$$\mathcal{M}_{3,P} = \frac{(g_3 - g_3')(M_K^2 - M_\pi^2)}{4\sqrt{3}F_\pi^2}\,(p_1^\mu - p_2^\mu)\epsilon_\mu^*\,,$$
$$\mathcal{M}_{1,S} = \frac{g_1 - (g_3 + g_3')(M_K^2 - M_\pi^2)}{4\sqrt{3}F_\pi^2}\,(p_1^\mu + p_2^\mu)\epsilon_\mu^*\,. \tag{2.71}$$

We express the matrix elements in the basis of the momentum vectors Eq. (2.5), using

$$P^\mu = (p_1^\mu + p_2^\mu) = \frac{P\cdot p_\psi}{m_\psi^2}\,p_\psi^\mu + P_{(0)}^\mu,$$
$$Q^\mu = (p_1^\mu - p_2^\mu) = \frac{Q\cdot p_\psi}{m_\psi^2}\,p_\psi^\mu + \left(\frac{Y\,(P\cdot p_\psi)}{X}\cos\theta_\eta - \frac{M_\eta^2 - M_\pi^2}{s}\right)P_{(0)}^\mu + Q_\parallel^\mu. \tag{2.72}$$

A natural order of magnitude estimate for the ratio of the chiral coupling constants is

$$\frac{g_3 - g_3'}{g_1} \sim \frac{1}{\Lambda^2}, \qquad \Lambda \simeq 4\pi F_\pi \simeq 1\,\text{GeV}. \tag{2.73}$$

Putting pieces together, we estimate the P-wave-to-S-wave ratio in the amplitude $\mathcal{F}_0$

$$\frac{\mathcal{F}_0^{(P)}(s)}{\mathcal{F}_0^{(S)}(s)} = \frac{(M_K^2 - M_\pi^2)\,Y(P\cdot p_\psi)}{\sqrt{3}\,\Lambda^2 X} + \ldots, \tag{2.74}$$

and replacing the kinematic functions X, Y, and $P\cdot p_\psi = (m_B^2 - s - m_\psi^2)/2$, we arrive at

$$\frac{\mathcal{F}_0^{(P)}(s)}{\mathcal{F}_0^{(S)}(s)} = \frac{(M_K^2 - M_\pi^2)}{\sqrt{3}\,\Lambda^2}\,\frac{\lambda^{1/2}(s, M_\eta^2, M_\pi^2)}{s} + \ldots, \tag{2.75}$$

where we have neglected terms of higher order in the chiral expansion.

While this is derived from a chiral Lagrangian, it is plausible that the chiral estimate for the P-wave should be valid up to $\sqrt{s} \simeq 1\,\text{GeV}$ due to the absence of final-state interactions. Since the final-state interactions for the S-wave increase its value significantly, we can derive an upper bound for the ratio from (2.75),

$$|\mathcal{F}_0^{(P)}(s)/\mathcal{F}_0^{(S)}(s)| \lesssim 0.05, \tag{2.76}$$

which should be valid in the region $\sqrt{s} \leq 1\,\text{GeV}$.

It is obvious from Eqs. (2.71) and (2.72) that the Lagrangian $\mathcal{L}_3$ also produces a P-wave in the transversity form factor $\mathcal{F}_\parallel$. Just for completeness, we in addition show a Lagrangian term that generates a P-wave in the remaining form factor $\mathcal{F}_\perp$:

$$\mathcal{L}_{4\perp} = \frac{g_{4\perp}}{8} t_L^\dagger\, u^\dagger\, \epsilon^{\mu\nu\alpha\beta} u_\mu \nabla_\alpha B\, \psi_\beta \langle \chi_+ u_\nu \rangle. \tag{2.77}$$

This also involves an explicit symmetry-breaking mass term, however, as indicated by the notation, it is of higher chiral order than the terms in Eq. (2.69).

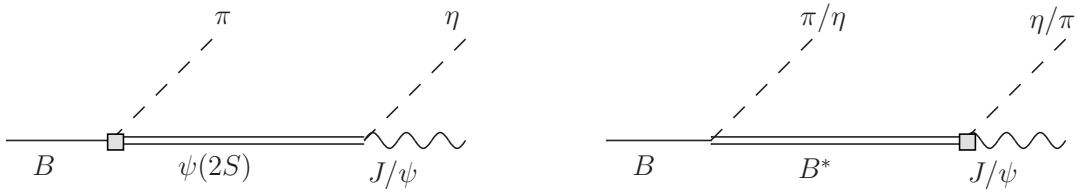

Figure 2.10: We depict the t-channel $\psi(2S)$ exchange diagram (left panel) and the t/u-channel diagrams for a B^* exchange (right panel). The weak decay vertex is marked by a gray square in both cases. Note that the u-channel $\psi(2S)$ exchange is negligible due to the isospin suppression of the decay $\psi(2S) \to J/\psi\pi^0$.

2.7.2 $\psi(2S)$-exchange

We calculate the contribution of t-channel exchange of the $\psi(2S) \equiv \psi'$ resonance to the decay amplitude $\bar{B}^0_d(p_B) \to J/\psi(p_\psi)\pi^0(p_1)\eta(p_2)$ as depicted in Figure 2.10 (left panel). We write the vertex for $\bar{B}^0_d(p_B) \to \psi'(q)\pi^0(p_1)$ in terms of an effective coupling constant ζ as

$$\frac{G_F}{\sqrt{2}} V_{cb}V^*_{cd} f_\psi m_\psi \, \zeta \, (p_B + p_1)_\mu \epsilon^{\mu *}(q,\nu), \tag{2.78}$$

where $\epsilon^*_\mu(q,\nu)$ denotes the polarization vector of the ψ' with helicity ν, which yields a partial width

$$\Gamma(\bar{B}^0_d \to \psi'\pi^0) = \frac{G_F^2 |V_{cb}|^2 |V_{cd}|^2 f_\psi^2 m_\psi^2}{2} \frac{|\zeta|^2}{16\pi} \frac{\lambda^{3/2}\big(m_B^2, m_{\psi'}^2, M_\pi^2\big)}{m_B^3 m_{\psi'}^2}. \tag{2.79}$$

From the branching fraction $\mathcal{B}\big(\bar{B}^0_d \to \psi'\pi^0\big) = (1.17 \pm 0.19) \times 10^{-5}$ [164] and the life time $\tau_{\bar{B}^0_d} = (1.519 \pm 0.005) \times 10^{-12}\,\mathrm{s}$ [44], we find

$$|\zeta| \approx 0.14. \tag{2.80}$$

The subsequent decay $\psi'(q) \to J/\psi(p_\psi)\eta(p_2)$ is parametrized in terms of an amplitude

$$i\,\xi \epsilon_{\mu\nu\alpha\beta}\, \epsilon^{\mu *}(p_\psi, \lambda)\, p_\psi^\nu\, \epsilon^\alpha(q,\nu)\, q^\beta, \tag{2.81}$$

leading to a partial width

$$\Gamma\big(\psi' \to J/\psi\eta\big) = \frac{\xi^2}{96\pi} \frac{\lambda^{3/2}\big(m_{\psi'}^2, m_\psi^2, M_\eta^2\big)}{m_{\psi'}^3}. \tag{2.82}$$

From the branching fraction $\mathcal{B}(\psi' \to J/\psi\eta) = (3.36 \pm 0.05)\%$ and the total width $\Gamma(\psi') = (296 \pm 8)\,\mathrm{keV}$ [44], we deduce the coupling $|\xi| \approx 0.218\,\mathrm{GeV}^{-1}$. Altogether, ψ'-exchange leads to a contribution to the $\bar{B}^0_d \to J/\psi\pi^0\eta$ transversity form factor $\mathcal{F}_\perp^{(\psi')}$ of the form

$$\mathcal{F}_\perp^{(\psi')}(s,t) = \frac{\zeta\xi\sqrt{s}X}{t - m_{\psi'}^2}. \tag{2.83}$$

The leading P-wave can be obtained from the partial-wave expansion (2.12), we find

$$\mathcal{F}_\perp^{(\psi')(P)}(s) = \sqrt{\frac{3}{2}}\zeta\xi\frac{\sqrt{s}}{Y}\left(w - \frac{w^2-1}{2}\log\frac{w+1}{w-1}\right), \tag{2.84}$$

with the kinematical variables X, Y as defined in the main text, and

$$w = \frac{1}{2XY}\left[\Sigma - 2m_{\psi'}^2 - s + \frac{\Delta_m}{s}\right], \quad \Sigma = m_B^2 + m_\psi^2 + M_\pi^2 + M_\eta^2. \tag{2.85}$$

Note that $w > 1$ *except* for the interval $s \in [s_1, s_2]$,

$$\begin{aligned} s_{1/2} &= \frac{1}{2}\left[\Sigma - m_{\psi'}^2 - \frac{(m_B^2 - M_\pi^2)(m_\psi^2 - M_\eta^2) \pm \lambda^{1/2}\big(m_B^2, m_{\psi'}^2, M_\pi^2\big)\lambda^{1/2}\big(m_{\psi'}^2, m_\psi^2, M_\eta^2\big)}{m_{\psi'}^2}\right] \\ &\approx \big\{(1.34\,\text{GeV})^2, (1.83\,\text{GeV})^2\big\}. \end{aligned} \tag{2.86}$$

The $\psi(2S)$-exchange mechanism contributes by far most of its strength in this interval, where the resonance can go on-shell, and the partial-wave approximation (2.84) is insufficient; however, the integrated partial width due to this mechanism, see Eq. (2.37), is two orders of magnitude smaller compared to the one integrated in the $a_0(980)$ region, Eq. (2.68). In addition, at energies around 1 GeV, in contrast, the P-wave fully dominates the $\psi(2S)$ exchange, and contributes to the differential decay rate according to

$$\left.\frac{\mathrm{d}\Gamma}{\mathrm{d}\sqrt{s}}\right|_{\psi(2S)} = \frac{G_F^2|V_{cb}|^2|V_{cd}|^2 f_\psi^2 m_\psi^2 XY\sqrt{s}}{2(4\pi)^3 m_B^3}\left|Y^2\mathcal{F}_\perp^{(\psi')(P)}(s)\right|^2. \tag{2.87}$$

We find this to be smaller than the $a_0(980)$ signal by about five orders of magnitude: this particular contribution to the P-wave as well as to the left-hand cut of the process is entirely negligible.

2.7.3 B^*-exchange in $\bar{B}_d^0 \to J/\psi\pi^0\eta$

An alternative mechanism generating a left-hand-cut structure is given by the exchange of a B^* meson in either the t- or u-channel, see Figure 2.10 (right panel). In contrast to the $\psi(2S)$-exchange discussed in the previous section, the B^* cannot go on-shell in the decay, therefore the associated left-hand cut is outside the physical decay region. On the other hand, the exchange of a B^* is not suppressed in any obvious manner (such as by the OZI mechanism), hence it is potentially much more sizable. The coupling of a B/B^* to a light pseudoscalar is given by the Lagrangian term [68]

$$\frac{g}{2}\mathrm{Tr}\big[\bar{H}_a H_b \gamma_\nu \gamma_5\big] u_{ba}^\nu, \tag{2.88}$$

where Tr[...] denotes the Dirac trace, a, b are flavor indices, and $H = \frac{1}{2}(1+\not{v})[B_\mu^*\gamma^\mu - B\gamma_5]$ is the covariant field combining the pseudoscalar and vector B mesons $(B^{-(*)}, \bar{B}^{0(*)}, \bar{B}_s^{(*)})$ of velocity v, taken to be mass-degenerate in the heavy-quark limit.[7] These fields are of mass dimension 3/2 as factors of $\sqrt{m_B}$ and $\sqrt{m_{B^*}}$ are absorbed in the B_μ^* and B fields. Heavy-flavor symmetry dictates that the same coupling g also determines the couplings of charmed D/D^* mesons to light pseudoscalars [with $m_B \to m_D$ in (2.88)]; the resulting partial width

$$\Gamma\big(D^{+*} \to D^+\pi^0\big) = \frac{g^2 m_D^2}{192\pi F_\pi^2}\frac{\lambda^{3/2}(m_{D^*}^2, m_D^2, M_\pi^2)}{m_{D^*}^5} \tag{2.89}$$

allows one to pin down the coupling $g \approx 0.58$. For the weak vertex $B^* \to J/\psi M_2$, $M_2 = \pi^0$, η, we use a Lagrangian with four different trace structures obeying the desired transformation

[7] Some more details on the Heavy-Meson Chiral Perturbation Theory formalism are given in Section 1.2.2.

behavior under heavy-quark spin symmetry [198],

$$\begin{aligned}\tilde{G}_F\, t_L^\dagger u^\dagger \Big\{ &\mathrm{Tr}\left[(\alpha_1 + \alpha_2\, \not{v}')\gamma^\mu(1-\gamma^5) J \gamma_\mu (1-\gamma^5)\bar{H}\right] \\ &+ \mathrm{Tr}\left[\gamma^\mu(1-\gamma^5)J\right]\mathrm{Tr}\left[(\beta_1+\beta_2\,\not{v}')\gamma_\mu(1-\gamma^5)\bar{H}\right]\Big\}, \\ \tilde{G}_F &= \frac{G_F}{\sqrt{2}} V_{cb}V_{cd}^* f_\psi m_\psi . \end{aligned} \tag{2.90}$$

The structure of this Lagrangian is motivated in Appendix A.2. $J = \frac{1}{2}(1+\not{v}')[\Psi_\mu \gamma^\mu - \eta_c \gamma_5]$ combines the lightest pseudoscalar (η_c) and vector (J/ψ) charmonium fields that carry velocity v'. Similarly to the B-meson fields they are of mass dimension 3/2 and taken to be mass-degenerate in the heavy-quark limit. We therefore can relate the required $B^* \to J/\psi M_2$ vertex to decays $B^0 \to J/\psi M_2$ and $B^0 \to \eta_c M_2$,

$$\begin{aligned}\Gamma\big(B^0 \to J/\psi\pi^0\big) &= \frac{\tilde{G}_F^2}{4F_\pi^2}\frac{\lambda^{1/2}(m_B^2, m_\psi^2, M_\pi^2)}{16\pi m_B^3}\frac{(m_B^2-m_\psi^2)^2}{4m_B m_\psi}|\tilde{\alpha}_1|^2 \approx 3\,\Gamma\big(B^0\to J/\psi\eta\big), \\ \Gamma\big(B^0 \to \eta_c\pi^0\big) &= \frac{\tilde{G}_F^2}{4F_\pi^2}\frac{\lambda^{1/2}(m_B^2, m_{\eta_c}^2, M_\pi^2) m_{\eta_c}}{16\pi m_B^2}\left|\tilde{\alpha}_2 + \frac{m_B^2+m_\psi^2}{2m_B m_\psi}\tilde{\alpha}_1\right|^2 \\ &\approx \frac{|V_{cd}|^2}{2|V_{cs}|^2}\Gamma\big(B^0\to\eta_c K^0\big), \qquad \tilde{\alpha}_1 = 4(\alpha_1+\beta_1), \quad \tilde{\alpha}_2 = 4(\alpha_2+\beta_2), \end{aligned} \tag{2.91}$$

for which the branching fractions are measured [44],

$$\begin{aligned}\mathcal{B}(B^0\to J/\psi\pi^0) &= (1.76\pm 0.16)\times 10^{-5}, \\ \mathcal{B}(B^0\to J/\psi\eta) &= (1.08\pm 0.24)\times 10^{-5}, \\ \mathcal{B}(B^0\to \eta_c K^0) &= (8.0\pm 1.2)\times 10^{-4}. \end{aligned} \tag{2.92}$$

We therefore can fix the (combinations of) couplings $|\tilde{\alpha}_1| \approx 0.055\,\mathrm{GeV}$, which is the average of the values determined from the branching fractions into $J/\psi\pi^0$ and $J/\psi\eta$, as well as $|\tilde{\alpha}_2 + (m_B^2+m_\psi^2)/(2m_B m_\psi)\cdot\tilde{\alpha}_1| \approx 0.028\,\mathrm{GeV}$. To satisfy the latter relation, we have two choices for $|\tilde{\alpha}_2|$,[8] $|\tilde{\alpha}_2| \approx 0.035\,\mathrm{GeV}$ or $|\tilde{\alpha}_2| \approx 0.091\,\mathrm{GeV}$, with the constraint $\tilde{\alpha}_2/\tilde{\alpha}_1 < 0$.

The B^*-exchange graphs for $B(p_B) \to J/\psi(p_\psi)\pi^0(p_1)\eta(p_2)$ then lead to an amplitude contribution of the form

$$\begin{aligned}\mathcal{M}^{\mathrm{eff}}_{B^*} \approx &-\frac{\tilde{G}_F g\sqrt{m_B^3 m_\psi}}{2\sqrt{3}F_\pi^2}\Bigg\{ p_1^\mu\left[\left(\tilde{\alpha}_1 + \frac{m_B^2+m_\psi^2}{2m_B m_\psi}\tilde{\alpha}_2\right)\frac{1}{t-m_{B^*}^2} + \frac{1}{m_{B^*}^2}\left(\tilde{\alpha}_1 + \frac{m_B}{m_\psi}\tilde{\alpha}_2\right)\right] \\ &+ p_2^\mu\left[\left(\tilde{\alpha}_1 + \frac{m_B^2+m_\psi^2}{2m_B m_\psi}\tilde{\alpha}_2\right)\frac{1}{u-m_{B^*}^2} + \frac{1}{m_{B^*}^2}\left(\tilde{\alpha}_1 + \frac{m_B}{m_\psi}\tilde{\alpha}_2\right)\right] \\ &+ i\epsilon^{\mu\nu\alpha\beta} p_{\psi\nu} p_{2\alpha} p_{1\beta}\frac{\tilde{\alpha}_2}{m_\psi m_B}\left(\frac{1}{t-m_{B^*}^2} - \frac{1}{u-m_{B^*}^2}\right)\Bigg\}\epsilon_\mu^*(p_\psi,\lambda) \\ = &-\frac{\tilde{G}_F g\sqrt{m_B^3 m_\psi}}{4\sqrt{3}F_\pi^2}\Bigg\{ Q^\mu\left[\left(\tilde{\alpha}_1 + \frac{m_B^2+m_\psi^2}{2m_B m_\psi}\tilde{\alpha}_2\right)\left(\frac{1}{t-m_{B^*}^2} - \frac{1}{u-m_{B^*}^2}\right)\right] \\ &+ P^\mu\left[\left(\tilde{\alpha}_1 + \frac{m_B^2+m_\psi^2}{2m_B m_\psi}\tilde{\alpha}_2\right)\left(\frac{1}{t-m_{B^*}^2} + \frac{1}{u-m_{B^*}^2}\right) + \frac{2}{m_{B^*}^2}\left(\tilde{\alpha}_1 + \frac{m_B}{m_\psi}\tilde{\alpha}_2\right)\right] \\ &+ i\epsilon^{\mu\nu\alpha\beta} p_{\psi\nu} P_\alpha Q_\beta \frac{\tilde{\alpha}_2}{m_\psi m_B}\left(\frac{1}{t-m_{B^*}^2} - \frac{1}{u-m_{B^*}^2}\right)\Bigg\}\epsilon_\mu^*(p_\psi,\lambda), \end{aligned} \tag{2.93}$$

[8] As a simple estimation of the error due to the unknown sign of $\tilde{\alpha}_1$ we focus on the linear combination of couplings $|\tilde{\alpha}_1 + (m_B^2+m_\psi^2)/(2m_B m_\psi)\cdot\tilde{\alpha}_2|$ entering the $B^* \to J/\psi M_2$ amplitude, which is affected by this uncertainty on a 30% level; therefore we prove the P-wave suppression for both values.

where terms of order $M_{\pi/\eta}^2/m_B^2$ or $(m_{B^*}-m_B)/m_B$ have been neglected. In order to project this expression onto the transversity form factors $\mathcal{F}_0$, $\mathcal{F}_\parallel$, we need to replace Q^μ by $Q^\mu_{(\parallel)} = Q^\mu + \gamma P^\mu + \ldots$, where γ can be read off from Eq. (2.5). We find that we can approximate γ according to

$$\gamma = 1 + \frac{2(t-m_B^2)}{m_B^2-m_\psi^2} + \mathcal{O}\big(s, M_\pi^2, M_\eta^2\big) = -1 - \frac{2(u-m_B^2)}{m_B^2-m_\psi^2} + \mathcal{O}\big(s, M_\pi^2, M_\eta^2\big), \tag{2.94}$$

such that

$$\begin{aligned}
\mathcal{F}_0^{(B^*)}(s,t,u) &= \frac{g\sqrt{m_B m_\psi}\,X}{\sqrt{3}F_\pi^2}\frac{1}{m_B^2-m_\psi^2}\left(\tilde\alpha_2 + \frac{m_B^2+m_\psi^2}{2m_B m_\psi}\tilde\alpha_1\right),\\
\mathcal{F}_\parallel^{(B^*)}(s,t,u) &= -\frac{g\sqrt{m_B^3 m_\psi\, s}}{4\sqrt{3}F_\pi^2}\left(\tilde\alpha_1 + \frac{m_B^2+m_\psi^2}{2m_B m_\psi}\tilde\alpha_2\right)\left[\frac{1}{t-m_{B^*}^2} - \frac{1}{u-m_{B^*}^2}\right],\\
\mathcal{F}_\perp^{(B^*)}(s,t,u) &= \frac{g\sqrt{m_B\, s}\,X}{4\sqrt{3m_\psi}F_\pi^2}\,\tilde\alpha_2\left[\frac{1}{t-m_{B^*}^2} - \frac{1}{u-m_{B^*}^2}\right].
\end{aligned} \tag{2.95}$$

The partial-wave expansion of $\mathcal{F}_0^{(B^*)}$ contains an S-wave only. We find that the S-wave expression induced by B^*-exchange does not actually include a left-hand cut: the t- and u-channel pole contributions cancel, leaving behind an effectively point-like source for an S-wave $\pi\eta$ pair. In this way, B^*-exchange provides a model for the coupling constant that was obtained purely phenomenologically by fitting to data in the main text. In order to compare the strength of the B^*-exchange-induced S-wave to the phenomenological one, we calculate the analogue of the (fitted and afterwards properly normalized) constant $\bar b_0^n \approx 2.8\cdot 10^{-10}\,\text{GeV}^{-3}$ by means of Eq. (2.57). We find a strength $|\bar b_0^{B^*}| \approx 1.6\cdot 10^{-10}\,\text{GeV}^{-3}$: the combination of the two couplings $\tilde\alpha_{1/2}$ is exactly the one fixed from $B^0\to\eta_c K^0$ above, hence the ambiguity in $\tilde\alpha_2$ just translates into a sign ambiguity once more. The effective coupling strength therefore indeed produces an S-wave rate of the correct order of magnitude, pointing towards an essential role of the B^* in the explanation of the production mechanism; a more systematic investigation of this strength is beyond the scope of the present article.

Our main focus here is rather on the P-waves in $\mathcal{F}_\parallel^{(B^*)}$ and $\mathcal{F}_\perp^{(B^*)}$, which are given by

$$\begin{aligned}
\mathcal{F}_\parallel^{(B^*)(P)}(s) &= -\frac{g\sqrt{m_B^3 m_\psi\, s}}{4\sqrt{2}F_\pi^2}\left(\tilde\alpha_1 + \frac{m_B^2+m_\psi^2}{2m_B m_\psi}\tilde\alpha_2\right)\frac{1}{XY}\left(v_+ - \frac{v_+^2-1}{2}\log\frac{v_++1}{v_+-1}\right.\\
&\qquad\left. - v_- + \frac{v_-^2-1}{2}\log\frac{v_-+1}{v_--1}\right),\\
\mathcal{F}_\perp^{(B^*)(P)}(s) &= \frac{g\sqrt{m_B\, s}}{4\sqrt{2m_\psi}F_\pi^2}\frac{\tilde\alpha_2}{Y}\left(v_+ - \frac{v_+^2-1}{2}\log\frac{v_++1}{v_+-1} - v_- + \frac{v_-^2-1}{2}\log\frac{v_-+1}{v_--1}\right),\\
v_\pm &= \frac{1}{2XY}\left[\Sigma - 2m_{B^*}^2 - s \pm \frac{\Delta_m}{s}\right],
\end{aligned} \tag{2.96}$$

and the pairs of terms depending on $v_\pm$, coming from the t- and u-channel pole terms, almost cancel each other. The D-waves, given by

$$\begin{aligned}
\mathcal{F}_\parallel^{(B^*)(D)}(s) &= -\frac{\sqrt{5}g\sqrt{m_B^3 m_\psi\, s}}{4\sqrt{2}F_\pi^2}\left(\tilde\alpha_1 + \frac{m_B^2+m_\psi^2}{2m_B m_\psi}\tilde\alpha_2\right)\frac{1}{XY}\left(v_+^2 - \frac{v_+(v_+^2-1)}{2}\log\frac{v_++1}{v_+-1}\right.\\
&\qquad\left. + v_-^2 - \frac{v_-(v_-^2-1)}{2}\log\frac{v_-+1}{v_--1} - \frac{4}{3}\right),
\end{aligned}$$

$$\mathcal{F}_\perp^{(B^*)(D)}(s) = \frac{\sqrt{5} g \sqrt{m_B\, s}}{4\sqrt{2m_\psi} F_\pi^2} \frac{\tilde{\alpha}_2}{Y} \left(v_+^2 + v_-^2 - \frac{4}{3} - \frac{v_+(v_+^2-1)}{2} \log \frac{v_+ + 1}{v_+ - 1} - \frac{v_-(v_-^2-1)}{2} \log \frac{v_- + 1}{v_- - 1} \right), \tag{2.97}$$

are actually as large as the P-waves around $\sqrt{s} \approx 1\,\text{GeV}$. Both $\tau = \parallel$ and $\tau = \perp$ P- and D-waves yield contributions to $\mathrm{d}\Gamma/\mathrm{d}\sqrt{s}$ suppressed relative to $\mathcal{F}_0^{(B^*)}$ by two orders of magnitude, proving yet again the strong dominance of the S-wave in this decay. This is illustrated in Figure 2.11 for the two sets of coupling strengths; there the respective P- and D-wave contributions to $\mathrm{d}\Gamma/\mathrm{d}\sqrt{s}$ are divided by the predicted differential decay rate as determined in equation (2.58), where only the S-wave is included and the $\pi\eta$ final-state interaction is considered. In Section 2.7.4 in the context of the $\pi^+\pi^-$ final state we argue that there is a preference in choosing the smaller value for the coupling $|\tilde{\alpha}_2| \approx 0.035\,\text{GeV}$; for that choice the P-wave contribution to $\mathrm{d}\Gamma/\mathrm{d}\sqrt{s}$ is suppressed relative to the S-wave contribution by even three orders of magnitude (see top panel of Figure 2.11).

2.7.4 B^*-exchange in $\bar{B}^0_d \to J/\psi\pi^+\pi^-$

In the $\bar{B}^0_d(p_B) \to J/\psi(p_\psi)\pi^+(p_1)\pi^-(p_2)$ case the absence of left-hand-cut structures is confirmed by the experimental analysis that shows that there are no considerable structures in the $J/\psi\pi$ channel within the Dalitz plot. However, this phenomenological argument does not exclude the possibility of crossed-channel effects occurring already in the weak decay mechanism, i.e. the B^* exchange. We rerun the calculation of the B^* t-channel exchange in that mode as well, in analogy to what we do for the $\pi^0\eta$ final state, to theoretically substantiate the neglect of any crossed-channel structures. There is no crossing symmetry for the $\pi^+\pi^-$ final state, such that there is no contribution from the u-channel exchange to the effective matrix element, which reads

$$\begin{aligned}
\mathcal{M}^{\text{eff}}_{B^*} &\approx \frac{\tilde{G}_F g \sqrt{m_B^3 m_\psi}}{F_\pi^2} \left\{ p_1^\mu \left(\tilde{\alpha}_1 + \frac{m_B^2 + m_\psi^2}{2 m_B m_\psi} \tilde{\alpha}_2 \right) \frac{1}{t - m_{B^*}^2} + (p_1^\mu + p_2^\mu) \left(\tilde{\alpha}_1 + \frac{m_B}{m_\psi} \tilde{\alpha}_2 \right) \frac{1}{2 m_{B^*}^2} \right. \\
&\qquad \left. + i \epsilon^{\mu\nu\alpha\beta} p_{\psi\nu} p_{2\alpha} p_{1\beta} \frac{\tilde{\alpha}_2}{m_\psi m_B} \frac{1}{t - m_{B^*}^2} \right\} \epsilon_\mu^*(p_\psi, \lambda) \\
&= \frac{\tilde{G}_F g \sqrt{m_B^3 m_\psi}}{2 F_\pi^2} \left\{ P^\mu \left[\left(\tilde{\alpha}_1 + \frac{m_B^2 + m_\psi^2}{2 m_B m_\psi} \tilde{\alpha}_2 \right) \frac{1}{t - m_{B^*}^2} + \left(\tilde{\alpha}_1 + \frac{m_B}{m_\psi} \tilde{\alpha}_2 \right) \frac{1}{m_{B^*}^2} \right] \right. \\
&\qquad \left. + Q^\mu \left(\tilde{\alpha}_1 + \frac{m_B^2 + m_\psi^2}{2 m_B m_\psi} \tilde{\alpha}_2 \right) \frac{1}{t - m_{B^*}^2} + i \epsilon^{\mu\nu\alpha\beta} p_{\psi\nu} P_\alpha Q_\beta \frac{\tilde{\alpha}_2}{m_\psi m_B} \frac{1}{t - m_{B^*}^2} \right\} \epsilon_\mu^*(p_\psi, \lambda).
\end{aligned} \tag{2.98}$$

Performing the same steps as in Section 2.7.3 yields the transversity amplitudes

$$\begin{aligned}
\mathcal{F}_0^{(B^*)}(s,t,u) &= -\frac{g\sqrt{m_B m_\psi}\, X}{F_\pi^2} \frac{1}{m_B^2 - m_\psi^2} \left(\tilde{\alpha}_2 + \frac{m_B^2 + m_\psi^2}{2 m_B m_\psi} \tilde{\alpha}_1 \right), \\
\mathcal{F}_\parallel^{(B^*)}(s,t,u) &= \frac{g\sqrt{m_B^3 m_\psi\, s}}{2 F_\pi^2} \left(\tilde{\alpha}_1 + \frac{m_B^2 + m_\psi^2}{2 m_B m_\psi} \tilde{\alpha}_2 \right) \frac{1}{t - m_{B^*}^2}, \\
\mathcal{F}_\perp^{(B^*)}(s,t,u) &= -\frac{g\sqrt{m_B\, s}\, X}{2\sqrt{m_\psi} F_\pi^2} \frac{\tilde{\alpha}_2}{t - m_{B^*}^2},
\end{aligned} \tag{2.99}$$

where in $\mathcal{F}_0^{(B^*)}$ the pole contribution cancels, such that it contains a point-like S-wave only, similarly to the result of Section 2.7.3.

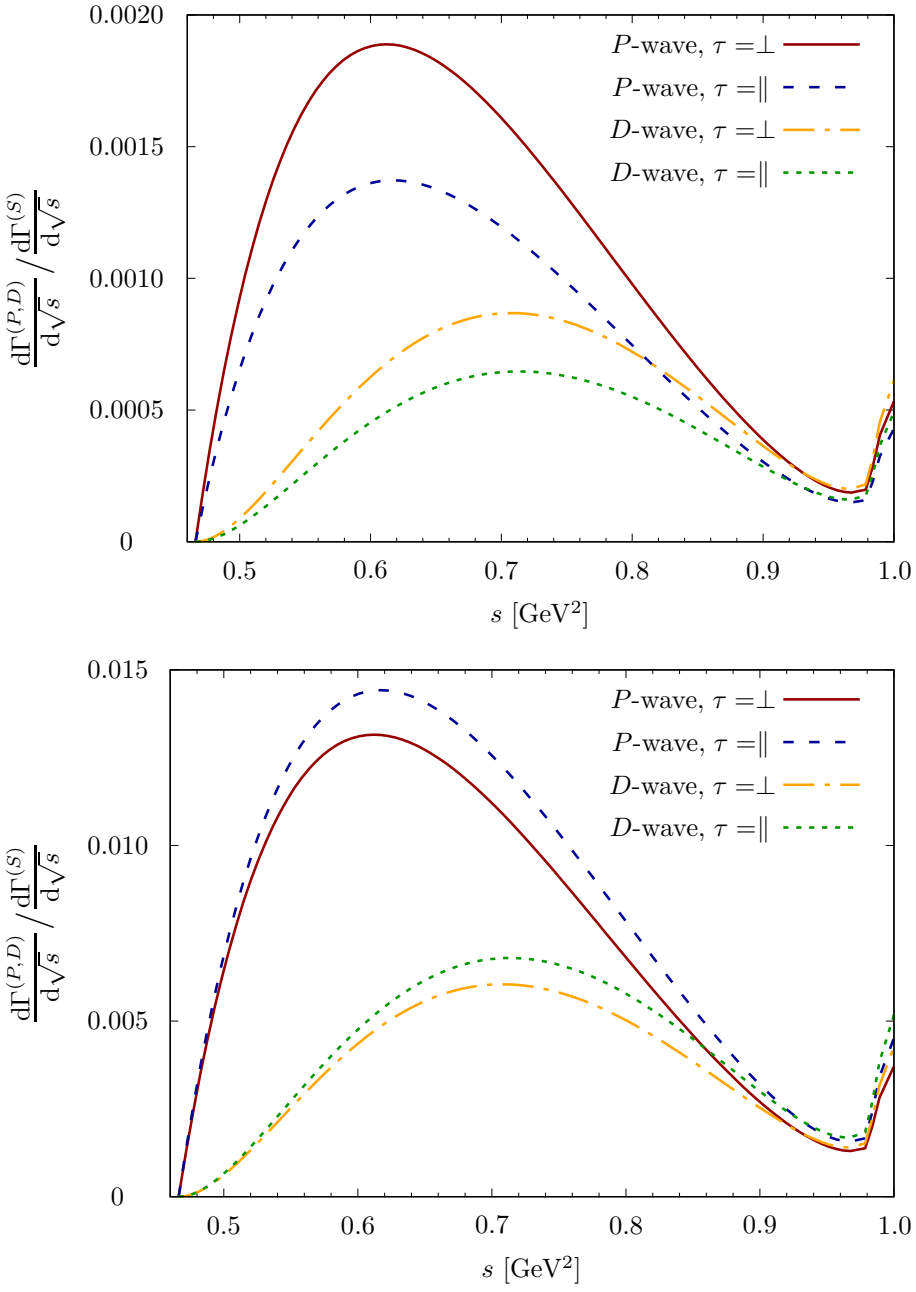

Figure 2.11: Relative size of the higher-wave contributions to the differential decay rate $d\Gamma/d\sqrt{s}$: the ratios of the $\tau = \perp$ P-to-S-wave (solid, red), $\tau = \parallel$ P-to-S-wave (dashed, blue), $\tau = \perp$ D-to-S-wave (dash-dotted, orange) and $\tau = \parallel$ D-to-S-wave (dotted, green) contributions are depicted for the two sets of couplings strengths $|\tilde{\alpha}_2| \approx 0.035\,\text{GeV}$ (top panel) or $|\tilde{\alpha}_2| \approx 0.091\,\text{GeV}$ (bottom panel). For the S-wave our predicted differential decay rate is used, including final-state-interaction effects and S-wave dominance, see Section 2.6.

We extract the B^*-exchange-induced S-wave strength $|\bar{b}_0^{B^*}| \approx 2.5 \cdot 10^{-10}\,\text{GeV}^{-3}$ that nearly saturates the phenomenological parameter $|\bar{b}_0^n| \approx 2.8 \cdot 10^{-10}\,\text{GeV}^{-3}$, revealing that the production mechanism may be approximately modeled by the B^* exchange. A comparison of Eqs. (2.95) and (2.99) reveals that the S-wave amplitudes differ by a factor $-\sqrt{3}$. The same relative factor appears when transferring the $\bar{B}^0_d \to J/\psi\pi\pi$ amplitude to the $\pi\eta$ channel for a prediction using the fitted $\pi\pi$ amplitude strength, such that one might expect comparable statements concerning the saturation between both the B^*-exchange-induced and phenomenological strengths. This is indeed the case when retaining leading symmetry relations and inserting the LO form factor normalizations Eq. (2.49). The worse saturation seen in Section 2.7.3 for the $\pi\eta$ scenario hence is caused by NLO chiral corrections.

The P-wave amplitudes $\mathcal{F}_\parallel^{(B^*)(P)}$ and $\mathcal{F}_\perp^{(B^*)(P)}$ read

$$\begin{aligned}
\mathcal{F}_\parallel^{(B^*)(P)}(s) &= \frac{g\sqrt{m_B^3 m_\psi\, s}}{2F_\pi^2}\sqrt{\frac{3}{2}}\left(\tilde{\alpha}_1 + \frac{m_B^2 + m_\psi^2}{2m_B m_\psi}\tilde{\alpha}_2\right)\frac{1}{XY}\left(v_+ - \frac{v_+^2 - 1}{2}\log\frac{v_+ + 1}{v_+ - 1}\right), \\
\mathcal{F}_\perp^{(B^*)(P)}(s) &= -\frac{g\sqrt{m_B\, s}}{2\sqrt{m_\psi}F_\pi^2}\sqrt{\frac{3}{2}}\frac{\tilde{\alpha}_2}{Y}\left(v_+ - \frac{v_+^2 - 1}{2}\log\frac{v_+ + 1}{v_+ - 1}\right).
\end{aligned} \tag{2.100}$$

Contrary to the exotic P-wave in the $\pi^0\eta$ system the $\pi^+\pi^-$ P-wave is not suppressed. We compare the B^*-exchange-induced P-waves with the full P-waves that we have fitted to the data, see Section 2.5.1,

$$\mathcal{CF}_\parallel^{(P)}(s) = \sqrt{\mathcal{N}_\pi s}\, a_\parallel \Omega_1^1(s), \quad \mathcal{CF}_\perp^{(P)}(s) = \sqrt{\mathcal{N}_\pi s}\, X a_\perp \Omega_1^1(s). \tag{2.101}$$

For simplicity we neglect here the correction due to ρ–ω mixing. Therefore we calculate the strengths $a_\tau^{(B^*)}$ ($\tau = \parallel, \perp$) that correspond to the fitted coupling strengths a_τ. For the two sets of couplings $|\tilde{\alpha}_2|$ these strengths are shown in Figure 2.12. Note that for $a_\tau^{(B^*)}$ s-dependent curves are shown due to the t-pole dynamics. The only non-analytic behavior (that might cause an effect from the left-hand cut) shows up at $s = 0$ due to square-root singularities in $a_\tau^{(B^*)}(s)$, i.e. below the $\pi^+\pi^-$ threshold. Further, the P-wave is kinematically suppressed near the threshold: the a_τ contributions to $\mathrm{d}\Gamma/\mathrm{d}\sqrt{s}$ are multiplied by $sY^2 = s\sigma_\pi^2 = s - 4M_\pi^2$. In the region where the P-wave becomes more important the strengths $a_\tau^{(B^*)}(s)$ can be well approximated by an analytic (almost constant) function, such that there is no conflict with describing the partial waves by a polynomial multiplied with the Omnès function, even if the B^* has considerable influence in the unphysical region. Focusing on that region above threshold, where P-waves are not suppressed, we even find that for one set of couplings $|\tilde{\alpha}_2|$ the strength $a_\parallel^{(B^*)}(s)$ converges to the fitted $a_\parallel$, the latter shown by a band regarding the uncertainty due to different fit scenarios. This is a remarkable outcome as it supports our suggestion we made in the context of the $\bar{B}^0_d \to J/\psi\pi^0\eta$ S-wave that the B^* plays an essential role in the production mechanism, see Section 2.7.3. The coupling $a_\parallel^{(B^*)}(s)$ that results from the other choice of $|\tilde{\alpha}_2|$ is more than twice as large as the fitted coupling. As the non-analyticity in the physical region is still small this does not contradict our Omnès-times-polynomial ansatz. However, this scenario appears to be less plausible: if the impact of the B^* to the production mechanism is that large, contributions from other mechanisms of similar size will be required that cancel each other. We therefore argue for a preference of using the former value of the coupling, i.e. $|\tilde{\alpha}_2| \approx 0.035\,\text{GeV}$. Finally we see that the couplings $a_\perp^{(B^*)}(s)$ are small compared to the (fitted or B^*-induced) $a_\parallel$ values, with a constant ratio

$$\left|\frac{a_\perp^{(B*)}}{a_\parallel^{(B*)}}\right| = \left|\frac{\mathcal{F}_\perp^{(P)}}{X\mathcal{F}_\parallel^{(P)}}\right| = \frac{2\tilde{\alpha}_2}{2m_B m_\psi\tilde{\alpha}_1 + (m_B^2 + m_\psi^2)\tilde{\alpha}_2} = \{0.14, 0.11\}, \tag{2.102}$$

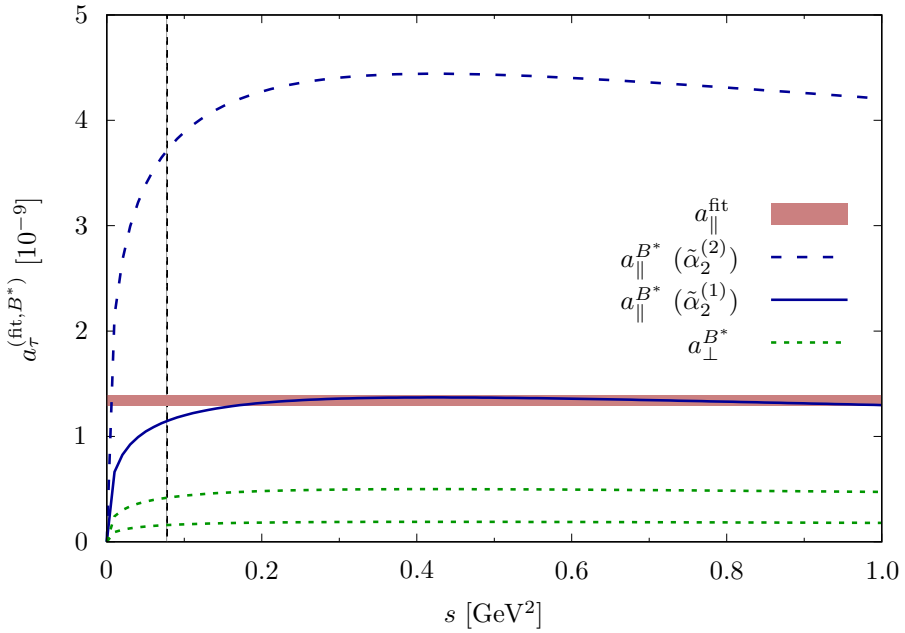

Figure 2.12: For the normalized coupling strength $a_\parallel$ a band (red) is shown, spanned by the results of different fit scenarios, see Section 2.5.1. The $a_\parallel^{(B^*)}$ curves (blue, solid for $\tilde{\alpha}_2^{(1)}$, dashed for $\tilde{\alpha}_2^{(2)}$) differ considerably for the two sets of couplings $\tilde{\alpha}_2$: while the dashed curve is considerably larger than the strength obtained in the fits, the solid curve nearly saturates the strength of the fitted P-wave and converges to the band, at least aside from the region around the threshold (indicated by the vertical line) and below. Both $a_\perp^{(B^*)}$ (green, dotted) are small compared to $a_\parallel^{(B^*)}$.

where the two results again correspond to the ambiguity in $|\tilde{\alpha}_2|$. There are no fitted $a_\perp$ results we can compare to, as we found it to be a redundant parameter in our fits. Instead in our fits we figured out a considerable contribution due to the $\mathcal{F}_0$ P-wave corresponding to the fit parameter a_0—there was no considerable preference for the choice of the transversity P-wave in our formalism.[9] Actually the transversity-0 P-wave is not explained by the B^* exchange, given that Eq. (2.99) rules out a P-wave. We test whether this discrepancy can be compensated by the $a_\perp^{B^*}$ contribution, which is indeed the case. This is demonstrated in Figure 2.13, where the $\langle Y_0^0\rangle$ distribution calculated with the B^*-exchange induced coupling strengths instead of the fitted subtraction polynomials is compared to the LHCb data (we confine ourselves to using

[9]Formally, in the combination $\langle Y_0^0\rangle + \langle Y_2^0\rangle$ the parameter a_0 is actually uncoupled from the $a_\parallel$ and $a_\perp$ parameters, which becomes obvious when considering the terms in the brackets in Eq. (2.52), written as

$$\langle Y_0^0\rangle \sim a_0^2 + (a_\parallel^2 + \beta_0 a_\perp^2)s + \beta_1 a_\perp^2 s^2 + ...$$
$$\langle Y_2^0\rangle \sim 2a_0^2 - (a_\parallel^2 + \beta_0 a_\perp^2)s - \beta_1 a_\perp^2 s^2 + ...,$$

where we denote $X^2 \equiv \beta_0 + \beta_1 s + ...$ However, we found that fitting the full set of parameters a_τ did not improve the data description compared to a two-parameter fit. Given the limited amount of data as well as the closeness to $s = 1$ GeV^2 we even could perform fits of similar fit quality by either using the a_0 parameter, entering as a constant term in the above relation, or the a_τ parameter that determines the strenght of a quadratic term. A quantitatively considerable decoupling of these terms requires more statistics.

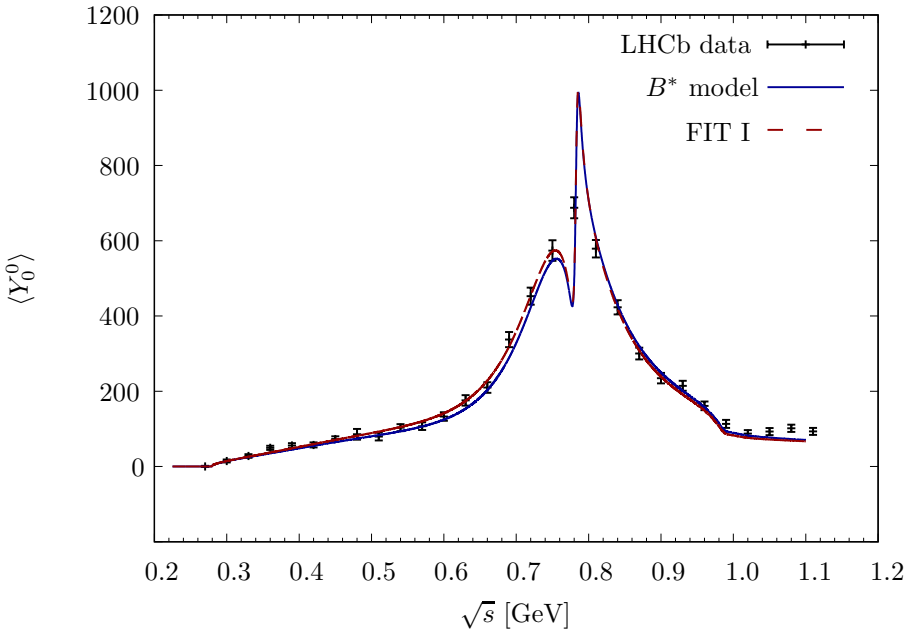

Figure 2.13: The $\langle Y_0^0 \rangle$ distribution with the coupling strengths constrained by the B^*-exchange model (blue solid line) is compared to the LHCb data. For completeness the fitted distribution (FIT I, see Section 2.5.1) (red, dashed) is depicted as well.

the preferred solution of $|\tilde{\alpha}_2|$). The data are remarkably well described by our theoretical curve. Consequently, there is evidence that describing the energy distribution in terms of the parameter $a_\perp$ is more expedient than using a_0. Constrained by heavy-meson and chiral symmetry, analyticity and unitarity, we achieve a 100% predictive capability, superseding any fit procedures and providing yet a test of heavy-meson symmetries. Of course this noticeable grade of quality may to some extent be accidental (actually, the equivalent estimation for the B^*-exchange induced strength for the $\langle Y_2^0 \rangle$ distribution is by far not that close to the fitted result, but still of the same order of magnitude) but this certainly demonstrates that modelling the short-distance physics by B^* exchange works really well; it just induces some restrictions upon which transversity P-waves contribute.

We next study whether these observations are corroborated by some chiral considerations, similar to those made in Section 2.7.1. There a chiral Lagrangian was constructed to demonstrate the neglect of the $\pi\eta$ P-wave. The $\pi\pi$ P-wave is already present at leading chiral order, cf. Eq. (2.34), from which we calculate the P-to-S-wave ratio. There are contributions to the form factors $\mathcal{F}_0$ and $\mathcal{F}_\parallel$. We find

$$\left|\frac{\mathcal{F}_0^{(P)}}{\mathcal{F}_0^{(S)}}\right| = \frac{Y(P\cdot p_\psi)}{\sqrt{3}X} \equiv \frac{Y a_0^\chi}{X b_0^\chi}, \quad P\cdot p_\psi = \frac{m_B^2 - s - m_\psi^2}{2}, \tag{2.103}$$

and compare the ratio

$$\frac{a_0^\chi}{b_0^\chi} = \frac{P\cdot p_\psi}{\sqrt{3}} = (5.0...5.28)\ \text{GeV}^2 \tag{2.104}$$

(the small value is obtained for $s = 0$, the large value for $s = 1$, we hence find a rather stable

ratio under a varying energy) to the corresponding ratio of fit parameters (see Table 2.1)

$$\frac{a_0}{b_0^n} = 4.51^{+0.88}_{-1.03}\ \text{GeV}^2. \tag{2.105}$$

In analogy the ratio

$$\left|\frac{\mathcal{F}_\parallel^{(P)}}{\mathcal{F}_0^{(S)}}\right| = \frac{\sqrt{2s}m_\psi}{\sqrt{3}X} \equiv \frac{\sqrt{s}a_\parallel^\chi}{Xb_0^\chi} \tag{2.106}$$

implies

$$\frac{a_\parallel^\chi}{b_0^\chi} = \sqrt{\frac{2}{3}}m_\psi = 2.53\ \text{GeV}, \tag{2.107}$$

which has at least the same order of magnitude as the ratio of the fitted strengths

$$\frac{a_\parallel}{b_0^n} = 5.03\ \text{GeV}. \tag{2.108}$$

In contrast to the above calculation of the B^* exchange modelling the short-distance physics this chiral estimation and comparison to the phenomenological fits results in a contribution from the transversity-0 P-wave that is of comparable size, and there is no evidence at all to prefer the transversity form factor $\mathcal{F}_\perp$, which emerges from a Lagrange density at higher order.

Let us summarize what we have learned from these considerations. We have discussed two distinct approaches to estimate the P-waves, on the one hand by explicitly calculating the B^* exchange diagrams, and on the other hand we have employed the chiral Lagrangian introduced in Section 2.7.1, from which we have calculated ratios between the S-wave and the various transversity P-waves. We have then extracted coupling strengths that are comparable to the fit parameters. The B^* exchange model rules out a transversity-0 P-wave, but a contribution from the other transversity P-waves proves quite satisfactory to describe the $\langle Y_0^0\rangle$ distribution. However, the comparison of the $\langle Y_2^0\rangle$ prediction shows larger discrepancies to the data and hence to our fit results; in particular the exclusion of a transversity-0 P-wave results in a negative $\langle Y_2^0\rangle$ distribution, while all LHCb data points are positive (however, with a significant uncertainty). Contrary, our chiral consideration entails a transversity-0 P-wave, and the $P^{\tau=0}$-wave-to-S-wave ratio is sufficiently comparable to the one obtained using the fit results. However, for the transversity-$\parallel$ P-wave-to-S-wave ratio the comparison of the chiral vs. fitted ratios is less convincing, but yields at least the same order of magnitude. This imprecise matching, together with the discrepancy in the $\langle Y_2^0\rangle$ distribution casts doubts on the mentioned 100% predictiveness employing the B^* exchange to model the short-disctance physics. Both ansätze yield suitable constraints for rough estimations, e.g. to decide whether one can expect a noticeable contribution from the P-wave or whether it is mandatory to take into account effects from left-hand cuts, but they do not provide strict constraints from which one can calculate accurate, precise numerical results.

2.8 $\bar{B}^0_{d/s} \to J/\psi \bar{K} K$: coupled-channel related predictions

As explained in Sections 1.3.4 and 2.4, in the coupled-channel treatment the relative strengths between the $\pi\pi$ or $\pi\eta$ and the isoscalar or isovector $\bar{K}K$ scalar form factors are fixed, thus the respective final states are related to each other unambiguously. We therefore are able to make predictions for the $\bar{B}^0_s \to J/\psi K^+K^-$ as well as the $\bar{B}^0_d \to J/\psi K^+K^-/K^0\bar{K}^0$ S-wave amplitudes. The latter we assume to dominate the differential decay rates in the energy region considered such that we make a prediction for the differential decay rates. In contrast, in the

$\mathcal{R}^{f_0/a_0}_{\rm th}$	$\delta_{12} = 90^\circ$	$\delta_{12} = 100^\circ$	$\delta_{12} = 110^\circ$	$\delta_{12} = 125^\circ$
$\sqrt{s_p} = 1.05$ GeV	0.35 ... 0.46	0.25 ... 0.35	0.16 ... 0.23	0.11 ... 0.15
$\sqrt{s_p} = 1.20$ GeV	0.33 ... 0.43	0.22 ... 0.31	0.15 ... 0.22	0.11 ... 0.15

Table 2.2: Theoretical determination of the ratio $\mathcal{R}^{f_0/a_0}$, Eq. (2.109), for different values of the phase δ_{12} entering in the determination of the $I = 1$ $\bar{K}K$ form factor, $\Gamma^{I=1}_{KK}$, and the upper integration limit s_p. The given range for the respective values is due to the uncertainty in the form factor normalizations.

case of the $\bar{B}^0_s$ decay the P-wave dominates the spectrum. There we calculate the S-wave background to the prominent $\phi(1020)$ resonance.

2.8.1 $\bar{B}^0_d \to J/\psi\bar{K}K$ spectral distributions

We discuss our results for the $\bar{B}^0_d \to J/\psi\bar{K}K$ decays, where $\bar{K}K$ can be either a neutral or a charged kaon pair. Note that a few data points are available for the latter channel [186]. In Ref. [147] properties of the $f_0(980)$ are deduced based on an amplitude analysis including both resonant and non-resonant terms performed in the same paper. However, on the physical axis a decomposition into resonant and non-resonant contributions is not possible in a model-independent way. Accordingly the only well-defined quantity that compares the $f_0(980)$ contribution to the $a_0(980)$ contribution is

$$\mathcal{R}^{f_0/a_0} = \frac{\int_{4M_K^2}^{s_p} \left|X^2 Y \sqrt{s}\, \Gamma^{I=0}_{KK}\right|^2 \mathrm{d}s}{\int_{4M_K^2}^{s_p} \left|X^2 Y \sqrt{s}\, \Gamma^{I=1}_{KK}\right|^2 \mathrm{d}s}, \tag{2.109}$$

which is dominated by the two scalar resonances for values of s_p that are not too large. Our determinations for this quantity are shown in Table 2.2 for different values of the input phase δ_{12} and of the upper integration limit s_p. There is some weak dependence on s_p, however, as the table clearly shows, $\mathcal{R}^{f_0/a_0}$ is very sensitive to the input phase δ_{12}. This sensitivity is even stronger than the uncertainty on the form factor normalizations, which are not accurately determined, cf. Table 2.2. A measurement of $\mathcal{R}^{f_0/a_0}$ would thus be very valuable to further constrain the so far badly determined phase δ_{12}.

Next we turn to our predictions for the physical final states, K^+K^- and $K^0\bar{K}^0$.[10] In a very naive picture, we would expect a $\bar{d}d$ source term to produce a pair of neutral kaons only, and no charged ones. Equation (2.50) in combination with Eq. (2.62) suggests that at (the unphysical point) $s = 0$, this naive view is indeed close to reality. If this behavior persisted in the energy region around 1 GeV, we would expect a destructive interference of $f_0(980)$ and $a_0(980)$ for charged kaons, but a constructive one for the neutral pairs.

In Figure 2.14 we present our results for $\langle Y^0_0 \rangle$ for physical $\bar{K}K$ states, namely K^+K^- (top panel) and $K^0\bar{K}^0$ (bottom panel), which differ by the sign of the interference term between the isoscalar and the isovector component, according to Eq. (2.62). A simple inspection of the figure shows that the interference pattern anticipated in the previous paragraph does not hold at all. To understand the origin of this, we show the two ($I = 0, 1$) kaon form factors in the Figures 2.15 (magnitude) and 2.16 (phases): we see that the $I = 1$ one completely dominates

[10] For simplicity, we discuss the neutral kaon channel in terms of the strong eigenstates. For even partial waves, the relation to the weak eigenstates, neglecting effects of CP-violation, is given by $\mathrm{d}\Gamma(\bar{B}^0_d \to J/\psi K_S K_S) = \mathrm{d}\Gamma(\bar{B}^0_d \to J/\psi K_L K_L) = \mathrm{d}\Gamma(\bar{B}^0_d \to J/\psi K^0 \bar{K}^0)/2$.

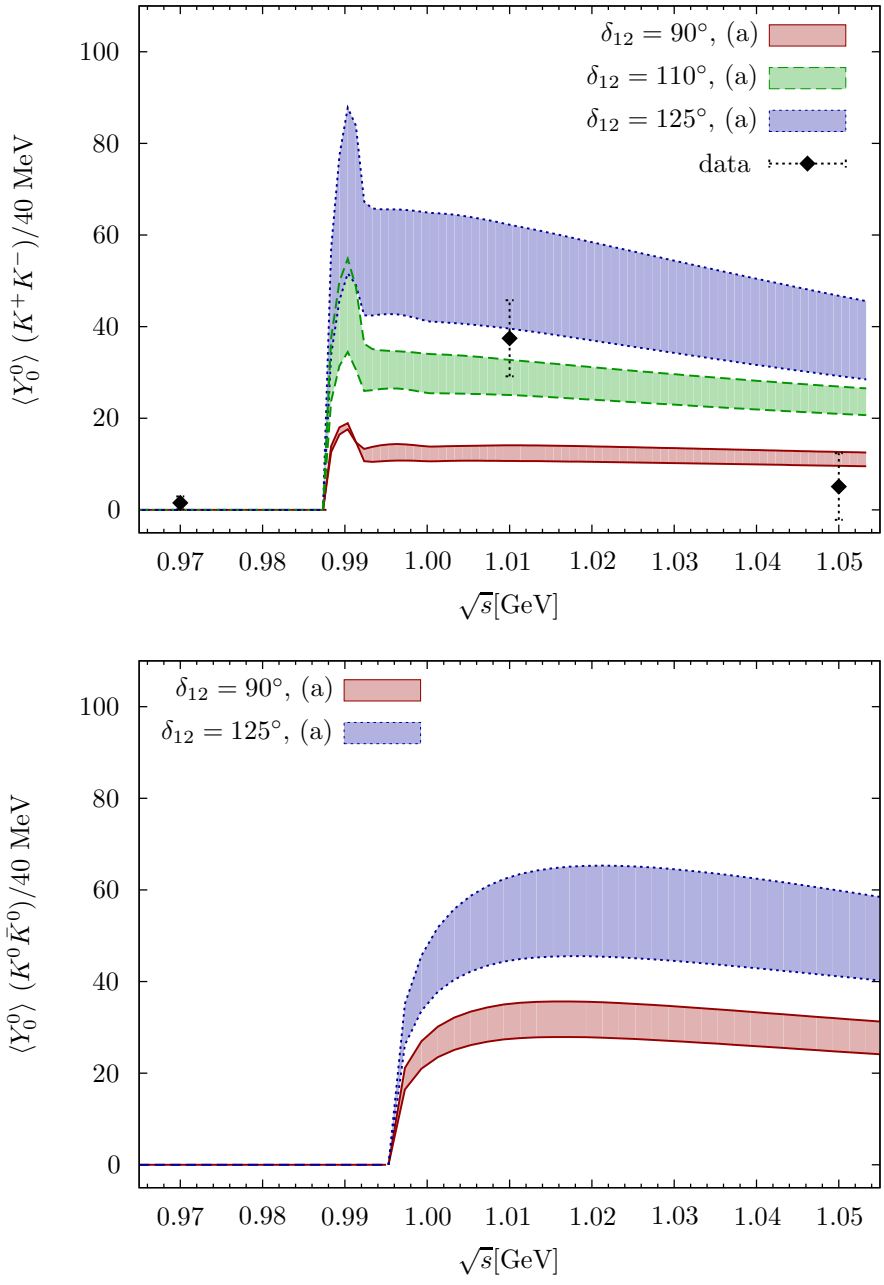

Figure 2.14: $\langle Y^0_0 \rangle(s)$ for $\bar{B}^0_d \to J/\psi K^+K^-$ (top) and $\bar{B}^0_d \to J/\psi K^0\bar{K}^0$ (bottom). The curves are calculated for different values of the phase δ_{12} (see text for further details). The error bands reflect the uncertainties in the normalizations of the form factors. The experimental points are taken from Ref. [186].

over the $I = 0$ form factor, or in other words, the $a_0(980)$ signal is much stronger than the $f_0(980)$ one; hence, both the K^+K^- and $K^0\bar{K}^0$ angular moments are dominated by the $I = 1$

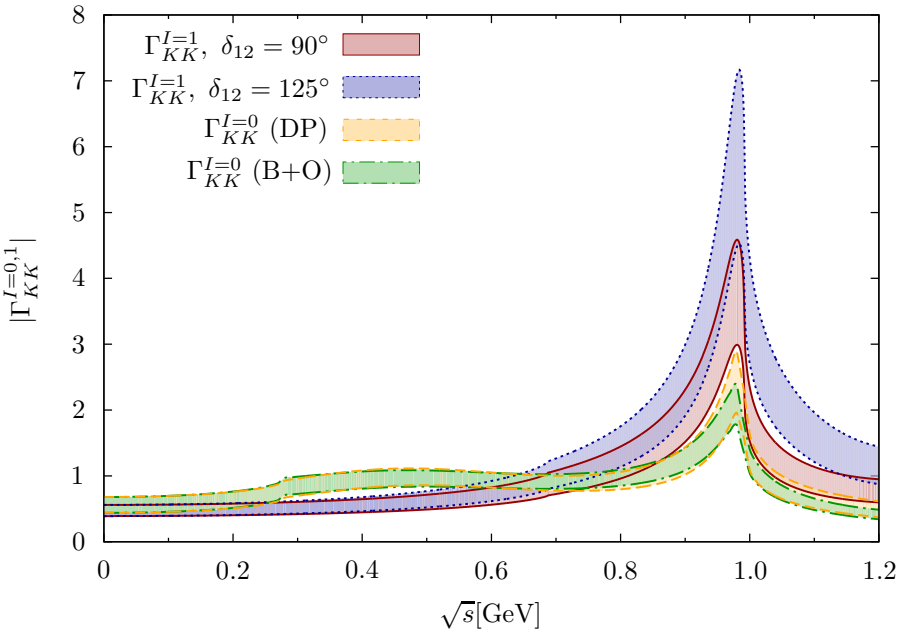

Figure 2.15: Moduli of the scalar form factors Γ^I_{KK} for $I = 0, 1$. The two bands for the $I = 0$ form factor refer to the T-matrix solutions of Ref. [127] (DP) and Refs. [37, 153] (B+O), respectively.

form factor, which explains why the interference pattern is not the one naively expected. The small value theoretically obtained for $\mathcal{R}^{f_0/a_0}$ is a direct consequence of the $I = 1$ dominance found here, as can be seen from its definition, Eq. (2.109). The difference in strengths of the two resonances is somewhat remarkable. It is *not* due to significant differences in the pole positions, as the $I = 1$ T-matrix of Ref. [140] uses an $a_0(980)$ pole position (on the second sheet) of

$$\sqrt{s^{\rm II}_{a_0(980)}} = \big(994 \pm 2 - i(25.4 \pm 5.0)\big)\,\text{MeV} \tag{2.110}$$

as a constraint [193,194], while the second-sheet pole of the $f_0(980)$ corresponding to our (main) $I = 0$ T-matrix parametrization is given by [195]

$$\sqrt{s^{\rm II}_{f_0(980)}} = \Big(996^{+4}_{-14} - i\big(24^{+11}_{-3}\big)\Big)\,\text{MeV}, \tag{2.111}$$

determined from pion–pion Roy equations. It seems, therefore, that rather the residues of the resonance couplings to the respective currents are very different, which might be in conflict with at least a simple interpretation of both scalar resonances as $\bar{K}K$ molecules: in such a picture, similar binding energies would imply similar coupling strengths to the $\bar{K}K$ channel according to the Weinberg criterion [196, 197], at least as long as the coupling to the second channel ($\pi\pi$ and $\pi\eta$) is weak enough to be perturbative.[11] More detailed investigations of the couplings of the scalars to $\bar{q}q$ operators, completing Ref. [195] also in the $I = 1$ sector, would be very interesting to clarify this issue.

[11] Note that the central values for the pole positions quoted in Eqs. (2.110), (2.111) also slightly discourage such a simple picture, as they lie somewhat *above* the $\bar{K}K$ threshold.

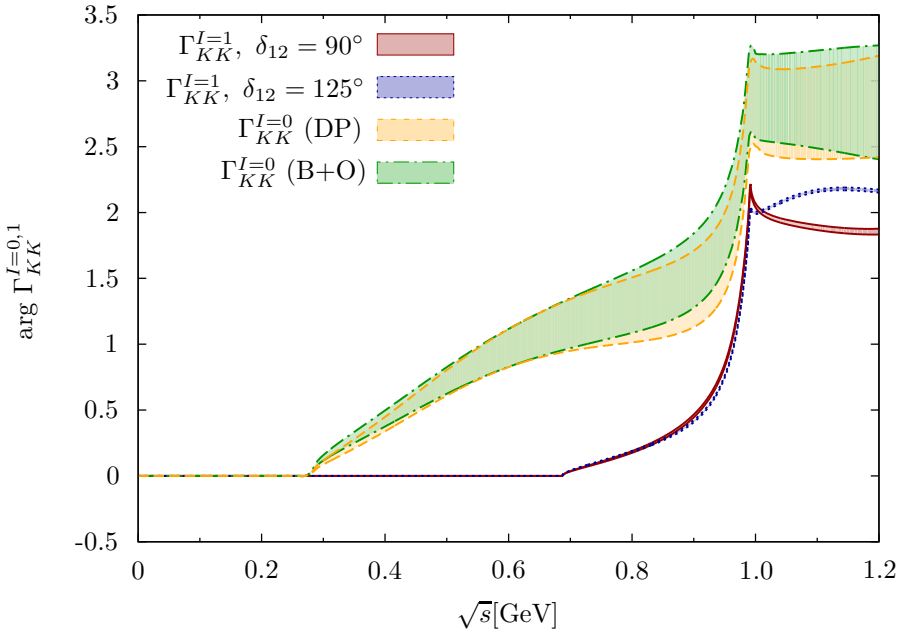

Figure 2.16: Phases of the scalar form factors Γ^I_{KK} for $I = 0, 1$. The two bands for the $I = 0$ form factor refer to the T-matrix solutions of Ref. [127] (DP) and Refs. [37, 153] (B+O), respectively.

It is remarkable to note that the *phases* of the two form factors, see bottom right panel of Figure 2.15, change almost perfectly in parallel, starting from the $\pi\eta$ threshold—the only difference is the low-energy phase growth in the isospin-0 channel, associated with the $f_0(500)$. In a single-channel phase-dispersive Omnès representation, the isospin-0 will then roughly equal the isospin-1 form factor, multiplied with a second Omnès function that contains the low-energy phase rise between $\pi\pi$ and $\pi\eta$ thresholds only. It is easily seen that this factor, leading to the famous $f_0(500)$ enhancement, simultaneously depletes the resonance signal of the $f_0(980)$ quite significantly: while it is (broadly) peaked around $\sqrt{s} = 500\,\text{MeV}$, it falls well below 1 around 1 GeV, the region of the second resonance.

Figure 2.17 depicts the described phase rise at low energies due to the $f_0(500)$ resonance (red, solid curve), given roughly by the difference of the isoscalar (green, dotted curve) and the isovector (orange, dash-dotted) $\bar{K}K$ form factor phases, as well as the corresponding Omnès functions. Our main interest here is to qualitatively illustrate the emergence of the $f_0(500)$ enhancement; we therefore refrain from including error bands due to the uncertainties in the form factor normalizations or different possible input phases $\delta_{1,2}$ (such as those presented in Figure 2.16)—we rather pick one configuration set ($\delta_{12} = 90°$ and the lower edge of the uncertainty bands) and approximate the phase difference by an exactly constant term above the $\pi\eta$ threshold. In the left panel of Figure 2.17 the Omnès solutions are shown. The green, dotted and the orange, dash-dotted curves are calculated as single-channel approximations based on the phases extracted from the coupled-channel form factor solutions shown in the right panel. Both solutions exhibit a prominent peak in the $f_0(980)/a_0(980)$ region. We observe the $f_0(500)$ enhancement in the $I = 0$ Omnès solution that is attended by the congruent bump in the Omnès solution constructed out of the phase difference (red, solid curve). Further, the figure shows the discussed depletion near 1 GeV in the $I = 0$ Omnès solution.

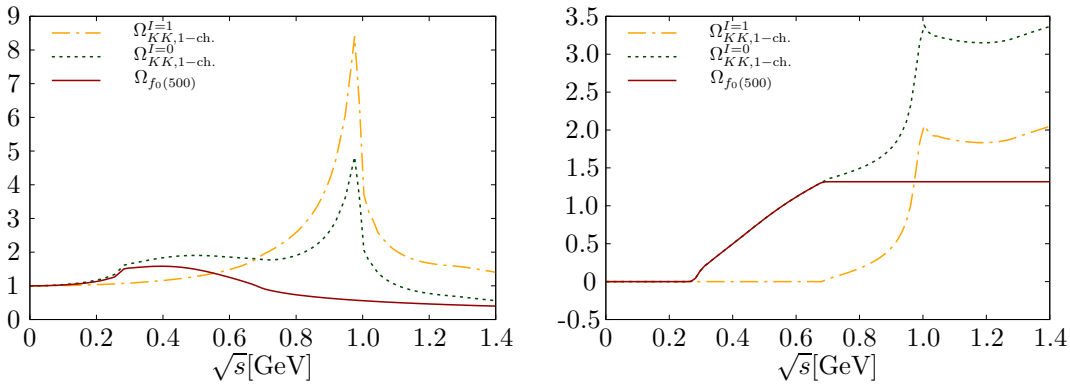

Figure 2.17: Illustration of the $f_0(500)$ enhancement emerging from the phase difference between isoscalar and isovector $K\bar{K}$ form factor phases. The left panel shows the Omnès solutions constructed as single-channel approximations for the $I = 0$ and $I = 1$ $\bar{K}K$ Omnès solutions, as well as the Omnès function constructed using the phase difference $\arg\Gamma^{I=0}_{KK}(s) - \arg\Gamma^{I=1}_{KK}(s)$. The right panel shows this phase difference (approximated by a constant term above the $\pi\eta$ threshold) as well as the phases extracted from the coupled-channel $\bar{K}K$ $I = 0$ and $I = 1$ form factors.

Finally, it can be seen in Figure 2.15 that the peak in the K^+K^- angular moment is located around $\sqrt{s} \simeq 990\,\text{MeV}$ and is quite narrow, whereas the $K^0\bar{K}^0$ threshold lies at $\sqrt{s} \simeq 995\,\text{MeV}$. Accordingly the peak in the $K^0\bar{K}^0$ distribution is phase-space suppressed.

There are three experimental points available in the charged kaon spectrum in the region we investigate, providing a test of our prediction, which is solely based on coupled-channel and isospin relations.[12] Each of the two data points that are located above threshold agrees with one of our different determinations of $\langle Y^0_0 \rangle$, depending on the value of the input phase δ_{12}. Tempting as it would be, we refrain from fitting these data points by modifying our theoretical input. We content ourselves with illustrating that new and improved data would help in constraining the $\pi\eta$–$\bar{K}K$ form factors, and thus our theoretical understanding of their final-state interactions and the properties of the $a_0(980)$ and (indirectly) the $f_0(980)$ resonances.

2.8.2 $\bar{B}^0_s \to J/\psi K^+K^-$ S-wave prediction

Having obtained the $\bar{B}^0_s \to J/\psi\pi^+\pi^-$ fit parameters, we can straightforwardly make a prediction for the $\bar{B}^0_s \to J/\psi K^+K^-$ S-wave amplitudes. The $\bar{s}s$ source that produces the kaons is purely isoscalar, such that we do not have to consider an $I = 1$ S-wave contribution (with an $a_0(980)$ resonance). Hence we can use in a direct way the relation between the $\pi\pi$ and the $K\bar{K}$ final states provided by the coupled-channel formalism, cf. Sections 1.3.4 and 2.4.5.

In particular an understanding of the S-wave background to the prominent $\phi(1020)$ is of interest. In the LHCb analysis [185], the $f_0(980)$ as well as a non-resonant S-wave content is reported within a mass window of $\pm 12\,\text{MeV}$ around the $\phi(1020)$, which contribute an S-wave fraction of $(1.1 \pm 0.1^{+0.2}_{-0.1})\%$—consistent with former measurements from LHCb, CDF, and ATLAS [199–201], with the newest LHCb analysis for the $\bar{B}^0_s \to J/\psi K^+K^-$ decay [202], as well as theoretical estimates [203]. We calculate the S-wave fraction in the same mass

[12] Note that the data we compare to is binned; to compare the spectrum with charged to the one with neutral kaon pairs in the final states we rescale the latter.

interval $\pm 12\,\text{MeV}$ around the $\phi(1020)$ mass adopting the LHCb Breit–Wigner parametrization for the $\phi(1020)$, but using the predicted S-wave for the $J/\psi K^+K^-$ final state. As discussed in Section 2.4.5, this S-wave can be obtained by replacing the pion scalar form factor and all pion masses and momenta by the respective kaon quantities and taking the resulting fit parameters from the pion case, after properly normalizing both $\pi\pi$ and $\bar{K}K$ experimental spectra.

The S-wave contribution to the $\phi(1020)$ peak region is given by

$$\mathcal{R}_{S/\phi} \equiv \frac{\int_{m_\phi-12\,\text{MeV}}^{m_\phi+12\,\text{MeV}} X^3 Y \sqrt{s}\,|\bar{c}_0^s \Gamma_K^s(\sqrt{s})|^2\,\mathrm{d}\sqrt{s}}{\int_{m_\phi-12\,\text{MeV}}^{m_\phi+12\,\text{MeV}} \sqrt{4\pi}\langle Y_0^0\rangle_{\bar{B}_s^0\to J/\psi K^+K^-}\,\mathrm{d}\sqrt{s}}, \tag{2.112}$$

where we can approximate the (normalized) angular moment in the region of interest by the S-wave and the $\phi(1020)$ contribution, cf. Eqs. (2.61) and (2.65). Using the B+O input, we obtain $\mathcal{R}_{S/\phi} = 1.1\%$, in agreement with the LHCb results. However, there is a notable uncertainty due to the estimated ambiguity in the phase input in the region of the $f_0(980)$ resonance discussed in Section 2.5.2. Using the DP phase instead of the B+O phase input yields a fraction of 1.95%.

2.9 Summary and outlook

In this chapter, we have described the strong-interaction part of the $\bar{B}^0_{d/s} \to J/\psi M_1 M_2$ decays, M_1M_2 being a light meson pair $\pi^+\pi^-$, $\pi^0\eta$, K^+K^- or $K^0\bar{K}^0$, by means of dispersively constructed scalar and vector pion form factors. This formalism respects all constraints from analyticity and unitarity. The non-strange and strange scalar form factors are calculated from a two-channel Muskhelishvili–Omnès formalism that in the isoscalar case requires the pion–pion elastic S-wave phase shift as well as modulus and phase of the corresponding $\pi\pi \to K\bar{K}$ amplitude as input. For the vector form factor, an elastic Omnès representation based solely on the pion–pion P-wave phase shift is sufficient, supplemented by an enhanced isospin-breaking contribution of ρ–ω mixing, which can be fixed from data on $e^+e^- \to \pi^+\pi^-$. The isovector scalar form factors are calculated using the approach of Ref. [140], where chiral constraints and unitarity have been imposed.

We employed the $\pi\pi$ spectra to determine the fit parameters and to demonstrate that for energies $\sqrt{s} \leq 1.02\,\text{GeV}$, a minimal description of all S- and P-waves (constructed in a form free of kinematical singularities) as the corresponding form factors, multiplied by real constants, is sufficient. Allowing for subtraction polynomials with linear s-dependence leads to a slightly improved fit quality solely in the case of one P-wave component, with a slope still compatible with zero within uncertainties. In particular considering the S-wave slope as a free fit parameter (as opposed to fixing it to zero) only yields a minimal improvement of the χ^2. In accordance with expectations from the underlying tree-level decay mechanism, below the onset of D-wave contributions that become important with the $f_2(1270)$, only the non-strange scalar and the vector form factors feature in the $\bar{B}^0_d$ decay, while the strange scalar form factor determines the $\bar{B}^0_s$ S-wave.

The overall fit quality in the energy range considered is at least as good as in the phenomenological fits by the LHCb collaboration [141, 142], where Breit–Wigner resonances and non-resonant background terms were used. However, since the dispersive analysis allows one to use input from other sources, our analysis calls for a much smaller number of parameters to be determined from the data. In addition, a comparison of the $\bar{B}^0_d$ S-wave obtained from the dispersive analysis with the one deduced from the LHCb analysis shows drastic differences in both modulus and phase: it is well-known that the $f_0(500)$ does not have a Breit–Wigner shape, and therefore such parametrizations should be avoided—especially when it comes to studies of CP violation that need a reliable treatment of the phases induced by the hadronic final-state

interactions [149]. The LHCb analysis of the $\bar{B}^0_s$ S-wave uses a Flatté parametrization of the $f_0(980)$, solely (corresponding to their Solution I) or combined with a non-resonant background (Solution II). Only Solution II yields a phase that is close to the phase of the strange scalar form factor, and approximately compatible with Watson's final-state interaction theorem in the elastic region.

Having shown that our formalism works, we have made predictions for the S-waves in $\bar{B}^0_{d/s} \to J/\psi\{\pi^0\eta, K^+K^-, \bar{K}^0K^0\}$, which are related to the corresponding $\pi^+\pi^-$ final states through channel coupling and chiral symmetry. For the $\bar{B}^0_s \to J/\psi K^+K^-$ S-wave only the results of the fit to the $\pi^+\pi^-$ final state are required to predict an S-wave fraction below the $\phi(1020)$ resonance of about 1.1%, in agreement with the findings by the LHCb collaboration. Describing the $\bar{B}^0_d$ modes involves the isovector scalar form factors that are constrained except for a free parameter δ_{12}. We demonstrated that experimental data for $\bar{B}^0_d \to J/\psi(\pi\eta, \bar{K}K)$ can be used to further constrain this parameter, that is crucial to pin down the $\pi\eta$ scattering amplitude. Around 1 GeV, the latter is dominated by the pole of the scalar meson $a_0(980)$. A high-accuracy determination of δ_{12} would, however, need further theoretical development.

In addition, in the scalar sector enhanced isospin-violating effects can occur around the two-kaon thresholds, driven by both the proximity of resonances in the isoscalar ($f_0(980)$) as well as isovector ($a_0(980)$) channels, and the 8 MeV gap between the K^+K^- and $K^0\bar{K}^0$ thresholds [204]. This phenomenon is usually referred to as a_0–f_0 mixing in the literature, and has been argued to be significant for, e.g., $\eta(1405) \to 3\pi$ [205, 206], weak decays of D_s/B_s mesons [207], and $J/\psi \to \phi\pi^0\eta$ [190, 208]. The predictions of the last mentioned theoretical calculations were confirmed experimentally at BES III [209, 210].

First steps towards a rigorous dispersive treatment of a_0–f_0 mixing are reported in Ref. [211, 212]. An adaption of this formalism to the reactions at hand will be pursued elsewhere. Here it would in particular be important to perform a detailed study of $\bar{B}^0_s \to J/\psi\pi^0\eta$, since the weak decay that drives the transition leads to a purely isoscalar source.

To extend our description of the form factors to higher energies, eventually covering most of the energy range accessible in $\bar{B}^0_{d/s} \to J/\psi\pi^+\pi^-$, inelastic channels with corresponding higher resonances have to be taken into account. Here, a formalism developed for the vector form factor [99] that correctly implements the analytic structure and unitarity, reduces to the Omnès representation in the elastic regime, but maps smoothly onto an isobar-model picture at higher energies should be extended to the scalar sector. There is an ongoing study that adopts this formalism to the considered $B_{d/s}$ decays [213]. Even an *extraction* of the scalar form factors from these high-precision LHCb data sets seems feasible, and should be pursued in the future.

Chapter 3

Analysis of the decay $D^+ \to K^-\pi^+l^+\nu_l$

3.1 Introduction

The pion–kaon system is one of the most prominent two-particle systems in hadronic reactions. Extracting information on pion–kaon phase shifts with high accuracy is therefore essential for precision studies of any process involving pions and kaons in the final state. We investigate the semileptonic decay $D^+ \to K^-\pi^+l^+\nu_l$ (abbreviated by D_{l4}), in particular we consider D_{e4}, where the final-state lepton is an electron. The D_{l4} decay is supposed to be the most suitable one for the purpose of such a phase-shift analysis [214]. This assumption relies on its analogy to the $K \to \pi\pi l\nu$ (K_{l4}) decays, from which the phase differences $\delta_0^0 - \delta_1^1$ for the isoscalar S- and isotriplet P-wave $\pi\pi$ scattering phase shifts were extracted [215–218]. Similar techniques applied to the D_{l4} decay seem to be feasible in order to gain information about the $I = 1/2$ πK phases. In particular an analysis of the full angular decay distribution including interference terms provides information about the πK S- and P-wave difference $\delta_1^{1/2} - \delta_0^{1/2}$. Alternative D-meson decays involving pion–kaon systems may also shed light on the pion–kaon phase shifts. For example the $D^+ \to K\pi\pi^+$ Dalitz plot is dominated by $I = 1/2$ πK partial waves. However, three-particle interactions considerably shape the phases of the involved amplitudes and therefore complicate the extraction of two-particle phase-shift information [130, 131].

In contrast to the K_{l4} decays, the D_{l4} decay gives access to dynamics also at higher energies with a clear resonant structure visible in the D_{l4} P-wave due to the $K^*(892)$. Achieving a high-precision phase-shift determination hence requires to accurately describe the hadron-physics aspects, taking into account the final-state interactions of the hadrons. We will treat this within a dispersive approach, being model-independent, and using πK phase shifts obtained from Roy–Steiner analyses [37]. This treatment is very closely related to the analysis of the decay $B \to \pi\pi l\nu$ (B_{l4}) [126], suggested to extract the Cabibbo–Kobayashi–Maskawa (CKM) matrix element $|V_{ub}|$. We use and develop further the method used there: Omnès representations, in which the crossed-channel effects are approximated by simple pole terms calculated in Heavy-Meson Chiral Perturbation Theory (HMChPT), are employed to describe the hadronic partial-wave amplitudes. By transferring this method to the D_{l4} decay, we are confronted with several challenging aspects: for example we have to scrutinize the application of HMChPT in the D_{l4} case, where the convergence of the heavy-mass and chiral expansions is much slower than for the B_{l4} amplitudes, and hence have to carefully consider the limitations of that description.

Further, we have to generalize the formalism of Ref. [126] to unequal-mass pseudoscalars in the final state.

Such a modified Omnès formalism, in which left-hand-cut structures are approximated by resonance exchange, is also utilized in the analyses of $\gamma\gamma \to \pi\pi$ [122], $\eta \to \pi\pi\gamma$ [129], and the $\Upsilon(3S) \to \Upsilon(1S)\pi\pi$ and $\Upsilon(4S) \to \Upsilon(1S, 2S)\pi\pi$ decays [219, 220]. A limiting factor of the approach, discussed in Ref. [126], is the restricted kinematic range: the dispersive formalism as applied there requires to fix the dilepton energy at a rather large value, forcing the pion momenta to be small, i.e. only a small part of the phase space can be described. We therefore propose a generalization of this formalism that allows for a reliable description of a much larger kinematic range, by extrapolating the dispersive representations to arbitrary dilepton energies. For this purpose we employ certain low-energy theorems that yield constraints for the dilepton energy dependency of the S-wave representation.

The organization of this chapter is as follows. In Section 3.2 the kinematics of the D_{l4} decay is reviewed and the definitions of the form factors constituting the matrix element as well as their partial-wave expansions are introduced. The dispersive representation of the partial waves using the modified Omnès formalism is presented in Section 3.3. Employing HMChPT expressions for the pole terms, their partial-wave projections (called inhomogeneities) and the reconstructed partial waves in the dispersive representation are explicitly derived. We discuss matching conditions, e.g. from high-energy constraints. A digression to D_{l3} form factors is performed in Section 3.4, introducing the soft-pion and soft-kaon theorems. These provide a cross-check for the calculated D_{l4} pole terms, as well as a tool for the extrapolation to smaller dilepton energies as mentioned above. We propose a parametrization in conformal variables for the subtraction polynomials and give a prediction for the S-wave. We summarize and discuss our results in Section 3.5 with a critical view on the presented formalism, working out the limitations and exposing certain weak points of our approach. Certain technical issues like investigating the analytic behavior of several kinematic functions and supplementary calculations, e.g. the determination and error analysis of coupling constants that contribute at NLO to the HMChPT Lagrangian, are relegated to the Appendices B.1-B.5.

3.2 Kinematics and decay rate

The kinematics of the decay $D^+(p_D) \to K^-(p_K)\pi^+(p_\pi)l^+(p_l)\nu_l(p_\nu)$ can be described by five variables, defined in three different reference frames, see Figure 3.1 [215, 221, 222]:

- the invariant dimeson mass squared, $s = (p_\pi + p_K)^2$;
- the invariant dilepton mass squared, $s_l = (p_l + p_\nu)^2$;
- the angle θ_K between the kaon in the πK center-of-mass frame $\Sigma_{\pi K}$ and the dimeson line-of-flight in the D^+ rest frame Σ_D;
- the angle θ_l between the charged lepton l in the $l\nu$ center-of-mass frame $\Sigma_{l\nu}$ and the dilepton line-of-flight in Σ_D;
- the angle ϕ between $\Sigma_{\pi K}$ and $\Sigma_{l\nu}$.

We define the two remaining Mandelstam variables as

$$t = (p_D - p_\pi)^2 \quad \text{and} \quad u = (p_D - p_K)^2, \tag{3.1}$$

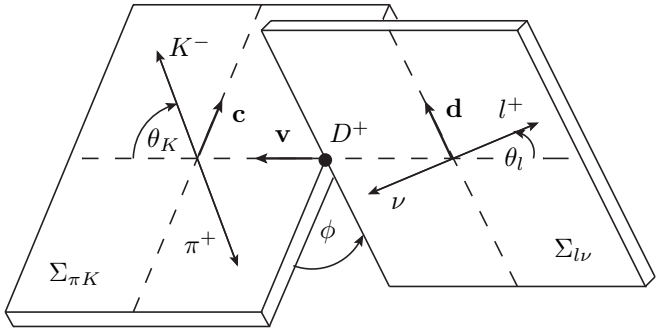

Figure 3.1: Definition of the kinematical variables for D_{l4}.

and introduce four additional vectors as combinations of the above four-momenta,

$$\begin{aligned} P &= p_K + p_\pi, \quad Q = p_K - p_\pi, \\ L &= p_l + p_{\nu_l}, \quad N = p_l - p_{\nu_l}, \\ P \cdot L &= \frac{m_D^2 - s - s_l}{2}. \end{aligned} \tag{3.2}$$

For later purposes we give the Mandelstam variable t in terms of s and $\cos\theta_K$,

$$t(s, \cos\theta_K) = \frac{3s_0 - s}{2} - XY\cos\theta_K + \frac{\Delta_m}{2s}, \tag{3.3}$$

where $3s_0 = m_D^2 + M_\pi^2 + M_K^2 + s_l$, $\Delta_m = (m_D^2 - s_l)(M_K^2 - M_\pi^2)$, and

$$X = [(P\cdot L)^2 - s_l s]^{1/2} = \frac{\lambda^{1/2}(m_D^2, s_l, s)}{2}, \quad Y = \frac{\lambda^{1/2}(s, M_\pi^2, M_K^2)}{s}, \tag{3.4}$$

with the Källén function

$$\lambda(a,b,c) = a^2 + b^2 + c^2 - 2ab - 2ac - 2bc. \tag{3.5}$$

A similar relation for $u(s, \cos\theta_K)$ yields

$$t - u = -2XY\cos\theta_K + \frac{\Delta_m}{s}. \tag{3.6}$$

Since the functions X and Y are only well-defined in the physical region $(M_\pi + M_K)^2 \le s \le (m_D - \sqrt{s_l})^2$, they have to be analytically continued outside this region according to

$$X = \begin{cases} |X|, & s \le (m_D - \sqrt{s_l})^2 \\ -|X|, & s \ge (m_D + \sqrt{s_l})^2 \\ i|X|, & \text{else} \end{cases}, \quad Y = \begin{cases} |Y|, & s \ge (M_\pi + M_K)^2 \\ -|Y|, & s \le (M_K - M_\pi)^2 \\ i|Y|, & \text{else} \end{cases}. \tag{3.7}$$

Note that this assumes values for s_l as physically accessible in the decay.

The D_{l4} matrix element can be written in terms of four dimensionless form factors F, G, R, and H,

$$\begin{aligned} \mathcal{M}_{fi} &= \frac{G_F}{\sqrt{2}} V_{cs} \underbrace{\langle \pi(p_\pi) K(p_K) | \bar{s}\gamma_\mu(1-\gamma_5)c | D(p_D)\rangle}_{\mathcal{M}_\mu^{\text{had}}} \times \underbrace{\bar{u}(p_\nu)\gamma^\mu(1-\gamma_5)v(p_l)}_{\mathcal{M}_{\text{lept}}^\mu}, \\ \mathcal{M}_\mu^{\text{had}} &= -\frac{i}{m_D}(P_\mu F + Q_\mu G + L_\mu R) - \frac{1}{m_D^3}\epsilon_{\mu\nu\rho\sigma} L^\nu P^\rho Q^\sigma H, \end{aligned} \tag{3.8}$$

where $G_F = 1.166365\times10^{-5}\,\mathrm{GeV}^{-2}$ is the Fermi constant, V_{cs} denotes the CKM matrix element for a $c \to s$ quark transition, and we define $\epsilon_{\mu\nu\rho\sigma}$ with the convention $\epsilon_{0123} = -\epsilon^{0123} = +1$. Considering the D_{e4} decay, with $m_e \ll 1$, the contribution from the form factor R can be neglected.

In order to calculate the differential decay distribution we take the absolute square of the matrix element Eq. (3.8) and sum over the lepton polarizations,

$$\begin{aligned}\sum_{\text{spins}} |M_{fi}|^2 &= 4G_F^2|V_{cs}|^2 H_{\mu\nu}L^{\mu\nu},\\ H_{\mu\nu} &= \mathcal{M}_\mu^{\text{had}}\left(\mathcal{M}_\nu^{\text{had}}\right)^*,\\ L^{\mu\nu} &= \frac{1}{8}\mathcal{M}_{\text{lept}}^{\mu}\left(\mathcal{M}_{\text{lept}}^{\nu}\right)^* = \frac{1}{2}\left(L^\mu L^\nu - N^\mu N^\nu - s_l g^{\mu\nu} - i\epsilon^{\rho\mu\sigma\nu}L_\rho N_\sigma\right).\end{aligned} \tag{3.9}$$

We obtain

$$\frac{\mathrm{d}^5\Gamma}{\mathrm{d}s\mathrm{d}s_l\mathrm{d}\cos\theta_K\mathrm{d}\cos\theta_l\mathrm{d}\phi} = \frac{G_F^2|V_{cs}|^2}{(4\pi)^6 m_D^3}XY\cdot\mathcal{I}(s,s_l,\theta_K,\theta_l,\phi), \tag{3.10}$$

with

$$\begin{aligned}\mathcal{I} =&\mathcal{I}_1 + \mathcal{I}_2\cos2\theta_l + \mathcal{I}_3\sin^2\theta_l\cos2\phi + \mathcal{I}_4\sin2\theta_l\cos\phi + \mathcal{I}_5\sin\theta_l\cos\phi + \mathcal{I}_6\cos\theta_l\\ &+ \mathcal{I}_7\sin\theta_l\sin\phi + \mathcal{I}_8\sin2\theta_l\sin\phi + \mathcal{I}_9\sin^2\theta_l\sin2\phi,\\ \mathcal{I}_1 =&\frac{1}{4m_D^2}\left[|F_1|^2 + \frac{3}{2}\sin^2\theta_K Y^2 s s_l\left(|F_2|^2 + \frac{|F_3|^2X^2}{m_D^4}\right)\right],\\ \mathcal{I}_2 =&-\frac{1}{4m_D^2}\left[|F_1|^2 - \frac{1}{2}\sin^2\theta_K Y^2 s s_l\left(|F_2|^2 + \frac{|F_3|^2X^2}{m_D^4}\right)\right],\\ \mathcal{I}_3 =&-\frac{Y^2 s s_l}{4m_D^2}\left(|F_2|^2 - \frac{|F_3|^2X^2}{m_D^4}\right)\sin^2\theta_K,\\ \mathcal{I}_4 =&\frac{Y\sqrt{ss_l}}{2m_D^2}\mathrm{Re}\left(F_1^*F_2\right)\sin\theta_K,\\ \mathcal{I}_5 =&\frac{YX\sqrt{ss_l}}{m_D^4}\mathrm{Re}\left(F_1^*F_3\right)\sin\theta_K,\\ \mathcal{I}_6 =&\frac{Y^2Xss_l}{m_D^4}\mathrm{Re}\left(F_2^*F_3\right)\sin^2\theta_K,\\ \mathcal{I}_7 =&\frac{Y\sqrt{ss_l}}{m_D^2}\mathrm{Im}\left(F_1F_2^*\right)\sin\theta_K,\\ \mathcal{I}_8 =&\frac{YX\sqrt{ss_l}}{2m_D^4}\mathrm{Im}\left(F_1F_3^*\right)\sin\theta_K,\\ \mathcal{I}_9 =&-\frac{Y^2Xss_l}{2m_D^4}\mathrm{Im}\left(F_2F_3^*\right)\sin^2\theta_K,\end{aligned} \tag{3.11}$$

where we use an alternative set of form factors F_i, $i = \{1\ldots3\}$ (F_4 is only relevant for $m_l \neq 0$),

$$F_1 = XF + \left[-Y(P\cdot L)\cos\theta_K + \left(\frac{M_K^2 - M_\pi^2}{s}\right)X\right]G, \quad F_2 = G, \quad F_3 = H, \tag{3.12}$$

which allows to express the $\mathcal{I}_i$, $i = 1\ldots9$, in such a compact form.[1] The partial-wave expansions

[1] These new form factors are introduced when rewriting the matrix element Eq. (3.8) instead of the standard

for the form factors $F_i(s, s_l, \cos\theta_K)$ in the helicity formalism read

$$\begin{aligned}
F_1(s, s_l, \cos\theta_K) &= \sum_{l=0}^{\infty} \tilde{F}_{1,l}(s, s_l) P_l(\cos\theta_K) \equiv X \sum_{l=0}^{\infty} f_l(s, s_l) P_l(\cos\theta_K), \\
F_2(s, s_l, \cos\theta_K) &= \sum_{l=1}^{\infty} \frac{1}{\sqrt{l(l+1)}} \tilde{F}_{2,l}(s, s_l) P_l'(\cos\theta_K) \equiv \sum_{l=1}^{\infty} g_l(s, s_l) P_l'(\cos\theta_K), \\
F_3(s, s_l, \cos\theta_K) &= \sum_{l=1}^{\infty} \frac{1}{\sqrt{l(l+1)}} \tilde{F}_{3,l}(s, s_l) P_l'(\cos\theta_K) \equiv \sum_{l=1}^{\infty} h_l(s, s_l) P_l'(\cos\theta_K).
\end{aligned} \tag{3.13}$$

In the following we will consider S- and P-waves only, assuming that higher partial waves are negligible in the here considered energy region. This assumption is based on several experimental observations by the FOCUS, BaBar and BES III collaborations [223–225], that the $K\pi$ system is P-wave dominated by the $\bar{K}^*(892)^0$ component; also S-wave contributions were found, while the D-wave sets in at a higher energy with a $\bar{K}_2^*(1430)^0$ resonance. Hence the form factors are expressed as

$$\begin{aligned}
F_1(s, s_l, \cos\theta_K) &= X\Big(|f_0(s, s_l)| e^{i\delta_0^{1/2}(s,s_l)} + \cos\theta_K |f_1(s, s_l)| e^{i\delta_1^{1/2}(s,s_l)}\Big), \\
F_2(s, s_l, \cos\theta_K) &= |g_1(s, s_l)| e^{i\delta_1^{1/2}(s,s_l)}, \\
F_3(s, s_l, \cos\theta_K) &= |h_1(s, s_l)| e^{i\delta_1^{1/2}(s,s_l)}.
\end{aligned} \tag{3.14}$$

Integrating Eq. (3.10) over the angles θ_l and ϕ in the limits $0 \leq \theta_l \leq \pi$ and $0 \leq \phi \leq 2\pi$ yields

$$\frac{\mathrm{d}^3\Gamma}{\mathrm{d}s\mathrm{d}s_l\mathrm{d}\cos\theta_K} = \frac{G_F^2 |V_{cs}|^2}{3(4\pi)^5 m_D^5} XY \left[|F_1|^2 + \sin^2\theta_K Y^2 s s_l \left(|F_2|^2 + \frac{|F_3|^2 X^2}{m_D^4}\right)\right]. \tag{3.15}$$

If we insert the partial-wave expanded form factors, neglect waves higher than P-waves, and integrate over the angle $\cos\theta_K$ in the limits $0 \leq \theta_K \leq \pi$, we obtain

$$\frac{\mathrm{d}^2\Gamma}{\mathrm{d}s\mathrm{d}s_l} = \frac{2G_F^2 |V_{cs}|^2}{3(4\pi)^5 m_D^5} XY \left[X^2 \left(|f_0|^2 + \frac{1}{3}|f_1|^2\right) + \frac{2}{3} Y^2 s s_l \left(|g_1|^2 + \frac{|h_1|^2 X^2}{m_D^4}\right)\right]. \tag{3.16}$$

The differential decay rates thus obtained depend on the magnitudes of the partial wave form factors only, while the information on the S- and P-wave phases is integrated out—the above relations hence are unsuitable for the target extraction of the phase-shift difference $\delta_0^{1/2}(s) - \delta_1^{1/2}(s)$. For the purpose of such an extraction, however, it is expedient to integrate Eq. (3.10) over the angle θ_K and the dilepton energy s_l (in the limit $0 \approx m_e^2 \leq s_l \leq (m_D - \sqrt{s})^2$)

basis of momenta P_μ, Q_μ, L_μ in a different basis of momentum vectors that correspond to the orthonormal basis of polarization vectors of the leptonic current, which directly links to the helicity basis, for details see Refs. [113, 160]. The partial-wave expansions of the $F_i(s)$ are then easily obtained, as they are well-known for helicity amplitudes $\mathcal{H}_\lambda(s)$,

$$\mathcal{H}_\lambda(s) = \sum_l \sqrt{2l+1} \mathcal{H}_\lambda^{(l)}(s) d_{\lambda 0}^l(\theta_K) e^{\lambda i\phi},$$

where the $d_{\lambda\lambda'}^l$ are the small Wigner-d functions, with

$$d_{00}^l(\theta_K) = P_l(\cos\theta_K), \quad d_{10}^l(\theta_K) = -d_{-10}^l(\theta_K) = -\frac{\sin\theta_K}{\sqrt{l(l+1)}} P_l'(\cos\theta_K).$$

instead. We define

$$\tilde{X}(s) = \int\int X(s,s_l)\mathrm{d}s_l\mathrm{d}\cos\theta_K = 2\int X(s,s_l)\mathrm{d}s_l,$$
$$\tilde{X}\langle\mathcal{I}_i(s)\rangle = \int\int X(s,s_l)\mathcal{I}_i(s,s_l,\cos\theta_K)\mathrm{d}\cos\theta_K\mathrm{d}s_l, \tag{3.17}$$

such that

$$\langle\mathcal{I}_i(s)\rangle = \frac{\int\int X(s,s_l)\mathcal{I}_i(s,s_l,\cos\theta_K)\mathrm{d}\cos\theta_K\mathrm{d}s_l}{2\int X(s,s_l)\mathrm{d}s_l}, \tag{3.18}$$

which allows to write the differential decay rate as

$$\frac{\mathrm{d}^3\Gamma}{\mathrm{d}s\mathrm{d}\phi\mathrm{d}\cos\theta_l} = \frac{G_F^2|V_{cs}|^2}{(4\pi)^6 m_D^3} Y\tilde{X}\langle\mathcal{I}(s,\theta_l,\phi)\rangle, \tag{3.19}$$

where $\langle\mathcal{I}(s,\theta_l,\phi)\rangle$ is decomposed in analogy to Eq. (3.11), with averages $\langle\mathcal{I}_i(s)\rangle$ that are accessible independently via variation in θ_l and ϕ. The following $\langle\mathcal{I}_i\rangle$ (the S–P-wave interference terms) depend on the desired phase shift difference $\delta_0^{1/2}(s) - \delta_1^{1/2}(s)$,

$$\begin{aligned}
\langle\mathcal{I}_4\rangle &= \frac{\pi Y\sqrt{s}}{8m_D^2}\langle X|f_0||g_1|\rangle\cos\left(\delta_0^{1/2}-\delta_1^{1/2}\right),\\
\langle\mathcal{I}_5\rangle &= \frac{\pi Y\sqrt{s}}{4m_D^4}\langle X^2|f_0||h_1|\rangle\cos\left(\delta_0^{1/2}-\delta_1^{1/2}\right),\\
\langle\mathcal{I}_7\rangle &= \frac{\pi Y\sqrt{s}}{4m_D^2}\langle X|f_0||g_1|\rangle\sin\left(\delta_0^{1/2}-\delta_1^{1/2}\right),\\
\langle\mathcal{I}_8\rangle &= \frac{\pi Y\sqrt{s}}{8m_D^4}\langle X^2|f_0||h_1|\rangle\sin\left(\delta_0^{1/2}-\delta_1^{1/2}\right),
\end{aligned} \tag{3.20}$$

with

$$\langle X^n|f_0||g_1|\rangle = \frac{\int\sqrt{s_l}X^n|f_0||g_1|\mathrm{d}s_l}{\int X\mathrm{d}s_l} \tag{3.21}$$

and similarly for $|g_1| \leftrightarrow |h_1|$. The last equality can be read off when inserting the $\mathcal{I}_i$, Eq. (3.11), explicitly into Eq. (3.18) and performing the angular integration. Hence in order to attain information on $\delta_0^{1/2} - \delta_1^{1/2}$, it is appropriate to determine either $\langle I_4\rangle$ and $\langle I_7\rangle$, or $\langle I_5\rangle$ and $\langle I_8\rangle$, since (assuming the absence of D- and higher partial waves)

$$\tan\left(\delta_0^{1/2}-\delta_1^{1/2}\right) = \frac{1}{2}\frac{\langle I_7\rangle}{\langle I_4\rangle} \quad\text{and}\quad \tan\left(\delta_0^{1/2}-\delta_1^{1/2}\right) = 2\frac{\langle I_8\rangle}{\langle I_5\rangle}. \tag{3.22}$$

3.3 Partial waves in the modified Omnès formalism

We study the partial-wave amplitudes f_0, f_1, g_1, and h_1 defined in the expansion Eq. (3.13) within dispersion theory, very closely related to the recent analysis of the B_{l4} decay [126]. The formalism, introduced in Ref. [102], is based on Omnès representations and was also used for an analysis of the related K_{l4} decays [128]. We do not apply dispersion theory to treat the s_l dependence of the amplitudes, so we consider them at fixed s_l and will suppress the s_l dependence for the moment. The range of s we consider here (confined by the physical decay region for a dilepton energy fixed at a rather large s_l) can be well described in the elastic approximation, where Watson's theorem [82] is valid, i.e. the phases of the partial-wave

amplitudes coincide with the pion–kaon scattering phase shifts (the elastic approximation works well up to the $K\rho$ "threshold" in the case of the P-wave and up to the $K\eta'$ threshold for the S-wave). Due to the principle of maximal analyticity they are analytic in the whole complex s-plane except for singularities dictated by unitarity and crossing symmetry. That is, there is a right-hand cut starting at the pion–kaon threshold $s = (M_\pi + M_K)^2$, as well as a left-hand cut due to the crossed process of πD scattering for $s \leq (M_K - M_\pi)^2$, which follows from Eq. (3.3),

$$t\left(\cos\theta_K = -1, s \leq (M_K - M_\pi)^2\right) \geq (m_D + M_\pi)^2. \tag{3.23}$$

Due to the lack of experimental information on πD scattering we will approximate the crossed process by D^*-pole terms. The form factors are split into pole and non-pole contributions, $F_i = F_i^{\text{pole}} + F_i^{\text{non-pole}}$. Instead of Eq. (3.13) we can perform a partial-wave expansion for the pole-term-subtracted amplitudes,

$$\begin{aligned}
F_1(s,z) =& F_1^{\text{pole}}(s,z) + X\sum_{l=0}^{\infty} M_l(s)P_l(z) = F_1^{\text{pole}}(s,z) + XM_0(s) + zXM_1^{(0)}(s) \\
=& F_1^{\text{pole}}(s,z) + X\left(M_0(s) - \frac{s(t-u)-\Delta_m}{sX^2}M_1(s)\right), \quad M_1(s) = \frac{X}{2Y}M_1^{(0)}(s), \\
F_2(s,z) =& F_2^{\text{pole}}(s,z) + \sum_{l=1}^{\infty} U_l(s)P_l'(z) = F_2^{\text{pole}}(s,z) + U_1(s), \\
F_3(s,z) =& F_3^{\text{pole}}(s,z) + \sum_{l=1}^{\infty} V_l(s)P_l'(z) = F_3^{\text{pole}}(s,z) + V_1(s),
\end{aligned} \tag{3.24}$$

with $z = \cos\theta_K$. D- and higher partial waves are suppressed. We have rescaled $M_1^{(0)}(s) \to M_1(s)$ in order to avoid singular behavior at the pseudo-threshold $s = \left(m_D - \sqrt{s_l}\right)^2$, where $X = 0$. Note that the amplitudes $M_0(s)$, $M_1(s)$, $U_1(s)$, and $V_1(s)$ have no poles by definition and are analytic except for a right-hand cut. Comparing Eq. (3.24) with Eq. (3.13) we directly infer that over the right-hand cut we have

$$\begin{aligned}
&\operatorname{Im} f_0(s) = \operatorname{Im} M_0(s), && \operatorname{Im} f_1(s) = \operatorname{Im}\left(\frac{2Y}{X}M_1(s)\right), \\
&\operatorname{Im} g_1(s) = \operatorname{Im} U_1(s), && \operatorname{Im} h_1(s) = \operatorname{Im} V_1(s).
\end{aligned} \tag{3.25}$$

Therefore we can rewrite the partial waves by

$$\begin{aligned}
&f_0(s) = M_0(s) + \hat{M}_0(s), && f_1(s) = \frac{2Y}{X}\left(M_1(s) + \hat{M}_1(s)\right), \\
&g_1(s) = U_1(s) + \hat{U}_1(s), && h_1(s) = V_1(s) + \hat{V}_1(s),
\end{aligned} \tag{3.26}$$

where we have introduced the inhomogeneities $\hat{M}_0(s)$, $\hat{M}_1(s)$, $\hat{U}_1(s)$, and $\hat{V}_1(s)$ that are real on the the right-hand cut by construction and are given by the respective partial-wave projections of the pole terms, e.g.

$$\hat{M}_l(s) = \frac{2l+1}{2}\int_{-1}^{1} \mathrm{d}z\, \frac{F_1^{\text{pole}}(s,z)}{X}P_l(z). \tag{3.27}$$

It is evident from Eq. (3.24) that the partial-wave expansions of F_2 and F_3 proceed in derivatives of Legendre functions; to project onto their partial waves we therefore use

$$\int_{-1}^{1} P_i'(z)\left[P_{j-1}(z) - P_{j+1}(z)\right]\mathrm{d}z = 2\delta_{ij}, \tag{3.28}$$

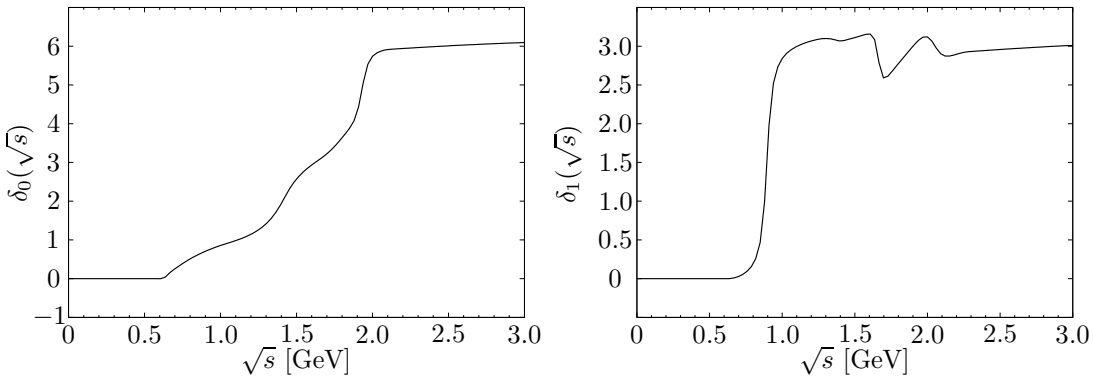

Figure 3.2: The πK phase shifts for $I = 1/2$ S- (left panel) and P-waves (right panel) are shown.

and find

$$\hat{U}_l(s) = \frac{1}{2}\int_{-1}^{1} \mathrm{d}z\, F_2^{\mathrm{pole}}(s,z)\,[P_{l-1}(z) - P_{l+1}(z)]\,, \tag{3.29}$$

and similarly for $\hat{V}_l$.

In order to construct the full partial-wave amplitudes we employ dispersion relations in terms of the Omnès formalism. In the following we will work in the elastic approximation and therefore start out with the elastic unitarity relation for the partial waves f_l, g_l, h_l. E.g. for f_0 the unitarity relation reads

$$\mathrm{Im}\, f_0(s) = f_0(s) e^{-i\delta_0(s)} \sin\delta_0(s). \tag{3.30}$$

In Eq. (3.26) the partial waves are given as the sum of the inhomogeneities $\hat{M}_0(s)$, $\hat{M}_1(s)$, $\hat{U}_1(s)$, and $\hat{V}_1(s)$, being the partial-wave projections of the pole terms, and of the functions $M_0(s)$, $M_1(s)$, $U_1(s)$, and $V_1(s)$, which possess no left-hand cuts or poles.

Together with Eq. (3.25) we can rewrite the partial-wave unitarity relations in favor of the pole-term-subtracted partial-wave amplitudes and their inhomogeneities,

$$\mathrm{Im}\, M_i(s) = \left(M_i(s) + \hat{M}_i(s)\right) e^{-i\delta_i(s)} \sin\delta_i(s). \tag{3.31}$$

This type of unitarity relations yields the following dispersive representation, also known as Khuri–Treiman type equation [103], see Section 1.3.3,

$$M_i(s) = \Omega_i(s)\left\{P_{n-1}(s) + \frac{s^n}{\pi}\int_{(M_\pi+M_K)^2}^{\infty} \frac{\hat{M}_i(s')\sin\delta_i(s')\mathrm{d}s'}{|\Omega_i(s')|(s'-s-i\epsilon)s'^n}\right\}, \tag{3.32}$$

and similarly for $U_1(s)$ and $V_1(s)$. The first part $\Omega_i(s)P_{n-1}(s)$ solves the homogeneous unitarity relation, where all inhomogeneities are turned off and therefore no left-hand-cut structure contributes.

The Omnès functions [80] for S- and P-waves, respectively, are constructed from a dispersion integral starting from the pion–kaon threshold $s = (M_\pi + M_K)^2$, including πK phase shifts $\delta_{0,1} \equiv \delta_{0,1}^{1/2}$,

$$\Omega_i(s) = \exp\left\{\frac{s}{\pi}\int_{(M_\pi+M_K)^2}^{\infty} \frac{\delta_i(s')\mathrm{d}s'}{s'(s'-s-i\epsilon)}\right\}. \tag{3.33}$$

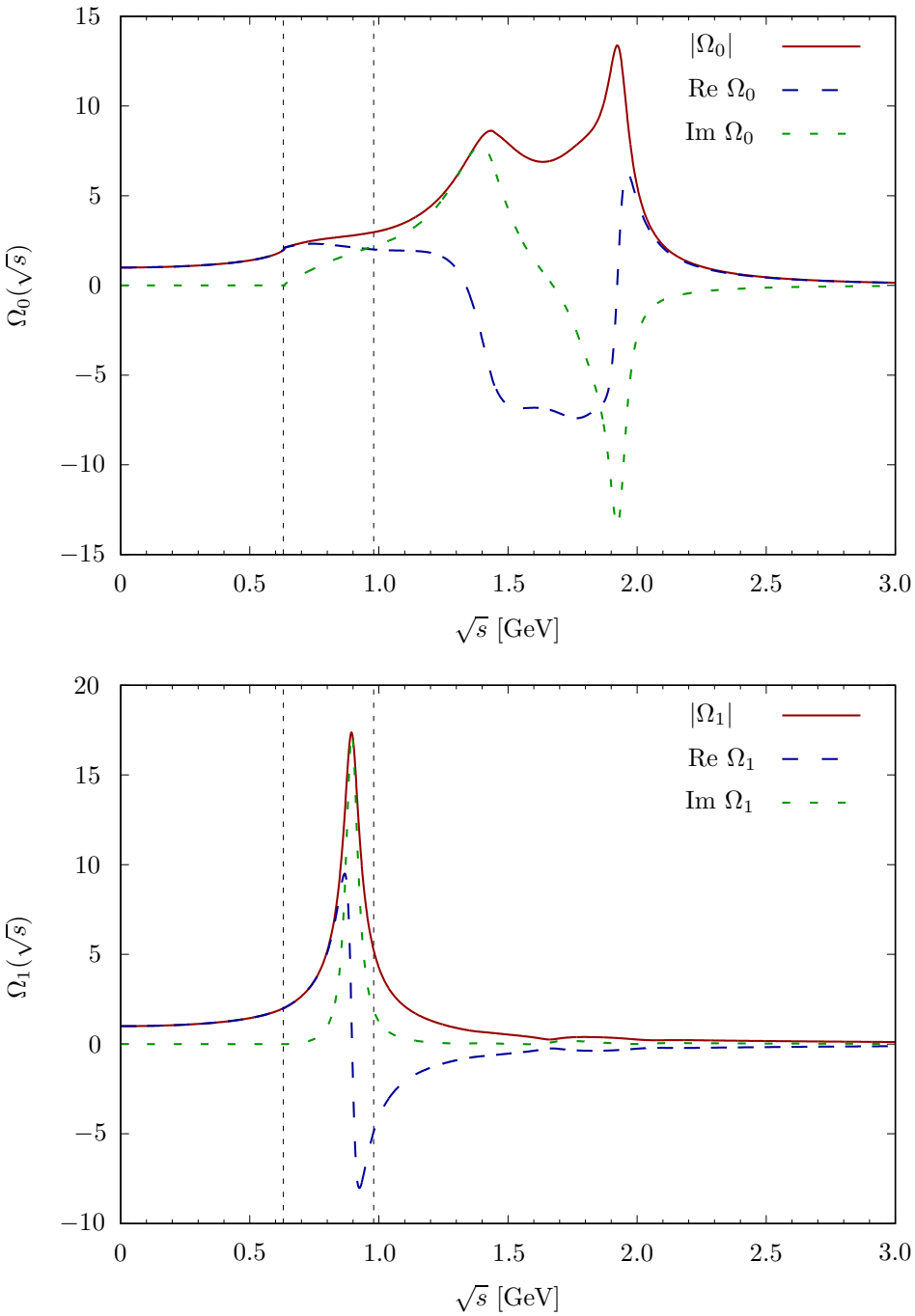

Figure 3.3: The modulus (red solid), real (blue dashed), and imaginary (green dotted) parts and of the πK Omnès solutions for the $I = 1/2$ S- (top panel) and P-waves (bottom panel) are shown.

Beyond a certain cutoff point s_0 the phase shifts are approximated by

$$\begin{aligned}
\delta_0(s) &= 2\pi + (\delta_0(s_0) - 2\pi)\frac{2}{1+(\frac{s}{s_0})^{3/2}}, & s_0 &= (2.1\text{ GeV})^2,\\
\delta_1(s) &= \pi + (\delta_0(s_0) - \pi)\frac{2}{1+(\frac{s}{s_0})^{3/2}}, & s_0 &= (2.3\text{ GeV})^2,
\end{aligned} \tag{3.34}$$

such that they approach a multiple of π for large s, which translates to the Omnès function behaving like $\sim s^{-n}$ for $\delta_i \to n\pi$ in the asymptotic s limit,

$$\begin{aligned}
\delta_0(s) &\to 2\pi : \ \Omega_0(s) \sim 1/s^2,\\
\delta_1(s) &\to \pi : \ \ \Omega_1(s) \sim 1/s.
\end{aligned} \tag{3.35}$$

The phase shifts and resulting Omnès solutions are shown in Figures 3.2 and 3.3. In the low-energy region $\sqrt{s} \lesssim 1$ GeV the Omnès solution for the P-wave exhibits a prominent peak due to the $K^*(892)$ resonance, while there is little structure in the S-wave—a rather rudimental rise is visible, adumbrating the broad κ resonance.

3.3.1 Inhomogeneities

We obtain explicit expressions of the inhomogeneities in the framework of HMChPT. The main concepts are briefly introduced in Section 1.2.2, and exemplified on the derivation of the contributing tree-level processes depicted in Figure 1.4; diagrams (B) and (C) contain the t-channel D^*-pole terms. The application of HMChPT in the case of D-mesons is quite precarious due to the handling of the charm quark as heavy; also the symmetry breaking by the kaon mass involves a large uncertainty. We will therefore consider next-to-leading order contributions as well. Furthermore, it was pointed out in Ref. [160] in connection with B_{l4} decays that HMChPT is only applicable for large values of s_l and small s. Due to a smaller phase space in D_{l4} decays, the range of s_l is restricted, $\sqrt{s_l} \leq m_D - M_K - M_\pi \approx 1.2$ GeV. An in-depth discussion on the reliability of HMChPT in our approach and the challenges and issues involved is presented in Section 3.5.

The form factors at NLO are calculated from the $\mathcal{O}(p)$ tree-level amplitudes Eq. (1.55), which implies for the form factors F, G, R and H, defined by Eq. (3.8), to be of the orders $\mathcal{O}(p^0)$, $\mathcal{O}(p^0)$, $\mathcal{O}(p)$, and $\mathcal{O}(p^{-1})$, respectively. We find

$$\begin{aligned}
R =& -\frac{1}{2F_\pi F_K}\Bigg(\frac{f_D m_D}{2} - \frac{f_{D_s} m_{D_s}}{2}\frac{v\cdot(p_K-p_\pi)+\mu+8\hat{m}\lambda_1+8p_K\cdot p_\pi\sigma_1+16v\cdot p_\pi\sigma_2}{v\cdot(p_K+p_\pi)+\mu}\\
&+\frac{g f_{D^*}\left(p_\pi^2 - v\cdot p_\pi m_{D^*}\right)}{\Delta + v\cdot p_\pi} - \frac{g^2 f_{D_s} m_{D_s}\left(p_\pi^2 (v\cdot p_K) + v\cdot p_\pi\,(p_K\cdot p_\pi)\right)}{(\Delta+v\cdot p_\pi)\,(v\cdot p_K + v\cdot p_\pi + \mu)} - 2\beta_2 m_D^2 v\cdot p_\pi\\
&-\frac{g^2 f_{D_s}\,(p_K\cdot p_\pi - (v\cdot p_\pi)\,(v\cdot p_K))}{(\Delta+v\cdot p_\pi)\,(v\cdot p_K + v\cdot p_\pi+\mu)} - \frac{2\beta_1 g p_K\cdot p_\pi + 2\beta_2 g m_{D^*}^2 v\cdot p_\pi v\cdot p_K}{\Delta + v\cdot p_\pi}\Bigg),\\
G =& \frac{(f_D - 2\beta_1)m_D}{4F_\pi F_K} + \frac{g m_D}{4F_\pi F_K}\frac{f_{D^*} v\cdot p_\pi + f_{D^*} m_{D^*} + 2\beta_1 v\cdot p_K + 2\beta_2 m_{D^*}^2 v\cdot p_K}{\Delta + v\cdot p_\pi},\\
H =& -\frac{1}{4F_\pi F_K}\left(\frac{2m_D^2\beta_1 g}{\Delta + v\cdot p_\pi} + \frac{g^2 f_{D_s^*} m_{D_s^*} m_D^2}{(\Delta+v\cdot p_\pi)\,(\Delta + v\cdot p_K + v\cdot p_\pi + \mu)}\right),\\
F =& -\frac{1}{4F_\pi F_K}\Bigg((f_D - 2\beta_1)m_D\\
&\qquad - \frac{g f_{D^*}(m_{D^*} v\cdot p_\pi + m_{D^*} m_D) + 2m_D\,(\beta_1 + \beta_2 m_{D^*} m_D)\,v\cdot p_K}{\Delta + v\cdot p_\pi}\Bigg).
\end{aligned} \tag{3.36}$$

By means of Eq. (3.12) the pole and non-pole contributions to the form factors F_1, F_2, and F_3 in HMChPT are obtained. In analogy to Ref. [226] we replace the effective P_a and P_a^* propagators by the full relativistic propagators to keep manifest Lorentz covariance and ensure the correct analytic behavior,

$$\begin{aligned}
\frac{1}{k\cdot v+\Delta} &= -\frac{2m_{D^*}}{(p_D-k)^2-m_{D^*}^2} \quad \overset{k=p_\pi}{\longrightarrow} \quad -\frac{2m_{D^*}}{t-m_{D^*}^2},\\
\frac{1}{k\cdot v+\mu} &= -\frac{2m_{D_s}}{(p_D-k)^2-m_{D_s}^2} \quad \overset{k=p_\pi+p_K}{\longrightarrow} \quad -\frac{2m_{D_s}}{s_l-m_{D_s}^2},\\
\frac{1}{k\cdot v+\Delta+\mu} &= -\frac{2m_{D_s^*}}{(p_D-k)^2-m_{D_s^*}^2} \quad \overset{k=p_\pi+p_K}{\longrightarrow} \quad -\frac{2m_{D_s^*}}{s_l-m_{D_s^*}^2},
\end{aligned} \tag{3.37}$$

and express the t-channel poles in terms of s and z, according to Eq. (3.3),

$$t(s,z)-m_{D^*}^2 = XY\,(y-z) \quad \text{with} \quad y=\frac{1}{2XY}\left(3s_0-s-2m_{D^*}^2+\frac{\Delta_m}{s}\right)\equiv\frac{\tilde{y}}{XY}. \tag{3.38}$$

Note that the numerators of the F_1^{pole} and F_2^{pole} amplitudes also have an angular dependence due to Eq. (3.3). It is therefore expedient to express the pole terms in the form

$$\begin{aligned}
F_1^{\text{pole}} =& \frac{\zeta_0+\zeta_1 z+\zeta_2 z^2}{y-z}, \quad F_2^{\text{pole}}=\frac{\xi_0+\xi_1 z}{y-z}, \quad F_3^{\text{pole}}=\frac{\gamma}{XY(y-z)},\\
\zeta_0 =& \frac{gm_{D^*}}{4F_\pi F_K Y s^2}\Bigg[\left(\beta_1+\beta_2 m_{D^*}^2\right)\Big[s^2-\left(M_K^2-M_\pi^2\right)^2\Big](m_D^2-s_l+s)\\
&+2sm_D^2 f_{D^*}\left(s-M_K^2+M_\pi^2+\frac{2\Delta s}{m_D}\right)\Bigg],\\
\zeta_1 =& \frac{gm_{D^*}}{4F_\pi F_K X s}\Bigg[\left(\beta_1+\beta_2 m_{D^*}^2\right)\Big[\left(M_K^2-M_\pi^2+s\right)(m_D^2-s_l+s)(P\cdot L)\\
&+2X^2\left(M_K^2-M_\pi^2-s\right)\Big]+2m_D^2 f_{D^*}(P\cdot L)s\Bigg],\\
\zeta_2 =& -\frac{gm_{D^*}}{2F_\pi F_K}(P\cdot L)Y\left(\beta_1+\beta_2 m_{D^*}^2\right),\\
\xi_0 =& -\frac{gm_{D^*}}{4F_\pi F_K XY}\left[\left(\beta_1+\beta_2 m_{D^*}^2\right)\left(s+M_K^2-M_\pi^2-s_l+m_D^2+\frac{\Delta_m}{s}\right)+2m_D^2 f_{D^*}\right],\\
\xi_1 =& \frac{gm_{D^*}}{2F_\pi F_K}\left(\beta_1+\beta_2 m_{D^*}^2\right), \quad \gamma=\frac{gm_D^2 m_{D^*}}{F_\pi F_K}\left(\frac{gm_{D_s^*}^2 f_{D_s^*}}{s_l-m_{D_s^*}^2}-\beta_1\right).
\end{aligned} \tag{3.39}$$

The non-pole contributions read

$$\begin{aligned}
F_1^{\text{non-pole}} =& \frac{Xgm_D f_{D^*}}{4F_\pi F_K}+\left[-Y(P\cdot L)z+\left(\frac{M_K^2-M_\pi^2-s}{s}\right)X\right]\frac{m_D}{4F_\pi F_K}\left(f_D-2\beta_1\right),\\
F_2^{\text{non-pole}} =& \frac{m_D}{4F_\pi F_K}\left(f_D-2\beta_1\right), \quad F_3^{\text{non-pole}}=0\,.
\end{aligned} \tag{3.40}$$

The s_l dependency of these form factors is of polynomial nature except for a pole $(s_l-m_{D_s^*}^2)^{-1}$ in the function γ entering F_3^{pole}.

The partial-wave projections of the non-pole parts of the amplitudes, $M_l(s)$, $U_l(s)$, and

$V_l(s)$, are obtained in analogy to Eqs. (3.27) and (3.29). We identify

$$\begin{aligned}
M_0^{\text{HMChPT}}(s) =& \frac{m_D}{4F_\pi F_K}\left\{\frac{M_K^2 - M_\pi^2}{s}\big(f_D - 2\beta_1\big) + \big(gf_{D^*} - f_D + 2\beta_1\big)\right\},\\
M_1^{\text{HMChPT}}(s) =& \frac{m_D}{4F_\pi F_K}\left\{\frac{1}{4}\big(s + s_l - m_D^2\big)\big(f_D - 2\beta_1\big)\right\},\\
U_1^{\text{HMChPT}}(s) =& \frac{m_D}{4F_\pi F_K}\left(f_D - 2\beta_1\right),\\
V_1^{\text{HMChPT}}(s) =& 0.
\end{aligned} \tag{3.41}$$

These functions are labeled by HMChPT in order to distinguish from the dispersively reconstructed amplitudes $M_l(s)$, $U_l(s)$, and $V_l(s)$ derived below, including a controlled final-state interaction. These dispersive representations involve subtraction polynomials that have to be determined. An approved ansatz to constrain these polynomials is to match them onto the respective HMChPT non-pole expressions, see e.g. Ref. [126].

We observe that due to the non-vanishing difference in the pseudoscalar masses, the pure pole-term-subtracted S-wave amplitude $M_0^{\text{HMChPT}}(s)$ has a contribution, which diverges for $s \to 0$,

$$M_0^{\infty}(s) \propto \frac{M_K^2 - M_\pi^2}{s}, \tag{3.42}$$

while the full amplitude $F_1^{\text{non-pole}}(s)$ is a polynomial in the Mandelstam variables. This poses a challenge for the matching approach. However, similarly to Ref. [219] we can get rid of that singularity in the partial wave by rewriting the singular expression in terms of the scattering angle $\cos\theta_K$ and the Mandelstam variables t and u according to Eq. (3.6). This entails on the one hand a redefinition of the S- and P-wave,

$$\begin{aligned}
\tilde{M}_0^{\text{HMChPT}}(s) =& \frac{m_D}{4F_\pi F_K}\Big[gf_{D^*} - f_D + 2\beta_1\Big],\\
\tilde{M}_1^{\text{HMChPT}}(s) =& -\frac{m_D}{4F_\pi F_K}\left[\frac{1}{4}\big(s + s_l - m_D^2\big) + \frac{X^2}{s_l - m_D^2}\right]\big(f_D - 2\beta_1\big),
\end{aligned} \tag{3.43}$$

and on the other hand additional contributions $\delta\hat{M}_0(s)$ and $\delta\hat{M}_1(s)$ to the inhomogeneities are introduced, stemming from polynomial S-wave amplitudes in the t- and u-channels that are projected onto the s-channel,

$$\delta\hat{M}_0(s) = \frac{m_D}{4F_\pi F_K}\frac{M_K^2 - M_\pi^2}{s}\big(f_D - 2\beta_1\big), \quad \delta\hat{M}_1(s) = \frac{m_D}{4F_\pi F_K}\frac{X^2}{s_l - m_D^2}\big(f_D - 2\beta_1\big). \tag{3.44}$$

Hence, the singularity is shifted to the inhomogeneities, away from the non-pole amplitudes, such that the subtraction polynomials can be matched to those. This procedure introduces poles $\sim (s_l - m_D^2)^{-1}$ in the P-wave projections of the non-pole and pole contributions, $\tilde{M}_1^{\text{HMChPT}}$ and $\delta\hat{M}_1$ (cancelling in the sum $\hat{M}_1 + \tilde{M}_1^{\text{HMChPT}}$). The only nontrivial analytic structure in s_l that resides in the final representation is due to these poles in $\tilde{M}_1^{\text{HMChPT}}$, $\delta\hat{M}_1$, and γ.

Our next step is to derive the inhomogeneities, given by the partial-wave projected pole terms, and supplemented by the contributions $\delta\hat{M}_{0,1}$, Eq. (3.44). We notice that the integrals in Eqs. (3.27) and (3.29) have the form of Legendre functions of second kind,

$$Q_l(y) = \frac{1}{2}\int_{-1}^{1} \mathrm{d}z \frac{P_l(z)}{y - z}. \tag{3.45}$$

The lowest of those functions ($l \leq 2$) explicitly read

$$Q_0(y) = \frac{1}{2}\log\left(\frac{y+1}{y-1}\right), \quad Q_1(y) = yQ_0(y) - 1, \quad Q_2(y) = \frac{3y^2-1}{2}Q_0(y) - \frac{3}{2}y. \tag{3.46}$$

Finally, the inhomogeneities can be written as

$$\begin{aligned}
\hat{M}_0(s) =& \frac{1}{X}\left[\zeta_0\, Q_0(y) + (\zeta_1 + y\zeta_2)\, Q_1(y)\right] + \delta\hat{M}_0(s),\\
\hat{M}_1(s) =& \frac{3Q_1(y)}{2Y}\left[\zeta_0 + y(\zeta_1 + y\zeta_2)\right] - \frac{\zeta_2}{2Y} + \delta\hat{M}_1(s),\\
\hat{U}_1(s) =& (\xi_0 + \xi_1 y)(Q_0(y) - Q_2(y)) - \xi_1,\\
\hat{V}_1(s) =& \frac{\gamma}{XY}(Q_0(y) - Q_2(y)).
\end{aligned} \tag{3.47}$$

They are depicted in Figure 3.4 for a fixed dilepton energy $s_l = 0.8\ \text{GeV}^2 \approx (m_D - 1\ \text{GeV})^2$. The coefficients $\beta_{1,2}$ that enter the amplitudes at NLO are determined in Appendix B.1, via matching the NLO HMChPT expression of the D_{l3} ($D \to \pi l\nu$ or $D \to Kl\nu$) or B_{l3} ($B \to \pi l\nu$) form factors $f_+(t)$ that depend on the same parameters $\beta_{1,2}$ onto a conformal parametrization. Such parametrizations are provided by a BES III analysis from a fit to data [227] in the case of the D_{l3} decays, and in the case of the B_{l3} decay we refer to an analysis performed by the Belle collaboration [228]. Whenever we perform explicit calculations or show figures we will use the results as determined in FIT II. We evade propagating the errors on the LO couplings and decay constants as the errors $\delta\beta_i$ on the couplings $\beta_{1,2}$ are expected to dominate the uncertainties. There is a considerable impact on the D_{l4} partial waves induced by the errors on the $\beta_{1,2}$. Therefore, the presented figures and the following numerical results have to be understood exemplarily as a demonstration of our formalism rather than accurate predictions. To improve the predictive power one would need to control the symmetry breaking effects and the convergence of the NLO terms better.

It is visible that the inhomogeneities are real above the pseudo-threshold $s = (M_K - M_\pi)^2 \equiv s_-$ and that there is a singular behavior at $s = s_-$. As discussed in Appendix B.3.1, where we study the analytic properties of the inhomogeneities in more detail, the S-wave $\hat{M}_0(s)$ diverges as $\hat{M}_0(s) \sim (s - s_-)^{-1/2}$, whereas the P-waves $\hat{M}_1(s)$, $\hat{U}_1(s)$, and $\hat{V}_1(s)$ grow like $(s - s_-)^{-3/2}$.

3.3.2 Subtraction polynomials

For energies above the threshold, where the inhomogeneities contribute to the dispersion integral in the representation of the pole-term-subtracted amplitude Eq. (3.32), we assume the inhomogeneities to be nearly constant in the physical region $s \lesssim 1\ \text{GeV}^2$, see Appendix B.4 and Figure B.11. Consequently, we need three subtractions in the case of the S-wave and two for the P-wave amplitudes. Remember that in the dispersive representation we deal with functions that are analytic except for the cut; following the discussion in Section 3.3 where a singularity at $s = 0$ was revealed in $M_0^{\text{HMChPT}}(s)$, we rename the amplitudes $M_i(s) \to \tilde{M}_i(s)$ (in analogy to the regular amplitude $\tilde{M}_0^{\text{HMChPT}}$ that is used for the matching in the following),

$$\begin{aligned}
\tilde{M}_0(s) =& \Omega_0(s)\left\{a_0 + a_1 s + a_2 s^2 + \frac{s^3}{\pi}\int_{(M_\pi+M_K)^2}^{\infty} \frac{\hat{M}_0(s')\sin\delta_0(s')\mathrm{d}s'}{|\Omega_0(s')|(s'-s-i\epsilon)s'^3}\right\},\\
\tilde{M}_1(s) =& \Omega_1(s)\left\{a_0' + a_1' s + \frac{s^2}{\pi}\int_{(M_\pi+M_K)^2}^{\infty} \frac{\hat{M}_1(s')\sin\delta_1(s')\mathrm{d}s'}{|\Omega_1(s')|(s'-s-i\epsilon)s'^2}\right\},
\end{aligned}$$

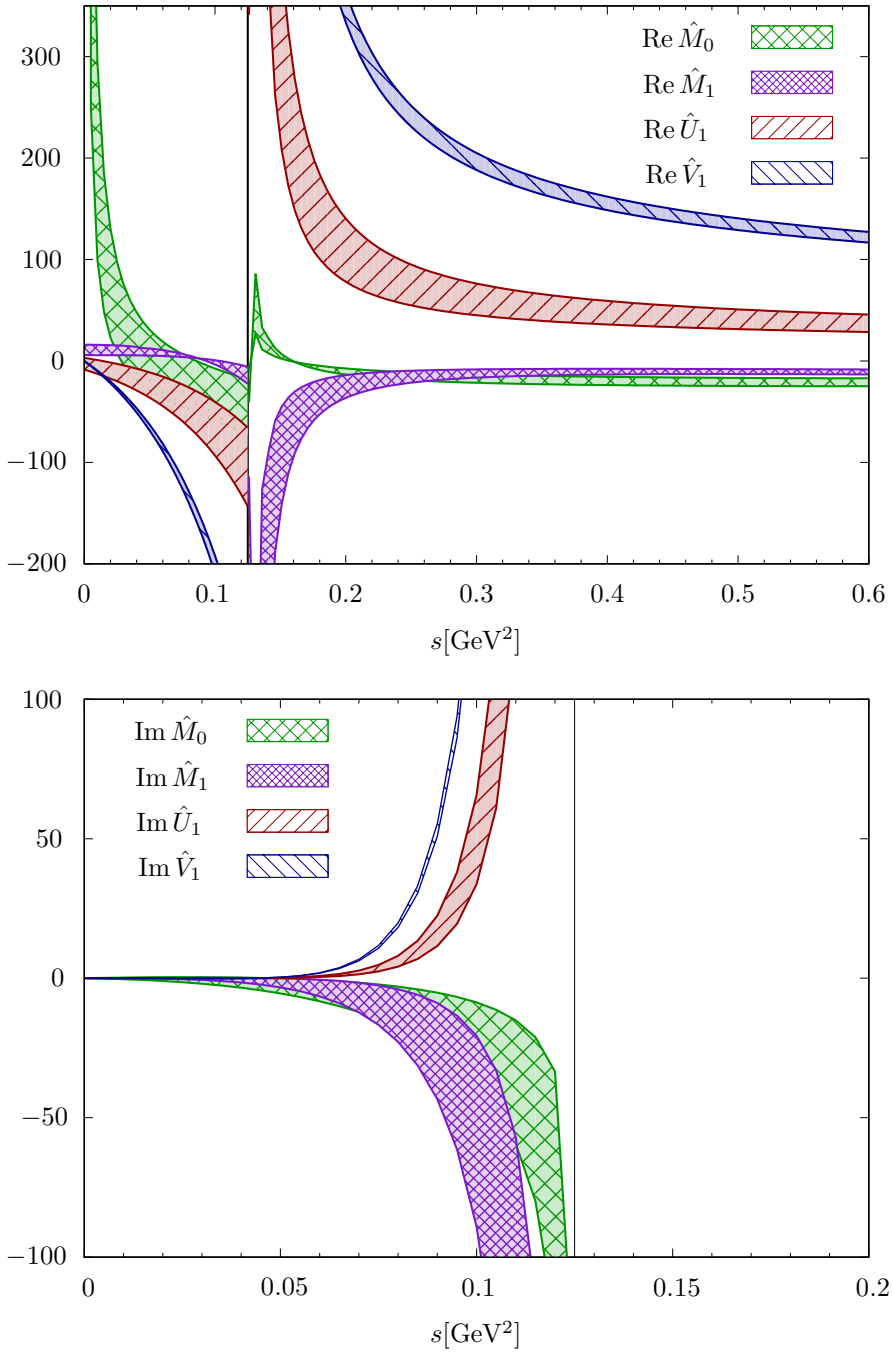

Figure 3.4: The real (top panel) and imaginary (bottom panel) parts of the inhomogeneities $\hat{M}_0(s)$ (green), $\hat{M}_1(s)$ (purple), $\hat{U}_1(s)$ (red), and $\hat{V}_1(s)$ (blue), are shown with error bands due to the uncertainties on $\beta_{1,2}$. The black line denotes the pseudo-threshold.

$$U_1(s) = \Omega_1(s)\left\{ b_0 + b_1 s + \frac{s^2}{\pi}\int_{(M_\pi+M_K)^2}^{\infty} \frac{\hat{U}_1(s')\sin\delta_1(s')\mathrm{d}s'}{|\Omega_1(s')|(s'-s-i\epsilon)s'^2}\right\},$$
$$V_1(s) = \Omega_1(s)\left\{ c_0 + c_1 s + \frac{s^2}{\pi}\int_{(M_\pi+M_K)^2}^{\infty} \frac{\hat{V}_1(s')\sin\delta_1(s')\mathrm{d}s'}{|\Omega_1(s')|(s'-s-i\epsilon)s'^2}\right\}. \tag{3.48}$$

We develop two approaches to constrain the subtraction polynomials. On the one hand we demonstrate a direct determination in analogy to Ref. [126], which relies on matching the subtraction polynomials to the non-pole HMChPT tree-level amplitudes. On the other hand we aim for a representation of subtraction "functions" that depend on the squared dilepton energy s_l employing certain low-energy theorems. In every respect parts of the subtraction polynomials are adjusted in order to ensure a proper high-energy behavior. The discussion of the latter method is relegated to Section 3.4.1 and we focus here on the direct method.

At low energies the subtraction constants of low orders are those that dominate the subtraction polynomials. In particular a_0, a_0', a_1', b_0, and c_0 can be determined via matching to the HMChPT non-pole contributions, Eq. (3.43), most reliable at very low energies. While in the context of the B_{l4} decay [126], $s = 0$ was assumed to be a good matching point because of the good convergence of the chiral expansion, the D_{l4} left-hand-cut structure extends to the pseudo-threshold and it seems to be more plausible to match the amplitudes above that point. In analogy to the subthreshold point in πK scattering, $s = M_K^2 + M_\pi^2$ might be a better choice.[2] As we match our amplitudes to *tree-level* amplitudes, where no rescattering is taken into account, we set $\Omega_i(s) \equiv 1$ (i.e. all scattering phases are set to zero), and only the subtraction polynomial is considered. We find the following set of subtraction constants,

$$\begin{aligned}
a_0 &= \tilde{M}_0^{\mathrm{HMChPT}}(M_K^2+M_\pi^2) = 20.2 \pm 1.8,\\
a_0' &= \tilde{M}_1^{\mathrm{HMChPT}}(M_K^2+M_\pi^2) = (-18.0 \pm 2.5)\ \mathrm{GeV}^2,\\
a_1' &= \frac{\mathrm{d}}{\mathrm{d}s}\tilde{M}_1^{\mathrm{HMChPT}}(s)\big|_{s=M_K^2+M_\pi^2} = 13.4 \pm 1.8,\\
b_0 &= U_1^{\mathrm{HMChPT}}(M_K^2+M_\pi^2) = -13.4 \pm 1.8,\\
c_0 &= V_1^{\mathrm{HMChPT}}(M_K^2+M_\pi^2) = 0,
\end{aligned} \tag{3.49}$$

where the β_i coefficients due to FIT II are taken, $\beta_1 = (0.25 \pm 0.02)$ GeV, $\beta_2 = (0.05 \pm 0.02)\ \mathrm{GeV}^{-1}$. The errors on the subtraction constants are propagated from the uncertainties of the couplings $\beta_{1,2}$, which are expected to dominate other uncertainties.

The remaining subtraction constants a_1, a_2, b_1, and c_1 become relevant at higher energies s, such that it is appropriate to fix them in a sense that they enforce the requested fall-off of the amplitudes at large s. According to Ref. [126], whose argumentation concerning the dispersive representation of constant inhomogeneities is summarized in Appendix B.5, we choose the subtraction constants as

$$a_1 = A\dot{\Omega}(0), \quad a_2 = A\left(\frac{1}{2}\ddot{\Omega}(0) - \dot{\Omega}^2(0)\right), \tag{3.50}$$

where A is the constant the corresponding inhomogeneity approaches. The first and second

[2] The choice of the matching point only affects the subtraction constants a_i', as the P-wave $\tilde{M}_1^{\mathrm{HMChPT}}$ is linear in s. We observe that there is no significant discrepancy in the subtraction constants evaluated by matching at $s = M_\pi^2 + M_K^2$ and $s = 0$. Note that in the case of nonzero matching points s_0 the subtraction polynomial is expanded in powers of $(s-s_0)^n$; the numbers a_i' presented here are then transferred to the polynomial $a_0' + a_1' s$ as given in Eq. (3.48).

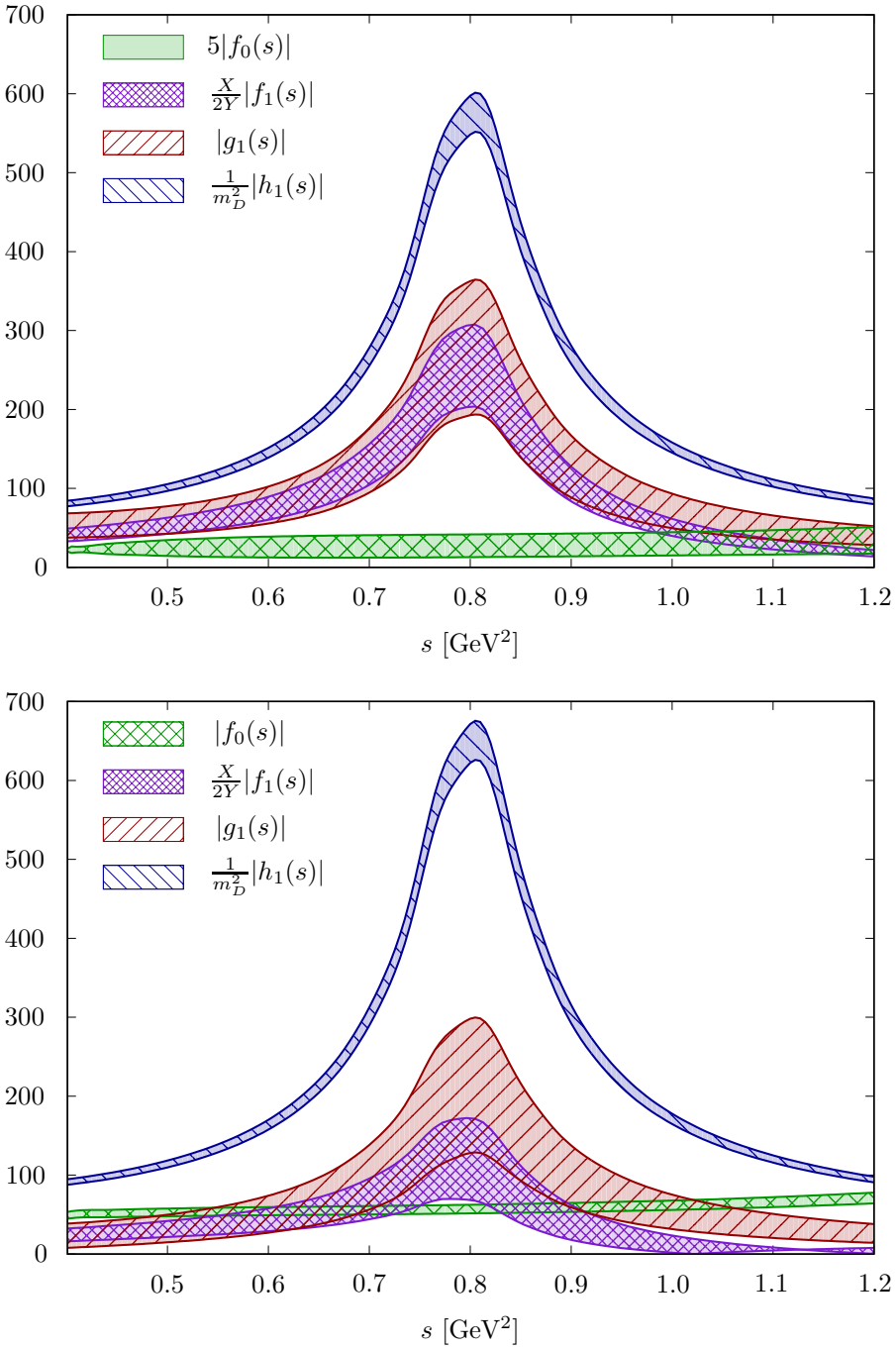

Figure 3.5: We depict the magnitudes of the partial waves $f_0(s) = \hat{M}_0(s) + M_0(s)$, $X/(2Y)f_1(s) = \hat{M}_1(s) + M_1(s)$, $g_1(s) = \hat{U}_1(s) + U_1(s)$ and $h_1(s)/m_D^2 = (\hat{V}_1(s) + V_1(s))/m_D^2$ (the latter being rescaled due to a clearer representation, as well as the S-wave $|f_0(s)|$ in the top panel). In the top panel the partial waves are derived with the FIT II results for the β_i couplings (according to the numerical results shown in the main text), in the bottom panel the FIT I results are used. The dilepton energy is fixed at $s_l = 0.8$ GeV^2.

derivative of the Omnès function at the origin read

$$\begin{aligned}\dot{\Omega}(0) &= \left.\frac{\mathrm{d}\Omega(s)}{\mathrm{d}s}\right|_{s=0} = \frac{1}{\pi}\int_{(M_\pi+M_K)^2}^{\infty}\frac{\delta(s')}{s'^2}\mathrm{d}s',\\ \ddot{\Omega}(0) &= \left.\frac{\mathrm{d}^2\Omega(s)}{\mathrm{d}s^2}\right|_{s=0} = \dot{\Omega}(0)^2 + \frac{2}{\pi}\int_{(M_\pi+M_K)^2}^{\infty}\frac{\delta(s')}{s'^3}\mathrm{d}s'.\end{aligned} \tag{3.51}$$

As the inhomogeneities are not exactly constant at tree level due to the perturbation of the singularities from the left-hand-cut structure at the pseudo-threshold, a matching point s_m has to be chosen, at which the inhomogeneities are evaluated to give the constant A; we choose the mass of the K^* resonance, $s_m = M_{K^*}^2$. With $\dot{\Omega}_0(0) = 1.12$ GeV^{-2}, $\dot{\Omega}_1(0) = 1.22$ GeV^{-2}, and $\ddot{\Omega}_0(0) = 2.43$ GeV^{-4} we find

$$\begin{aligned}a_1 =& \hat{M}_0(s_m)\,\dot{\Omega}_0(0) = (-23.7 \pm 4.3)\ \text{GeV}^{-2}\,,\\ a_2 =& \hat{M}_0(s_m)\left(\frac{1}{2}\ddot{\Omega}_0(0) - \dot{\Omega}_0^2(0)\right) = (0.8 \pm 0.1)\ \text{GeV}^{-4}\,,\\ b_1 =& \hat{U}_1(s_m)\,\dot{\Omega}_1(0) = (39.3 \pm 9.0)\ \text{GeV}^{-2}\,,\\ c_1 =& \hat{V}_1(s_m)\,\dot{\Omega}_1(0) = (154.5 \pm 6.6)\ \text{GeV}^{-2}\,.\end{aligned} \tag{3.52}$$

Due to the linear nature of the HMChPT non-pole amplitude M_1^{HMChPT} the subtraction constant a_1' has been fixed by the low-energy matching. Hence the full $\tilde{M}_1$ subtraction polynomial is determined, and no high-energy constraint has been implemented so far. To build in the requested fall-off at large energies we calculate the constant a_1' in the sense of Eq. (3.50), $a_1' = \hat{M}_1(s_m)\,\dot{\Omega}_1(0) = -14.6 \pm 3.3$. We observe that this number is not compatible with the value determined in Eq. (3.49). Consequently, the question arises whether the low-energy or the high-energy constraint has higher priority, or whether it is suitable to combine both results and use their sum as proposed in Ref. [126]. To answer this question we employ a naive unitarisation approach: we ignore any left-hand cuts, such that the terms in the bracket in Eq. (3.48) reduce to a pure polynomial, given by the partial-wave projection of the HMChPT non-pole term. The partial wave is then constructed by multiplying the complete partial-wave projection of the HMChPT expression $\hat{M}_1 + \tilde{M}_1$ by the respective Omnès function in order to build in the final-state interaction. This poses a criterion: the naively unitarised partial wave should approximately match the dispersively constructed one. We observe that indeed the implementation of both (low-energy and high-energy) constraints to fix a_1', i.e. taking the sum of the above quoted values, yields the best agreement, hence we fix this constant to

$$a_1' = \hat{M}_1(s_m)\,\dot{\Omega}_1(0) = -1.2 \pm 1.4. \tag{3.53}$$

The full partial waves are depicted in Figure 3.5. In order to illustrate the uncertainty induced by the NLO couplings β_i we show the partial waves evaluated with the FIT I results as well; a further discussion of the impact of the β_i uncertainty on the partial waves is relegated to Appendix B.1.2. Figures 3.6 and 3.6 illustrate the impact of the low-energy and high-energy constraints that are used to fix the subtraction constants, and employed in particular in the determination of a_1'. We show the partial waves with the full subtraction polynomials as determined above (red, solid curves), without implementing the high-energy constraints (blue, dashed), and without matching in the low-energy region (green, dotted). In the case of $f_1(s)$ we additionally depict a curve (green, dot-dashed) where only the constant a_0' is determined by means of the low-energy matching, but not the linear term. We finally compare these curves to the naively unitarised partial waves (black, dot-dot-dashed). We observe that the set of subtraction constants we developed above, including both low- and high-energy constraints,

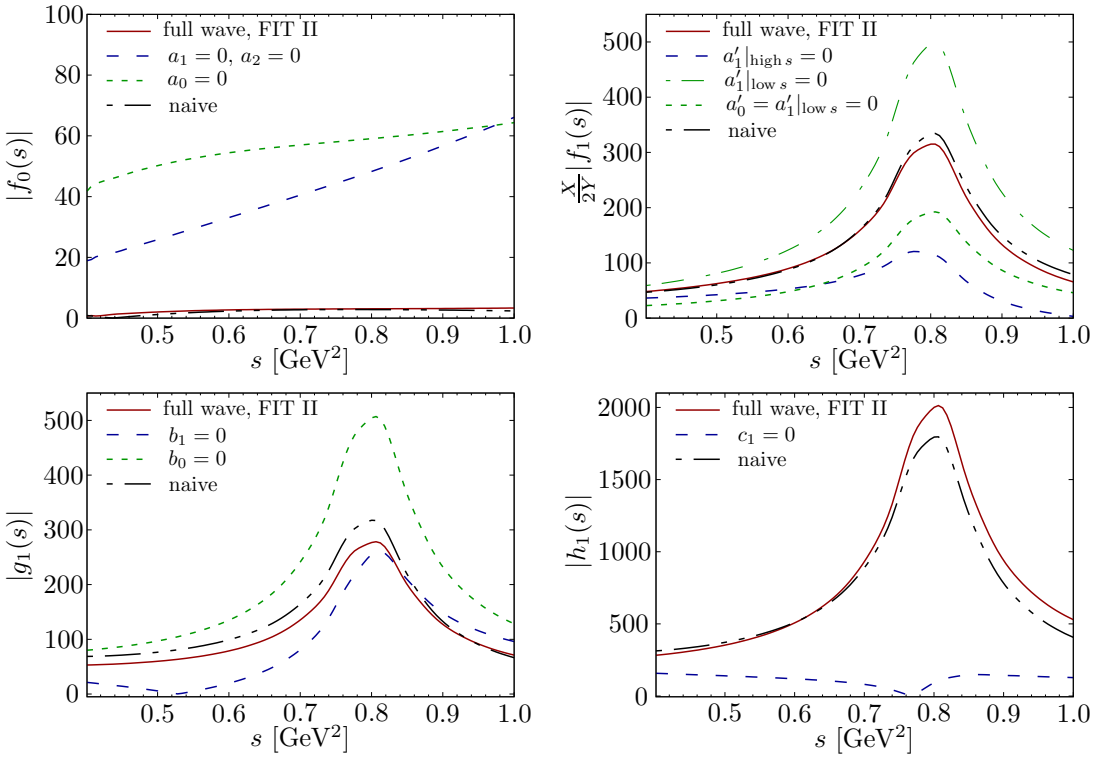

Figure 3.6: We depict the magnitudes of the various S- and P-waves (for fixed $s_l = 0.8$ GeV^2 and corresponding to to the FIT II results for the β_i couplings) with modified subtraction polynomials. They are compared to the respective partial waves obtained using a naive unitarisation approach (black, dot-dot-dashed). The red, solid curves correspond to the waves and subtraction polynomials as discussed in the main text, the other curves show dispersively constructed partial waves without implementing high-energy (blue, dashed) and low-energy (green, dotted) constraints. We disregard the propagation on the $\beta_{1,2}$ errors for this illustration.

provides the best accordance. The agreement between the naively and rigorously unitarized solutions is of astonishing quality—the neglect of left-hand-cut structures hence entails a rather moderate effect, at least in regard to the considerable uncertainty due to NLO corrections in the HMChPT amplitudes. We will come back to this comparison in Section 3.5.

We can further calculate the partial decay rate, Eq. (3.16), for a fixed $s_l = 0.8$ GeV^2, shown in Figure 3.8. The S-wave is formidably suppressed: integrating the full decay rate and the S-wave contribution over s yields the S-wave ratio (for the specific s_l we consider here)

$$\mathcal{R}_{\text{S}-\text{wave}} \lesssim 0.5\%, \tag{3.54}$$

where the range is due to the uncertainty on the couplings β_i. This ratio is an order of magnitude smaller than the one obtained from the branching fractions published in the BES III analysis, Ref. [225], $\mathcal{R}^{\text{exp}}_{\text{S}-\text{wave}} \approx 6\%$. The observed difference however is plausible due to the variability of and integration over the dilepton energy, considered in the experimental analysis; there is no evidence for assuming a stable S-wave fraction for different s_l. Furthermore, there is a large discrepancy between the ratio determined with the FIT I and the FIT II sets. For the FIT I scenario we find $\mathcal{R}^{\text{FIT I}}_{\text{S}-\text{wave}} \lesssim 10\%$, hence in this case the S-wave has a considerable contribution

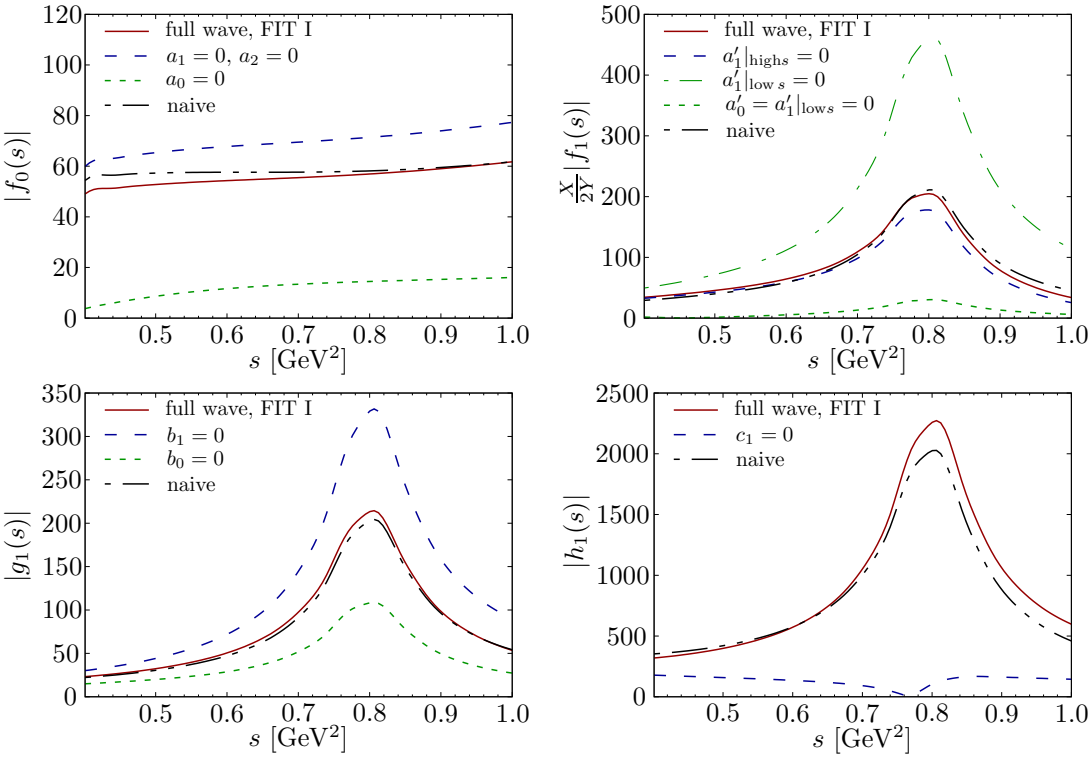

Figure 3.7: In analogy to Figure 3.6 we compare the magnitudes of the various S- and P-waves using the FIT I results of $\beta_{1,2}$ to the respective partial waves obtained in a naive unitarisation approach (black, dot-dot-dashed). The red, solid curves correspond to the waves as discussed in the main text, the other curves show dispersively constructed partial waves without implementing high-energy (blue, dashed) and low-energy (green, dotted) constraints. We disregard the propagation on the $\beta_{1,2}$ errors for this illustration.

to the decay rate. This is also evident in Figure 3.8, where in the FIT I decay rate a smooth increase in the region of the κ is visible.

We notice that the S-wave suppression in the FIT II constellation is even amplified compared to the FIT I results (note the rescaling in the top panel of Figure 3.5). This is traced back to the strong dependency of the inhomogeneities (and accordingly the dispersive integrals and subtraction polynomials) on the $\beta_{1,2}$ coefficients. The dispersive representations Eq. (3.48) before multiplying by the S- and P-wave Omnès functions, $\tilde{M}_i(s)\Omega_i^{-1}(s)$, differ drastically for the various fit configurations: for FIT I the considered sum is considerably larger for the S-wave than for the P-wave, which has a compensating effect on the strong dominance of the P-wave Omnès function over the S-wave one due to the $K^*(872)$ resonance. Considering the peak region, where a difference in the $\tilde{M}_i(s)\Omega_i^{-1}(s)$ has the most significant impact, we find

$$\begin{aligned}
&\left|\tilde{M}_0(s)\Omega_0^{-1}(s)\right|\Big|_{s=m^2_{K^*(872)}} = 21.9, \qquad \left|\tilde{M}_1(s)\Omega_1^{-1}(s)\right|\Big|_{s=m^2_{K^*(872)}} = 7.8 \quad \text{for FIT I,} \\
&\left|\tilde{M}_0(s)\Omega_0^{-1}(s)\right|\Big|_{s=m^2_{K^*(872)}} = 6.9, \qquad \left|\tilde{M}_1(s)\Omega_1^{-1}(s)\right|\Big|_{s=m^2_{K^*(872)}} = 15.1 \quad \text{for FIT II} \qquad (3.55)
\end{aligned}$$

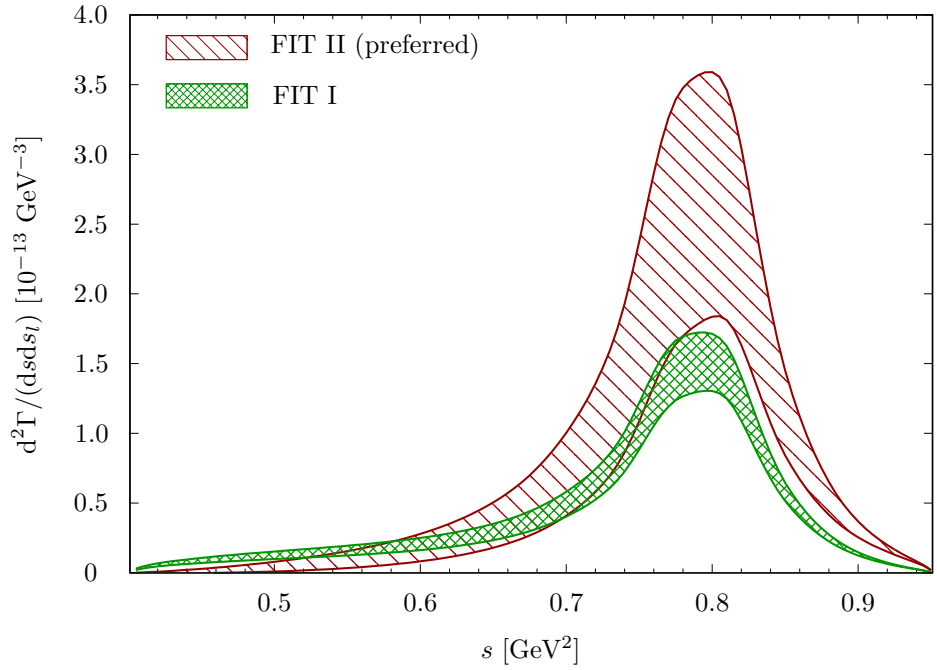

Figure 3.8: Differential decay width $\mathrm{d}^2\Gamma/\mathrm{d}s\mathrm{d}s_l$, evaluated for $s_l = 0.8$ GeV^2 and for the sets of NLO couplings β_i determined in FIT I and FIT II. The uncertainty band refers to the error on the β_i.

(this calculation is just of an illustrating nature such that we disregard the error propagation here).

We finally investigate the stability of the partial waves determined in the dispersive formalism for varying s_l in the vicinity of the considered energy. We rerun the calculations for different s_l with 0.7 GeV$^2 \leq s_l \leq 0.9$ GeV^2. The magnitudes of the partial waves for dilepton energies 0.7 GeV$^2 \leq s_l \leq 0.9$ GeV^2 (illustrated by the bands) are displayed in Figure 3.9, where we have turned off the uncertainty on the couplings β_i to visualize the effect of varying s_l. The effect of a variation in s_l on the partial waves is rather small, in particular in view of the amount of uncertainty induced by NLO corrections. Hence the existence of poles in $s_l - m^2_{D^{(*)}_{(s)}}$ does not play a significant role in the s_l region considered here. On the one hand, the poles are well separated from the physically allowed region. There is a pole in $s_l - m^2_{D_s^*}$ entering the h_1 partial wave via the $\hat{V}_1(s)$ inhomogeneity; for the largest value $s_l = 0.9$ GeV^2 of the above considered energies there is a gap of about 3.6 GeV^2. On the other hand, h_1 enters the decay rate Eq. (3.16) in a term $\propto X^2|h_1|^2$, we therefore investigate

$$\frac{X^2}{(s_l - m^2_{D_s^*})^2} = \frac{1}{4} + \mathcal{O}\left(\frac{s}{s_l - m^2_{D_s^*}}, \frac{m^2_{D_s^*} - m^2_D}{s_l - m^2_{D_s^*}}\right). \tag{3.56}$$

The closer the dilepton energy approaches the pole position, the smaller the s energy range becomes, manifestly suppressing the contribution of the terms $\propto (s_l - m^2_{D_s^*})^{-1}$. Another pole has been artificially introduced in the inhomogeneity $\hat{M}_1$, which is closer to the physical region ($s_l - m^2_D|_{s_l=0.9\ \mathrm{GeV}^2} \approx 2.6$ GeV^2), but still sufficiently separated. Furthermore, we expect little

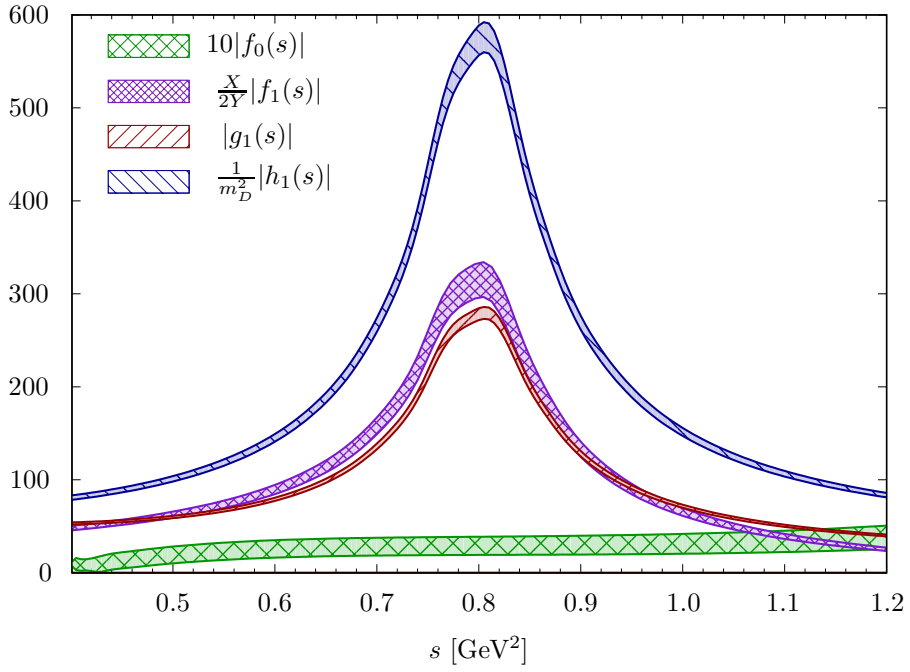

Figure 3.9: We show the magnitudes of the partial waves $f_0(s) = \hat{M}_0(s)+M_0(s)$, $X/(2Y)f_1(s) = \hat{M}_1(s)+M_1(s)$, $g_1(s) = \hat{U}_1(s)+U_1(s)$ and $h_1(s)/m_D^2 = (\hat{V}_1(s)+V_1(s))/m_D^2$ for dilepton energies $0.7\ \text{GeV}^2 \leq s_l \leq 0.9\ \text{GeV}^2$ (illustrated by the bands). The error on $\beta_{1,2}$ is set off. Note that $|f_0|$ and $|h_1|$ are rescaled due to a clearer representation.

impact from this term as the pole cancels in the combination $\hat{M}_1 + \tilde{M}_1$ such that it can only contribute to the correction due to the left-hand-cut structure, being of moderate significance, see the discussion above.

3.4 Connection to D_{l3} form factors

A digression to the semileptonic $D \to \pi l\nu$ (D_{l3}) decay, connected to the D_{l4} decay by means of low-energy theorems, not only provides a tool to confirm the form factor expressions, Eq. (3.36), but rather allows us to extrapolate our analysis to the region of lower dilepton energies. So far we assume s_l to be fixed to a rather large value (we choose $s_l = 0.8\ \text{GeV}^2 \approx (m_D - 1\ \text{GeV})^2$), as demanded in the modified Omnès formalism, used to obtain the dispersive representations of the partial waves, Eq. (3.48), consisting of a dispersive integral and a subtraction polynomial multiplied by the respective Omnès function. We develop a method to generalize the representations Eq. (3.48) for non-fixed s_l. The basic idea is that the subtraction *constants* are strictly speaking subtraction *functions*, depending on s_l, for which we propose a parametrization. For this purpose we exploit that the D_{l3} decay, having a simpler structure compared to D_{l4}, can be well described in conformal variables with very low polynomials [229], employed in certain experimental analyses, see e.g. Refs. [227, 228, 230–232]. Theoretical studies using the light-cone sum-rule approach, lattice QCD, or dispersion theory yield useful and promising constraints [233–235].

In the case of the S-wave we can even make a prediction how such a parametrized s_l

dependency explicitly looks like, combining the soft-pion and soft-kaon theorems, introduced in this section.

3.4.1 Low-energy theorems

In analogy to the Callan–Treiman theorem for K_{l3} decays, the D_{l4} hadronic decay matrix elements, Eq. (3.8) fulfill two low-energy theorems, which connect the D_{l4} with the D_{l3} matrix elements,

$$\begin{aligned} iF_K\langle\pi^+K^-|\bar{s}\gamma_\mu(1-\gamma_5)c|\,D^+\rangle &= \langle\pi^0\left|\bar{d}\gamma_\mu(1-\gamma_5)c\right|D^+\rangle \qquad \text{for } p_K\to 0,\\ iF_\pi\langle\pi^+K^-|\bar{s}\gamma_\mu(1-\gamma_5)c|\,D^+\rangle &= 0 \qquad\qquad\qquad\qquad\quad \text{for } p_\pi\to 0, \end{aligned} \tag{3.57}$$

where in the first expression an isospin rotation has been performed. This allows to express the D_{l4} form factors in terms of the D_{l3} form factors f_+ and f_-, defined via

$$\langle\pi^0\left|\bar{d}\gamma_\mu(1-\gamma_5)c\right|D^+\rangle = \frac{1}{\sqrt{2}}\left[(p_D+p_\pi)_\mu f_+ + (p_D-p_\pi)_\mu f_-\right]. \tag{3.58}$$

For $p_K\to 0$ the relations read

$$\frac{\sqrt{2}F_K}{m_D}(F-G-R) = f_+ - f_- + \mathcal{O}(M_K^2) \quad\text{and}\quad \frac{\sqrt{2}F_K}{m_D}R = f_+ + f_- + \mathcal{O}(M_K^2), \tag{3.59}$$

while for $p_\pi\to 0$ we find

$$\frac{F_\pi}{m_D}(F+G-R) = \mathcal{O}(M_\pi^2) \quad\text{and}\quad \frac{F_\pi}{m_D}R = \mathcal{O}(M_\pi^2). \tag{3.60}$$

For further investigations we take the sum of the respective two soft-pion or soft-kaon relations, being independent of the form factors R and f_- (the information about those is contained in the difference that is hence suppressed by the squared lepton mass),

$$\frac{F_\pi}{m_D}(F+G)|_{p_\pi\to 0} = \mathcal{O}(M_\pi^2), \quad \frac{\sqrt{2}F_K}{m_D}(F-G)|_{p_K\to 0} = 2f_+ + \mathcal{O}(M_K^2). \tag{3.61}$$

By taking the low-energy limits $p_{\pi,K}\to 0$ naively, the Mandelstam variables reduce to

$$\begin{aligned} s|_{p_\pi=0} &= M_K^2, & t|_{p_\pi=0} &= m_D^2, & u|_{p_\pi=0} &= s_l,\\ s|_{p_K=0} &= M_\pi^2, & t|_{p_K=0} &= s_l, & u|_{p_K=0} &= m_D^2, \end{aligned} \tag{3.62}$$

which in this form actually spoils the on-shell relation $s+t+u=3s_0$. However, this relation can still be satisfied: we can shift the Mandelstam variables by terms of orders $\mathcal{O}(M_{\pi,K}^2)$, respectively, given that the low-energy relations are valid up to those orders. In that sense we allow for the shifts $s\to s+a_1^{\pi,K}M_{\pi,K}^2$, $t\to t+a_2^{\pi,K}M_{\pi,K}^2$ and $u\to u+a_3^{\pi,K}M_{\pi,K}^2$, with the constraint $a_1^{\pi,K}+a_2^{\pi,K}+a_3^{\pi,K}=1$.

It is consequently not completely determined how to distribute the mass squares among the Mandelstam variables. However, we establish three criteria that yield different, independent constraints on the parameters $a_i^{\pi,K}$. These are not necessarily compatible to each other, such that we also need to investigate the impact of disregarding certain conditions in order to find the best compromise.

First, the deviation from the exact soft-pion or soft-kaon point, given by Eq. (3.62), should be minimal. From the explicit form of the HMChPT form factors at NLO, Eqs. (3.36) and (B.1), we read off the conditions

$$a_2^K = 0, \quad a_1^K = a_3^K \to a_1^K = 1-a_3^K = \frac{1}{2}, \quad a_2^\pi = 0, \quad a_1^\pi = 1-a_3^\pi, \tag{3.63}$$

which yield a cancelation among the various shifts and result in an exact reproduction of the low-energy relations.

The following second and third criteria aim at the usability of the low-energy theorems: the soft-pion and soft-kaon theorems are employed to find constraints on the yet undetermined subtraction polynomials of our partial wave amplitudes; details and concrete calculations are shown below. Transferring the low-energy theorems as given in Eq. (3.61) to relations that contain the dispersively constructed partial-wave amplitudes $M_{0,1}(s)$, $U_1(s)$, and $V_1(s)$ requires to change the set of form factors (F, G) to (F_1, F_2), related by Eq. (3.12). For our second criterion we demand that in performing this transition no artificial, significant corrections are generated. Since the dispersive representation describes the pole-term-*subtracted* amplitudes, there is actually no need to replace the complete F and G form factors and we will apply the following considerations for the pole-term-subtracted parts. In the soft-kaon limit the form factor F_1 reduces to $F_1 = X\big[F + f(a_1^K, a_3^K)G\big]$, such that

$$F - G = \frac{F_1}{X} - \big(f(a_1^K, a_3^K) + 1\big)F_2, \quad \text{with} \quad f(a_1^K, a_3^K) = -1 + \mathcal{O}(M_K^2). \tag{3.64}$$

However, the neglect of $\mathcal{O}(M_K^2)$ corrections has to be examined carefully, since the kaon mass is not distinctly small on the considered energy range (in particular compared to the pion mass) and may yield quite considerable corrections. Indeed, expanding the function $f(a_1^K, a_3^K) + 1$ in the kaon and the pion masses reveals that the leading term is of order $\mathcal{O}(M_K^2/M_\pi^2)$,

$$f(a_1^K, a_3^K) = -1 + \frac{M_K^2}{M_\pi^2}\left(2a_1^K + 2 + \mathcal{O}(M_\pi^2)\right). \tag{3.65}$$

The $\mathcal{O}(M_\pi^2)$ correction in the bracket contains a pole in s_l, but it lies outside the physical region, i.e. also when considering s_l as a dynamic variable in the following this pole will not be approached, ensuring the smallness of that correction. In order to achieve a minimal deviation from the soft-kaon theorem in its original form, Eq. (3.61), we set $a_1^K = -1$, canceling the otherwise large and therefore spoiling correction term. This value is not compatible with the one given in Eq. (3.63) due to our first criterion. However, we decide to loosen the constraints given there in favor of the second criterion in order to avoid the described large artificial correction term; the $\mathcal{O}(M_K^2)$ correction that enters via a deviation from the exact soft-kaon point is at least theoretically well-founded. We have fixed $a_2^K = 0$ as demanded by Eq. (3.63), since we treat t-channel poles and the relations are therefore most sensitive to a shift in t. This implies $a_3^K = 2$, constrained by the on-shell relation. With these shifts the artificial terms that enter the soft-kaon relation when changing the set of form factors are suppressed. At the same time this choice of a_i^K yields an $\mathcal{O}(M_K^2)$ correction to Eq. (3.61) that is of a similar magnitude as the correction term resulting from an evaluation at the soft-kaon point. In the soft-pion limit the relation $t|_{p_\pi=0} = m_D^2$ holds such that the pole at $t = m_{D^*}^2$ is approached very closely; the denominator shrinks to $\mathcal{O}(m_D\Delta)$. Therefore any deviation from the original soft-pion relation, Eq. (3.61), where the numerator cancels exactly, requires a careful treatment. We consider the soft-pion analogon to Eq. (3.65), which is obtained by interchanging $\pi \leftrightarrow K$ and taking the sum $F + G$ instead of the difference. Fixing $a_1^\pi = -1$ and $a_3^\pi = 2$ in analogy to the soft-kaon case[3] the term proportional to M_π^2/M_K^2 cancels and the next correction is of order $\mathcal{O}(M_\pi^2/(s_l - m_D^2))$, which is sufficiently small (numerically confirmed).

As a third criterion we demand that the soft-pion and soft-kaon points should be chosen in energy regions where a partial-wave expansion of the amplitudes is well-defined and an analytic continuation of the partial waves into the unphysical region can be performed. A condition

[3]Concerning the first criterion, the sum $F + G$ is s- and u-independent, such that this condition is met in either case and the choice of a_1^π and a_3^π remains unconstrained.

precedent to the convergence of the expansion applies to the scattering angle: $|z| = |\cos\theta_K| < 1$. For a detailed discussion concerning the function $z(s,t,u)$ see Appendix B.3. We observe there that the above choice of $a_i^{\pi K}$ is compatible with this criterion.

We end up with the modified soft-pion and soft-kaon points

$$\begin{aligned} &s|_{p_\pi=0} = M_K^2 - M_\pi^2, \quad t|_{p_\pi=0} = m_D^2, \quad u|_{p_\pi=0} = s_l + 2M_\pi^2, \\ &s|_{p_K=0} = M_\pi^2 - M_K^2, \quad t|_{p_K=0} = s_l, \quad u|_{p_K=0} = m_D^2 + 2M_K^2. \end{aligned} \tag{3.66}$$

Note, however, that we deal with certain criteria that yield conditions on the $a_i^{K,\pi}$ that are not directly compatible. We argue that the second criterion is the preferred one in order to determine a_1^K and a_3^K. This choice however implicates an error on a 50% level for the soft-kaon relation compared to the exact relation, originating from the significance of $\mathcal{O}(M_K^2)$ corrections, which should be kept in mind.

The given set of shifted soft-pion and soft-kaon points allows to rewrite the low-energy relations, Eq. (3.61), in a compact form: the pole-term-subtracted parts are given in terms of the partial-wave expansion of $F_1(s)$ according to Eq. (3.13),

$$\begin{aligned} \mathcal{O}(M_\pi^2) =& F^{\text{pole}} + G^{\text{pole}} + \sum_{l=0}^{\infty} M_l P_l(z)\Big|_{p_\pi\to 0} = -\frac{g m_D f_{D^*}}{2F_\pi F_K} + \delta\hat{M}_0 + \tilde{M}_0\Big|_{s=M_K^2-M_\pi^2} \\ \mathcal{O}(M_K^2) =& f_+ - \frac{F_K}{\sqrt{2}m_D}\Big[F^{\text{pole}} - G^{\text{pole}} + \sum_{l=0}^{\infty} M_l P_l(z)\Big]\Big|_{p_K\to 0} \\ =& f_+^{\text{non-pole}} - \frac{F_K}{\sqrt{2}m_D}\Big[\delta\hat{M}_0 + \tilde{M}_0\Big]\Big|_{s=M_\pi^2-M_K^2} \end{aligned} \tag{3.67}$$

In the respective second steps the explicit expressions for the pole terms obtained in HMChPT, Eq. (3.36), are inserted, which yields a cancellation between the D_{l3} and D_{l4} pole terms in the soft-kaon limit, and a constant term in the soft-pion case. Furthermore, the sum over partial waves reduces to a contribution from the S-wave, the only surviving wave in the $p_{\pi,K} \to 0$ limit. We assign two reasons for that. First, due to a chiral argument only S- and P-waves can contribute at the considered chiral order; higher powers of the scattering angle are attributed to terms $\propto (t-u)^n$ that arise at higher chiral orders. Second, the scattering angle $z = \cos\theta_K$, Eq. (3.6), evaluated at the soft pion/kaon points, Eq. (3.66), becomes $z = \mathcal{O}(M_{\pi,K}^2)$, respectively; we evaluate z numerically at the specific points and find $|z|_{p_\pi\to 0} \lesssim 0.03$ and $|z|_{p_K\to 0} \lesssim 0.08$. This implicates a suppression of all odd waves. The insertion of the partial-wave expansion in the above relations is not trivial. If the low-energy theorems are evaluated in the unphysical region it is mandatory to assure the convergence of the expansion, which is restricted to certain regions in the Mandelstam plane, see the discussion in Appendix B.3.

Note that we aim for an expression of the subtraction functions of the *redefined* S-wave amplitude $\tilde{M}_0(s,s_l)$, in order to have a direct cross check with the subtraction constants that we have determined in Section 3.3 at a fixed $s_l = 0.8\ \text{GeV}^2 \approx (m_D - 1\ \text{GeV})^2$. We insert the dispersive representation, Eq. (3.48), into Eq. (3.67) and solve the soft-pion relation for $a_1(s_l)$, which allows to eliminate one of the subtraction functions,

$$\begin{aligned} a_1(s_l) =& -\frac{a_0(s_l)}{M_K^2} - a_2(s_l)M_K^2 - M_K^4\,\mathcal{I}(M_K^2 - M_\pi^2, s_l) \\ & - \frac{\delta\hat{M}_0(M_K^2 - M_\pi^2) - \frac{g m_D f_{D^*}}{2F_\pi F_K}}{\Omega_0(M_K^2 - M_\pi^2)\cdot M_K^2} + \mathcal{O}(M_\pi^2), \\ \mathcal{I}(s,s_l) =& \frac{1}{\pi}\int_{(M_\pi+M_K)^2}^{\infty} \frac{\hat{M}_0(s',s_l)\sin\delta_0(s')\mathrm{d}s'}{|\Omega_0(s')|(s'-s-i\epsilon)s'^3}. \end{aligned} \tag{3.68}$$

The $a_2(s_l)$ function is already fixed in the sense of the constraints on the subtraction constants presented in Ref. [126] and reviewed in Section 3.3 and Appendix B.5: as $a_2(s_l)$ is associated with the highest power in s in the subtraction polynomial it is the dominant contribution at high dimeson energies, and needs to be adjusted to ensure a proper high-energy behavior. The fixing of a_2 presented Appendix B.5 is based on the nearly constant behavior of $\hat{M}_0(s)$ at $s \lesssim 1\ \mathrm{GeV}^2$, approximated by the constant $A = \hat{M}_0(s)$, and is straightforwardly generalized to s_l dependent quantities. We find that a variation of s_l yields a negligibly small distortion of the shape of the inhomogeneities and mainly induces a constant shift, such that we remain at the assumption of a nearly constant behavior in s, i.e.

$$a_2(s_l) = \hat{M}_0(s_m, s_l)\Big(\frac{1}{2}\ddot{\Omega}_0(0) - \dot{\Omega}_0^2(0)\Big). \tag{3.69}$$

Inserting Eqs. (3.68) and (3.69) into the S-wave $\tilde{M}_0(s, s_l)$, Eq. (3.48), yields

$$\begin{aligned}\tilde{M}_0(s, s_l) =& \Omega_0(s)\Bigg\{ a_0(s_l)\Big(1 - \frac{s}{M_K^2}\Big) - sM_K^4\,\mathcal{I}(M_K^2 - M_\pi^2, s_l) + s^3\,\mathcal{I}(s, s_l) \\ &+ \hat{M}_0(s_m, s_l)\Big(\frac{1}{2}\ddot{\Omega}_0(0) - \dot{\Omega}_0^2(0)\Big)(s^2 - sM_K^2) - \frac{\delta\hat{M}_0(M_K^2 - M_\pi^2) - \frac{gm_D f_{D^*}}{2F_\pi F_K}}{\Omega_0(M_K^2 - M_\pi^2)\cdot M_K^2}\, s\Bigg\}.\end{aligned} \tag{3.70}$$

We can finally determine a parametrization for the unknown function $a_0(s_l)$ from the matching to the D_{l3} form factor as given by the soft-kaon constraint in Eq. (3.67),

$$\begin{aligned}\frac{\sqrt{2}m_D}{F_K} f_+^{\text{non-pole}}(s_l) =& \Omega_0(M_\pi^2 - M_K^2)\Bigg\{ 2a_0(s_l) + \hat{M}_0(s_m, s_l)\Big(\ddot{\Omega}_0(0) - \dot{\Omega}_0^2(0)\Big)M_\pi^4 \\ &+ M_\pi^6\left(\mathcal{I}(M_\pi^2 - M_K^2, s_l) + \mathcal{I}(M_K^2 - M_\pi^2, s_l)\right)\Bigg\} - \frac{gm_D f_{D^*}}{2F_\pi F_K} \\ &- \left(\delta\hat{M}_0(M_\pi^2 - M_K^2) - \frac{gm_D f_{D^*}}{2F_\pi F_K}\right)\left(1 - \frac{\Omega_0(M_\pi^2 - M_K^2)}{\Omega_0(M_K^2 - M_\pi^2)}\right) + \mathcal{O}(M_K^2),\end{aligned} \tag{3.71}$$

In the last equality we have made use of $\delta\hat{M}_0(s) = -\delta\hat{M}_0(-s)$. This formula is correct up to orders $\mathcal{O}(M_K^2, M_\pi^2)$ and smaller due to the validity of the low-energy theorems and the NLO HMChPT expressions. So far we have kept also terms beyond that order, in order to conceptually demonstrate the formalism. In the following we restrict ourselves to the specific case and disregard terms of higher than quadratic order in the light meson masses.

The above expression is free of pole terms as they were canceled out due to the low-energy relations, see Section 3.4.1. Therefore we choose a parametrization for $f_+(s_l)$ of the following form,

$$f_+(s_l) = \frac{c_{\text{fix}}}{s_l - m_{D^*}^2} + \sum_k \alpha_k z(s_l)^k, \tag{3.72}$$

with the conformal variable $z(t, t_0)$ defined by

$$z(t, t_0) = \frac{\sqrt{t_+ - t} - \sqrt{t_+ - t_0}}{\sqrt{t_+ - t} + \sqrt{t_+ - t_0}}, \tag{3.73}$$

with $t_0 = t_+(1 - \sqrt{1 - t_-/t_+})$ and $t_\pm = (m_D \pm M_\pi)^2$, for details see Appendix B.1. This representation differs from the one presented there: only the non-pole part of $f_+(s_l)$ is parametrized

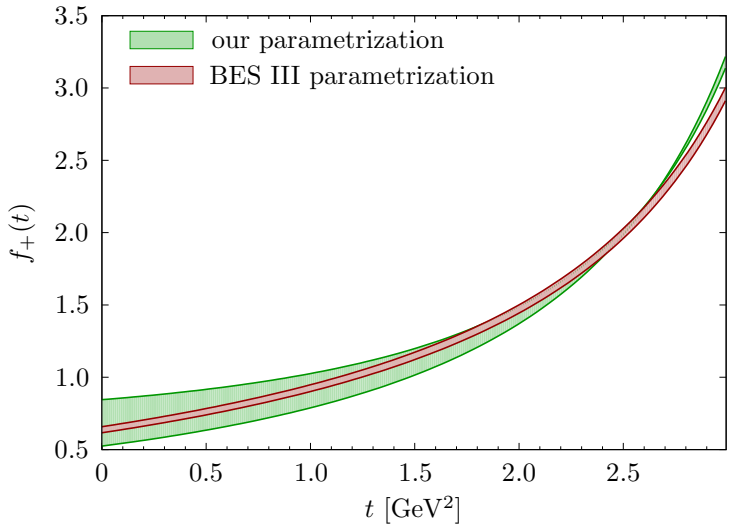

Figure 3.10: D_{l3} form factor $f_+(t)$: the green band shows our proposed parametrization, where the pole term is expressed in the HMChPT framework. The non-pole part is parametrized by a polynomial in the conformal variable z, with the coefficients determined by matching to the conformal parametrization as determined by the BES III collaboration (red error band).

by a conformal polynomial, while the pole-term contribution is added to the conformal polynomial with the residue (c_{fix}) fixed by the HMChPT expression.

The coefficients α_k are determined from matching the above proposed parametrization for $f_+(s_l)$ to the conformal parametrization determined in the BES III analysis [227]. Using a two-parameter parametrization we obtain $\alpha_0 = 0.79 \pm 0.06$ and $\alpha_1 = -2.1 \pm 0.6$ (performing a three-parameter fit results in an α_2 compatible with zero within the error margin and the fit quality is not improved further). In Figure 3.10 the form factor $f_+(t)$ for both the BES III conformal parametrization and our pole-term-separated conformal parametrization is depicted with the respective error bands.

Putting pieces together we finally find a very simple conditional equation for the subtraction function $a_0(s_l)$,

$$\begin{aligned} a_0(s_l) =& \frac{m_D}{\sqrt{2}F_K\Omega_0(M_\pi^2 - M_K^2)}\left[\frac{-f_D + 2\beta_1 + 2gf_{D^*}}{4\sqrt{2}F_\pi}\left(1 - \frac{\Omega_0(M_\pi^2 - M_K^2)}{\Omega_0(M_K^2 - M_\pi^2)}\right)\right. \\ &\left. + \frac{gf_{D^*}}{2\sqrt{2}F_\pi} + \alpha_0 + \alpha_1 z(s_l)\right] + \mathcal{O}(M_{\pi,K}^2) \\ \equiv& \gamma_0 + \gamma_1 z(s_l) + \mathcal{O}(M_{\pi,K}^2). \end{aligned} \tag{3.74}$$

With $\Omega_0(\mathcal{M}_\pi^2 - M_K^2) \approx 0.80$ and $\Omega_0(\mathcal{M}_K^2 - M_\pi^2) \approx 1.34$ we determine the coefficients γ_i to $\gamma_0 = 27.3 \pm 0.9$ and $\gamma_1 = -31.7 \pm 9.1$. It is rather interesting to compare this result to the one obtained in Section 3.3 where (at a dilepton energy fixed at $s_l = 0.8$ GeV^2, for which $z(0.8\text{ GeV}^2) \approx 0.1$) the subtraction polynomials are matched in the low-energy regime to the non-pole HMChPT expressions, resulting in $\bar{a}_0 = 20.2 \pm 1.8$. We can even reproduce the analytic expression for determining a_0 by means of matching if we set the phases to zero (corresponding to $\Omega_i(s) \equiv 1$), and replace the conformal parametrization of $f_+^{\text{non-pole}}$ by the HMChPT term. Evaluating Eq. (3.74) at the same dilepton energy $s_l = 0.8$ GeV^2 we obtain

$a_0(0.8\ \text{GeV}^2) = 23.7 \pm 1.9 \pm 0.5$, where the first (second) error is due to the uncertainties on $\alpha_{0,1}$ ($\beta_{1,2}$).[4] The comparison between both ansätze shows that they yield comparable results. This is actually quite satisfactory, given the sources of uncertainty for our approach: on the one hand we have made several rough estimations, such as neglecting corrections of orders $\mathcal{O}(M_\pi^2, M_K^2)$ while employing HMChPT and the low-energy theorems, on the other hand some steps were though well motivated not strictly constrained, e.g. choosing the fit region for the β_i determination or the evaluation points of the low-energy theorems.

In principle the $a_1(s_l)$ subtraction function, Eq. (3.68), could be determined in a next step by inserting the parametrization obtained for $a_0(s_l)$, Eq. (3.74). However, regarding the above mentioned concern of the validity of the HMChPT amplitudes up to corrections of order $\mathcal{O}(M_\pi^2, M_K^2)$, we have a closer look at the rewritten low-energy theorems, Eq. (3.67). The pole terms that enter these relations are only correct up to orders $\mathcal{O}(M_\pi^2, M_K^2)$. Evaluated at the respective soft-pion or soft-kaon points, only the s-independent part of the subtraction polynomial, $a_0(s_l)$, contributes to the relations at the considered order. We therefore cannot expect to obtain any reasonable numerical result for the $a_1(s_l)$ function.

As a consequence the above determinations of the subtraction constants/functions should not be regarded as high-precision predictions but we rather want to provide a method how one can parametrize such functions. Further input is however highly demanded, in particular for a more precise determination of the β_i parameters.

3.5 Discussion and summary

The main area of concern in our analysis is of conceptual nature, originating from applying HMChPT in the case of D_{l4} decays, where the scale separation between the heavy decaying meson and the light final-state mesons is not that stringent as it is e.g. in the case of the B_{l4} analysis from which we adapt the formalism. On the one hand $m_D \ll m_B$, and on the other hand the situation is even compounded by the kaon in the final state, with $M_K \gg M_\pi$. For this reason it is up to debate whether the application of HMChPT in our analysis is meaningful. Our attempt to increase its reliability by including NLO effects induces the problem that such effects yield significant contributions, due to the slow convergence of the expansion in $1/m_D$ and the light meson masses/momenta. There is hence a considerable impact on the D_{l4} partial waves from tiny variations in the couplings induced by these subleading terms. We discuss in Appendix B.1 the determination of the coefficients $\beta_{1,2}$, the coupling constants to the semileptonic current in the NLO Lagrangian, as well as a detailed investigation how the uncertainty in these couplings influences the dispersion integrals for the D_{l4} partial waves. Two issues thwart our attempts: first, the determination of the β_i, for which we fit the HMChPT D_{l3} and B_{l3} form factors to data, using conformal parametrizations and theory input from lattice QCD and light-cone sum-rules, exhibits a substantial uncertainty. We find e.g. a non-controllable sensitivity to the chosen fit interval. Further, the fit parameters are strongly correlated, inhibiting their disentanglement in the fits. Second, even if we could control the uncertainty in these couplings better, we would have to deal with a considerable impact on the D_{l4} partial waves, where the uncertainty is even amplified, shown by the large error bands e.g. in Figure 3.5.

A further point of criticism is that only a small phase space is covered (small s, large s_l),

[4] There is a large uncertainty in the determination of the couplings β_i, and the quoted error refers to the uncertainty when using the β_i as determined in FIT II. We therefore quote the result in dependency on the parameter β_1 as well: $a_0(0.8\ \text{GeV}^2) = 17.8 \pm 1.9 + 23.6\beta_1$. For the less preferred set of β_i couplings corresponding to FIT I we obtain $a_0(0.8\ \text{GeV}^2) = 25.1 \pm 1.9$, and if the β_i corrections are set off, $\beta_i = 0$, the result is $a_0(0.8\ \text{GeV}^2) = 17.8 \pm 1.9$.

such that it becomes less attractive for experimentalists to adopt our formalism. We therefore tried to improve on this by extrapolating to smaller dilepton energies. We employed low-energy theorems to find s_l dependent subtraction polynomials. This turned out cautiously satisfactory, as we were confronted with another major issue, which is generated by using low-energy theorems. The soft-pion and soft-kaon theorems are valid up to orders $\mathcal{O}(M_\pi^2)$ and $\mathcal{O}(M_K^2)$, respectively. The same holds for the Mandelstam variables, i.e. the soft-kaon points are given by $s = M_\pi^2 + \mathcal{O}(M_K^2)$, which is in particular problematic as $M_K \gg M_\pi$. Hence it is not fundamentally evident whether the soft-kaon theorem is evaluated at e.g. $s = M_\pi^2$ (below the πK threshold) or $s = M_\pi^2 + 2M_K^2$ (well above the πK threshold). We have discussed several constraints and criteria on how to choose the soft-pion and soft-kaon points: we demanded a minimal deviation from the relations as evaluated at the exact soft-pion/soft-kaon points (which are not used as we demand the on-shell relation to be fulfilled), as well as a reduction of induced $\mathcal{O}(M_{\pi,K}^2)$ effects in the calculations performed in Section 3.4. However, these are no axiomatic criteria and do not induce stringent and distinct conditions.

We are confronted with the issue that (similar to our concerns in the determination of the β_i coefficients) even small fluctuations in the Mandelstam variables induce significant variations in the D_{l4} amplitudes. These variations are even amplified when approaching the pseudo-threshold $s_- = (M_K - M_\pi)^2$, where the D_{l4} amplitudes become singular. For instance the original soft-kaon point $s = M_\pi^2$ is located in the unphysical region below the pseudo-threshold. If s is (even marginally) shifted to larger values $s > s_-$ the singularity is crossed, which completely determines the behavior of the D_{l4} amplitudes.

As a consequence we refrain from our original proposition to rigorously control the final-state interaction as presented in this thesis, supposed to deduce high-precision πK phase-shift information.

We conclude with three main statements: first, it is highly problematic to employ HMChPT in high-precision analyses of decays of D-mesons due to the slow convergence, in particular in the combination with kaons in the final states. Second, the extrapolation to lower s_l by means of low-energy theorems does not show great promise: on the one hand only constraints for the (small) S-wave component can be derived, and on the other hand even for these constraints the predicitveness is restricted by the validity of the low-energy theorems up to orders of the squared light meson masses, such that there is freedom in choosing the evaluation point. Third, a comparison between the fully dispersively constructed partial-wave amplitudes as presented in this thesis and the partial waves obtained in a naive unitarization approach revealed a good accordance, in particular in regard of the large uncertainties involved in the dispersive treatment. In such an approach we have described the amplitudes by polynomials in s multiplied by the respective Omnès functions. We have shown that linear polynomials in s should deliver a sufficient amount of flexibility. Undisputably, our formalism has powerful merits like the model independence and the inherent fulfillment of unitarity and analyticity. However, it involves a degree of complexity that must not be overlooked. Therefore one might deliberate whether a simplified version is more suitable. As long as the diverse uncertainties discussed above inhibit an accurate treatment of the partial waves, we recommend the suggested simplified approach of unitarizing the partial waves, which seems to attain a well-balanced compromise of complexibility and benefit.

Thesis summary and outlook

In this thesis we have employed dispersion relations to analyze heavy-meson decays. The dispersive framework relies on a crucial correlation between scattering and decay processes: accurately known scattering phase shifts serve as input to the dispersive construction of decay amplitudes, exploiting the universality of strong final-state interactions and Watson's theorem. This redundantizes any modelling of resonant terms in the final-state interaction. Dispersion relations hence provide a tight control of the strong final-state interactions in a model-independent way, respecting the fundamental constraints from unitarity and analyticity. At the same time a thorough understanding of the hadronic final-state interactions in decay processes delivers highly valuable knowledge on scattering dynamics. This has been demonstrated very successfully in the extraction of pion–pion scattering phase shifts and scattering lengths from K_{l4} decays, measured with an impressive precision.

We have pursued both objectives, exploiting scattering data to constrain decay amplitudes, as well as deducing scattering information from our decay analyses. We have exemplified this concretely by the decays of heavy B- and D-mesons. In particular we have analyzed the non-leptonic decays of a $\bar{B}^0_{d,s}$-meson into J/ψ and two light mesons, $\pi^+\pi^-$, $\pi^0\eta$, K^+K^- or $\bar{K}^0K^0$, and the semileptonic $D^+ \to \pi^+K^-l^+\nu$ decay. The pairwise rescattering of the final-state hadrons as well as crossed-channel effects were described in an Omnès formalism. In the considered B-meson decays the interaction of the light final-state meson pairs has been described by scalar and vector form factors. The neglect of rescattering with the J/ψ is inspired by phenomenological observations and symmetry-related arguments. For the scalar form factors we pursued a coupled-channel approach, mandatory due to the strong coupling between the S-wave $\pi\pi$ and $\bar{K}K$ ($\pi\eta$ and $\bar{K}K$) in the isoscalar (isovector) case. We solved two-channel Muskhelishvili–Omnès equations based on three input functions in the isoscalar case: the $\pi\pi$ elastic S-wave phase shift, and modulus and phase of the $\pi\pi \to \bar{K}K$ amplitude. In the case of the isovector scalar form factors we adopted the Muskhelishvili–Omnès equations as solved in Ref. [140] that relies on unitarity and chiral constraints. For the pion vector form factor an elastic approximation is well reliable. We used a single-channel Omnès representation for which the elastic $\pi\pi$ phase shift serves as input. Isospin-violating effects due to the ρ–ω mixing have been taken into account without introducing further degrees of freedom as the strength could be fixed from data of the pion vector form factor.

We established our framework on the decays $\bar{B}^0_{d,s} \to J/\psi\pi^+\pi^-$. Fitting the spectra to LHCb data revealed fits of a similar fit quality as in the experimental analysis for energies $\sqrt{s} \lesssim 1.02$ GeV, yet with a significantly reduced number of fit parameters. A description in terms of S- and P-waves, which are represented by the respective form factors multiplied by real subtraction constants, is satisfactory. The benefit gathered by the regard for D-wave corrections or linear subtraction polynomials is superfluous: D-waves become important at energies near the $f_2(1270)$ resonance and higher, above the region considered here; allowing for free linear slopes has an effect only for one P-wave component, and does not induce a considerable improvement on the fit quality. Consequently, by studying the $\bar{B}^0_{d,s} \to J/\psi\pi^+\pi^-$

modes we assessed conspicuous benefits in our dispersive approach compared to the formalism employed in former experimental analyses, where Breit–Wigner representations supplemented by non-resonant background have been used. We achieved by construction unitarity, analyticity, model-independency, and (in contrast to the Breit–Wigner parametrization) the correct phase motion according to Watson's theorem, without diminishing the quality of the fits. Quite on the contrary the predictive power is enhanced given the reduced number of free fit parameters.

In a next step we employed these fit results in order to make predictions for the $\bar{B}^0_d \to J/\psi\{\pi^0\eta, K^+K^-, \bar{K}^0K^0\}$ decay spectra and the $\bar{B}^0_s \to J/\psi K^+K^-$ S-wave. The light meson pairs in these channels are linked to the $\pi^+\pi^-$ system by coupled-channel and chiral symmetry relations, which can be transferred (as explicitly shown) to the full decay amplitudes. For $\bar{B}^0_s \to J/\psi K^+K^-$, dominated by the P-wave $\phi(1020)$ resonance, we obtained an S-wave contribution of about 1.1%, which is compatible with the background determined in the LHCb analysis. Since the kaons emerge from a purely isoscalar $\bar{s}s$ source, the non-strange decay modes $\bar{B}^0_d \to J/\psi\{\pi^0\eta, K^+K^-, \bar{K}^0K^0\}$ involve both the isoscalar and isovector scalar form factors, the latter exhibiting a rather large uncertainty due to a yet undetermined parameter δ_{12}. We recommend an experimental exploration of these decays in order to constrain this parameter, mandatory for an accurate determination of the $\pi\eta$ scattering amplitude.

The second part of this thesis deals with the D_{l4} analysis. A motivation to study this decay is its analogy to the K_{l4} decay, which was employed for a highly accurate extraction of $\pi\pi$ phase shifts: the D_{l4} decay might be used for a similar extraction of πK phases. Also here we employed the powerful tools of dispersion relations. In a modified Omnès formalism left-hand cut structures have been approximated by pole terms. We have explicitly calculated the corresponding exchange processes in HMChPT, which served as input simplifying the framework of Khuri–Treiman equations. According to the concern of the reliability of heavy-quark and chiral symmetries in the case of D-meson decays and a final-state kaon NLO corrections in the HMChPT amplitudes have been taken into account. A similar formalism was applied in the study of $B \to \pi\pi l\nu$ [126], which we have generalized to unequal-mass mesons in the final state. A delimiting factor of this approach is that it requires to fix the dilepton energy s_l to a large value, where HMChPT can be applied. We have developed a strategy how to increase the covered phase space and to extrapolate the amplitudes to smaller s_l by means of parametrizing the s_l-dependent subtraction polynomials in conformal variables. Certain low-energy theorems supposed to constrain these functions have been applied in the case of the S-wave. The predictive power however is impaired by several conceptual issues that have to be faced when applying soft-pion and soft-kaon theorems in such a context, in particular on account of the numerical significance of corrections of orders $\mathcal{O}(M_K^2)$, evident in the choice of the evaluation points of the respective low-energy theorems, as well as in the rather slow convergence of the HMChPT expansion.

A promising project that is closely related to the $\bar{B}^0$ analyses but not pursued in this thesis is a study of the $\bar{B}^0_s \to J/\psi\pi^0\eta$ decay in an analogous formalism. This process features a purely isoscalar source providing an ideal basis to investigate isospin-violating effects, which become evident in the phenomenon of a_0–f_0 mixing. Furthermore, the extension to energies above ~ 1 GeV has not been treated so far. This requires the consideration of further inelastic channels in the scalar sector as well as higher partial waves. Data of a sufficient precision also allows to accomplish an extraction of the scalar form factor in that energy range.

Appendix A

Supplements to the $\bar{B}^0_{d/s} \to J/\psi M_1 M_2$ analyses

A.1 Isospin basis and unitarity relations

Often the scalar form factors are defined as follows,

$$\langle 0\,|(\bar{q}q)_I|\,M_1M_2\rangle_I = \mathcal{B}_0^{q,\Delta}\mathcal{F}^{q,I}_{M_1M_2}(s) \tag{A.1}$$

(further information on the scalar currents $\bar{q}q$ and the parameters $\mathcal{B}_0^{q,\Delta}$ are given in Section 2.4.2), where the isospin basis is used. The isospin-0 pion and kaon states read

$$|\pi\pi\rangle_{I=0} = -\frac{1}{\sqrt{3}}\left(|\pi^-\pi^+\rangle + |\pi^+\pi^-\rangle + |\pi^0\pi^0\rangle\right), \quad |K\bar{K}\rangle_{I=0} = -\frac{1}{\sqrt{2}}(|K^+K^-\rangle + |K^0\bar{K}^0\rangle). \tag{A.2}$$

A comparison with the form factors $\mathcal{B}_0^{q,\Delta}\Gamma^{q,I}_{M_1M_2}(s) = \left\langle 0\,|(\bar{q}q)_I|\,M_1^iM_2^i\right\rangle_I$ defined in Section 1.3.4 in the euclidean basis $|M_1^iM_2^i\rangle$ (or using physical states, e.g. $M_1^+M_2^-$, respectively) yields $\mathcal{F}^{q,I=0}_{\pi\pi}(s) = \sqrt{3}\Gamma^{q,I=0}_{\pi\pi}(s)$ and $\mathcal{F}^{q,I=0}_{KK}(s) = \sqrt{2}\Gamma^{q,I=0}_{KK}(s)$. The normalization constants we have deduced by means of the Feynman–Hellmann theorem refer to those $\Gamma^{q,I=0}_{M_1M_2}(s)$.

The relation between the form factors in the isospin and the euclidean basis is meaningful for the formulation of the unitarity relations. The partial waves (S-waves) that enter are defined in the partial-wave expansions of the $\pi\pi \to \pi\pi$ amplitude $T^I(s,z)$, the $\pi\pi \to \bar{K}K$ amplitude $G^I(s,z)$ and the $\bar{K}K \to \bar{K}K$ amplitude $R^I(s,z)$, given by

$$\begin{aligned}
T^I(s,z) =& 16\pi\sum_{J=0}^{\infty}(2J+1)\,2\,t^I_J(s)P_J(z),\\
G^I(s,z) =& 16\pi\sum_{J=0}^{\infty}(2J+1)\,\sqrt{2}\,g^I_J(s)P_J(z),\\
R^I(s,z) =& 16\pi\sum_{J=0}^{\infty}(2J+1)\,r^I_J(s)P_J(z)
\end{aligned} \tag{A.3}$$

(note the different symmetry factors $\sqrt{2}$). From the above considerations one can deduce the

unitarity relations

$$\begin{aligned}
\sqrt{3}\,\mathrm{Im}\,\Gamma_\pi \sim& \frac{1}{2}\,2\,t_0^0\,\sigma_{\pi\pi}\sqrt{3}\,\Gamma_\pi + \sqrt{2}\,g_0^0\,\sigma_{KK}\sqrt{2}\,\Gamma_K,\\
\mathrm{Im}\,\Gamma_\pi \sim& t_0^0\,\sigma_{\pi\pi}\Gamma_\pi + \frac{2}{\sqrt{3}}\,g_0^0\,\sigma_{KK}\Gamma_K,\\
\sqrt{2}\,\mathrm{Im}\,\Gamma_K \sim& \frac{1}{2}\,\sqrt{2}\,g_0^0\,\sigma_{\pi\pi}\sqrt{3}\,\Gamma_\pi + r_0^0\,\sigma_{KK}\sqrt{2}\,\Gamma_K,\\
\mathrm{Im}\,\Gamma_K \sim& \frac{\sqrt{3}}{2}\,g_0^0\,\sigma_{\pi\pi}\Gamma_\pi + r_0^0\,\sigma_{KK}\Gamma_K,\\
\text{with}\quad \sigma_{M_1M_2} =& \frac{\lambda^{1/2}(s, m_{M_1}^2, m_{M_2}^2)}{s},
\end{aligned} \tag{A.4}$$

explaining the occurrence of the factor $2/\sqrt{3}$ in the isoscalar pion–kaon coupled-channel formulation.

The corresponding relations in the isovector case follow analogously. The isospin-1 $\pi\eta$ and $\bar{K}K$ states read

$$|\pi\eta\rangle_{I=1} = |\pi\eta\rangle, \quad |K\bar{K}\rangle_{I=1} = -\frac{1}{\sqrt{2}}(|K^+K^-\rangle - |K^0\bar{K}^0\rangle), \tag{A.5}$$

from which $\mathcal{F}^{q,I=0}_{\pi\eta}(s) = \Gamma^{q,I=0}_{\pi\eta}(s)$ and $\mathcal{F}^{q,I=0}_{K\bar{K}}(s) = \sqrt{2}\Gamma^{q,I=0}_{K\bar{K}}(s)$ follows. The relevant partial waves are defined in the expansions of the $\pi\eta \to \pi\eta$ and $\pi\eta \to \bar{K}K$ amplitudes

$$U^I(s,z) = 16\pi\sum_{J=0}^{\infty}(2J+1)\;u_J^I(s)P_J(z), \quad V^I(s,z) = 16\pi\sum_{J=0}^{\infty}(2J+1)\,v_J^I(s)P_J(z), \tag{A.6}$$

and of the $\bar{K}K \to \bar{K}K$ amplitude $R^I(s,z)$. They are combined in the unitarity relations

$$\begin{aligned}
\mathrm{Im}\,\Gamma_{\pi\eta} \sim& u_0^1\,\sigma_{\pi\eta}\,\Gamma_{\pi\eta} + \sqrt{2}\,v_0^1\,\sigma_K\,\Gamma_{\bar{K}K},\\
\sqrt{2}\,\mathrm{Im}\,\Gamma_{\bar{K}K} \sim& \sqrt{2}\,v_0^1\,\sigma_{\pi\eta}\,\Gamma_{\pi\eta} + r_0^1\,\sigma_K\,\Gamma_{\bar{K}K},
\end{aligned} \tag{A.7}$$

where the relative factor $\sqrt{2}$ between the two channels appears.

A.2 Construction of an weak-interaction HMChPT Lagrangian

The concern of this appendix is to motivate the structure of the Lagrangian Eq. (2.90) in Section 2.7.3, following Refs. [198, 236]. It describes weak-interaction processes involving heavy mesons, heavy quarkonia and light pseudoscalars. In order to properly implement the constraints from the heavy-quark (HQ) spin symmetry the operators Q_1, Q_2,[1] see Eq. (2.18) (we suppress here the superscripts c for the operators to avoid confusion with the HQ fields $Q^{b,c}_{v,v'}$ that have velocities v, v' and polarizations ϵ, ϵ'), are written as Lorentz tensors (with two Lorentz indices that will be contracted in the end),

$$\begin{aligned}
Q_1 = \bar{d}\gamma_\mu(1-\gamma^5)c\bar{c}\gamma^\mu(1-\gamma^5)b \quad &\longrightarrow \quad Q_1^{\mu\nu}(v,v') = \bar{d}\gamma^\mu(1-\gamma^5)Q^c_{v'}\bar{Q}^c_{v'}\gamma^\nu(1-\gamma^5)Q^b_v,\\
Q_2 = \bar{c}\gamma_\mu(1-\gamma^5)c\,\bar{d}\gamma^\mu(1-\gamma^5)b \quad &\longrightarrow \quad Q_2^{\mu\nu}(v,v') = \bar{Q}^c_{v'}\gamma^\mu(1-\gamma^5)Q^c_{v'}\,\bar{d}\gamma^\nu(1-\gamma^5)Q^b_v.
\end{aligned} \tag{A.8}$$

[1] The weak interactions are not invariant under HQ spin rotations, therefore the effective weak Hamiltonian at the quark level (involving the operators Q_1 and Q_2) is considered for studying the transformation properties.

Under the velocity-dependent HQ spin rotations the fields Q_v^b and $Q_{v'}^c$ transform as

$$\begin{aligned} Q_v^b &\to \gamma^5 \not{\epsilon} \, Q_v^b, \\ Q_{v'}^c &\to \gamma^5 \not{\epsilon}' \not{\epsilon}' \, Q_{v'}^c, \end{aligned} \tag{A.9}$$

where $v \cdot \epsilon = v' \cdot \epsilon' = 0$, and the antiquark field $\bar{Q}_{v'}^c$ as

$$\bar{Q}_{v'}^c \to \bar{Q}_{v'}^c (-\gamma^5 \not{\epsilon}' \not{\epsilon}'^*) \; . \tag{A.10}$$

The resulting transformation properties of the operators $Q_1^{\mu\nu}(v, v')$ and $Q_2^{\mu\nu}(v, v')$ must be reproduced in the hadronic representation of the operator.

One can show that the operator Q_1 is left invariant assuming that the matrices $\gamma^\mu(1-\gamma^5)$ and $\gamma^\nu(1-\gamma^5)$ transform as

$$\begin{aligned} \gamma^\mu(1-\gamma^5) &\to \gamma^\mu(1-\gamma^5)\gamma^5 \not{\epsilon}' \not{\epsilon}'^*, \\ \gamma^\nu(1-\gamma^5) &\to -\gamma^5 \not{\epsilon}' \not{\epsilon}' \, \gamma^\nu(1-\gamma^5)\gamma^5 \not{\epsilon} \not{\epsilon}^*, \end{aligned} \tag{A.11}$$

together with $\not{\epsilon}^* \not{\epsilon} = - \not{\epsilon} \not{\epsilon}^*$ and $\epsilon \cdot \epsilon^* = -1$. It seems thus necessary that the matrices $\gamma^\mu(1-\gamma^5)$, $\gamma^\nu(1-\gamma^5)$ appear in the effective hadronic Lagrangian. For the operator $Q_2^{\mu\nu}(v, v')$ we consider the spurion transformation of $\gamma^\mu(1-\gamma^5)$, $\gamma^\nu(1-\gamma^5)$ under HQ spin symmetry to be

$$\begin{aligned} \gamma^\mu(1-\gamma^5) &\to -\gamma^5 \not{\epsilon}' \not{\epsilon}' \, \gamma^\mu(1-\gamma^5)\gamma^5 \not{\epsilon}' \not{\epsilon}'^*, \\ \gamma^\nu(1-\gamma^5) &\to \gamma^\nu(1-\gamma^5)\gamma^5 \not{\epsilon} \not{\epsilon}^* \; . \end{aligned} \tag{A.12}$$

The heavy-meson fields that enter the HMChPT Lagrangians, encoded in the two matrices[2]

$$\begin{aligned} J &= \frac{1+\not{v}'}{2} \left(\gamma^5 \eta_c - \not{\Psi}\right) \frac{1-\not{v}'}{2} \to \frac{1+\not{v}'}{2} \left(\gamma^5 \eta_c - \not{\Psi}\right), \\ H &= \frac{1+\not{v}}{2} \left(\gamma^5 B^0 - \not{B}^*\right), \end{aligned} \tag{A.13}$$

exhibit the proper transformation properties under the spin rotations of the two heavy quarks, Eq. (A.9),

$$\begin{aligned} H &\to \gamma^5 \not{\epsilon} \not{\epsilon} \, H, \\ J &\to \gamma^5 \not{\epsilon}' \not{\epsilon}' \, J, \end{aligned} \tag{A.14}$$

and under the spin rotation of the heavy charm antiquark, Eq. (A.10),

$$J \to J(-\gamma^5 \not{\epsilon}' \not{\epsilon}'^*). \tag{A.15}$$

In addition to spin rotations the Lagrangian under consideration is required to behave properly under Lorentz transformations, which is achieved by implementing traces. The simplest Lagrangian representation of the operator Q_1 incorporates two independent terms,

$$\begin{aligned} \mathcal{L}_1^{\mu\nu} = \; & A_1 \mathrm{Tr}\left(\gamma^\mu(1-\gamma^5) J \gamma^\nu(1-\gamma^5) H\right) \\ & + A_2 \mathrm{Tr}\left(\not{v} \, \gamma^\mu(1-\gamma^5) J \gamma^\nu(1-\gamma^5) H\right), \end{aligned} \tag{A.16}$$

and for the operator Q_2 the Lagrangian has two independent terms as well, which have a double trace form,

$$\begin{aligned} \mathcal{L}_2^{\mu\nu} = \; & B_1 \mathrm{Tr}\left(\gamma^\mu(1-\gamma^5) J\right) \mathrm{Tr}\left(\gamma^\nu(1-\gamma^5) H\right) \\ & + B_2 \mathrm{Tr}\left(\gamma^\mu(1-\gamma^5) J\right) \mathrm{Tr}\left(\not{v}' \, \gamma^\nu(1-\gamma^5) H\right). \end{aligned} \tag{A.17}$$

[2]Note that the factor $(1- \not{v}')/2$ on the right of J is superfluous; due to $v' \cdot \psi = 0$ it can be moved to the left.

Appendix B

Supplements to the D_{l4} analysis

B.1 Fixing the next-to-leading order couplings $\beta_{1,2}$

B.1.1 Analysis of D_{l3} and B_{l3} decay form factors

The NLO correction terms induced by the Lagrangian Eq. (1.53) incorporate two new coupling constants β_1 and β_2, which are unknown so far. For an estimation of those we employ that from the same Lagrangian Eq. (1.53) we can calculate the HMChPT tree-level amplitudes for the D_{l3} decay, the form factors $f_\pm$ therefore depend on the same coefficients $\beta_{1,2}$,

$$\begin{aligned} f_+ =& -\frac{g f_{D^*} m_{D^*}}{2\sqrt{2}F_\pi}\frac{1}{\Delta + v\cdot p_\pi} - \frac{f_D - 2\beta_1 - 2\beta_2 p_D\cdot p_\pi}{2\sqrt{2}F_\pi} + \mathcal{O}\left(\frac{M_\pi}{m_D}, \frac{\Delta}{m_D}\right), \\ f_- =& \frac{g f_{D^*}}{2\sqrt{2}F_\pi}\frac{m_{D^*} - 2\Delta}{\Delta + v\cdot p_\pi} - \frac{f_D - 2g f_{D^*} + 2\beta_1 - 2\beta_2 p_D\cdot p_\pi}{2\sqrt{2}F_\pi} + \mathcal{O}\left(\frac{M_\pi}{m_D}, \frac{\Delta}{m_D}\right). \end{aligned} \tag{B.1}$$

We consider the form factor f_+ and replace the effective propagator by the full relativistic one according to Eq. (3.37). The considered correction appears in form of a linear polynomial,

$$f_+ = -\frac{1}{2\sqrt{2}F_\pi}\left(f_D - 2\beta_1 - \beta_2(m_D^2 - t) - \frac{2g f_{D^*} m_{D^*}^2}{t - m_{D^*}^2}\right). \tag{B.2}$$

A parametrization of the D_{l3} form factor in terms of a series expansion in conformal variables, which converges very quickly and which fulfills analyticity, is well reliable. The idea of such an expansion is that the complex plane is mapped onto the unit circle, by mapping the variable t onto the variable z by

$$z(t, t_0) = \frac{\sqrt{t_+ - t} - \sqrt{t_+ - t_0}}{\sqrt{t_+ - t} + \sqrt{t_+ - t_0}}, \tag{B.3}$$

with $t_0 = t_+(1 - \sqrt{1 - t_-/t_+})$ and $t_\pm = (m_D \pm M_\pi)^2$. This is illustrated in Figure B.1. The physical region of the D_{l3} decay is mapped onto an interval $z \in [-0.167, 0.167]$, shown by the gray-shaded box.

An appropriate form factor expansion reads[1]

$$f_+(t) = \sum_{k=0}^{\infty} a_k(t_0) z^k(t, t_0), \tag{B.4}$$

[1] D decays are well described by such a simplified conformal parametrization, where a unitarity-entailing function $\Phi(t, t_0)$ that is often found in the literature is set to 1. Elaborated discussions concerning unitarity bounds as well as effects arising from above-threshold poles can be found e.g. in Refs. [237–241].

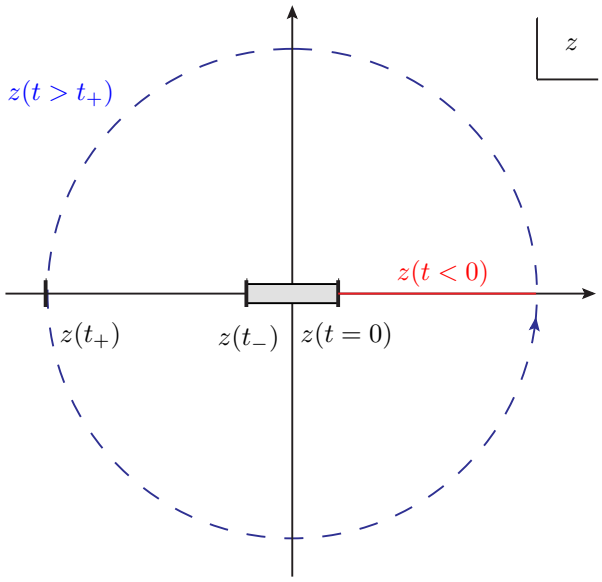

Figure B.1: We show the conformal mapping of the complex t-plane onto the unit circle. The physical region for the D_{l3} decay is shown by the gray box on the real axis, with $z(t_-) < z < z(t = 0)$ and $|z(t_-)| = |z(0)| \approx 0.167$. The left-hand cut $t < 0$ is mapped onto the positive real axis (red). When increasing t, $z(t)$ runs along the negative real axis until $z(t_+) = -1$, and moves along the unit circle for energies $t > t_+$ (blue).

as long as no sub-threshold poles exist, which is the case for the D_{l3} decay, where the lowest pole appears just above the threshold ($m_{D^*} - \sqrt{t_+} > 0$) with a narrow width. Due to the good convergence the series can be truncated at a low order $k_{\max}$. A common choice of $k_{\max}$ is $k_{\max} = 1$ or 2.

We take the results of a BES III analysis [227], where a conformal three-parameter parametrization is used, i.e. $k_{\max} = 2$. There the coefficients of the series expansion are determined by fitting to the data, yielding the form factor shown in Figure B.2 (solid red curve with error band). Note that in the experimental analysis the decay $D^0 \to \pi^- l\nu$ is explored, while we discuss the isospin-related $D^+ \to \pi^0 l\nu$ decay amplitude, differing by a factor $\sqrt{2}$, however, this is taken into consideration in the definition of the form factors $f_\pm$ in the hadronic matrix element, cf. Eq. (3.58), such that the BES III and our form factors are in accordance.[2] Matching the HMChPT expression, Eq. (B.2), onto the BES III form factor at an appropriate matching point/region enables us to fix the constants β_1 and β_2. As HMChPT works best for large t a good choice might be the upper end of the physical region, $t \lesssim t_-$, although, the closer this region is constrained the stronger a mismatch for lower t shows up, i.e. matching for instance pointwise at $t_{\max} = t_-$ yields large discrepancies between the obtained HMChPT form-factor normalization and that of the z parametrization. Therefore we consider two scenarios, choosing the region $2\ \text{GeV}^2 \leq t \leq t_-$ (FIT I) and the whole physical region $0\ \text{GeV}^2 \leq t \leq t_-$ (FIT II), in which we fit to the conformal parametrization. Of course, the latter choice is a stretch beyond the range where HMChPT is thought to be well applicable, but it allows for a phenomenology-compatible

[2] For the direct comparison of our form factor parametrization to the one used in the BES III analysis we take into consideration a relative sign due to different conventions concerning an overall phase factor.

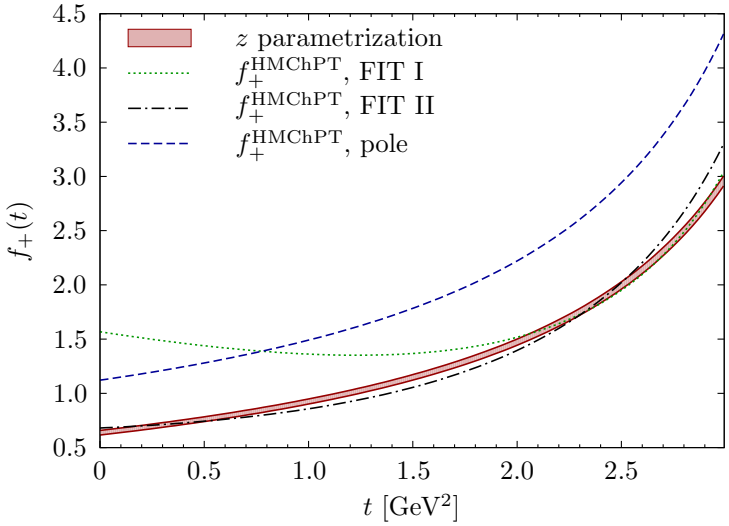

Figure B.2: D_{l3} form factor $f_+(t)$: the solid red curve with error band shows a conformal parametrization as determined by the BES III collaboration. The other curves correspond to HMChPT expressions with different β_i correction terms as determined in the fit scenarios described in the main text: FIT I (green dotted curve) and FIT II (black dash-dotted), and the HMChPT pole term contributing at LO (blue dashed curve).

representation of the form factor, such that for instance the deviation in the normalization is not too large.

For FIT I we find $\beta_1 = (0.31 \pm 0.03)$ GeV and $\beta_2 = (-0.15 \pm 0.05)$ GeV^{-1}, corresponding to the dotted green curve of Figure B.2, and for FIT II we obtain $\beta_1 = (0.25 \pm 0.02)$ GeV and $\beta_2 = (-0.05 \pm 0.02)$ GeV^{-1}, depicted by the black dash-dotted curve. The FIT II results in particular reflect the purpose of the fit constellation: by construction the β_i account for a finetuning of the NLO corrections in the form factor normalization. Considering the β_i fit polynomial (in t), $2\beta_1 + \beta_2(m_D^2 - t) \equiv \tilde{\beta} + t\tilde{\beta}'$, the constant term $\tilde{\beta}$ is determined to cancel with the fixed NLO terms, such that for FIT II $f_+^{\mathrm{NLO}} \approx f_+^{\mathrm{LO}}$. Exactly this constant part hence differs in the various fit configurations.

Both fit results are of the same order of magnitude, but the results for the parameter β_1 differ on a 20% level, and those for β_2 even more (though this can actually be partly traced back to the correlation between both parameters—the correlation coefficient $\rho_{\beta_1\beta_2}$ is $\rho_{\beta_1\beta_2} > 0.9$). Unfortunately, even small deviations in the β_i coefficients that enter the D_{l4} amplitudes cause a significant impact on the latter as we show in Appendix B.1.2. This originates from the rather slow convergence of the HMChPT expansion where the chiral symmetry is broken by the kaon mass and the heavy-quark symmetry by the D-meson mass, both inducing large corrections, see the discussion in Section 3.5.

It is therefore expedient to further constrain the determination of the β_i by considering other decay channels as well. The same HMChPT Lagrangian from which the $D \to \pi l\nu$ vector form factor $f_+(t)$, Eq. (B.2), is obtained yields the $D \to Kl\nu$ vector form factor, being of the same form as for $D \to \pi l\nu$, with the replacements $(p_\pi, M_\pi) \to (p_K, M_K)$ and $(F_\pi, f_D, m_{D^*}) \to (F_K, f_{D_s}, m_{D_s^*})$. Compared to the $D \to \pi l\nu$ decay now the light meson in the final state is the much heavier kaon such that HMChPT is less justified. We therefore refrain from fitting the complete physical region but restrict ourselves to the region of small kaon momentum transfer,

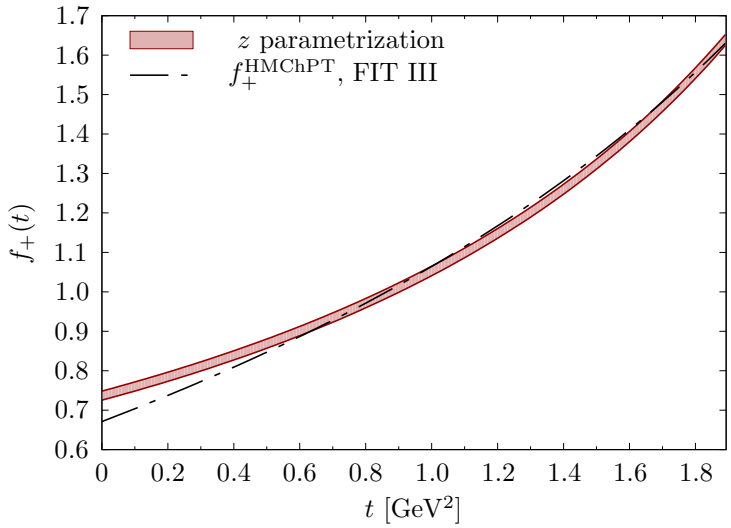

Figure B.3: $D \to Kl\nu$ form factor $f_+(t)$: the solid red curve with error band shows a conformal parametrization as determined by the BES III collaboration. The black, dash-dotted curve corresponds to the HMChPT expression with the FIT III β_i fit results.

$1\ \mathrm{GeV}^2 \leq t \leq t_- = (m_D - M_K)^2$. We employ a parametrization similar to Eq. (B.4), but take into account a below-threshold resonant pole and remove the related dynamical singularity by dividing by the Blaschke factor $z(t, m_{D_s^*})$,

$$f_+(t) = \frac{1}{z(t, m_{D_s^*})} \sum_{k=0}^{\infty} a_k(t_0) z^k(t, t_0). \tag{B.5}$$

A fit to the BES III parametrization [227], shown in Figure B.3 yields $\beta_1 = (0.14 \pm 0.05)$ GeV and $\beta_2 = (0.02 \pm 0.05)\ \mathrm{GeV}^{-1}$ (FIT III). Consequently, including the $D \to Kl\nu$ channel does not allow to further constrain the β_i values but rather increases the uncertainty.

As a last fit configuration (FIT IV) we examine the $B \to \pi l\nu$ decay. The benefit of this decay is that due to $m_B \gg m_D$ and $M_\pi \ll M_K$ the application of HMChPT symmetry is much more reliable than it is the case for the $D \to \{\pi, K\} l\nu$ decay channel, such that a good convergence can be expected. Note that there is a dependencey on the heavy mass [75], $\beta_1^P \sim \sqrt{m_P}$, $\beta_2^P \sim 1/\sqrt{m_P}^3$ (we neglect here logarithmic corrections), such that $\beta_1^D = \sqrt{m_D/m_B}\beta_1^B$, $\beta_2^D = \sqrt{m_B/m_D}^3 \beta_2^B$. This has to be taken into account in a direct comparison of the fit result to the former fits. Similar to the $D \to Kl\nu$ parametrization the appearance of a subthreshold-pole is taken into account by dividing out the pole term or $z(t, m_{B^*})$, respectively, see Eq. (B.5). We hence rewrite the $B \to \pi l\nu$ vector form factor (obtained from Eq. (B.2) with the replacements $(f_D, f_{D^*}, m_D, m_{D^*}) \to (f_B, f_{B^*}, m_B, m_{B^*})$) into such a parametrization, which we then fit to the results of a Belle analysis [228], where a two-parameter BCL parametrization [237] is fitted to tagged $B^- \to \pi^0 l^- \nu$ and $\bar{B}^0 \to \pi^+ l^- \nu$ data combined with lattice-QCD results in the high-t region (obtained by the FNAL/MILC collaboration [242]) and with light-cone sum-rule calculations for $t = 0$ [243]. The phase space for the B_{l3} decay, $0 < t < t_- = (m_B - M_\pi)^2$, is much larger than the D_{l3} phase space and it is a matter of discretion which energy region we include in our fit. Instead of stating a criterion that determines the specific energy regions in which we assume HMChPT to work reliably well, we consider different energy intervals in order

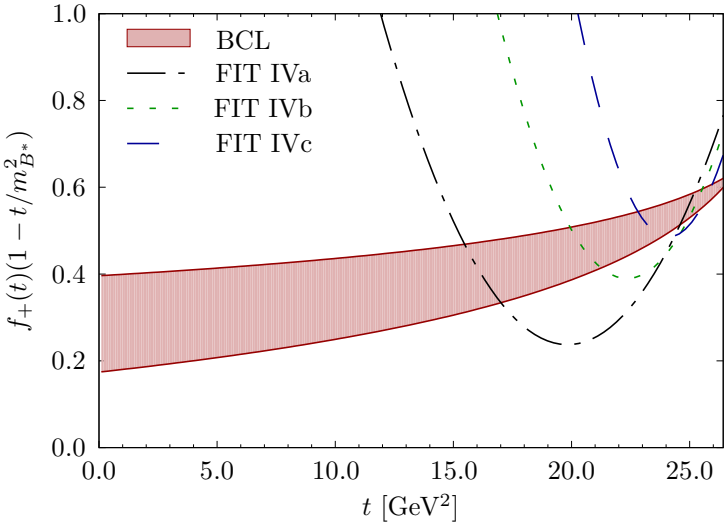

Figure B.4: $B \to \pi l \nu$ form factor $f_+(t)$: the solid red curve with error band shows a conformal parametrization as determined by the Belle collaboration. The other curves correspond to the HMChPT expressions with the β_i fit results as determined in the fits FIT IVa (black, dot-dashed), FIT IVb (green, dotted), and FIT IVc (blue, dashed).

to investigate whether this choice has a significant influence on the fit results. We perform fits in the intervals $t_{\text{start}} < t < t_-$ with $t_{\text{start}} = \{14\ \text{GeV}^2, 18\ \text{GeV}^2, 22\ \text{GeV}^2\}$ (FIT IVa-c), and find the following sets of coefficients β_i,

$$\begin{aligned}
\beta_1^B &= (0.84 \pm 0.06)\ \text{GeV}, \quad \beta_2^B = (-0.09 \pm 0.01)\ \text{GeV}^{-1} \quad \text{(FIT IVa)},\\
\beta_1^B &= (0.96 \pm 0.06)\ \text{GeV}, \quad \beta_2^B = (-0.15 \pm 0.02)\ \text{GeV}^{-1} \quad \text{(FIT IVb)},\\
\beta_1^B &= (1.14 \pm 0.07)\ \text{GeV}, \quad \beta_2^B = (-0.26 \pm 0.04)\ \text{GeV}^{-1} \quad \text{(FIT IVc)}.
\end{aligned} \tag{B.6}$$

Hence the specific choice of t_{start} has indeed a considerable impact on the fit results, revealing discrepancies between the different values. The fit is shown in Figure B.4. There is a significant difference between the HMChPT pole term, $f_{+,\text{pole}}^{\text{HMChPT}} \cdot (1 - t/m_{B^*}^2) = 1.12$, and the BCL parametrization, for which we determine the pole residue 0.75±. Evidently, the pole strength predicted by HMChPT does not feature a good agreement with the BCL one, necessitating large correction terms. This causes the huge discrepancies in the slopes of the various parametrizations that we observe in Figure B.4.

We compare the determined values with the fit results of FIT I-III and take into consideration the respective scaling with the heavy mass mentioned above. The range of the β_1 obtained in the B-decay thus translates to the range $0.46\ \text{GeV} < \beta_1^D < 0.72\ \text{GeV}$, which differs to the values obtained in FIT I and II roughly by a factor 2.

We do not discuss a combined fit for the following reasons: in such a combined fit the B-decay would dominate over the D-decay modes, due to the larger phase space, and in particular, we would enforce this dominance by assigning a weighting factor on the B_{l3} distribution, given its better control over the heavy quark flavor and chiral symmetry violations. We hence assume the B_{l3} fit results to be the most promising ones, and state at least bounds on the β_i coefficients respecting the range quoted in Eq. (B.6), $\beta_1^B \geq 0.78\ \text{GeV}$, $\beta_2^B \leq -0.08\ \text{GeV}^{-1}$, but we cannot provide a more accurate determination. These bounds are actually to be regarded as rather

suggestive than strict bounds, respecting the strong correlation between the β_i^P that hence cannot be disentangled properly.

We do not use these results to state bounds on the β_i^D couplings as proposed above—severe symmetry violating effects in the D-meson decays need to be taken into account, causing a lowering of these bounds, as seen in fitting the β_i^D directly.

Recently the $\beta_i^{B,D}$ coefficients were determined in Ref. [235], where the respective scalar B_{l3} and D_{l3} form factors were fitted to data, combined with theory input. When comparing to our fit results, we notice a sign difference in the definition of the β_i^P coefficients, $\beta_1^P|_{\text{lit}} = -\beta_1^P|_{\text{this work}}$. Facing the same challenge of correlated variables they show various possible (β_1, β_2) pairs that yield a similar fit quality. However, for the most data sets they find positive β_1^B values which hence translate to negative coefficients using our definition. Consequently instead of further constraining or imposing stronger bounds on the $\beta_i^{B,D}$ this comparison yet enlarges the range of possible $\beta_i^{B,D}$ values and hence the uncertainty on the fits (and in particular the choice of the best fit configuration).

We conclude that it seems very difficult to fix the NLO coefficients to a sufficient precision, given the inherent complication of symmetry breaking effects, the significant dependency on t_{start}, and the strong correlation between β_1^P and β_2^P that entangles both parameters.

For the calculations performed in this thesis we will use the FIT II results. We resort to the D_{l3} decay in order to avoid estimating the symmetry breaking effects in translating the results from the B_{l3} decay. The D_{l3} amplitudes are furthermore related to the D_{l4} amplitudes, into which the β_i enter, via the soft-kaon theorem. As a consequence the D_{l3}-to-D_{l4} relation not only relies on heavy-meson and chiral symmetry—it is less afflicted by assumptions and hence theoretically better justified. An adjustment of the low-energy behavior seems to be reasonable here because we find a quite bad compatibility between the HMChPT and the conformal parametrization for small t. At leading-order only the pole term contributes to the HMChPT expression, shown by the blue dashed curve. The fixed part of next-to-leading order expression ($\propto f_D$) even worsens the deviation between the BES III and the HMChPT curves gets larger. Therefore FIT II allows for a better adjustment of the β_i correction terms in order to somewhat compensate this NLO effect.

Nevertheless, all numerical results that depend on this coefficient should be considered as a demonstration of our method for a particular set of input parameters, but not as powerful predictions, given the uncertainty on these parameters and, in particular, the (unfortunately large) effect of that uncertainty in the D_{l4} NLO amplitudes.

B.1.2 Impact of the $\beta_{1,2}$ uncertainty on D_{l4} partial waves

In this section we demonstrate the impact of the uncertainty of the couplings $\beta_{1,2}$ on the D_{l4} partial waves. For this purpose we consider the two fit scenarios FIT I and FIT II, for which we have found $\beta_1 = (0.31 \pm 0.03)$ GeV and $\beta_2 = (-0.15 \pm 0.05)$ GeV^{-1} (FIT I), and $\beta_1 = (0.25 \pm 0.02)$ GeV and $\beta_2 = (0.05 \pm 0.02)$ GeV^{-1} (FIT II). The latter fit configuration we have assessed to most likely show promise for determining a meaningful set of couplings (see the discussion in the previous section). Even if we restrict ourselves to those two sets and disregard a further spreading of the β_i interval (as it is indicated by considerations of other fit configurations), we face relative errors on a 10 to 40% level. Given such a large uncertainty it is mandatory to study to what extend our dispersively constructed partial waves, Eq. (3.48), are affected.

To begin with we investigate in which combinations the β_i coefficients enter the pole and non-pole terms in the D_{l4} amplitudes. The pole terms F_1^{pole} and F_2^{pole}, Eq. (3.38), have contributions $\propto \beta_1 + \beta_2 m_{D^*}^2$, evaluated to (-0.30 ± 0.23) GeV in the FIT I configuration and (0.05 ± 0.10) GeV in the FIT II one. Exemplarily we consider the functions ζ_0 and ζ_1 that appear in the numerator

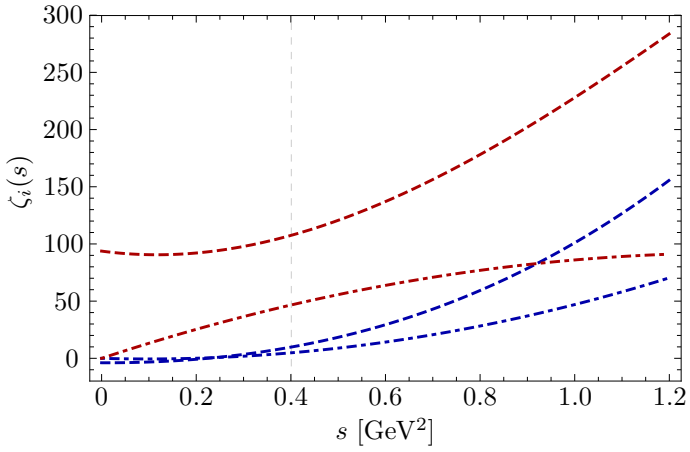

Figure B.5: The figure shows the functions $a_i(s)$ and $b_i(s)$, defined by $\zeta_i(s) = (\beta_1 + \beta_2 m_{D^*}^2)a_i(s) + b_i(s)$, for $i = 0, 1$. The $\zeta_i(s)$ contribute to the numerator of the pole term F_1^{pole}, Eq. (3.38). The blue curves depict the contributions to $\zeta_0(s)$, $Ys^2a_0(s)$ (blue, dashed) and $Ys^2b_0(s)$ (blue, dot-dashed), and the red curves refer to $\zeta_1(s)$, $2Xs\,a_1(s)$ (red, dashed) and $2Xs\,b_1(s)$ (red, dot-dashed). A very rough approximation yields $a_i(s) \approx 2b_i(s)$ above the πK threshold (indicated by the gray line). Kinematical singularities have been factored out to achieve a clearer representation.

of F_1^{pole}, Eq. (3.38), and that have the structure $\zeta_i(s) = (\beta_1 + \beta_2 m_{D^*}^2)a_i(s) + b_i(s)$; they are depicted in Figure B.5, where we compare the terms $a_i(s)$ and $b_i(s)$. We observe that the respective β_i independent parts $b(s)$ are of similar magnitudes as the terms $a_i(s)$, such that the various values obtained for the β_i combinations indeed cause significant variations. If we approximate $a_i(s) \approx 2b_i(s)$ (this is motivated by Figure B.5), the two fit results yield the functions $0.4b_i(s)$ and $1.1b_i(s)$. Hence the even relatively small variation in the β_i values (at least compared to the large variation if further decay modes are considered) propagates to effects in the D_{l4} pole terms that completely determine their structure.

To the non-pole expressions at NLO, Eq. (3.43), employed for the matching of the subtraction polynomial in Section 3.3, only β_1 contributes, in the combination $f_D - 2\beta_1$. For simplicity we consider M_1^{HMChPT} and U_1^{HMChPT} (being proportional to $f_D - 2\beta_1$) and find that the variation between the FIT I and FIT II β_1 results cause a 30% relative error.

The full partial waves (their magnitudes) evaluated for the FIT I and the FIT II sets of $\beta_{1,2}$ are displayed in Section 3.3, Figure 3.5, with the uncertainty bands induced by the β_i error ranges. For both fit results we find a strong effect as the partial waves exhibit large uncertainty bands, most prominent in the $\bar{K}^*(892)^0$. Combining the FIT I and FIT II uncertainties we observe e.g. a relative error of roughly 70% in the $M_1(s)$ peak region. Also the magnitude and the shape of $M_0(s)$ are influenced sizably.

B.2 Low-energy theorems in HMChPT

In this appendix we apply low-energy theorems to the HMChPT tree-level amplitudes at NLO, see Section 1.2.2, serving as a confirmation of the calculated D_{l4} and D_{l3} form factors. In particular the soft-pion and the soft-kaon theorems that entail certain relations of combinations of these form factors in the kinematical limits $p_\pi \to 0$ and $p_K \to 0$, as introduced in Sec-

tion 3.4.1, have to be fulfilled. We evaluate the form factors F, G and R defined via Eq. (3.8) from the tree-level amplitudes Eq. (1.55) and calculate the combinations in the respective limits according to Eqs. (3.59) and (3.60). For $p_\pi \to 0$ we find

$$F + G - R\,|_{p_\pi \to 0} = -\frac{2m_D \lambda_1 \hat{m} f_{D_s}}{F_\pi F_K\,(v\cdot p_K + \mu)} = \mathcal{O}(M_\pi^2)\,, \quad R\,|_{p_\pi \to 0} = \frac{2m_D \lambda_1 \hat{m} f_{D_s}}{F_\pi F_K\,(v\cdot p_K + \mu)} = \mathcal{O}(M_\pi^2)\,, \tag{B.7}$$

thus satisfying the soft-pion theorem. For $p_K \to 0$ the combination reads

$$\begin{aligned} F - G - R\,|_{p_K \to 0} &\\ &= \frac{m_D}{2F_\pi F_K}\left(-\frac{g f_{D^*} m_D}{v\cdot p_\pi + \Delta} - g f_{D^*} - f_{D_s}\frac{2\lambda_1(\hat{m}+m_s)}{v\cdot p_\pi + \mu} + 2\beta_1 + \mathcal{O}\left(\frac{M_\pi}{m_D}, \frac{\Delta}{m_D}\right)\right)\,, \\ R\,|_{p_K \to 0} &= -\frac{m_D}{2F_\pi F_K}\left(\frac{g f_{D^*}\Delta}{v\cdot p_\pi + \Delta} - f_{D_s}\frac{2\lambda_1(\hat{m}+m_s)}{v\cdot p_\pi + \mu} + f_D - 2\beta_2 p_D\cdot p_\pi - g f_{D^*}\right). \end{aligned} \tag{B.8}$$

This is compared to the sum and difference of the D_{l3} form factors $f_\pm$, defined via Eq. (3.58),

$$\begin{aligned} f_+ + f_- &= -\frac{1}{\sqrt{2}F_\pi}\frac{g f_{D^*}\Delta}{v\cdot p_\pi + \Delta} - \frac{f_D - g f_{D^*} - 2\beta_2 p_D\cdot p_\pi}{\sqrt{2}F_\pi} + \mathcal{O}\left(\frac{M_\pi}{m_D}, \frac{\Delta}{m_D}\right), \\ f_+ - f_- &= -\frac{1}{\sqrt{2}F_\pi}\frac{g f_{D^*} m_D}{v\cdot p_\pi + \Delta} + \frac{-g f_{D^*} + 2\beta_1}{\sqrt{2}F_\pi} + \mathcal{O}\left(\frac{M_\pi}{m_D}, \frac{\Delta}{m_D}\right), \end{aligned} \tag{B.9}$$

exhibiting that the D_{l3} and D_{l4} form factors differ by a correction

$$\frac{f_{D_s} m_{D_s} \lambda_1 (m_s + \hat{m})}{F_\pi F_K (v\cdot p_\pi + \mu)} \propto M_K^2,$$

hence the soft-kaon theorem is fulfilled as well.

B.3 Analytic properties of kinematical functions

In this appendix we have a closer look at the analytic properties of some kinematical functions defined in Section 3.2, with a particular interest in their behavior below the πK threshold. This is mandatory to investigate e.g. whether the partial-wave expansion Eq. (3.13) in the unphysical region converges.

To begin with, we consider the analytic continuation of the square root of the Källén function $\lambda(s, M_\pi^2, M_K^2)$, from which we learn about the analytic structure of the πK center-of-mass momentum $Y(s)$. In Figure B.6 $\lambda(s + i\epsilon, M_\pi^2, M_K^2)$ is plotted in the complex plane. Above the πK threshold (blue curve) both its real and (tiny) imaginary part are positive. Approaching the region below the threshold, $s < (M_\pi + M_K)^2$, $\lambda(s + i\epsilon, M_\pi^2, M_K^2)$ runs into the real negative region, still in the upper half plane (red curve). Further decreasing s, a sign change in the imaginary part happens at $s = M_\pi^2 + M_K^2$, the real part still being negative (green curve), until the energy is lowered to below the pseudo-threshold $s = (M_K - M_\pi)^2$, where the Källén function runs into the fourth quadrant (orange curve). The square root of that function is positive-real in the scattering region $s \geqslant (M_\pi + M_K)^2$. The cut of the square root is commonly taken on the negative real axis, such that the demonstrated encircling of the origin demands to continue the square root function on the second Riemann sheet. Consequently $Y(s)$ must be negative-real for energies below the pseudo-threshold. An analogous encircling of the origin is observed when considering the function $\lambda(s, m_D^2, s_l)$, which yields the requirement to continue the function $X(s)$ on different Riemann sheets, resulting in the prescriptions Eq. (3.7).

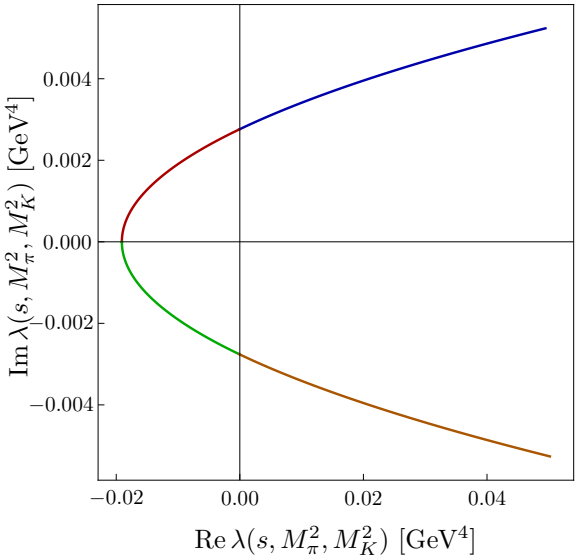

Figure B.6: The Källén function $\lambda(s+i\epsilon, M_\pi^2, M_K^2)$ ($\epsilon = 0.01$) is plotted in the complex plane for several s regions: $s \geq (M_K + M_\pi)^2$ (blue curve), $M_\pi^2 + M_K^2 \leq s < (M_K + M_\pi)^2$ (red curve), $(M_K - M_\pi)^2 \leq s < M_\pi^2 + M_K^2$ (green curve), and $s \leq (M_K - M_\pi)^2$ (orange curve).

The product $X(s)Y(s)$ enters the kinematical function $y(s)$, Eq. (3.38), shown in Figure B.7. Due to the zeros in the kinematical functions X and Y the function $y(s)$ diverges for $s = (M_K \pm M_\pi)^2 \equiv s_\pm$. Expanding $y(s)$ around these points yields

$$y(s) = \begin{cases} (\zeta_+)^{-1} \cdot (s - s_+)^{-1/2} + \mathcal{O}(s - s_+)^{1/2}, & \text{near } s = s_+, \\ -i(\zeta_-)^{-1} \cdot (s - s_-)^{-1/2} + \mathcal{O}(s - s_-)^{1/2}, & \text{near } s = s_-, \end{cases}$$

with

$$\zeta_\pm = \frac{\lambda^{1/2}\left(s_l, m_D^2, s_\pm\right)\sqrt{M_K M_\pi}}{(M_\pi \pm M_K)\left\{\mp m_D^2 M_K - s_l M_\pi + (M_K \pm M_\pi)(m_{D^*}^2 \pm M_K M_\pi)\right\}} \lessgtr 0. \tag{B.10}$$

We consider next the scattering angle $z(s,t,u)$ in dependency on the Mandelstam variables, Eq. (3.6), with a particular interest on its motion in the unphysical region, supposed for studying the convergence behavior of the partial-wave expansion, demanding $|z(s,t,u)| < 1$. In Figure B.8 we show the regions in the Mandelstam plane ($t - u$ versus s) that comply with this requirement, by means of a density plot of the magnitude of the angle $|z(s,t,u)|$ in the vicinity of the physical decay region. Expectedly, there is an overlap with the decay region (black encircled shaded area, compare also to Figure 1.5). In addition there are areas in the unphysical part of the Mandelstam plane, complying with the required bound on $z(s,t,u)$ (green encircled). Once an amplitude is expanded into partial waves at unphysical energies hence a careful consideration is mandatory whether the considered energies are located inside such a shaded area in the Mandelstam plane.

B.3.1 Analytic properties of the inhomogeneities

In Section 3.3 we perform a partial-wave decomposition of the D_{l4} pole terms to derive the inhomogeneities, Eq. (3.47). These are expressed in terms of Legendre functions of second kind

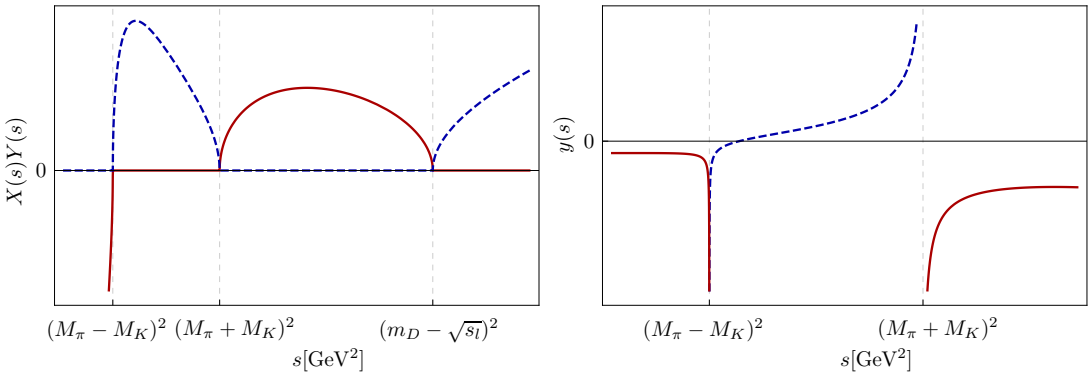

Figure B.7: The real (solid, red curves) and imaginary (blue, dashed) parts of the kinematic functions $X(s)Y(s)$ (left panel) and $y(s)$ (right panel) are shown.

$Q_l(y)$, Eq. (3.46). The purpose of this appendix is to study of some analytic properties of the inhomogeneities in order to understand the singular behavior at the pseudo-threshold. We also discuss the difference to the equal-mass case, where both final-state pseudoscalars are pions, see Ref. [126].

The lowest of the Legendre functions, $Q_0(y)$, involves the logarithm of $(y(s)-1)/(y(s)+1)$ (and by means of the recursion relations those for higher l do as well). Taking up the discussion of the previous section, where we considered the function $y(s)$, we investigate the analytic behavior of $(y(s)-1)/(y(s)+1)$ to obtain the proper analytical continuation of $Q_0(y)$ into the unphysical region. Assigning a tiny imaginary part $i\epsilon$ to the variable s, the function $(y(s+i\epsilon)-1)/(y(s+i\epsilon)+1)$ is plotted for several energy regions in Figure B.9 (left panel). In the physical region above the πK threshold the function runs from the first into the fourth quadrant. Lowering s to below the threshold the function approaches the third and at s_0 (determined by $\operatorname{Im} y(s) = 0$) the second quadrant. The encircling of the origin demands to copy the complex plane when considering the logarithm of that function. Hence at $s = s_0$, $Q_0(y)$ moves onto the second Riemann sheet. This is illustrated in the right panel, where the real and imaginary part and the argument of $(y(s)-1)/(y(s)+1)$ (twice the imaginary part of $Q_0(y)$) are depicted. In the physical region the argument is zero, while below the threshold it falls to -2π. Consequently, at the pseudo-threshold the imaginary part of $Q_0(y)$ is nonzero.

The real part of $Q_0(y)$ diverges for $s = 0$ and if $y = -1$, the latter corresponding to two solutions

$$s_{1,2} = \frac{1}{2}\left(3s_0 - m_{D^*}^2 - \frac{(m_D^2 - M_\pi^2)(s_l - M_K^2)}{m_{D^*}^2} \pm \frac{\sqrt{\lambda\,(s_l, M_K^2, m_{D^*}^2)}\sqrt{\lambda\,(m_D^2, M_\pi^2, m_{D^*}^2)}}{m_{D^*}^2}\right). \tag{B.11}$$

As the higher Legendre functions $Q_1(y)$ and $Q_2(y)$ emanate from $Q_0(y)$ by multiplication with y, which diverges for $s = (M_K \pm M_\pi)^2 \equiv s_\pm$ due to the zeros in the kinematical functions X and Y, there might in addition be singular behavior for $Q_1(y)$ and $Q_2(y)$ at the pseudo- and the normal threshold. Expanding around $s = s_\pm$ yields

$$\left.\begin{aligned} Q_1(s) &= \mathcal{O}(s - s_+), \\ Q_2(s) &= \mathcal{O}(s - s_+)^{1/2}, \end{aligned}\right\} \quad \text{near } s = s_+;$$

$$\left.\begin{aligned} Q_1(s) &= -\pi(\zeta_-)^{-1} \cdot (s - s_-)^{-1/2} + \mathcal{O}(s - s_-)^{1/2}, \\ Q_2(s) &= \tfrac{3i\pi}{2}(\zeta_-)^{-2} \cdot (s - s_-)^{-1} + \mathcal{O}(1), \end{aligned}\right\} \quad \text{near } s = s_-, \tag{B.12}$$

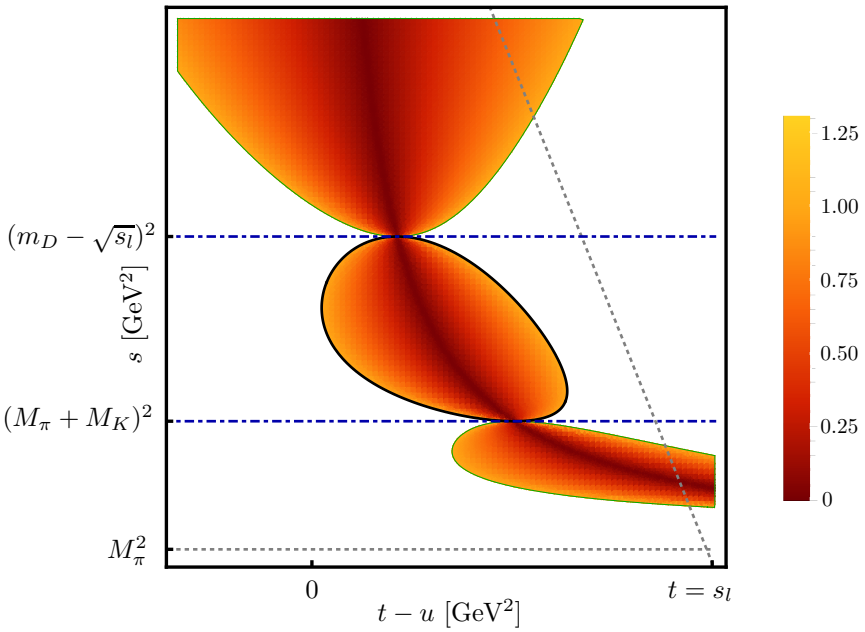

Figure B.8: We show the magnitude of the scattering angle $z(s,t,u)$ depending on the Mandelstam variables in a density plot with $t-u$ versus s. The regions for $|z(s,t,u)| > 1$ are excluded. There is an overlap with the physical decay region, shown by the shaded, black encircled area. The regions that obey $z(s,t,u) \leq 1$ and lie in the unphysical region are encircled by a green curve.

where ζ_- is defined in Eq. (B.10). We find that the singularities cancel at $s = s_+$, but due to the non-vanishing imaginary part of $Q_0(y)$ at s_-, they survive at the pseudo-threshold. From Eq. (3.47), by counting every power of y and inverse power of Y as $\mathcal{O}(s-s_\pm)^{1/2}$, we find that the inhomogeneities are regular at threshold, but behave according to

$$\begin{aligned} \hat{M}_0 &= \mathcal{O}(s-s_-)^{-1/2}, \\ \hat{M}_1 &= \mathcal{O}(s-s_-)^{-3/2}, \\ \hat{U}_1 &= \mathcal{O}(s-s_-)^{-3/2}, \\ \hat{V}_1 &= \mathcal{O}(s-s_-)^{-3/2}. \end{aligned} \tag{B.13}$$

at the pseudo-threshold.

B.3.2 Comparison to the equal-mass case

In Ref. [126], where the two final-state Goldstone bosons have equal mass (two pions), it is found that at the pseudo-threshold (i.e. at $s = 0$) the inhomogeneities $\hat{M}_0$, $\hat{U}_1$, $\hat{V}_1$ display singular behavior of $\mathcal{O}(s)^{1/2}$, while $\hat{M}_1$ has a singularity of $\mathcal{O}(s)^{3/2}$. We consider briefly the equal-mass case (denoted by the superscript "eq") in order to understand these discrepancies. The main point to remark is that in the equal-mass case, the kinematic function $Y(s)$ reduces to $\sigma_\pi(s) = \sqrt{1-4M_\pi^2/s}$. Consequently, near the pseudo-threshold $y^{\mathrm{eq}}(s)$ behaves like $\mathcal{O}(s)^{1/2}$, whereas in the non-equal-mass case $y(s)$ diverges as $\mathcal{O}(s-s_-)^{-1/2}$. Expanding the $Q_i^{\mathrm{eq}}(s)$ around $s = 0$, we find $Q_i^{\mathrm{eq}}(s) = \mathrm{const} + \mathcal{O}(s)^{1/2}$. Further, by means of Eq. (3.47) and the

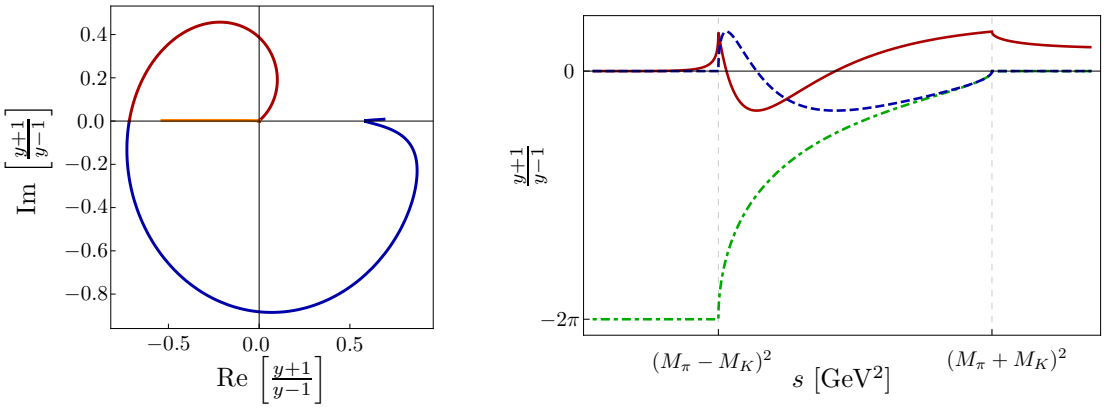

Figure B.9: Left panel: the function $(y(s+i\epsilon)+1)/(y(s+i\epsilon)-1)$ ($\epsilon = 0.01$) is plotted in the complex plane for several s regions: $s \geq s_0$ (blue curve), $0 \leq s < s_0$ (red curve), and $s \leq 0$ (orange curve on the real negative axis); s_0 solves $\mathrm{Im}\, y(s) = 0$. Right panel: the same function is plotted as a function of s; we show the real part (solid, red), the imaginary part (dashed, blue), and the argument (dot-dashed, green). The latter is zero in the physical region (above the πK threshold), and is analytically continued to the unphysical region, where it reaches a constant value -2π below the pseudo-threshold. The (pseudo-)thresholds are indicated by the dashed gray lines.

appropriate behavior of $y^{\mathrm{eq}}(s)$ and $Y^{\mathrm{eq}}(s)$, we recover the above mentioned square-root behavior of the equal-mass inhomogeneities.

There is also a discrepancy in the way the inhomogeneities modify when going from the equal-mass to the non-equal-mass case, as they do not change "synchronously". That is, in the equal-mass case, the inhomogeneities $\hat{M}_0^{\mathrm{eq}}$, $\hat{U}_1^{\mathrm{eq}}$, $\hat{V}_1^{\mathrm{eq}}$ all have the same square-root behavior at pseudo-threshold, while in the non-equal-mass case $\hat{M}_0$ is of a different order compared to $\hat{U}_1$, $\hat{V}_1$, while the latter now show the same behavior as $\hat{M}_1$. However, this becomes plausible when comparing the behavior of the Legendre functions—all $Q_i^{\mathrm{eq}}(s)$ behave the same way in the case of equal-mass particles, but this is not the case for the non-equal-mass functions $Q_i(s)$ (e.g. due to a cancellation of constant terms etc.). That is, $\hat{U}_1$ and $\hat{V}_1$ show a different pseudo-threshold behavior due to a contribution from $Q_2(s)$. On the other hand $\hat{M}_1$ behaves like $\hat{U}_1$ and $\hat{V}_1$, because the lower order in $(s - s_-)$ in the "non-Legendre" part of $\hat{M}_1$ (compared to $\hat{U}_1$ and $\hat{V}_1$) is compensated by a higher order in $Q_1(s)$.

B.3.3 Analyticity aspects when applying low-energy theorems

In Section 3.4.1 we apply certain low-energy theorems that constrain the D_{l4} amplitudes at specific (unphysical) points in the Mandelstam plane. We aim for constraints on the partial waves and therefore investigate in this appendix whether a partial-wave expansion is appropriate at these points. As an example we examine the soft-kaon relation, where the D_{l3} form factor f_+ is matched to a D_{l4} form factor combination, and consider the original soft-kaon point $s_{\mathrm{SKP}} = M_\pi^2 < s_-$, $t_{\mathrm{SKP}} = s_l$, $u_{\mathrm{SKP}} = m_D^2$. Naively evaluating the D_{l4} expressions for $s = s_{\mathrm{SKP}}$ yields an imaginary part, while f_+ is real.

The origin of the described inconsistency can be understood by studying the analytic structure of the partial waves themselves. Consider e.g. the Legendre function of second kind $Q_0(y)$, depending on the kinematical function $y(s)$, Eq. (3.38). The unphysical region is reached via an analytic continuation, where $\mathrm{Im}\ Q_0(y) = \arg((y+1)/(y-1))/2$ is continued to the second

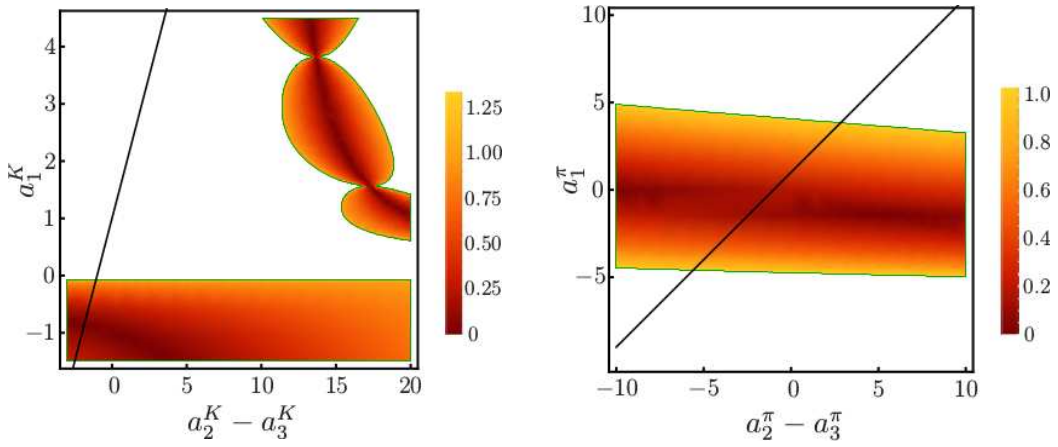

Figure B.10: We show the magnitude of the scattering angle $z(a_1^{\pi,K}, a_2^{\pi,K} - a_3^{\pi,K})$ evaluated at the soft-kaon (left panel) and soft-pion (right panel) points Eq. (3.62), which shifted by $a_i^{\pi,K} M_{\pi,K}^2$ (supposed to retain the on-shell condition $s+t+u = 3s_0$). We depict the dependency of $|z(a_1^{\pi,K}, a_2^{\pi,K} - a_3^{\pi,K})|$ on the shift parameters $a_1^{\pi,K}$ and $a_2^{\pi,K} - a_3^{\pi,K}$ in a density plot, excluding the regions for $|z| > 1$. The black curve contains those soft-kaon and soft-pion points, respectively, that are allowed by the on-shell constraint (transferred to the shift-parameters) $a_1^{\pi,K} + a_2^{\pi,K} + a_3^{\pi,K} = 1$, where we fix $a_2^{\pi,K} = 0$.

Riemann sheet and approaches $-\pi$ below the pseudo-threshold, see Figure B.9 (right panel). Hence, this implies an imaginary part for the D_{l4} partial waves below the threshold, in particular at the considered soft-kaon point. However, the soft-kaon theorem states a relation between the D_{l3} and D_{l4} amplitudes if the kaon dynamics in the D_{l4} decay is switched off, $p_K \to 0$. If we take $M_K \to 0$ the energy interval between the πK threshold and pseudo-threshold shrinks to one point (implying a jump by π in Im $Q_0(y)$) and the function $(y+1)/(y-1)$ does not encircle the origin as shown in the left panel of Figure B.9. We propose to consider the D_{l4} partial waves in the physical region (where they are real) and then apply the limit $p_K \to 0$ directly, such that the analytic continuation to the second Riemann sheet is avoided.

We take up the discussion of Appendix B.3 and observe that the exact soft-kaon point ($s = M_\pi^2$, $t = s_l$, $u = m_D^2$) lies outside the shaded areas (not shown in Figure B.8), such that an expansion in powers of $z(s,t,u)$ is not meaningful. Nevertheless, this issue is fixed as there is freedom to shift the Mandelstam variables by orders $\mathcal{O}(M_K^2)$. We introduce in Section 3.4.1 the shifted soft-kaon points $s = M_\pi^2 + a_1^K M_K^2$, $t = s_l + a_2^K M_K^2$, $u = m_D^2 + a_3^K M_K^2$ supposed to retain the on-shell condition $s+t+u = 3s_0$, which implies $a_1^K + a_2^K + a_3^K = 1$, used to eliminate one parameter. At the same time these shifts exhibit two yet undetermined degrees of freedom. The provided flexibility enables us to impose criteria to constrain the remaining parameters as well, such as demanding the soft-kaon point to match an energy region where $|z| \leq 1$. To investigate the implications on the a_i^K we evaluate $|z(s,t,u)|$ at the shifted soft-kaon point and show $|z(a_1^k, a_2^K - a_3^K)|$ as a function of the a_i^K in Figure B.10 (left panel). We furthermore depict those points that are allowed by the on-shell constraint, where we restrict ourselves to solutions where t remains unshifted, such that $a_2^K = 0$, as motivated in Section 3.4.1, hence $a_1^K = 1 - a_3^K$. In the right panel we depict the analogous dependency of the cosine of the scattering angle on the shifted soft-pion point $|z(a_1^\pi, a_2^\pi - a_3^\pi)|$. We observe that particularly the soft-kaon and soft-pion points that are proposed in Eq. (3.66) ($a_1^{\pi,K} = -1$, $a_2^{\pi,K} = 0$, $a_3^{\pi,K} = 2$) coincide with regions where the requirement $|z(s,t,u)| \leq 1$ is fulfilled.

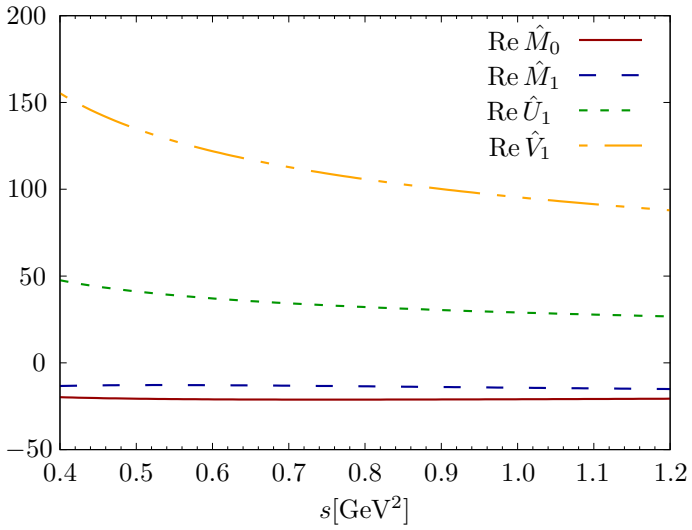

Figure B.11: Inhomogeneities $\hat{M}_0(s)$ (red), $\hat{M}_1(s)$ (blue), $\hat{U}_1(s)$ (green) and $\hat{V}_1(s)$ (black) depicted in the scattering region $(M_\pi + M_K)^2 \leq s \lesssim 1.2$ GeV^2.

We conclude that when applying low-energy theorems to partial waves in a first step one has to assure that the partial-wave expansion is valid at the respective evaluation point. Furthermore, the analytic behavior must be treated carefully and reexamined to ensure e.g. a correct continuation to Riemann sheets.

B.4 Order of subtractions

We examine the order of the subtraction polynomials, required for the dispersive integral to converge. In addition to the large-s behavior of the Omnès function the asymptotic behavior of the inhomogeneities has to be investigated, see Table B.1. In the top line the behavior of the full inhomogeneities for large s is given, while in the middle only the leading order in the heavy-meson approximation is considered, i.e. the inhomogeneities were first expanded in $1/m_D$ and subsequently in $1/s$. When comparing this with Figure B.11, it appears that this large-s behavior sets in at higher energies and that the inhomogeneities are nearly constant in the low-energy regime $s \lesssim 1$ GeV^2 we are interested in. Thus assuming nearly constant inhomogeneities we need three subtractions in the case of $M_0(s)$ and two for the P-wave amplitudes. In order to estimate the constant A, the inhomogeneities are evaluated at a specific matching point s_m, $A = \hat{M}_i(s_m)$, and are approximated by that result over the considered energy range.

However, one could raise concerns over that assumption, as it originates from a rough and rather hand-wavy estimate. Once the proposed method is adopted to high-precision studies with an anticipated predictive power, further criteria should be established to quantify the assumption of constant behavior, or at least examine to what extent the results are affected if either a linear behavior is assumed or the matching point s_m at which the amplitude is evaluated is slightly shifted.

	$\hat{M}_0(s)$	$\hat{M}_1(s)$	$\hat{U}_1(s)$	$\hat{V}_1(s)$
$s \to \infty$	$\log s$	$s \log s$	$1/s$	$1/s$
subtractions	3	3	1	1
$s \to \infty$, $m_D \to \infty$	$1/\sqrt{s}$	const	$1/\sqrt{s}$	$1/\sqrt{s}$
subtractions	2	2	1	1
$s \lesssim 1$ GeV	const	const	const	const
subtractions	3	2	2	2

Table B.1: Large-s behavior of the inhomogeneities (top line), large-s behavior in the heavy-meson approximation (middle line), and behavior for the region of interest, $s \lesssim 1$ GeV (bottom line), together with the minimal order of subtractions required for convergence of the dispersive integral.

B.5 Dispersive representation of constant inhomogeneities

A partial wave $f(s)$, which is a constant A at tree level, is written as

$$f(s) = A\Omega(s). \tag{B.14}$$

On the other hand the partial wave is given by an expression as in Eq. (3.32),

$$f(s) = \Omega(s)\left\{a_0 + a_1 s + \cdots + a_{n-1}s^{n-1} + \frac{s^n}{\pi}\int_{(M_\pi+M_K)^2}^{\infty} \frac{A\sin\delta(s')\mathrm{d}s'}{|\Omega(s')|(s'-s-i\epsilon)s'^n}\right\}, \tag{B.15}$$

which coincides with Eq. (B.14) when fixing the subtraction constants in an appropriate way. Therefore the dispersive representation of the inverse of the Omnès function is used,

$$\Omega^{-1}(s) = 1 - \dot{\Omega}(0)s - \frac{s^2}{\pi}\int_{(M_\pi+M_K)^2}^{\infty} \frac{\sin\delta(s')\mathrm{d}s'}{|\Omega(s')|s'^2(s'-s)} \tag{B.16}$$

in the case of an Omnès function falling off as $\sim 1/s$ (as for the P-wave), and

$$\Omega^{-1}(s) = 1 - \dot{\Omega}(0)s - \left[\frac{1}{2}\ddot{\Omega}(0) - \dot{\Omega}^2(0)\right]s^2 - \frac{s^3}{\pi}\int_{(M_\pi+M_K)^2}^{\infty} \frac{\sin\delta(s')\mathrm{d}s'}{|\Omega(s')|s'^3(s'-s)} \tag{B.17}$$

if it behaves like $\sim 1/s^2$ for large s (as for the S-wave). To ensure the equality between Eqs. (B.14) and (B.15) (and thus a reasonable high-energy behavior) the subtraction constants are chosen as

$$a_0 = 0, \quad a_1 = A\dot{\Omega}(0), \quad a_2 = A\left(\frac{1}{2}\ddot{\Omega}(0) - \dot{\Omega}^2(0)\right). \tag{B.18}$$

Bibliography

[1] S. L. Glashow, Nucl. Phys. **22** (1961) 579.

[2] S. Weinberg, Phys. Rev. Lett. **19** (1967) 1264.

[3] A. Salam, Conf. Proc. C **680519** (1968) 367.

[4] H. Fritzsch, M. Gell-Mann and H. Leutwyler, Phys. Lett. B **47** (1973) 365 .

[5] G. Aad *et al.* [ATLAS Collaboration], Phys. Lett. B **716** (2012) 1 [arXiv:1207.7214].

[6] S. Chatrchyan *et al.* [CMS Collaboration], Phys. Lett. B **716** (2012) 30 [arXiv:1207.7235].

[7] N. Cabibbo, Phys. Rev. Lett. **10** (1963) 531.

[8] M. Kobayashi and T. Maskawa, Prog. Theor. Phys. **49** (1973) 652.

[9] A. B. Carter and A. I. Sanda, Phys. Rev. Lett. **45** (1980) 952.

[10] A. B. Carter and A. I. Sanda, Phys. Rev. D **23** (1981) 1567.

[11] I. I. Y. Bigi and A. I. Sanda, Nucl. Phys. B **193** (1981) 85.

[12] B. Aubert *et al.* [BaBar Collaboration], Phys. Rev. Lett. **87** (2001) 091801 [hep-ex/0107013].

[13] K. Abe *et al.* [Belle Collaboration], Phys. Rev. Lett. **87** (2001) 091802 [hep-ex/0107061].

[14] R. Aaij *et al.* [LHCb Collaboration], Phys. Rev. Lett. **114** (2015) 041801 [arXiv:1411.3104 [hep-ex]].

[15] R. Aaij *et al.* [LHCb Collaboration], Phys. Lett. B **736** (2014) 186 [arXiv:1405.4140 [hep-ex]].

[16] R. Aaij *et al.* [LHCb Collaboration], Phys. Rev. D **87** (2013) 112010 [arXiv:1304.2600 [hep-ex]].

[17] R. Aaij *et al.* [LHCb Collaboration], Phys. Rev. Lett. **115** (2015) 031601 [arXiv:1503.07089 [hep-ex]].

[18] R. Aaij *et al.* [LHCb Collaboration], JHEP **1711** (2017) 170 [arXiv:1709.03944 [hep-ex]].

[19] R. Aaij *et al.* [LHCb Collaboration], JHEP **1612** (2016) 087 [arXiv:1611.03076 [hep-ex]].

[20] The LHCb Collaboration [LHCb Collaboration], LHCb-CONF-2017-004, CERN-LHCb-CONF-2017-004.

[21] The LHCb Collaboration [LHCb Collaboration], LHCb-CONF-2016-015, CERN-LHCb-CONF-2016-015.

[22] S. K. Choi *et al.* [Belle Collaboration], Phys. Rev. Lett. **91** (2003) 262001 [hep-ex/0309032].

[23] D. Acosta *et al.* [CDF Collaboration], Phys. Rev. Lett. **93** (2004) 072001 [hep-ex/0312021].

[24] V. M. Abazov *et al.* [D0 Collaboration], Phys. Rev. Lett. **93** (2004) 162002 [hep-ex/0405004].

[25] B. Aubert *et al.* [BaBar Collaboration], Phys. Rev. D **71** (2005) 071103 [hep-ex/0406022].

[26] B. Aubert *et al.* [BaBar Collaboration], Phys. Rev. Lett. **95** (2005) 142001 [hep-ex/0506081].

[27] Q. He *et al.* [CLEO Collaboration], Phys. Rev. D **74** (2006) 091104 [hep-ex/0611021].

[28] C. Z. Yuan *et al.* [Belle Collaboration], Phys. Rev. Lett. **99** (2007) 182004 [arXiv:0707.2541 [hep-ex]].

[29] I. Adachi [Belle Collaboration] [arXiv:1105.4583 [hep-ex]].

[30] A. Bondar *et al.* [Belle Collaboration], Phys. Rev. Lett. **108** (2012) 122001 [arXiv:1110.2251 [hep-ex]].

[31] N. Brambilla *et al.*, Eur. Phys. J. C **71** (2011) 1534 [arXiv:1010.5827 [hep-ph]].

[32] F. K. Guo, C. Hanhart, U.-G. Meißner, Q. Wang, Q. Zhao and B. S. Zou, Rev. Mod. Phys. **90** (2018) 015004 [arXiv:1705.00141 [hep-ph]].

[33] B. R. Martin, D. Morgan and G. Shaw, *Pion–Pion Interactions in Particle Physics,* Academic Press, London, 1976.

[34] G. Colangelo, J. Gasser and H. Leutwyler, Nucl. Phys. B **603** (2001) 125 [hep-ph/0103088].

[35] B. Ananthanarayan, G. Colangelo, J. Gasser and H. Leutwyler, Phys. Rept. **353** (2001) 207 [hep-ph/0005297].

[36] R. García-Martín, R. Kamiński, J. R. Peláez, J. Ruiz de Elvira, and F. J. Ynduráin, Phys. Rev. D **83** (2011) 074004 [arXiv:1102.2183 [hep-ph]].

[37] P. Büttiker, S. Descotes-Genon, and B. Moussallam, Eur. Phys. J. C **33** (2004) 409 [arXiv:0310283 [hep-ph]].

[38] J. R. Peláez and A. Rodas, Phys. Rev. D **93** (2016) 074025 [arXiv:1602.08404 [hep-ph]].

[39] J. R. Peláez, A. Rodas and J. Ruiz de Elvira, Eur. Phys. J. C **77** (2017) 91 [arXiv:1612.07966 [hep-ph]].

[40] S. Chatrchyan *et al.* [CMS Collaboration], JHEP **1306** (2013) 081 [arXiv:1303.4571 [hep-ex]].

[41] S. Chatrchyan *et al.* [CMS Collaboration], Nature Phys. **10** (2014) 557 [arXiv:1401.6527 [hep-ex]].

[42] H. D. Politzer, Phys. Rev. Lett. **30** (1973) 1346.

[43] D. J. Gross and F. Wilczek, Phys. Rev. Lett. **30** (1973) 1343.

[44] C. Patrignani *et al.* [Particle Data Group Collaboration], Chin. Phys. C **40** (2016) 100001.

[45] J. H. Christenson, J. W. Cronin, V. L. Fitch and R. Turlay, Phys. Rev. Lett. **13** (1964) 138.

[46] J. J. Aubert *et al.* [E598 Collaboration], Phys. Rev. Lett. **33** (1974) 1404.

[47] J. E. Augustin *et al.* [SLAC-SP-017 Collaboration], Phys. Rev. Lett. **33** (1974) 1406 [Adv. Exp. Phys. **5** (1976) 141].

[48] M. L. Perl *et al.*, Phys. Rev. Lett. **35** (1975) 1489.

[49] S. W. Herb *et al.*, Phys. Rev. Lett. **39** (1977) 252.

[50] F. Abe *et al.* [CDF Collaboration], Phys. Rev. Lett. **74** (1995) 2626 [hep-ex/9503002].

[51] S. Abachi *et al.* [D0 Collaboration], Phys. Rev. Lett. **74** (1995) 2632 [hep-ex/9503003].

[52] J. Charles *et al.* [CKMfitter Group], Eur. Phys. J. C **41** (2005) 1 [hep-ph/0406184].

[53] H. Burkhardt *et al.* [NA31 Collaboration], Phys. Lett. B **206** (1988) 169.

[54] G. D. Barr *et al.* [NA31 Collaboration], Phys. Lett. B **317** (1993) 233.

[55] A. Alavi-Harati *et al.* [KTeV Collaboration], Phys. Rev. Lett. **83** (1999) 22 [hep-ex/9905060].

[56] V. Fanti *et al.* [NA48 Collaboration], Phys. Lett. B **465** (1999) 335 [hep-ex/9909022].

[57] S. Weinberg, Physica A **96** (1979) 327.

[58] S. Weinberg, PoS CD **09** (2009) 001 [arXiv:0908.1964 [hep-th]].

[59] J. Gasser and H. Leutwyler, Annals Phys. **158** (1984) 142.

[60] J. Gasser and H. Leutwyler, Nucl. Phys. B **250** (1985) 465.

[61] C. Vafa and E. Witten, Phys. Rev. Lett. **53** (1984) 535.

[62] K. A. Olive *et al.* [Particle Data Group Collaboration], Chin. Phys. C **38** (2014) 090001.

[63] U.-G. Meißner, Rept. Prog. Phys. **56** (1993) 903 [hep-ph/9302247].

[64] S. Scherer, Adv. Nucl. Phys. **27** (2003) 277 [hep-ph/0210398].

[65] J. Gasser, Lect. Notes Phys. **629** (2004) 1 [hep-ph/0312367].

[66] V. Bernard and U.-G. Meißner, Ann. Rev. Nucl. Part. Sci. **57** (2007) 33 [hep-ph/0611231].

[67] B. Kubis, arXiv:0703274 [hep-ph].

[68] M. B. Wise, Phys. Rev. D **45** (1992) R2188.

[69] C. L. Y. Lee, M. Lu and M. B. Wise, Phys. Rev. D **46** (1992) 5040.

[70] J. P. Lees *et al.* [BaBar Collaboration], Phys. Rev. Lett. **111** (2013) 111801 [arXiv:1304.5657 [hep-ex]].

[71] J. P. Lees *et al.* [BaBar Collaboration], Phys. Rev. D **88** (2013) 052003 Erratum: [Phys. Rev. D **88** (2013) 079902] [arXiv:1304.5009 [hep-ex]].

[72] S. Ahmed *et al.* [CLEO Collaboration], Phys. Rev. Lett. **87** (2001) 251801 [hep-ex/0108013].

[73] A. Anastassov *et al.* [CLEO Collaboration], Phys. Rev. D **65** (2002) 032003 [hep-ex/0108043].

[74] S. Aoki *et al.*, Eur. Phys. J. C **77** (2017) 112 [arXiv:1607.00299 [hep-lat]].

[75] G. Burdman and J. F. Donoghue, Phys. Lett. B **280** (1992) 287.

[76] M. Altenbuchinger, Ph.D. Thesis, University of Munich, 2013.

[77] C. G. Boyd, B. Grinstein and R. F. Lebed, Nuovo Cim. A **109** (1996) 863 [hep-ph/9508242].

[78] W. Lucha, D. Melikhov and S. Simula, Phys. Lett. B **735** (2014) 12 [arXiv:1404.0293 [hep-ph]].

[79] R. J. Eden, P. V. Landshoff, D. I. Olive and J. C. Polkinghorne, *The Analytic S-Matrix*, Cambridge University Press, 2002.

[80] R. Omnès, Nuovo Cim. **8** (1958) 316.

[81] N. I. Muskhelishvili, *Singular Integral Equations*, Wolters-Noordhoff Publishing, Groningen, 1953 [Dover Publications, 2nd edition, 2008].

[82] K. M. Watson, Phys. Rev. **95** (1954) 228.

[83] S. R. Amendolia *et al.* [NA7 Collaboration], Nucl. Phys. B **277** (1986) 168.

[84] A. Aloisio *et al.* [KLOE Collaboration], Phys. Lett. B **606** (2005) 12 [hep-ex/0407048].

[85] R. R. Akhmetshin *et al.*, JETP Lett. **84** (2006) 413 [Pisma Zh. Eksp. Teor. Fiz. **84** (2006) 491] [hep-ex/0610016].

[86] R. R. Akhmetshin *et al.* [CMD-2 Collaboration], Phys. Lett. B **648** (2007) 28 [hep-ex/0610021].

[87] B. Aubert *et al.* [BaBar Collaboration], Phys. Rev. Lett. **103** (2009) 231801 [arXiv:0908.3589 [hep-ex]].

[88] F. Ambrosino *et al.* [KLOE Collaboration], Phys. Lett. B **700** (2011) 102 [arXiv:1006.5313 [hep-ex]].

[89] M. Fujikawa *et al.* [Belle Collaboration], Phys. Rev. D **78** (2008) 072006 [arXiv:0805.3773 [hep-ex]].

[90] J. Kambor, C. Wiesendanger and D. Wyler, Nucl. Phys. B **465** (1996) 215 [hep-ph/9509374].

[91] J. Stern, H. Sazdjian and N. H. Fuchs, Phys. Rev. D **47** (1993) 3814 [hep-ph/9301244].

[92] M. Knecht, B. Moussallam, J. Stern and N. H. Fuchs, Nucl. Phys. B **457** (1995) 513 [hep-ph/9507319].

[93] B. Ananthanarayan and P. Büttiker, Eur. Phys. J. C **19** (2001) 517 [hep-ph/0012023].

[94] M. Zdráhal and J. Novotný, Phys. Rev. D **78** (2008) 116016 [arXiv:0806.4529].

[95] P. Stoffer [arXiv:1412.5171].

[96] J. Gasser and U.-G. Meißner, Nucl. Phys. B **357** (1991) 90.

[97] F. K. Guo, C. Hanhart, F. J. Llanes-Estrada and U.-G. Meißner, Phys. Lett. B **678** (2009) 90 [arXiv:0812.3270].

[98] J. F. De Troconiz and F. J. Yndurain, Phys. Rev. D **65** (2002) 093001 [hep-ph/0106025].

[99] C. Hanhart, Phys. Lett. B **715** (2012) 170 [arXiv:1203.6839].

[100] G. P. Lepage and S. J. Brodsky, Phys. Rev. D **22** (1980) 2157.

[101] B. Moussallam, Eur. Phys. J. C **14** (2000) 111 [hep-ph/9909292].

[102] A. V. Anisovich and H. Leutwyler, Phys. Lett. B **375** (1996) 335 [hep-ph/9601237].

[103] N. N. Khuri and S. B. Treiman, Phys. Rev. **119** (1960) 1115.

[104] J. T. Daub, Diplomarbeit, Universität Bonn, 2013.

[105] J. F. Donoghue, J. Gasser and H. Leutwyler, Nucl. Phys. B **343** (1990) 341.

[106] S. Descotes-Genon, Ph.D. Thesis, Université de Paris-Sud, France, 2000.

[107] M. Hoferichter, C. Ditsche, B. Kubis and U.-G. Meißner, JHEP **1206** (2012) 063 [arXiv:1204.6251 [hep-ph]].

[108] H. Hellmann, *Einführung in die Quantenchemie*, Franz Deuticke, Leipzig, 1937.

[109] R. P. Feynman, Phys. Rev. **56** (1939) 340.

[110] S. Aoki *et al.*, Eur. Phys. J. C **74** (2014) 2890 [arXiv:1310.8555 [hep-lat]].

[111] R. J. Dowdall, C. T. H. Davies, G. P. Lepage and C. McNeile, Phys. Rev. D **88** (2013) 074504 [arXiv:1303.1670 [hep-lat]].

[112] J. T. Daub, H. K. Dreiner, C. Hanhart, B. Kubis and U.-G. Meißner, JHEP **1301** (2013) 179 [arXiv:1212.4408 [hep-ph]].

[113] J. T. Daub, C. Hanhart and B. Kubis, JHEP **1602** (2016) 009 [arXiv:1508.06841 [hep-ph]].

[114] M. Albaladejo, J. T. Daub, C. Hanhart, B. Kubis and B. Moussallam, JHEP **1704** (2017) 010 [arXiv:1611.03502 [hep-ph]].

[115] M. Battaglieri *et al.*, Acta Phys. Polon. B **46** (2015) 257 [arXiv:1412.6393 [hep-ph]].

[116] J. Dalseno *et al.* [Belle Collaboration], Phys. Rev. D **79** (2009) 072004 [arXiv:0811.3665 [hep-ex]].

[117] B. Aubert *et al.* [BaBar Collaboration], Phys. Rev. D **80** (2009) 112001 [arXiv:0905.3615 [hep-ex]].

[118] Y. Nakahama *et al.* [Belle Collaboration], Phys. Rev. D **82** (2010) 073011 [arXiv:1007.3848 [hep-ex]].

[119] J. P. Lees *et al.* [BaBar Collaboration], Phys. Rev. D **85** (2012) 112010 [arXiv:1201.5897 [hep-ex]].

[120] G. Barton, *Introduction to Dispersion Techniques in Field Theory,* W. A. Benjamin, New York (1965).

[121] B. El-Bennich, A. Furman, R. Kamiński, L. Leśniak, B. Loiseau and B. Moussallam, Phys. Rev. D **79** (2009) 094005 [*Erratum ibid.* D **83** (2011) 039903] [arXiv:0902.3645 [hep-ph]].

[122] R. García-Martín and B. Moussallam, Eur. Phys. J. C **70** (2010) 155 [arXiv:1006.5373 [hep-ph]].

[123] M. Hoferichter, D. R. Phillips and C. Schat, Eur. Phys. J. C **71** (2011) 1743 [arXiv:1106.4147 [hep-ph]].

[124] F. Stollenwerk, C. Hanhart, A. Kupść, U.-G. Meißner and A. Wirzba, Phys. Lett. B **707** (2012) 184 [arXiv:1108.2419 [nucl-th]].

[125] M. Hoferichter, B. Kubis and D. Sakkas, Phys. Rev. D **86** (2012) 116009 [arXiv:1210.6793 [hep-ph]].

[126] X.-W. Kang, B. Kubis, C. Hanhart and U.-G. Meißner, Phys. Rev. D **89** (2014) 053015 [arXiv:1312.1193 [hep-ph]].

[127] L. Y. Dai and M. R. Pennington, Phys. Rev. D **90** (2014) 036004 [arXiv:1404.7524 [hep-ph]].

[128] G. Colangelo, E. Passemar and P. Stoffer, Eur. Phys. J. C **75** (2015) 172 [arXiv:1501.05627 [hep-ph]].

[129] B. Kubis and J. Plenter, Eur. Phys. J. C **75** (2015) 283 [arXiv:1504.02588 [hep-ph]].

[130] F. Niecknig and B. Kubis, JHEP **1510** (2015) 142 [arXiv:1509.03188 [hep-ph]].

[131] F. Niecknig and B. Kubis, Phys. Lett. B **780** (2018) 471 [arXiv:1708.00446 [hep-ph]].

[132] S. M. Flatté, Phys. Lett. B **63** (1976) 224.

[133] J. A. Oller, E. Oset and J. R. Peláez, Phys. Rev. D **59** (1999) 074001 [*Erratum ibid.* D **60** (1999) 099906; *Erratum ibid.* D **75** (2007) 099903] [hep-ph/9804209].

[134] D. Black, A. H. Fariborz and J. Schechter, Phys. Rev. D **61** (2000) 074030 [hep-ph/9910351].

[135] A. Gómez Nicola and J. R. Peláez, Phys. Rev. D **65** (2002) 054009 [hep-ph/0109056].

[136] A. Furman and L. Leśniak, Phys. Lett. B **538** (2002) 266 [hep-ph/0203255].

[137] V. Bernard, N. Kaiser and U.-G. Meißner, Phys. Rev. D **44** (1991) 3698.

[138] J. J. Dudek *et al.* [Hadron Spectrum Collaboration], Phys. Rev. D **93** (2016) 094506 [arXiv:1602.05122 [hep-ph]].

[139] Z.-H. Guo, L. Liu, U.-G. Meißner, J. A. Oller and A. Rusetsky, Phys. Rev. D **95** (2017) 054004 [arXiv:1609.08096 [hep-ph]].

[140] M. Albaladejo and B. Moussallam, Eur. Phys. J. C **75** (2015) 488 [arXiv:1507.04526 [hep-ph]].

[141] R. Aaij *et al.* [LHCb Collaboration], Phys. Rev. D **90** (2014) 012003 [arXiv:1404.5673 [hep-ex]].

[142] R. Aaij *et al.* [LHCb Collaboration], Phys. Rev. D **89** (2014) 092006 [arXiv:1402.6248 [hep-ex]].

[143] B. Aubert *et al.* [BaBar Collaboration], Phys. Rev. Lett. **90** (2003) 091801 [hep-ex/0209013].

[144] J. Li *et al.* [Belle Collaboration], Phys. Rev. Lett. **106** (2011) 121802 [arXiv:1102.2759 [hep-ex]].

[145] T. Aaltonen *et al.* [CDF Collaboration], Phys. Rev. D **84** (2011) 052012 [arXiv:1106.3682 [hep-ex]].

[146] V. M. Abazov *et al.* [D0 Collaboration], Phys. Rev. D **85** (2012) 011103 [arXiv:1110.4272 [hep-ex]].

[147] R. Aaij *et al.* [LHCb Collaboration], Phys. Rev. D **87** (2013) 052001 [arXiv:1301.5347 [hep-ex]].

[148] R. Aaij *et al.* [LHCb Collaboration], Phys. Rev. D **86** (2012) 052006 [arXiv:1204.5643 [hep-ex]].

[149] S. Gardner and U.-G. Meißner, Phys. Rev. D **65** (2002) 094004 [hep-ph/0112281].

[150] W. H. Liang and E. Oset, Phys. Lett. B **737** (2014) 70 [arXiv:1406.7228 [hep-ph]].

[151] U.-G. Meißner and J. A. Oller, Nucl. Phys. A **679** (2001) 671 [hep-ph/0005253].

[152] T. A. Lähde and U.-G. Meißner, Phys. Rev. D **74** (2006) 034021 [hep-ph/0606133].

[153] I. Caprini, G. Colangelo and H. Leutwyler, Eur. Phys. J. C **72** (2012) 1860 [arXiv:1111.7160 [hep-ph]];

[154] I. Caprini, G. Colangelo and H. Leutwyler, in preparation.

[155] M. Bayar, W. H. Liang and E. Oset, Phys. Rev. D **90** (2014) 114004 [arXiv:1408.6920 [hep-ph]].

[156] J. J. Xie and E. Oset, Phys. Rev. D **90** (2014) 094006 [arXiv:1409.1341 [hep-ph]].

[157] S. Stone and L. Zhang, Phys. Rev. Lett. **111** (2013) 062001 [arXiv:1305.6554 [hep-ex]].

[158] P. Colangelo, F. De Fazio and W. Wang, Phys. Rev. D **81** (2010) 074001 [arXiv:1002.2880 [hep-ph]].

[159] W. F. Wang, H. n. Li, W. Wang and C.-D. Lü, Phys. Rev. D **91** (2015) 094024 [arXiv:1502.05483 [hep-ph]].

[160] S. Faller, T. Feldmann, A. Khodjamirian, T. Mannel and D. van Dyk, Phys. Rev. D **89** (2014) 014015 [arXiv:1310.6660 [hep-ph]].

[161] P. Colangelo, F. De Fazio and W. Wang, Phys. Rev. D **83** (2011) 094027 [arXiv:1009.4612 [hep-ph]].

[162] M. Beneke, G. Buchalla, M. Neubert and C. T. Sachrajda, Nucl. Phys. B **606** (2001) 245 [hep-ph/0104110].

[163] M. Beneke, G. Buchalla, M. Neubert and C. T. Sachrajda, Nucl. Phys. B **591** (2000) 313 [hep-ph/0006124].

[164] V. Chobanova *et al.* [Belle Collaboration], Phys. Rev. D **93** (2016) 031101 [arXiv:1512.06895 [hep-ex]].

[165] J. Bijnens and A. Celis, Phys. Lett. B **680** (2009) 466 [arXiv:0906.0302 [hep-ph]].

[166] G. Ecker, J. Gasser, A. Pich and E. de Rafael, Nucl. Phys. B **321** (1989) 311.

[167] E. Oset *et al.*, Int. J. Mod. Phys. E **25** (2016) 1630001 [arXiv:1601.03972 [hep-ph]].

[168] M. F. Heyn and C. B. Lang, Z. Phys. C **7** (1981) 169.

[169] C. Hanhart, A. Kupść, U.-G. Meißner, F. Stollenwerk and A. Wirzba, Eur. Phys. J. C **73** (2013) 2668 [Eur. Phys. J. C **75** (2015) 242] [arXiv:1307.5654 [hep-ph]].

[170] M. Ablikim *et al.* [BES III Collaboration], Phys. Lett. B **753** (2016) 629 [arXiv:1507.08188 [hep-ex]].

[171] S. Gardner and H. B. O'Connell, Phys. Rev. D **57** (1998) 2716 [Phys. Rev. D **62** (2000) 019903] [hep-ph/9707385].

[172] H. Leutwyler, hep-ph/0212324.

[173] C. Hanhart, S. Holz, B. Kubis, A. Kupść, A. Wirzba and C. W. Xiao, Eur. Phys. J. C **77** (2017) 98 [arXiv:1611.09359 [hep-ph]].

[174] S. Gardner, H. B. O'Connell and A. W. Thomas, Phys. Rev. Lett. **80** (1998) 1834 [hep-ph/9705453].

[175] B. Ananthanarayan, I. Caprini, G. Colangelo, J. Gasser and H. Leutwyler, Phys. Lett. B **602** (2004) 218 [hep-ph/0409222].

[176] D. H. Cohen *et al.*, Phys. Rev. D **22** (1980) 2595.

[177] A. Etkin *et al.*, Phys. Rev. D **25** (1982) 1786.

[178] B. Hyams *et al.*, Nucl. Phys. B **64** (1973) 134.

[179] G. Grayer *et al.*, Nucl. Phys. B **75** (1974) 189.

[180] B. Hyams *et al.*, Nucl. Phys. B **100** (1975) 205.

[181] J. R. Batley *et al.* [NA48/2 Collaboration], Eur. Phys. J. C **54** (2008) 411.

[182] J. R. Batley *et al.* [NA48/2 Collaboration], Eur. Phys. J. C **70** (2010) 635.

[183] B. Aubert *et al.* [BaBar Collaboration], Phys. Rev. D **79** (2009) 032003 [arXiv:0808.0971 [hep-ex]].

[184] P. del Amo Sanchez *et al.* [BaBar Collaboration], Phys. Rev. D **83** (2011) 052001 [arXiv:1011.4190 [hep-ex]].

[185] R. Aaij *et al.* [LHCb Collaboration], Phys. Rev. D **87** (2013) 072004 [arXiv:1302.1213 [hep-ex]].

[186] R. Aaij *et al.* [LHCb Collaboration], Phys. Rev. D **88** (2013) 072005 [arXiv:1308.5916 [hep-ex]].

[187] R. Aaij *et al.* [LHCb Collaboration], Phys. Lett. B **742** (2015) 38 [arXiv:1411.1634 [hep-ex]].

[188] C. Hanhart, AIP Conf. Proc. **1735** (2016) 020015 [arXiv:1512.02190 [hep-ph]].

[189] D. V. Bugg, J. Phys. G **34** (2007) 151 [hep-ph/0608081].

[190] C. Hanhart, B. Kubis and J. R. Peláez, Phys. Rev. D **76** (2007) 074028 [arXiv:0707.0262 [hep-ph]].

[191] G. Ecker and C. Zauner, Eur. Phys. J. C **52** (2007) 315 [arXiv:0705.0624 [hep-ph]].

[192] W. H. Liang, J. J. Xie and E. Oset, Eur. Phys. J. C **75** (2015) 609 [arXiv:1510.03175 [hep-ph]].

[193] G. Isidori, L. Maiani, M. Nicolaci and S. Pacetti, JHEP **0605** (2006) 049 [hep-ph/0603241].

[194] F. Ambrosino *et al.* [KLOE Collaboration], Phys. Lett. B **681** (2009) 5 [arXiv:0904.2539 [hep-ex]].

[195] B. Moussallam, Eur. Phys. J. C **71** (2011) 1814 [arXiv:1110.6074 [hep-ph]].

[196] S. Weinberg, Phys. Rev. **130** (1963) 776.

[197] V. Baru, J. Haidenbauer, C. Hanhart, Y. Kalashnikova and A. E. Kudryavtsev, Phys. Lett. B **586** (2004) 53 [hep-ph/0308129].

[198] T. Mannel, W. Roberts and Z. Ryzak, Phys. Lett. B **248** (1990) 392.

[199] R. Aaij *et al.* [LHCb Collaboration], LHCb-CONF-2012-002.

[200] T. Aaltonen *et al.* [CDF Collaboration], Phys. Rev. Lett. **109** (2012) 171802 [arXiv:1208.2967 [hep-ex]].

[201] G. Aad *et al.* [ATLAS Collaboration], JHEP **1212** (2012) 072 [arXiv:1208.0572 [hep-ex]].

[202] R. Aaij *et al.* [LHCb Collaboration], JHEP **1708** (2017) 037 [arXiv:1704.08217 [hep-ex]].

[203] S. Stone and L. Zhang, Phys. Rev. D **79** (2009) 074024 [arXiv:0812.2832 [hep-ph]].

[204] N. N. Achasov, S. A. Devyanin and G. N. Shestakov, Phys. Lett. B **88** (1979) 367.

[205] J. J. Wu, X. H. Liu, Q. Zhao and B. S. Zou, Phys. Rev. Lett. **108** (2012) 081803 [arXiv:1108.3772 [hep-ph]].

[206] F. Aceti, W. H. Liang, E. Oset, J. J. Wu and B. S. Zou, Phys. Rev. D **86** (2012) 114007 [arXiv:1209.6507 [hep-ph]].

[207] W. Wang, Phys. Lett. B **759** (2016) 501 [arXiv:1602.05288 [hep-ph]].

[208] J. J. Wu, Q. Zhao and B. S. Zou, Phys. Rev. D **75** (2007) 114012 [arXiv:0704.3652 [hep-ph]].

[209] M. Ablikim *et al.* [BES III Collaboration], Phys. Rev. D **83** (2011) 032003 [arXiv:1012.5131 [hep-ex]].

[210] M. Ablikim *et al.* [BES III Collaboration], arXiv:1802.00583 [hep-ex].

[211] B. Moussallam and M. Albaladejo, PoS **CD 15** (2015) 057 [arXiv:1510.06626 [hep-ph]].

[212] M. Albaladejo and B. Moussallam, Eur. Phys. J. C **77** (2017) 508 [arXiv:1702.04931 [hep-ph]].

[213] S. Ropertz, Master Thesis, University of Bonn, 2016.

[214] B. Ananthanarayan and K. Shivaraj, Phys. Lett. B **628** (2005) 223 [hep-ph/0508116].

[215] A. Pais and S. B. Treiman, Phys. Rev. **168** (1968) 1858.

[216] L. Rosselet *et al.*, Phys. Rev. D **15** (1977) 574.

[217] S. Pislak *et al.* [BNL-E865 Collaboration], Phys. Rev. Lett. **87** (2001) 221801 [Erratum-ibid. **105** (2010) 019901] [hep-ex/0106071].

[218] J. R. Batley *et al.* [NA48/2 Collaboration], Eur. Phys. J. C **54** (2008) 411.

[219] Y. H. Chen, J. T. Daub, F.-K. Guo, B. Kubis, U.-G. Meißner and B. S. Zou, Phys. Rev. D **93** (2016) 034030 [arXiv:1512.03583 [hep-ph]].

[220] Y. H. Chen, M. Cleven, J. T. Daub, F. K. Guo, C. Hanhart, B. Kubis, U. G. Meißner and B. S. Zou, Phys. Rev. D **95** (2017) 034022 [arXiv:1611.00913 [hep-ph]].

[221] N. Cabibbo and A. Maksymowicz, Phys. Rev. **137** (1965) B438 [Erratum-ibid. **168** (1968) 1926].

[222] J. Bijnens, G. Colangelo and J. Gasser, Nucl. Phys. B **427** (1994) 427 [hep-ph/9403390].

[223] J. M. Link *et al.* [FOCUS Collaboration], Phys. Lett. B **535** (2002) 43 [hep-ex/0203031].

[224] P. del Amo Sanchez *et al.* [BaBar Collaboration], Phys. Rev. D **83** (2011) 072001 [arXiv:1012.1810 [hep-ex]].

[225] M. Ablikim *et al.* [BES III Collaboration], Phys. Rev. D **94** (2016) 032001 [arXiv:1512.08627 [hep-ex]].

[226] T.-M. Yan, H.-Y. Cheng, C.-Y. Cheung, G.-L. Lin, Y. C. Lin and H.-L. Yu, Phys. Rev. D **46** (1992) 1148 [Erratum-ibid. D **55** (1997) 5851].

[227] M. Ablikim *et al.* [BES III Collaboration], Phys. Rev. D **92** (2015) 072012 [arXiv:1508.07560 [hep-ex]].

[228] A. Sibidanov *et al.* [Belle Collaboration], Phys. Rev. D **88** (2013) 032005 [arXiv:1306.2781 [hep-ex]].

[229] R. J. Hill, eConf C **060409** (2006) 027 [hep-ph/0606023].

[230] B. Aubert *et al.* [BaBar Collaboration], Phys. Rev. D **76** (2007) 052005 [arXiv:0704.0020 [hep-ex]].

[231] D. Besson *et al.* [CLEO Collaboration], Phys. Rev. D **80** (2009) 032005 [arXiv:0906.2983 [hep-ex]].

[232] J. P. Lees *et al.* [BaBar Collaboration], Phys. Rev. D **91** (2015) 052022 [arXiv:1412.5502 [hep-ex]].

[233] A. Khodjamirian, C. Klein, T. Mannel and N. Offen, Phys. Rev. D **80** (2009) 114005 [arXiv:0907.2842 [hep-ph]].

[234] N. Carrasco *et al.* [ETM Collaboration], PoS LATTICE **2015** (2016) 261 [arXiv:1511.04877 [hep-lat]].

[235] D. L. Yao, P. Fernandez-Soler, M. Albaladejo, F. K. Guo and J. Nieves, Eur. Phys. J. C **78** (2018) 310 [arXiv:1803.03171 [hep-ph]].

[236] B. Moussallam, unpublished notes and private communication.

[237] C. Bourrely, I. Caprini and L. Lellouch, Phys. Rev. D **79** (2009) 013008 Erratum: [Phys. Rev. D **82** (2010) 099902] [arXiv:0807.2722 [hep-ph]].

[238] B. Ananthanarayan, I. Caprini and I. Sentitemsu Imsong, Eur. Phys. J. A **47** (2011) 147 [arXiv:1108.0284 [hep-ph]].

[239] I. Sentitemsu Imsong, A. Khodjamirian, T. Mannel and D. van Dyk, JHEP **1502** (2015) 126 [arXiv:1409.7816 [hep-ph]].

[240] I. Caprini, B. Grinstein and R. F. Lebed, Phys. Rev. D **96** (2017) 036015 [arXiv:1705.02368 [hep-ph]].

[241] B. Grinstein and R. F. Lebed, Phys. Rev. D **92** (2015) 116001 [arXiv:1509.04847 [hep-ph]].

[242] J. A. Bailey *et al.*, Phys. Rev. D **79** (2009) 054507 [arXiv:0811.3640 [hep-lat]].

[243] A. Bharucha, JHEP **1205** (2012) 092 [arXiv:1203.1359 [hep-ph]].

Danksagung

Bei der Fertigstellung meiner Doktorarbeit waren verschiedene Personen involviert, die mir fachlich, moralisch oder logistisch eine große Unterstützung waren, wofür ich sehr dankbar bin.

An erster Stelle möchte ich meinem Doktorvater Prof. Bastian Kubis großen Dank aussprechen, für die Möglichkeit, an einem herausfordernden Thema zu arbeiten, mit einer gut gelenkten dynamischen Entwicklung dieses Themas im Laufe der Forschungszeit. Trotz seines engen Terminplans konnte er immer Zeit erübrigen, um über Fortschritte meiner Projekte zu diskutieren und gemeinsam ungelöste Probleme zu bewundern. Ich bekam immer wieder hilfreiche Impulse, von fachlichen Brainstormings über Ermunterungen zur Teilnahme an Konferenzen bis hin zu wertvollen Tipps wie dem doppelten Espresso extra vor meinen Vorträgen. Er brachte mir während der letzten Jahre viele Dinge bei, nicht nur über die Physik, sondern auch methodisch und persönlich.

Auch von meinem Zweitgutachter, Prof. Christoph Hanhart, konnte ich vieles lernen. In zahlreichen Diskussionen vermittelte er immer wieder die Freude an dem, was wir tun, wofür ich sehr dankbar bin.

Ich möchte der ganzen Arbeitsgruppe danken, für das gegenseitige Interesse an der Forschung der Gruppenmitglieder und den Austausch darüber. Besonderer Dank hierbei geht an Dr. Franz Niecknig, seinerzeit mein Büronachbar. Er scheute sich nie vor tiefschürfenden und schwierigen, dafür sehr erhellenden Diskussionen. Auch Dr. Peter Stoffer war jederzeit hilfsbereit und es war sehr angenehm, mit ihm zu arbeiten. Ich danke all meinen Kollaborateuren für die erfolgreiche Zusammenarbeit, aus denen Publikationen entstanden sind.

Für die finanzielle Unterstützung durch den CRC 110 “Symmetries and the Emergence of Structure in QCD” möchte ich an dieser Stelle auch die Deutsche Forschungsgemeinschaft erwähnen und mich dafür bedanken.

Ohne meine netten Bürokollegen wäre die Zeit der Doktorarbeit sehr trist gewesen. Daher danke ich Nico Klein, Deborah Rönchen, Shahin Bour und Franz Niecknig, für die Plaudereien, das gemeinsame Frustbekämpfen, der Bamsi-Dragi-Etablierung, für unterhaltsame (sehr hitzigen) politische Diskussionen zwischen Franz und Shahin, 15-minütige Abschiedsprozeduren mit Nico, und besonders für die Mittagspausen-Rhein-Brückenrunden-Läufe mit Franz. Meine Pflanzen und ich danken Matthias Frink und Mark Lenkewitz für lustige Abende mit Wii-Bowlen und Waldmeister. Beide zeigten sich immer sehr hilfsbereit. Ich möchte Erik Wilbring für die schöne Rundreise durch China danken, insbesondere für den nächtlichen Aufstieg zum Hua Shan, zu dem Franz und ich ihn genötigt haben. Meiner Freundin Julia Haller danke ich für viel Geduld und Verständnis für Zeiten des Arbeitseifers und Ausklinkens.

Gerade für das letzte Jahr meiner Promotionsphase danke ich all den logistischen Helfern, die sich um die kleine Caro gekümmert haben, und es mir dadurch ermöglicht haben, meine Arbeit abzuschließen. Ich danke Bastian, mir den Freiraum gegeben zu haben, meine Arbeitszeit sehr flexibel gestalten zu können. Ich danke Franz, der mir jeden Abend nach seiner Arbeit die nötige Ruhe verschaffte, um mich der Doktorarbeit widmen zu können. Ich danke meinen Schwiegereltern für die Möglichkeit, bei ihnen zu arbeiten, und für die regelmäßigen Babysit-

terdienste. Für letztere danke ich auch Helene Niecknig und Armin Dressler, sowie Michael Berling, der jederzeit einspringen konnte und mir während der letzten Jahre eine große Stütze war. Caro danke ich für den ab und an nötigen Wechsel des Blickwinkels.

Zuletzt möchte ich meinen Eltern danken, die es mir erst ermöglicht haben, den Weg bis hin zu dieser Doktorarbeit zu gehen und mich dabei immer ermutigt haben.